Metal-organic frameworks: The design, synthesis and investigation of new materials

Warren, Anna

Award date:
2011

Awarding institution:
University of Bath

Metal-Organic Frameworks: The Design, Synthesis and Investigation of New Materials

Anna J. Warren

A thesis submitted for the degree of Doctor of Philosophy

University of Bath

Department of Chemistry

June 2011

Contents

Acknowledgements

I am extremely thankful to my supervisors Paul Raithby, Andy Burrows and Mary Mahon whose assistance, guidance and support throughout my PhD has enabled me to develop an understanding of the subject.

I am also grateful to a number of people who helped me during my PhD, particular thanks go to Chris Richardson and Simon Brayshaw. A special thanks also goes to Steffi Schiffers, Sarica Fuertes Lorda, Chris Woodall, John Warren and Tom Robinson for help and encouragement during long hours of beamtime. I would also like to thank the Burrows group, including Laura Fisher, Vio Pop and Luke Keenan, for their help in the lab, and for enlightening discussions.

It is also a pleasure to thank a number of beamline staff who helped in numerous synchrotron experiments, including John Warren (Daresbury), Simon Teat and Christine Beavers (ALS) and Dave Allan, Harriott Nowell, Sarah Barnett and Kirsten Christensen (Diamond), without their help and support many of the experiments carried out would not have been possible.

Special thanks go to my parents Martin and Jane Stevenson and especially Mark Warren for all his help and support during the last four years, without which, the time during my PhD, and being in Bath would not have been so enjoyable.

Finally I would like to thank both the EPSRC and CCDC for financial support, making the research carried out in this thesis possible.

Abstract

The research in this thesis describes the synthesis and characterisation of new metal-organic framework (MOF) materials, in addition to assessment of systematically selected known materials for their gas storage potential. The majority of these compounds were characterised using single crystal X-ray diffraction techniques.

In Chapter 1 the background to MOFs is introduced, with a brief description of their applications and in particular their use as gas storage materials.

Thirteen new compounds were synthesised and characterised in Chapter 2 in an attempt to obtain a series of compounds with larger pores than $[Cu_2(bza)_4(pyz)]$. Of these, ten were shown to contain the paddle wheel SBU, with the majority containing larger pores.

The use of the Environmental Gas Cell (EGC) was investigated in Chapter 3. The compound $[Zn_2(ox)(atz)_2]\cdot 2MeOH$ was tested and shown *via* single crystal X-ray diffraction to contain 0.42 molecules of SO_2 per asymmetric unit.

In Chapter 4 the synthesis and characterisation of eleven new frameworks, using the bisox ligand and a range of silver(I) salts are described. In particular, one structure exhibited a solid state interconversion on removal of the solvent, monitored using powder X-ray diffraction and TGA.

Seven new compounds based on functionalised β-diketonate ligands, Group 13 and lanthanide metals were synthesised and characterised in Chapter 5. This series of compounds demonstrated that the construction of mixed-metal organic frameworks can be achieved through a two-step reaction forming a metalloligand as an intermediate, and also how hydrogen bonding networks can also be formed from the same ligands.

The final chapter in this thesis concerns the use of the Cambridge Structural Database (CSD) as a means of examining MOF structures that contain guest solvent and gas molecules. The aim of this investigation was to gain an understanding of how these guests interact with the frameworks, with a view to informing the design of new framework materials.

Publications

Andrew D. Burrows, Christopher G. Frost, Mary F. Mahon, Paul R. Raithby, Christopher Richardson and Anna J. Stevenson. **Solid state interconversion of cages and coordination networks *via* conformational change of a semi-rigid ligand**. *Chem. Commun.*, 2010, **46**, 5064.

Andrew D. Burrows, Christopher G. Frost, Mary F. Mahon, Paul R. Raithby, Catherine L. Renouf, Christopher Richardson and Anna J. Stevenson. **Dipyridyl β-diketonate complexes: versatile polydentate metalloligands for metal-organic frameworks and hydrogen-bonded networks**. *Chem. Commun.*, 2010, **46**, 5067.

Andrew D. Burrows, David J. Kelly, Mary F. Mahon, Paul R. Raithby, Christopher Richardson and Anna J. Stevenson. **Silver coordination networks and cages based on a semi-rigid bis(isoxazolyl) ligand**. *Dalton Trans.*, 2011, **40**, 5483.

Abbreviations

NCacac	3-cyano-2,4-pentanedionate
ALS	Advanced Light Source
H_2abdc	2-aminobenzene-1,4-dicarboxylic acid
Hanthr	9-anthracenecarboxylic acid
atz	3-amino-1,2,4-triazole
H_2bdc	1,4-benzenedicarboxylic acid
NH_2H_2bdc	2-aminoterephthalic acid
BET	Brunauer-Emmett-Teller
Hbiphen	Biphenyl-4-carboxylic acid
bipy	4,4’-bipyridine
2,2’-bipy	2,2’-bipyridine
Bismim	4-bis(imidazol-1-yl-methyl)benzene
Bisox	1,4-bis((3,5-dimethylisoxazol-4-yl)methyl)benzene
H_2bpdc	biphenyl-4,4’-dicarboxylic acid
H_2bpdcNH_2	2-aminobiphenyl-4,4’-dicarboxylic acid
H_2bpdcNHBoc	2-(*tert*-butylcarbamate)-biphenyl-4,4’dicarboxylic acid
H_3btb	1,3,5-benzenetribenzoic acid
Hbza	Benzoic acid
caa	3-cyanoacetylacetonate
CH_2Cl_2	Dichloromethane
CH_3Cl	Chloroform
CSD	Cambridge Structural Database
dabco	1,4-diazabicyclo[2.2.2]octane
dbm	Dibenzoylmethanato
ddn	1,12-dodecanedinitrile
DEF	*N*,*N*-diethylformamide
H_2dhtp	2,5-dihydroxyterephthalic acid
DiMepyz	2,3-dimethylpyrazine
dma	*N*,*N*-dimethylacetamide
DMF	*N*,*N*-dimethylformamide
DMSO	Dimethylsulfoxide
DOE	Department of Energy

DPH	2,4-dinitrophenylhydrazine
dpni	*N,N'*-di-(4-pyridyl)-1,4,5,8-napthalene tetracarboxydiimide)
EGC	Environmental gas cell
EtOH	Ethanol
Et_2O	Diethyl ether
H_2fbpdc	2-formyl-biphenyl-4,4'-dicarboxylic acid
H_2fma	Fumaric acid
HIbza	4-iodobenzoic acid
4,5-idca	4,5-imidazoledicarboxylicacid
IM	Imidazolate
IMPT	Intermolecular perturbation theory
3-hypa	*trans*-3-(3-pyridyl) acrylic acid
H3L	1,3-di(3-pyridyl)propane-1,3-dione
H4L	1,3-di(4-pyridyl)propane-1,3-dione
MeCN	Acetonitrile
MeIM	2-methylimidazolate
MeOH	Methanol
Mepyz	2-methylpyrazine
MOF	Metal-organic framework
MMOF	Mixed-metal organic framework
H_2ndc	2,6-napthalenedicarboxylic acid
H_2nhbpdc	2-[(2,4-dinitrophenyl)hydrazonemethyl]biphenyl-4,4'-dicarboxylic acid
NHBoc	*tert*-butylcarbamate
obebi	1,1'-(2,2'-Oxybis(ethane-2,1-diyl))bis(1H-imidazole)
H_2ox	Oxalic acid
paa	3-(4-pyridyl)acetylacetonate
pda	2,4-pentanedionate
H_2pdc	3,5-pyridinedicarboxylic acid
H_3pdc	3,5-pyrazoledicarboxylic acid
ppd	3-(pyridyl)-2,4-propanedione
H_2ppt	3-(2-phenol)-5-(4-pyridyl)-1,2,4-triazole
$H_2$2,4-pydca	Pyridine-2,4-dicarboxylic acid

4-pyrdpm	5-(4-pyridyl)-4,6-dipyrrinato
2,4'-Py_2S	2,4'-thiobis(pyridine)
pytrz	4-(3-pyridinyl)-1,2,4-triazole
pyz	Pyrazine
NH_2pyz	2-aminopyrazine
H_2salphdc	*N,N'*-phenylenebis(salicylideneimine)dicarboxylate
H_2SIP	5-sulfoisophthalic acid
SBU	Secondary building unit
TGA	Thermogravimetric analysis
timb	1,2,4,5-tetrakis(imidazol-1-ylmethyl)benzene
H_3tma	1,3,5-benzenetricarboxylic acid
TMSCN	Trimethylsilylcyanide
H_2tpdc	p-terphenyl-4,4''-dicarboxylic acid
tpp	5,10,15,20-tetra(4-pyridyl)-21H, 23H-porphine
tpt	2,4,6-tri(4-pyridyl)-1,3,5-triazine
ZIF	Zeolitic imidazolate framework

Chapter 1 – Introduction

1.1 Metal-Organic Frameworks

Metal-organic frameworks (MOFs) are a relatively new class of compounds that have been developed over the last 20 years. They are constructed from metal centres linked to each other via organic spacers through coordination bonds.[1] These motifs extend the structure into one, two or three dimensions as seen in Figure 1.1 The bridging organic linker must contain at least one carbon atom sandwiched between two donor atoms which act as the coordination site to the metal.[2] Through careful selection of the metal ion, bridging linker and reaction conditions, it is possible to form targeted MOF materials.[3] The pores created within these structures are what makes them ideal for uses such as catalysis, ion exchange, gas adsorption and separations. The pore sizes can be controlled through different strategies such as changing the length, or functionalising the organic linker, to tune the pore surface for its application.

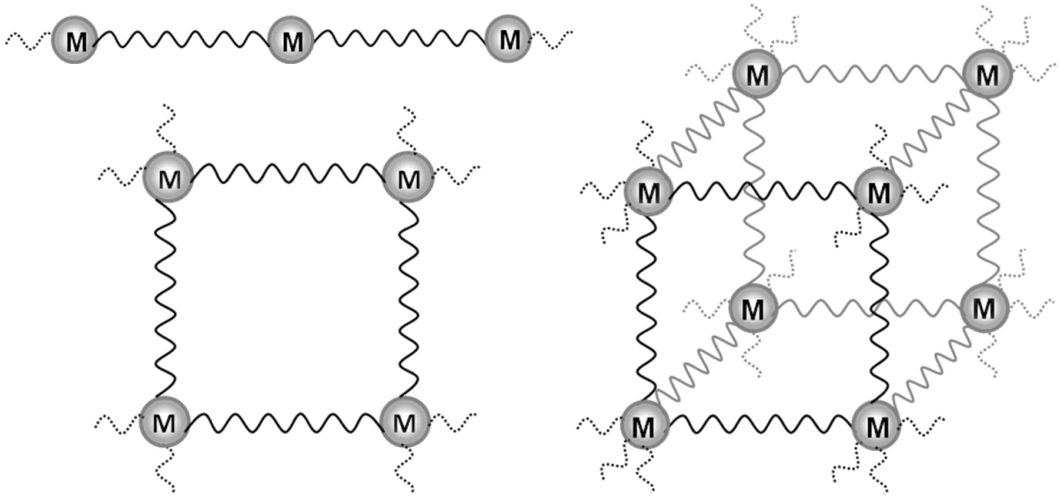

Figure 1.1: Schematic representation of one-, two- and three dimensional MOFs having bridging ligands with at least one carbon atom in-between donor atoms[2]

The coordination geometry of the metal ion is one of the main factors in determining the dimensionality of the MOF that is formed. If, for example, a metal with tetrahedral geometry was used, where all sites were coordinated to a rigid linker, then it is likely that a diamondoid network would be formed. However, there are cases where tetrahedral coordination of the metal is seen, but due to coordinating counter ions, the expected topology is not observed. In the case of $[Ag_2(pyz)_3(CF_3SO_3)_2]$ (pyz = pyrazine), the silver centres have approximately tetrahedral geometry, but one of these sites has a coordinated triflate anion and instead of a three dimensional framework being formed, a one dimensional molecular ladder is observed (Figure 1.2).[4]

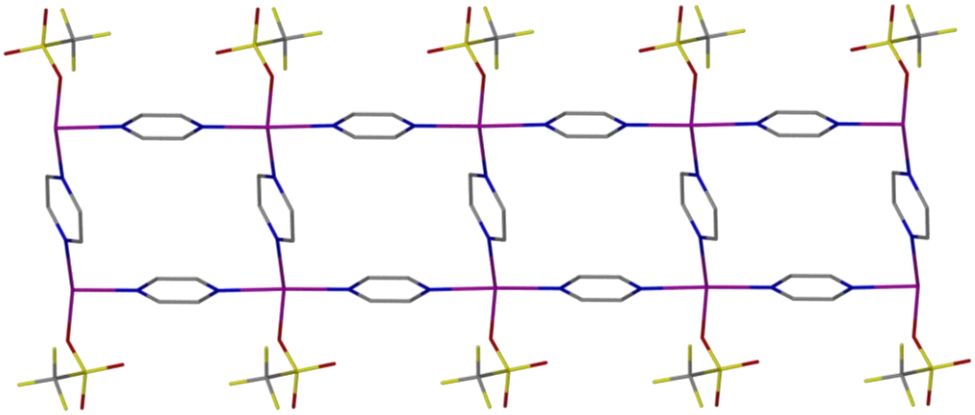

Figure 1.2: Molecular ladder of $[Ag_2(pyz)_3(CF_3SO_3)_2]$ (pyz = pyrazine). Hydrogen atoms have been omitted for clarity[4]

Another factor which greatly affects the network formed is the linker used. If a rigid linker is adopted, the possible prediction of the structure formed is easier. However, if a more flexible ligand is used it can adopt many conformations, and so the variety of possible frameworks increases.

These two factors of the metal geometry and the linker mean a variety of different network architectures can be formed during MOF synthesis. Figures 1.3 and 1.4 show some examples of different networks that can arise due to the presence of different metal geometries and linear linkers. There are very few examples of systems within the literature where the same ligand and metal centre serves to generate one-, two- and three dimensional network structures.[5]

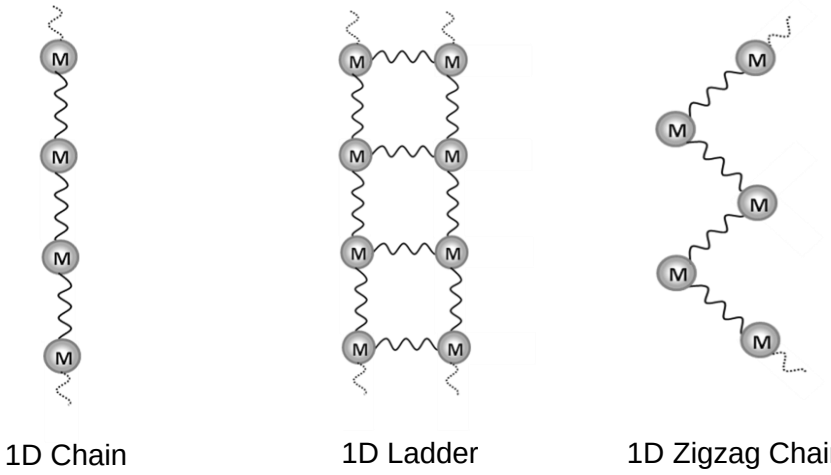

Figure 1.3: Schematic representation of some simple one dimensional networks that have been structurally characterised for MOFs[6]

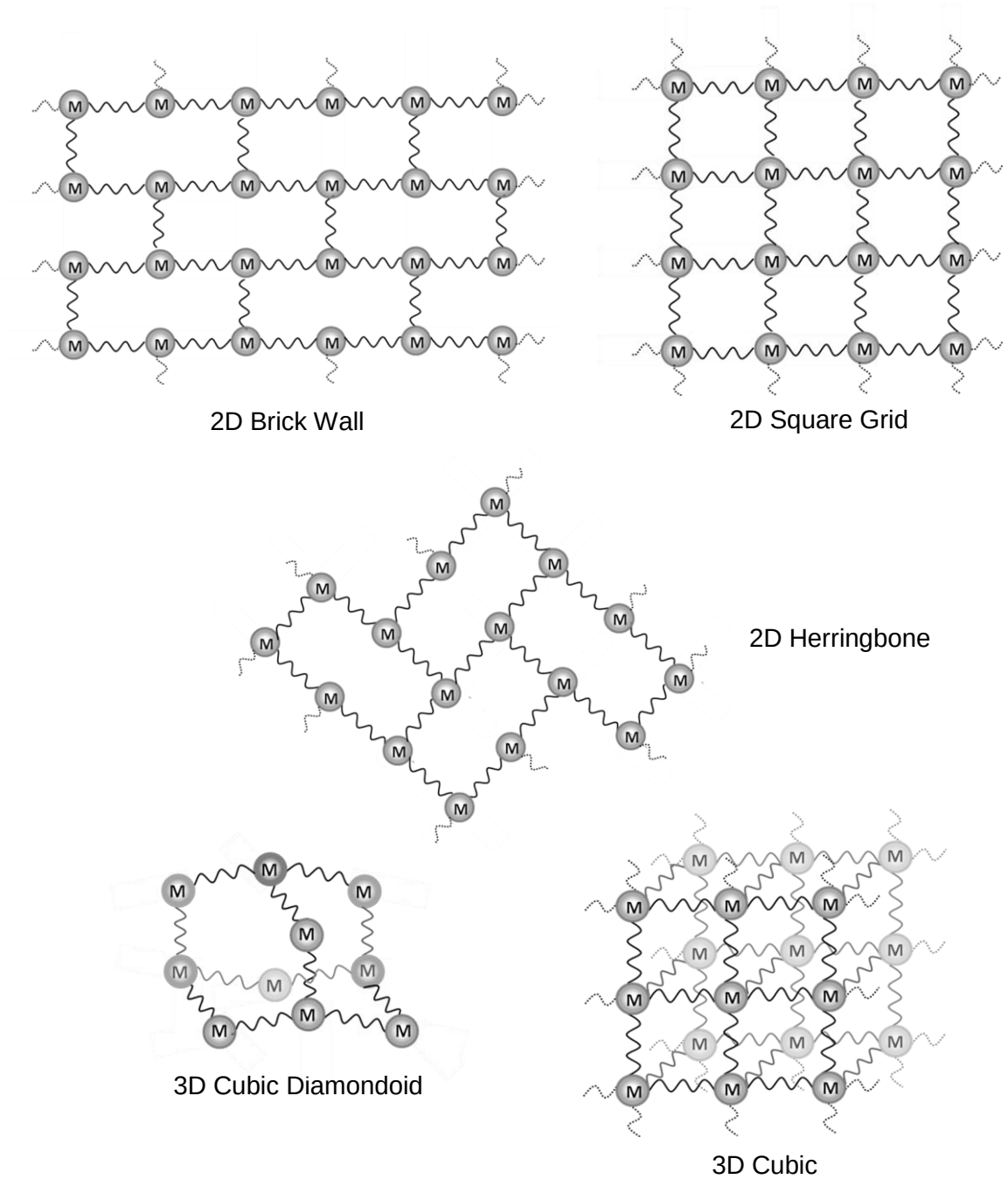

Figure 1.4: Schematic representation of some simple two- and three dimensional network architectures that have been structurally characterised for MOFs[6]

For one dimensional frameworks the stoichiometry is the main factor that influences the type of structure formed; it can either be 1:1 or 1:1.5 (metal ion:ligand). For a 1:1 ratio, the zigzag structure is one of the most common networks formed. In this structure, the polymer chains often pack efficiently so cavities are very rarely seen. The helical polymer can also be formed from a 1:1 ratio but is much more uncommon. Despite this, there is extensive research into these latter structures due to their inherent

chirality, irrespective of the starting materials. Like the zigzag chains, helical structures do not generally contain pores. If a 1:1.5 stoichiometric ratio of metal to ligand is used, a molecular ladder structure is often obtained. The difference between this and the zigzag or helical structures, is that there are now cavities present within the architecture, which may be large enough to house individual or pairs of guest molecules.[7]

The topology of a two dimensional network is determined by two primary factors; how the terminal ligands are coordinated (i.e. degree of chelation), and the ratio of metal to ligand. The square grid network is the simplest and most common of the two dimensional coordination polymers, and it arises from a 1:2 ratio of metal to ligand. These structures contain pores which are able to encase guest molecules that lie in the sheets of the network.[6] The brick wall and herringbone structures are produced from a 1:1.5 metal to ligand ratio, which is the same as that used to form some of the one dimensional systems and this is where problems can arise in the prediction of framework formation.

Two of the simplest three dimensional structures are those made from interlinking tetrahedra or octahedra to form the cubic diamondoid and the cubic networks, respectively. The octahedral networks are much less common than the tetrahedral frameworks, but both types of structure can show a high degree of porosity. However, with such high porosity, there are many associated problems that can arise, including the presence of guest molecules which occupy this pore space.

Reaction conditions also impact on the MOF formed. The same concentration of reagents may be used during the synthesis, but at a slightly different temperature, or in a more dilute solution, and a completely different structure may be formed.[8]

Many groups of frameworks have been synthesised where the ligand and reaction conditions are constant, while the metal salt is altered. Where a charge in the system must be balanced, the anion from the metal salt can play a vital role. For example, in the case of the reactions between $Cd(NO_3)_2$, $Cd(ClO_4)_2$ and $Cd(BF_4)_2$ and 1,2,4,5-tetrakis(imidazol-1-ylmethyl)benzene (timb), three isostructural materials are obtained. When the same ligand is reacted under the same conditions with $CdCl_2$ or $CdSO_4$, then

two new structures are obtained (Figure 1.5).[8] This demonstrates how important the anion can be in structure formation.

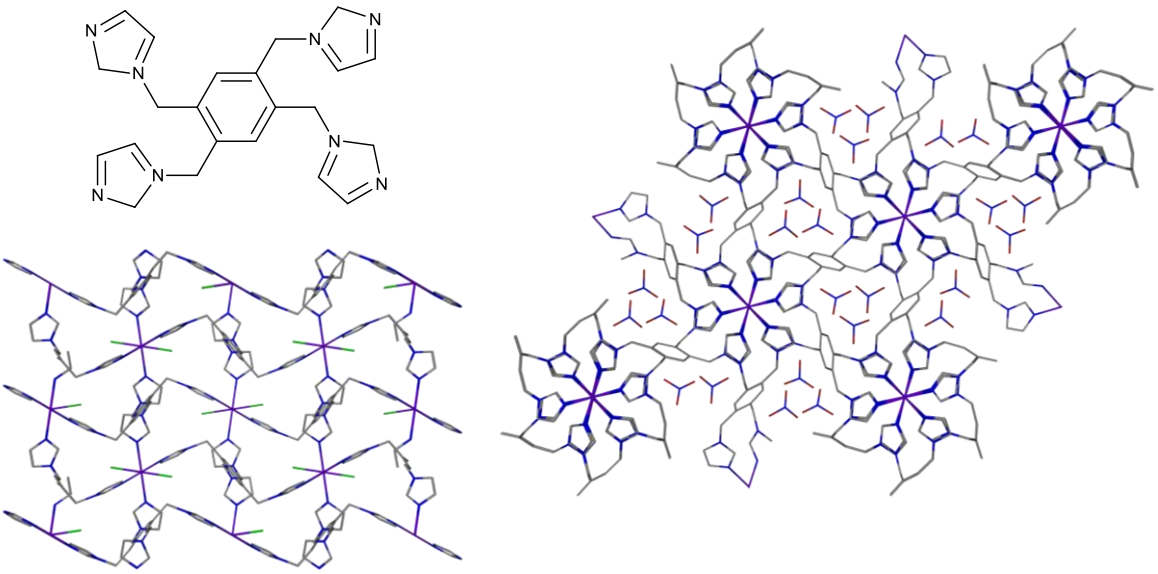

Figure 1.5: Tetrakis(imidazol-1-ylmethyl)benzene (timb) (top left), $[Cd(timb)Cl_2]\cdot 2H_2O$ (bottom left) and $[Cd_2(timb)_3](NO_3)_4\cdot 6H_2O$ (right)[8]

Generally, *d*-block transition metals are used during the synthesis of framework structures. This is due to the predictability of the likely geometries that would be formed around the metal centres. The most common connectivities are two, three, four and six coordinate. Although these metals are good for predicting what structures may be formed, it is hard to form a material with a greater connectivity than six. For this reason lanthanides are often used in MOF synthesis as they have been shown to have metal connectivities up to twelve. Their coordination geometries however are harder to predict, and so expected topologies of networks that may be formed are harder to rationalise.

1.2 MOF Synthesis

The synthetic procedure for MOF formation is generally quite straightforward, whereby the specified metal salt and the appropriate ligand are placed together in a suitable solvent. These reactions can then either be heated to a particular temperature, though many occur at room temperature. Although the technical details underpinning the syntheses are easy, it is often difficult to form crystals from the reaction, and single crystal X-ray diffraction is the main method for analysing the samples made. In order to form single crystals, many of the reaction conditions have to be altered before crystals can be formed, making the process time consuming.

For many of the potential applications of network materials, it is important for pores to be present, and for these to be accessible. When trying to synthesise porous networks, many difficulties can arise. Generally systems avoid large pores, and will adapt to alleviate their formation. Common methods of stopping their formation include the following:

1) When a network is cationic, counter ions can occupy the pores.[9, 10]
2) Guest molecules may occupy the pores.[11] Removal of these guests can often cause the collapse of the framework.
3) Interpenetrated structures may be produced (See section 1.5).[12]

There are other issues which can be encountered during the synthesis of MOFs. If a particularly labile metal ion is used in the synthesis, while coordination will frequently occur, the prediction of the geometry will be very difficult. One strategy to overcome this problem is to incorporate the use of secondary building units (SBUs) into the motif.

1.3 Secondary Building Units

Tailor made syntheses of MOFs can be assisted by taking into account the concept of SBUs. SBUs are small units constructed from one or more metal ions and the donor atoms of multidentate linkers creating rigid entities which are repeated throughout the whole network. The most commonly used linkers are carboxylate ligands, which lock the metal ions, the primary building units, into place, thereby maintaining the shape of this SBU within the gross structure. SBUs can be used to construct more complicated network structures, whilst maintaining high porosity and structural stability. Consideration of the chemical and geometric make up of the SBU together with the linker geometry allows the topology of the network to be predicted. Also, since the majority of SBUs are constructed from carboxylates the combination of these with metal cations lead to neutral networks, therefore there is no requirement for the presence of counter ions which would occupy pore space. If neutral ligands were employed in MOF construction, the charge of the metal would not be balanced and a counter ion would need to be housed within the pores.[13]

One of the most common SBUs is the dimetallic tetracarboxylate $M_2(O_2CR)_4$ unit, also known as a paddle wheel unit. The $M_2(O_2CR)_4$ unit is a ‘square’ SBU because the geometry of the SBU is approximately square planar. There are many reports in the

literature, particularly with copper(II) ions that exhibit this geometry. These examples contain mono-,[14] di-[15] and tri-carboxylates,[16] and one of the best known examples, which has been highly studied, is the material arising from 1,3,5-benzenetricarboxylate (trimesate (tma)), $[Cu_3(tma)_2(H_2O)_3]$[16] (HKUST-1, Figure 1.6). The SBU is constructed from a dimetallic unit, in which each copper centre has approximate square pyramidal geometry. Four of the carboxylate groups from the four tma ligands coordinate to the copper centres in a bridging bidentate manner, at approximately 90º to each other. Positioned in the axial position is a water molecule, which projects into the pores of the MOF. The other carboxylate functionalities on the tma coordinate to other copper paddle wheel units, and link the whole structure into three dimensions. The structure is highly porous, and has been shown to have a Brunauer-Emmett-Teller (BET) surface area of 692 $m^2\ g^{-1}$.[16]

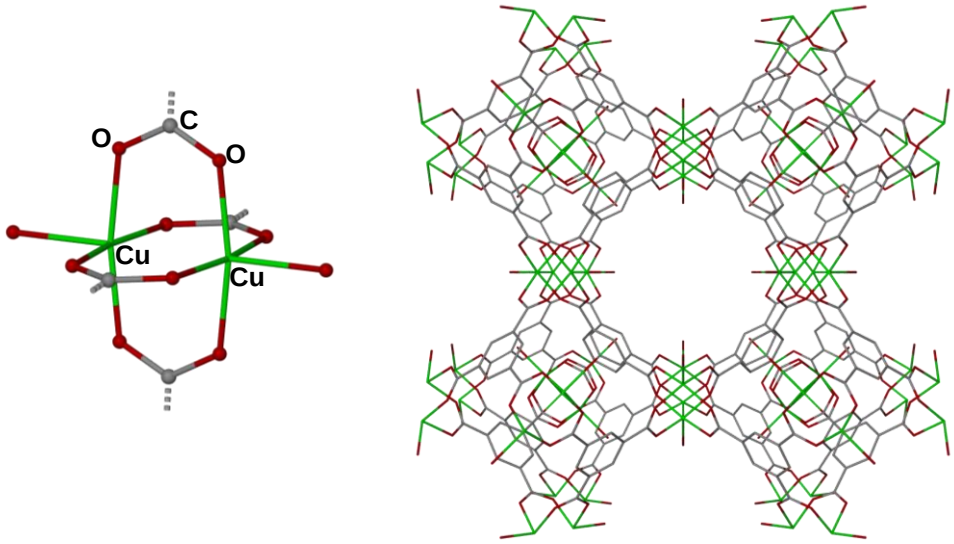

Figure 1.6: The SBU (left) and the gross packing (right) present in $[Cu_3(tma)_2(H_2O)_3]$ (tma = 1,3,5-benzenetricarboxylate). Hydrogen atoms have been omitted for clarity[16]

Another well known example of a framework constructed from a repeating SBU is MOF-5 ($[Zn_4O(bdc)_3]$) (bdc = 1,4-benzenedicarboxylate). The SBU consists of a central tetrahedral oxide ion coordinated to four tetrahedral zinc atoms, which are the primary building units. The carboxylates then coordinate to these zinc centres forming the secondary building unit, now with octahedral geometry. Due to this linking through the bridging of the bdc, a three dimensional cubic network is formed Figure 1.7.[17]

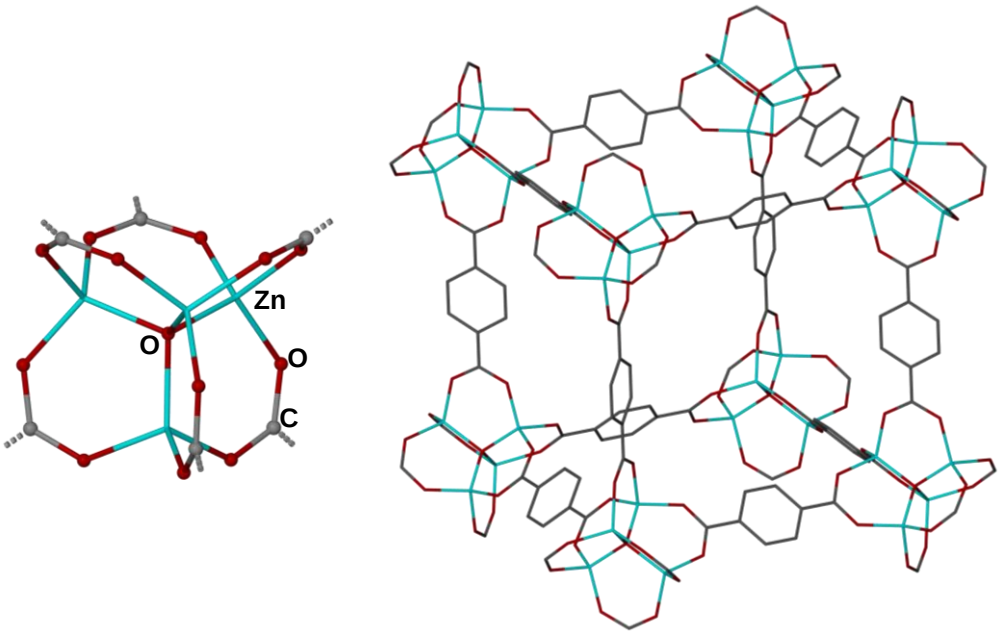

Figure 1.7: The SBU (left) and the three dimensional cubic network (right) of $[Zn_4O(bdc)_3]$ (bdc = 1,4-benzenedicarboxylate). Solvent molecules and hydrogen atoms have been omitted for clarity[17]

1.4 Isoreticular Series

MOF-5 was first characterised by *Yaghi et al.*.[18] This highly porous network, which has since been shown to be capable of adsorbing many gases, led the group to increase the linker length, as seen in Figure 1.8 in an attempt to increase the pore size. The same gross structure as MOF-5 results, due to the same SBU being present at the vertices of each cube, and as the linker length increases, so does the pore size. These networks are known as an isoreticular series. *Yaghi et al.* also synthesised a variety of frameworks using functionalised carboxylates. Again the same SBU is formed, but due to the functionality most of these result in a decrease in pore size (Figure 1.9).[18]

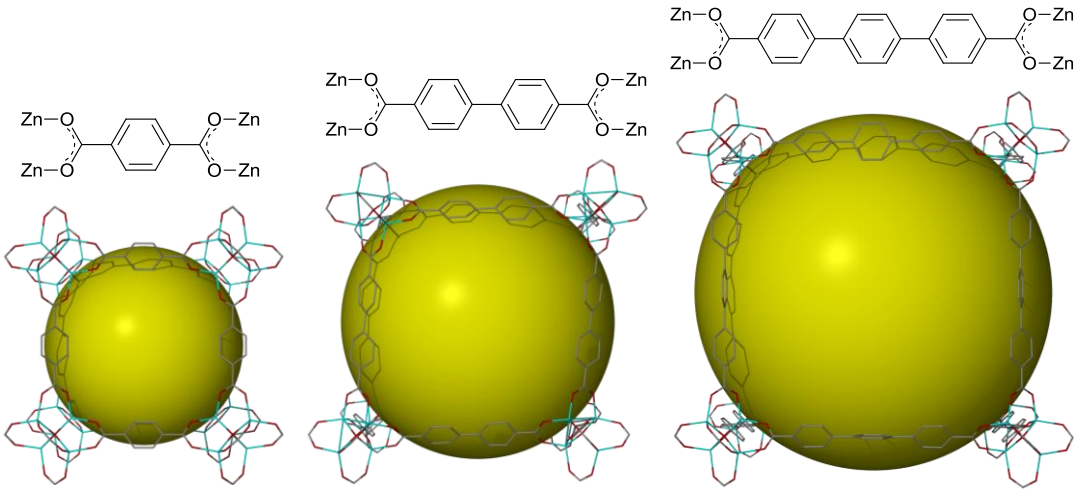

Figure 1.8: Isoreticular MOFs based on the $Zn_4O(O_2CR)_6$ SBU with different linker lengths. The yellow spheres represent the largest van der Waals spheres that would fit within a single framework cube. Hydrogen atoms have been omitted for clarity[18]

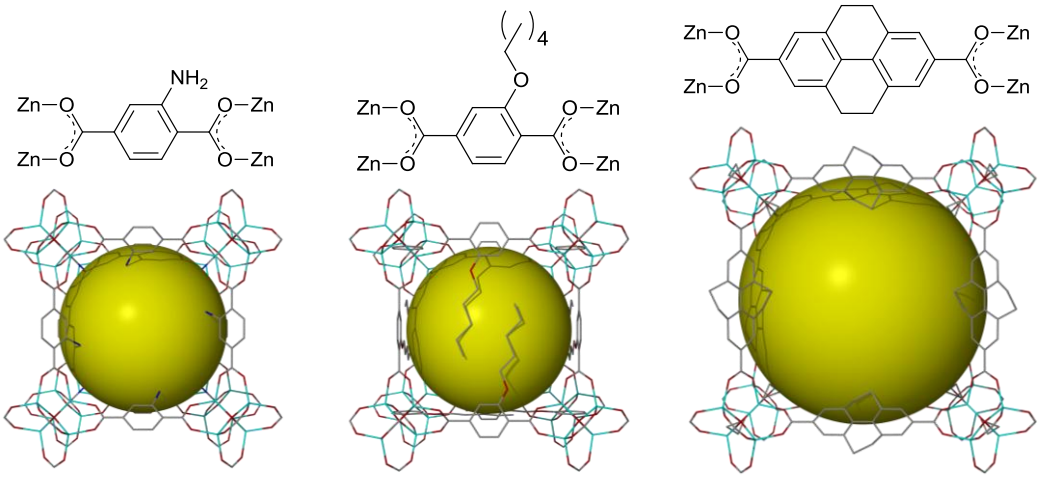

Figure 1.9: Isoreticular MOFs based on the $Zn_4O(O_2CR)_6$ SBU with different functionalised linkers. The yellow spheres represent the largest van der Waals spheres that would fit within a single framework cube. Hydrogen atoms have been omitted for clarity[18]

1.5 Interpenetration

Another issue which can arise during the synthesis of MOFs is the network becoming interpenetrated. Increased size of the bridging ligands (Figure 1.8) in MOF structures can produce larger cavities than those seen in zeolites. The pore diameters in dehydrated zeolites are approximately 6 Å, whereas in MOFs cavities have been seen up to 16 Å in size, accounting for more than half the volume of the crystal.[19] However, linker length increase does not always give larger pores; instead of increasing the cavity size a second network can interpenetrate the first, as seen in Figure 1.10. Interpenetration is where a second network can become interwoven through the first,

causing a reduction in pore size when compared to the pore size of the non-interpenetrated structure. It can be seen as the polymeric equivalent to molecular catenanes and rotaxanes.[20] The only way in which the networks can now be separated is through the breaking of bonds.[21]

In Figure 1.10 is the structure of IRMOF-15 [$Zn_4O(tpdc)_3$] (tpdc = p-terphenyl-4,4''-dicarboxylate) which is isoreticular with the MOF-5 structure previously seen in Figure 1.7.[17] The structure consists of the same $Zn_4O(O_2CR)_6$ SBUs but now linked together by bridging tpdc linkers. In this case, the structure is doubly interpenetrated with another interwoven network (Figure 1.10). It has also been shown that the comparative non-interpenetrating structure can be synthesised, by using more dilute solutions during the synthesis (Figure 1.8).[17]

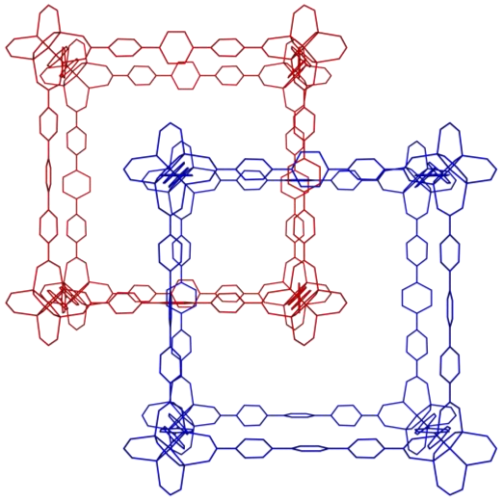

Figure 1.10: Doubly interpenetrated network of IRMOF-15 [$Zn_4O(tpdc)_3$] (tpdc = p-terphenyl-4,4''-dicarboxylate.[17] *Hydrogen atoms have been omitted for clarity*

More recently, research has been carried out looking at the effect of temperature and concentration on the products formed. The MOF [Cd(bipy)(bdc)] (bipy = 4,4'-bipyridine) has a structure consisting of dinuclear $Cd_2N_2O_8$ SBUs linked into a square grid by the bdc linkers. These two dimensional square grids are then pillared by the bipy ligands to form the three dimensional cubic network. This has been previously reported as a doubly interpenetrated structure. *Zawarotko et al*. managed to synthesise the non-interpenetrated form of this material at 85 °C. These studies at different temperatures and concentrations revealed that at lower starting material concentrations the non-interpenetrated form is favoured, whereas at higher concentrations both forms are observed. It was also noted that at higher concentrations and temperatures the interpenetrated form is preferred.[22]

Interpenetration is not always seen as a disadvantage in a MOF, as in some structures it does not completely eliminate the pores. Its presence can actually increase the surface area, which is beneficial in gas storage.[23] Moreover, the interpenetrated structure stability is often enhanced due to the presence of weak interactions between the constituent networks.

It is possible for structures to contain more than two interpenetrating networks at one time. In coordination polymers, ten interpenetrating nets have been observed in the diamondoid compound $[Ag(ddn)_2][NO_3]$ (ddn = 1,12-dodecanedinitrile).[24]

In general, if the pore within a structure gets larger, then more interpenetration is likely to be observed. However, *Robson et al.* reported on the structure of $[(Cu_2(O_2CCH_3)_4)_3(tpt)_2]\cdot 2MeOH$ (tpt = 2,4,6-tri(4-pyridyl)-1,3,5-triazine), in which large pores were present, but through non-bonding interactions they were able to overcome the problem of interpenetration. The structure consists of copper acetate dimers linked in the axial position to tpt ligands, extending the structure into two dimensions. The hexagonal pores within the structure are approximately 18 Å in diameter, and would be expected to be involved in interpenetration. However, in this particular structure the layers are puckered, and through π-π non-bonding interactions, they stack in an alternating fashion, thereby negating the need for interpenetration to occur.[25]

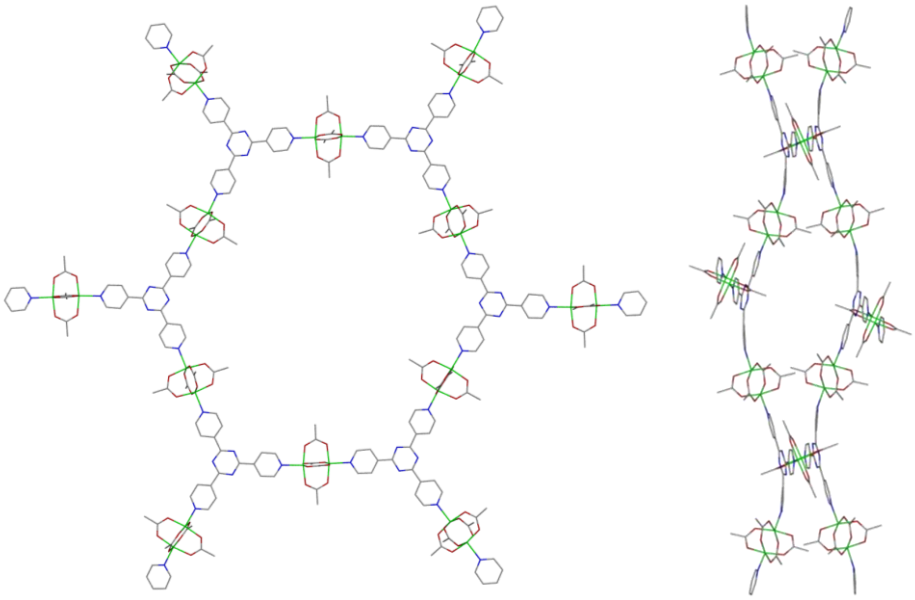

Figure 1.11: The two dimensional hexagonal grid structure of $[(Cu_2(O_2CCH_3)_4)_3(tpt)_2]\cdot 2MeOH$ (tpt = 2,4,6-tri(4-pyridyl)-1,3,5-triazine) (left) and the view of the puckered layers (right). Hydrogen atoms have been omitted for clarity[25]

A more recent strategy employed to avoid interpentration, is to synthesise a MOF with a bulky functional group on the linker which fills the pore space.[26] For example, *Tefler et al.* examined this method using the $Zn_4O(O_2CR)_6$ SBU linked with a biphenyl-4,4'-dicarboxylate (bpdc) linker, producing the isoreticular structure as seen in Figure 1.12. The linker was functionalised with a bulky *tert*-butylcarbamate (NHBoc) group which was subsequently removed via thermolysis to produce the non-interpenetrated amine functionalised structure.[27]

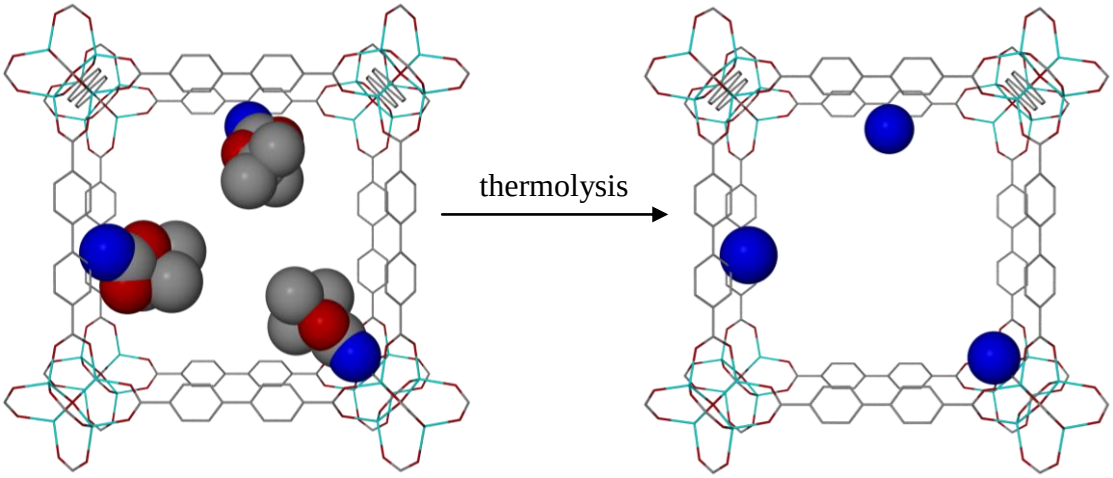

Figure 1.12: The structure of $[Zn_3O(bpdcNHBoc)_3]\cdot 5H_2O$ (left) and $[Zn_3O(bpdcNH_2)_3]$ (right) after thermolysis (bpdcNHBoc =2-(tert-butylcarbamate)-biphenyl-4,4'dicarboxylate, $bpdcNH_2$ = 2-aminobiphenyl-4,4'-dicarboxylate). Hydrogen atoms have been omitted for clarity[27]

Increased pore size can sometimes be stabilised by the presence of guest molecules, rather than interpenetration. It is possible to remove these guest molecules from the network, affording a highly porous material with gas storage potential.[11] Unfortunately, removal of guest molecules often leads to framework collapse.

1.6 Mixed Metal Systems

Heterometallic systems are those which contain two different metals within the network structure. As stated previously, most reactions to form MOFs are simple to carry out, but formation of desired products can often be hard to control, with little predictability.[28, 29] This is where mixed metal systems have an advantage, as these can be formed in a stepwise manner, affording more control over the network formation. The first step is to form a metalloligand through the reaction of a metal centre with an appropriate bifunctional ligand. The binding to this first metal provides high thermodynamic stability and/or kinetic inertness, which can then allow the addition of

another metal to the complex. This metalloligand can then be reacted further with a suitable metal to form a targeted mixed metal system.

The metalloligand can act as a building block to construct more complicated networks, whilst maintaining rigidity and stability within the network. It can work in a similar manner to a SBU, by extending the size of channels but often reducing the need for interpentration to occur.

One such example of a mixed metal system was reported by *Cohen et al.* who produced metalloligands of the type $[M(4\text{-pyrdpm})_3]$ (M = cobalt(III)/iron(III), 4-pyrdpm = 5-(4-pyridyl)-4,6-dipyrrinato) (Figure 1.13). The metals in these compounds have approximate octahedral geometry, and the ligands are deprotonated in the reaction to produce a neutral compound. The free pyridyl groups project out from the metalloligand with an approximate trigonal planar geometry, in preparation of coordination to another metal. It was predicted that reacting this metalloligand with a suitable metal with trigonal planar geometry would form a two dimensional MOF constructed from six membered rings.

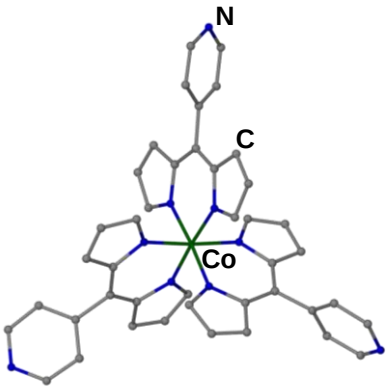

Figure 1.13: The metalloligand $[Co(4\text{-pyrdpm})_3]$ (4-pyrdpm = 5-(4-pyridyl)-4,6-dipyrrinato). Hydrogen atoms and solvent molecules have been omitted for clarity[30]

This cobalt(III) containing metalloligand was reacted with AgO_2CSO_3 which maintained the 3-fold symmetric centre as anticipated, where the $[Co(4\text{-pyrdpm})_3]$ complexes were linked with silver(I) via the pyridyl nitrogen atoms to adjacent metalloligands. Each silver(I) centre is coordinated to three pyridyl groups and one triflate counterion, in a distorted tetrahedral arrangement. The cobalt(III) centre maintains its octahedral geometry, which creates the expected 3-fold symmetric centre (Figure 1.14). The mixed metal network is doubly interpenetrated, reducing the channel size within the structure, and there are also two molecules of acetonitrile within each

pore, suggesting that the material would be porous if these solvent molecules could be removed.[30]

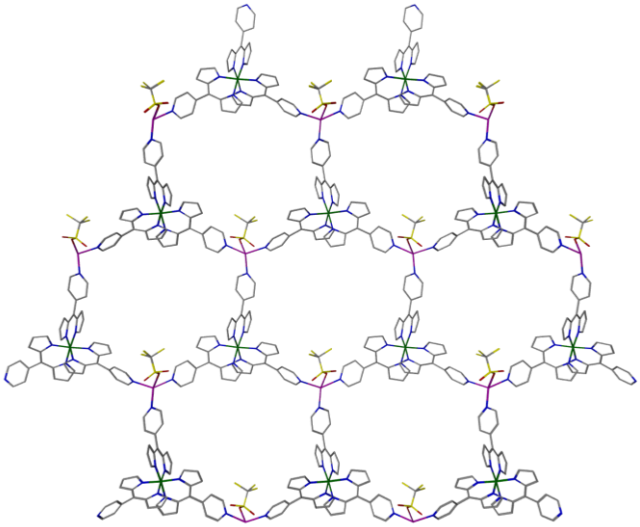

Figure 1.14: The mixed metal system [Co(4-pyrdpm)$_3$Ag(O_2CCF_3)] (4-pyrdpm = 5-(4-pyridyl)-4,6-dipyrrinato). Hydrogen atoms and solvent molecules have been omitted for clarity[30]

Transition metal lanthanide mixed metal supramolecular compounds attract much attention in this area due to their properties which are highly exploitable in many application areas, including magnetism, molecular sensors, luminescent materials and adsorption materials.[31] Ligands can be tailored to bind both to transition metals and lanthanides, by utilising the chemical preferences of the metals. A structure which demonstrates this property is that of [GdCo(3,5-pdc)$_2$(3,5-Hpdc)$(H_2O)_7$]·H_2O (3,5-H_2pdc = 3,5-pyridinedicarboxylic acid). Here the gadolinium(III) ions exist with eight coordinate geometry coordinating to five oxygen atoms from four different 3,5-pdc ligands, and three coordinated water ligands. The nitrogen atom from one of the 3,5-pdc ligands is protonated, thus forming the pyridinium cation, and the other two 3,5-pdc ligands coordinate to the elongated axial positions of the cobalt(II) ions through the nitrogen atoms. The octahedral coordination sphere of the cobalt(II) is completed by coordination of four water molecules in the equatorial positions. This structure extends into a two dimensional layered network, where these layers stack on top of each other through the π-π stacking of the parallel pyridinium groups. Overall the chemical preference of the two metals is exploited, through the coordination of the harder lanthanide metal to the carboxylate groups, and the coordination of the softer cobalt(II) centre to the softer nitrogen donor groups.[32]

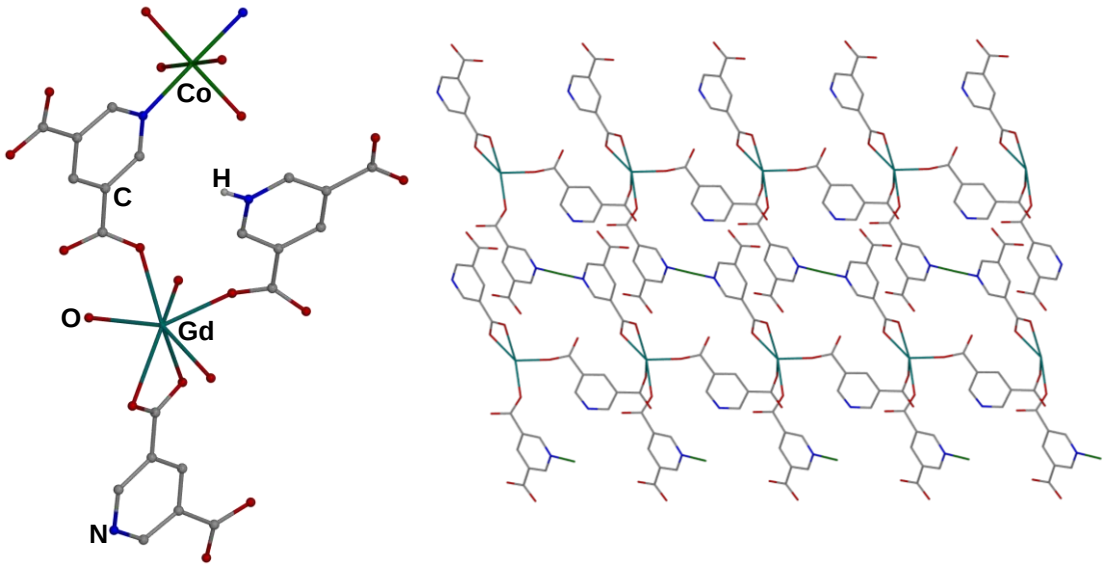

Figure 1.15: Asymmetric unit of [GdCo(3,5-pdc)$_2$(3,5-Hpdc)(H$_2$O)$_7$]·H$_2$O (3,5-pdc = 3,5-pyridinedicarboxylate, 3,5-Hpdc = 3,5-pyridiniumdicarboxylate) (left) and its two dimensional layered structure (right). Coordinated and guest water molecules have been removed in the packing diagram for simplicity, and hydrogen atoms, except on the pyridinium nitrogen, have been omitted for clarity[32]

Mixed-metal systems in which one of the metals is coordinatively unsaturated are attractive materials for catalysis. In a similar manner to the previous examples, the networks can be formed via a two-step self assembly reaction. The metalloligand that is formed can act as the framework linker, whilst also containing an unsaturated metal centre. This can then be reacted with another metal to form the vertices of the framework, and the unsaturated metal centres will be housed within the pores.[13] One example of this structural type is the compound [Zn$_2$(OH)$_2$(Cu(salphdc))$_2$]·2DMF (salphdc = *N,N'*-phenylenebis(salicylideneimine)dicarboxylate) (Figure 1.16). In this structure, the first step is the formation of [Cu(H$_2$salphdc)], the metalloligand, leaving the dicarboxylic acid on the metalloligand free to coordinate with the zinc(II) centres to form the corners of the framework. The pores of the structure then contain unsaturated copper(II) centres, which could be exploited in highly selective molecular recognition and heterogeneous catalysis.[33]

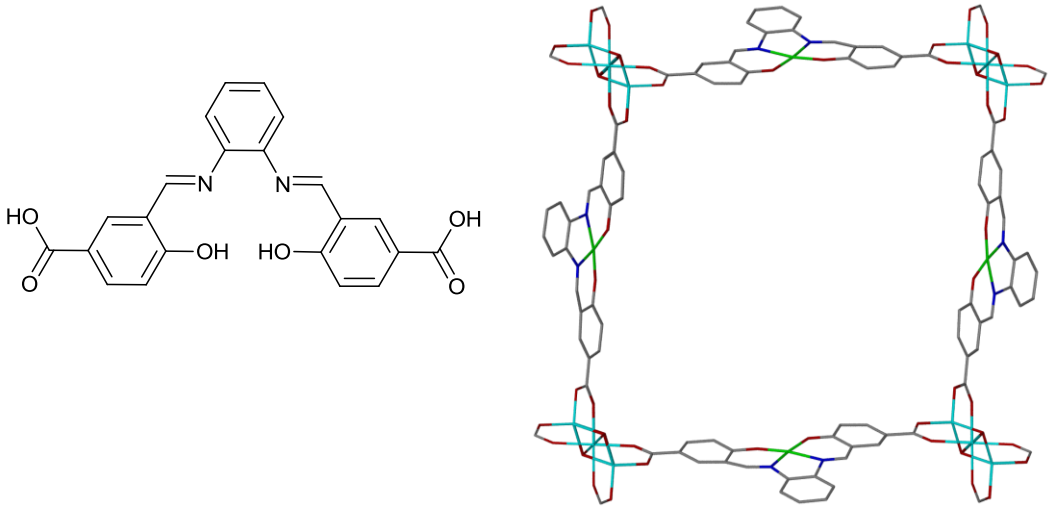

Figure 1.16: H_4salphdc (left) and the structure of $[Zn_2(OH)_2(Cu(salphdc))_2]\cdot 2DMF$ (right) (salphdc = N,N'-phenylenebis(salicylideneimine)dicarboxylate). The zinc metal centres are shown in blue and the unsaturated copper centres are shown in green. Hydrogen atoms have been omitted for clarity[33]

1.7 Metal-Organic Framework Linkers

1.7.1 Flexible Bridging Ligands

As mentioned previously, the prediction of MOF structures becomes much more difficult when flexible ligands are used. Here conformational isomerism in the ligands is possible, and hence supramolecular isomerism in the coordination polymer can be obtained. For many years, the use of flexible ligands was not exploited due to this fact, but more recently these ligand types have been employed as they can allow the network to reversibly respond to the presence or absence of guest molecules.[34]

There are many examples in the literature which have exploited the use of flexible ligands for desired properties, and to design a range of new framework materials.[35-38] Due to the nature of the ligand, and its lack of predictability the metal cations, guest anions and solvent molecules play a vital role in network formation.

1,1'-(2,2'-Oxybis(ethane-2,1-diyl))bis(1H-imidazole) (obebi) is an example of a flexible ligand that has been used in MOF synthesis (Figure 1.17). As a linker, it can adopt two different conformations, the *cis* and the *trans*, and through the reaction with a variety of metal salts and carboxylic acids, a range of frameworks could be obtained from one through to three dimensional structures. When the ligand was reacted with

zinc(II) or cobalt(II) with bdc, two different network structures were obtained, [Zn(bdc)(obebi)]·1.5H_2O and [Co(bdc)(obebi)].[36]

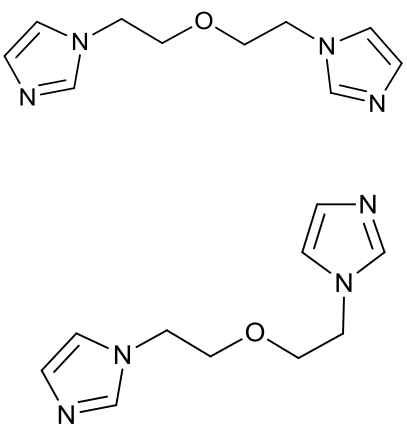

Figure 1.17: The cis (top) and trans (bottom) conformations of 1,1'-(2,2'-Oxybis(ethane-2,1-diyl))bis(1H-imidazole) (obebi)[36]

In [Zn(bdc)(obebi)]·1.5H_2O, the zinc(II) centres exist with approximate tetrahedral geometry coordinating to two nitrogen atoms from two obebi ligands and two oxygen atoms from two bdc ligands. The obebi ligands both adopt the *cis* conformation, and the two of these bridge two zinc(II) centres together forming a $Zn_2(obebi)_2$ unit. The linear bdc ligands then link each unit together forming a three dimensional triply interpenetrated diamondoid framework (Figure 1.18).[36]

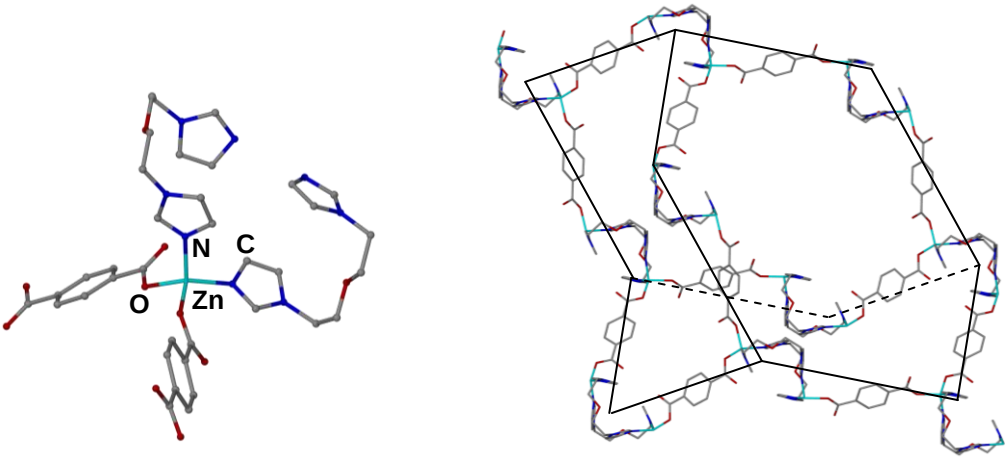

Figure 1.18: The building unit (left) and a diamondoid cage (right) of [Zn(bdc)(obebi)]·1.5H_2O. Solvent molecules and hydrogen atoms have been omitted for clarity[36]

The [Co(bdc)(obebi)] framework is constructed from distorted octahedral cobalt(II) centres. These cobalt(II) centres coordinate to four oxygen atoms from two bdc ligands,

and two nitrogen atoms from two obebi ligands. Only one of the obebi ligands connects two adjacent cobalt atoms together, adopting the *cis* conformation, forming a left-handed helical chain. The linear bdc ligands then link to adjacent cobalt(II) centres, and each Co(obebi) chain has a right-handed helical arrangement. The gross packing of this network forms two dimensional zigzagged chains (Figure 1.19).[36]

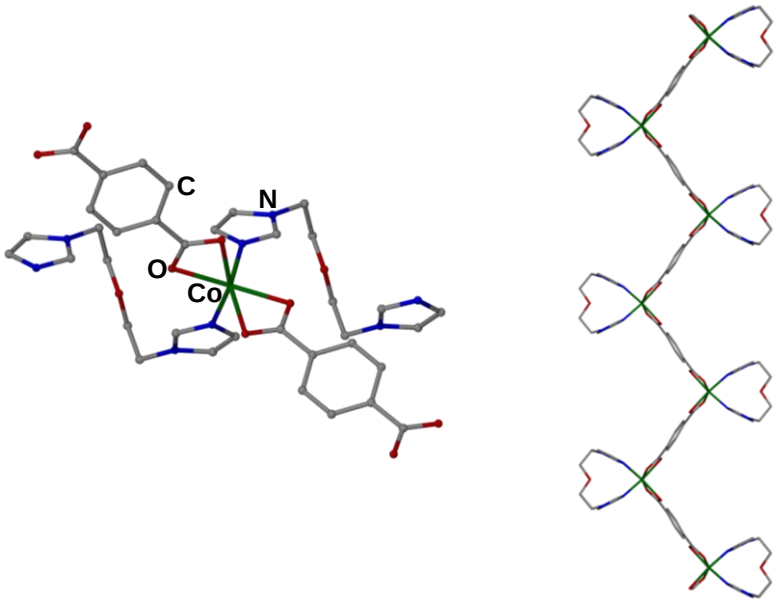

Figure 1.19: The building unit (left) and a two dimensional zigzag chain (right) of [Co(bdc)(obebi)]. Hydrogen atoms have been omitted for clarity[36]

1.7.2 Carboxylate Ligands

Carboxylates are one of the most common types of linkers used in MOF synthesis owing to the formation of SBUs as seen in many structures. Carboxylates are considered to be hard ligands, so form strong bonds with hard metal centres. The main choice of metals used to bind to carboxylates are transition metals, which can form a wide variety of coordination geometries affording many different network architectures.[7] There are also numerous examples where carboxylates coordinate to lanthanide metals, with coordination numbers typically between eight and twelve. The carboxylate groups have been shown to coordinate in a variety of modes, forming coordination bonds. Figure 1.20 shows some of the possible binding modes of bdc.[39]

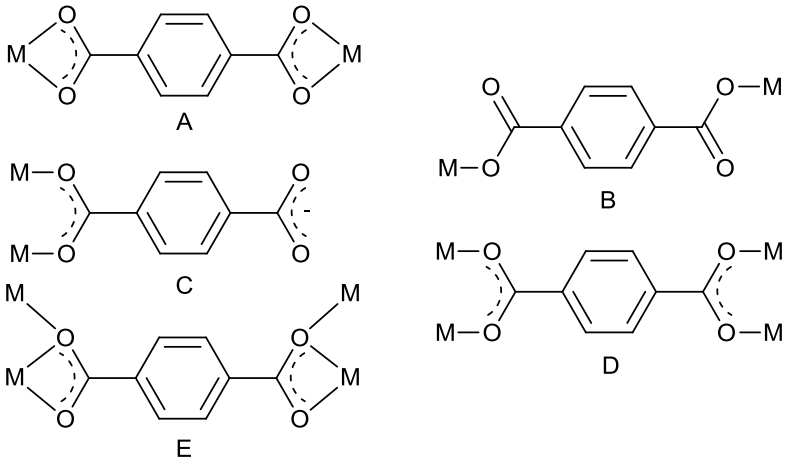

Figure 1.20: The coordination modes of bdc; (A) chelating bis-bidentate, (B) bis-monodentate, (C) mono-bidentate, (D) bridging bis-bidentate, (E) chelating/bridging bis-bidentate[39]

1.7.3 Nitrogen Donor Ligands

Nitrogen donor ligands have been widely employed as linkers in MOF synthesis. Pyridine-based ligands show better donor ability towards the metal centres in comparison to primary amines, producing more stable networks. The metal-N coordination bond is relatively labile in comparison to a metal-carboxylate bond, and this allows easy rearrangements during self-assembly, often leading to supramolecular isomerism, and producing a range of new structural motifs. This can have an impact on the porosity of the network, often reducing it due to this lability.

Unlike carboxylates, most pyridyl ligands are neutral, and once reacted with a cationic metal centre the network produced will retain a charge that must be balanced by counter ions, which have to be incorporated into the framework. These anions are often located within the pores of the network, reducing the size of this cavity. However, cationic frameworks have some advantages, as the presence of the anions can reduce or stop interpenetration from occurring, due to the reduction in excessive pore space. There are cases where the anions in the pores can be reversibly exchanged with other anions, as they interact so weakly with the framework that the exchange does not disrupt the overall architecture. These materials have a functional use due to their switching ability.[40, 41]

An example of this anion exchange occurs with $[Cu_3(\mu_3\text{-pytrz})_3(\mu_3\text{-O})(H_2O)](ClO_4)_{2.5}(BF_4)_{1.5}\cdot 5.25H_2O$ (pytrz = 4-(3-pyridinyl)-1,2,4-triazole) (Figure 1.21). This structure

has been shown to be capable of exchanging the tetrafluoroborates completely with perchlorates. The structure consists of three copper(II) centres with square planar geometry linked via a μ_3-bridging central atom. The other three positions of the copper coordinate to the pytrz ligands, which bridge the copper centres to each other. This forms a triangular trinuclear SBU, which through coordination to eight other SBUs generates a nanosized pore within the structure, constructed of $Cu_{24}(pytrz)_{12}$ units. This pore is occupied by four perchlorate and twelve tetrafluoroborate anions, with the remaining perchlorate anions positioned between these cages. It is possible to then completely exchange the tetrafluorborates with perchlorate ions, which are then positioned in approximately the same positions as the tetrafluoroborate ions were originally.[42]

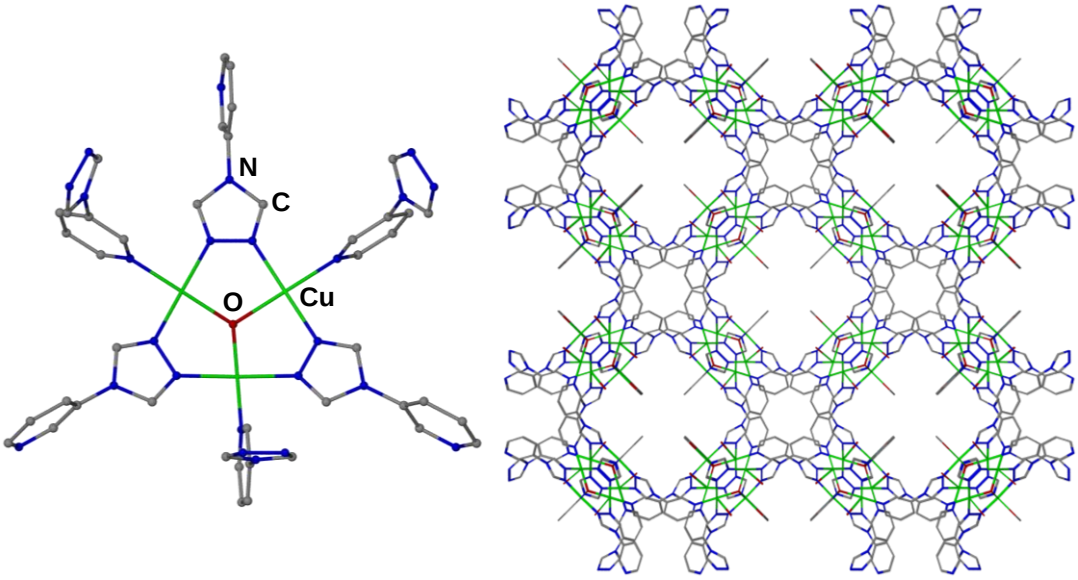

Figure 1.21: The SBU (left) and packing (right) of $[Cu_3(\mu_3\text{-pytrz})_3(\mu_3\text{-O})(H_2O)](ClO_4)_{2.5}(BF_4)_{1.5}\cdot 5.25H_2O$ (pytrz = 4-(3-pyridinyl)-1,2,4-triazole). Counter ions, guest water molecules and hydrogen atoms have been omitted for clarity[42]

Silver(I) ions are readily available and have soft metal centres with a high affinity for relatively soft nitrogen ligands, they are able to form complexes with many different geometries. For these reasons, a great deal of research has been conducted into the use of nitrogen containing ligands coordinating to silver(I) centres. Coordination numbers for silver(I) compounds have been characterised between two and six, showing a variety of geometries,[43] the most common observed geometry however, is tetrahedral.

Figure 1.22 shows some of the ligands which display both nitrogen donor and acid functionalities; these have been used to coordinate to both lanthanide and transition

metals. The harder lanthanide metals prefer coordination to the harder carboxylate functional groups, whilst some of the softer transition metals prefer coordination to the softer N-containing groups.[44]

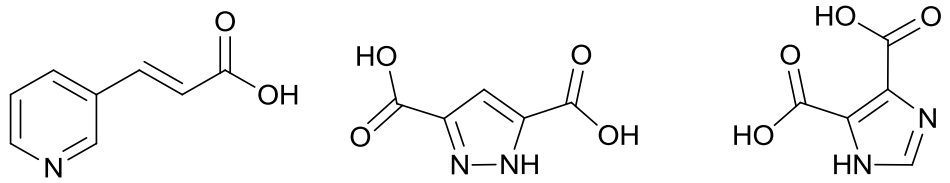

Figure 1.22: Trans-3-(3-pyridyl) acrylic acid (3-hypa) (left), 3,5-pyrazoledicarboxylic acid (H_3pdc) (middle), 4,5-imidazoledicarboxylicacid (4,5-idca) (right)[44]

1.7.4 β-diketonate Ligands

β-diketonates are an attractive class of ligand that have been used in MOF synthesis, as they offer two coordinating sites to a metal centre. Moreover, depending on which metal centre is used, different coordination geometries around the metals can be obtained. In the case of $Co(NCacac)_2$ (NCacac = 3-cyano-2,4-pentanedionate) the cobalt has a tetragonally elongated octahedral coordination with four oxygens from two NCacac ligands in the equatorial plane, and nitrogen atoms in the axial positions, from nitrile groups from adjacent molecules. This links the structure into a three dimensional net, where the ligand acts as both an intermolecular linker via the nitrile group and chelating linker (Figure 1.23).[45]

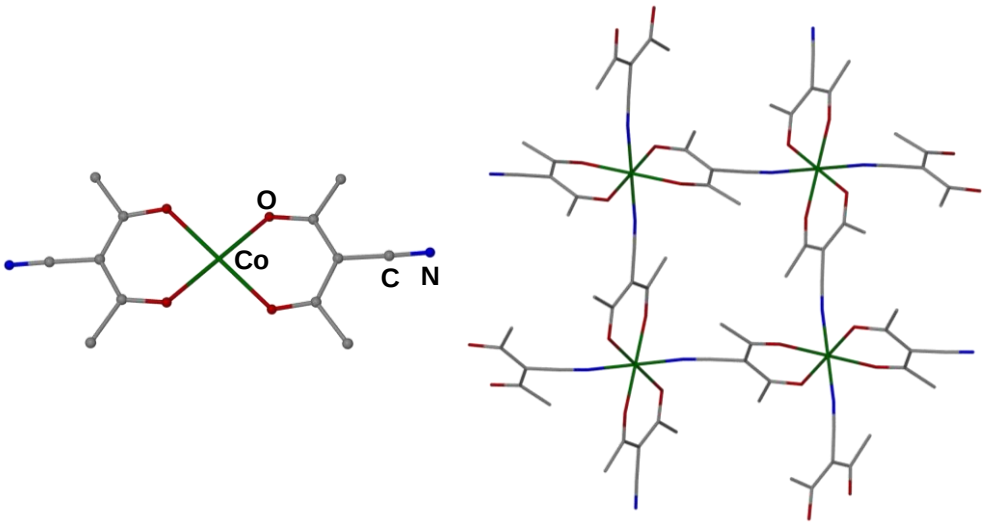

Figure 1.23: The structure of $Co(NCacac)_2$ (NCacac = 3-cyano-2,4-pentanedione) with the building unit (left) and the three dimensional network (right). Hydrogen atoms have been omitted for clarity[45]

With each β-diketonate ligand bearing one negative charge, neutral MOFs often result when they are reacted with metal ions, this means guest counter ions are not required. As is seen in Figure 1.23, three dimensional networks can be formed through the functionalisation in the 3-position, where this additional functional group can coordinate to adjacent metal centres. However, compounds can also be made in which initial metalloligand complexes are formed through the coordination of the oxygens to the metal, and then the functional groups on the backbone are free to coordinate to a second metal, forming a mixed metal compound. One such example is the reaction of beryllium(II) with 3-(pyridyl)-2,4-propanedione (ppd), where two ligands coordinate to the beryllium centre giving it approximately tetrahedral geometry. The pyridyl group being present in the 3-position of the ligand affords a linear linker, which then coordinates to $Cu_2(\mu\text{-}Br)_2$ units to form the two dimensional square grid complex $[Cu_2Br_2(Be(ppd)_2)_2]\cdot 5.33CHCl_3$ (Figure 1.24).[46]

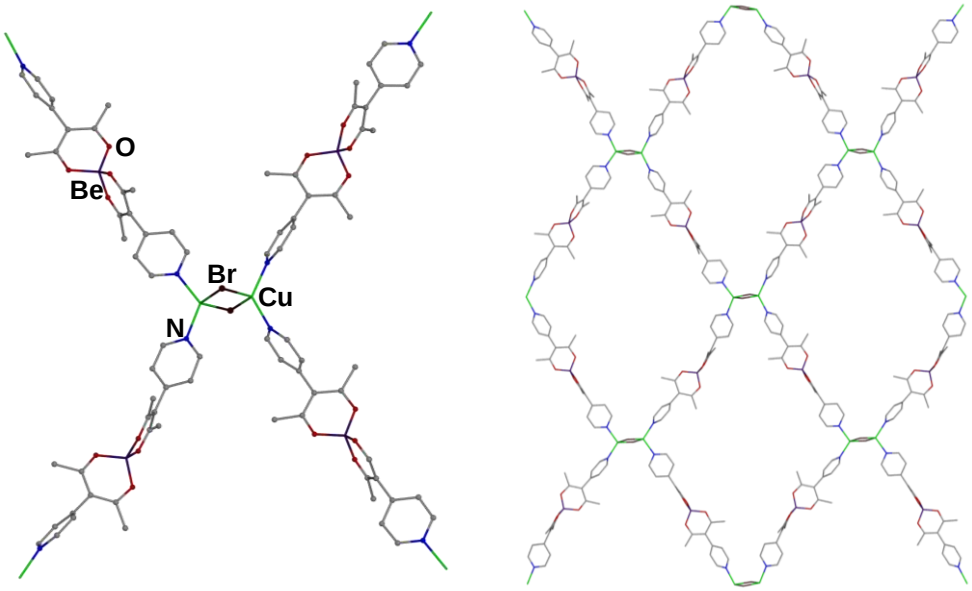

Figure 1.24: Building unit (left) and two dimensional square grid of $[Cu_2Br_2(Be(ppd)_2)_2]\cdot 5.33CHCl_3$ (right) (ppd = 3-(pyridyl)-2,4-propanedione). Hydrogen atoms and solvent molecules have been omitted for clarity[46]

The MOF geometry can be further regulated by the central metal ion used. In Figure 1.24 a tetrahedral beryllium(II) centre is present affording a linear building unit. However, if octahedral metal centres were used, such as aluminium(III) and iron(III), triangular complexes $Al(pda)_3$ and $Fe(pda)_3$ (pda = 2,4-pentanedionate) would be formed. The backbone of the β-diketonate can also be functionalised in several positions, which can change the orientation of the second functional group in the metalloligand. Furthermore, the metalloligand can be altered by increasing the length of

the organic unit (Figure 1.25), or using alternative functional groups. These changes will result in different directionalities in the frameworks formed.[47]

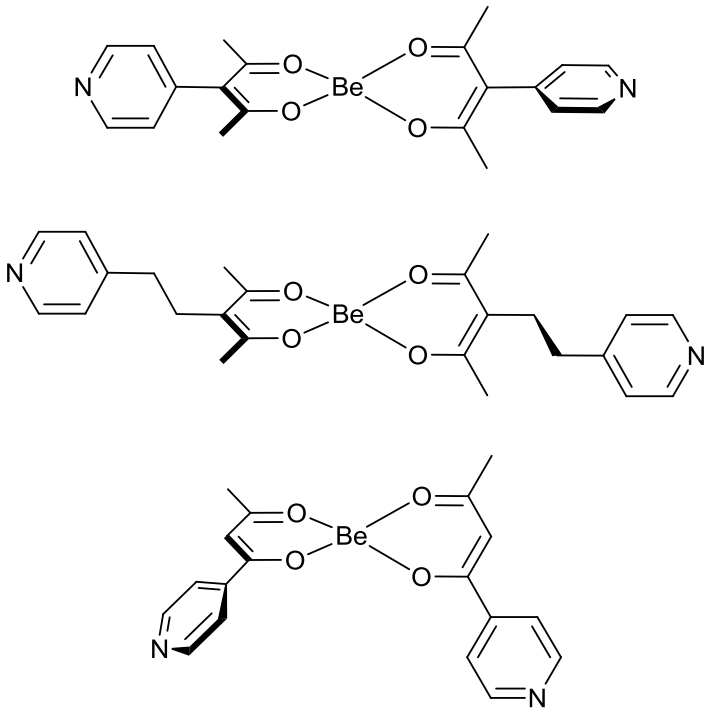

Figure 1.25: Some different geometries obtained when changing the position of the pyridyl group and linker length[47]

1.7.5 Mixed Linker MOFs

MOFs containing a mixture of two different linkers, for example a carboxylate linker and a nitrogen donor linker are also known. For example, $[Zn(bdc)(bipy)_{0.5}]$ (bdc = 1,4-benzenedicarboxylate, bipy = 4,4'-bipyridine) has a structure constructed from a $Zn_2(O_2CR)_4$ paddle wheel SBU, where the bdc ligands link the zinc paddle wheels into a two dimensional square grid. The bipy ligand then coordinates in the axial position of the zinc, and acts as a pillar to link the square grids together, extending the structure into three dimensions (Figure 1.26).[48] The framework is doubly interpenetrated, reducing the pore size.

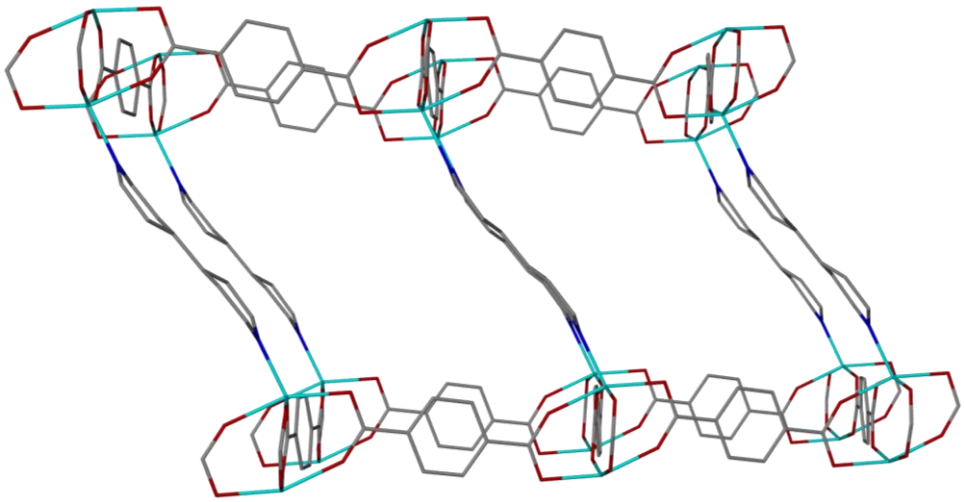

Figure 1.26: The structure of [Zn(bdc)(bipy)$_{0.5}$] (bdc = 1,4-benzenedicarboxylate, bipy = 4,4'-bipyridine). Hydrogen atoms have been omitted for clarity[48]

Another approach adopted involves using two different dicarboxylates to give access to materials with higher porosities. H_2bdc and 1,3,5-benzenetribenzoic acid (H_2btb) have been used to synthesise, under the same procedures with $Zn(NO_3)_2$, the highly porous and well studied materials MOF-5 and MOF-177 ($[Zn_4O(btb)_2]\cdot(DEF)_{15}(H_2O)_3$) respectively. When these two ligands are reacted together with $Zn(NO_3)_2\cdot 6H_2O$ they afford the MOF $[Zn_4O(bdc)(btb)_{4/3}]$ (UMCM-1, Figure 1.27), which contains the same $Zn_4O(O_2CR)$ SBU, but with two coordinated bdc ligands and four coordinated btb ligands. This structure forms a highly porous material that contains both micropores and mesopores, which give it both a high surface area and easily accessible mesopores. The surface area of this material exceeds that observed for both MOF-5 and MOF-177, with a Langmuir value of 6500 m^2g^{-1}. This demonstrates how new porous materials can be obtained through the coordination copolymerization of two topologically different linkers which possess the same coordinating functionality.[49]

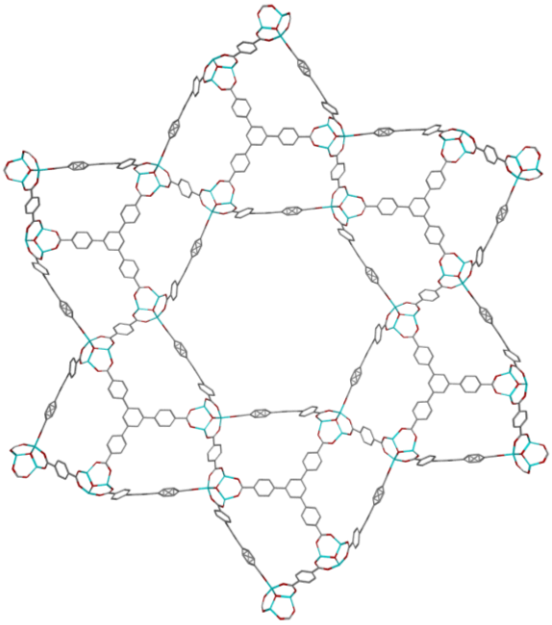

Figure 1.27: Crystal structure of UMCM-1 ([$Zn_4O(bdc)(btb)_{4/3}$]) showing the large central mesopore. Hydrogen atoms have been omitted for clarity[49]

One strategy is to use two topologically similar ligands, in this case the use of bdc and 2-aminobenzene-1,4-dicarboxylate (abdc), which have been used to previously make MOF-5 (colourless crystals) and IRMOF-3 (orange crystals) ([$Zn_4O(abdc)_3$], Figure 1.9). *Matzger et al.* first observed that if both H_2bdc and H_2abdc were reacted together in different ratios with $Zn(NO_3)_2{\cdot}4H_2O$ in DEF, then it was possible to obtain the MOF with differing amounts of bdc and abdc, according to the initial concentrations used. Nitrogen sorption experiments were carried out on all samples and it was observed that Brunauer-Emmett-Teller (BET) approximations ranged from 3170 $m^2\,g^{-1}$ (MOF-5 BET) to 2660 $m^2\,g^{-1}$ (IRMOF-3 BET). Thus, as the abdc content increases, the presence of the amino groups block the pores. These findings demonstrate the possibilities of accessing a range of systems with varying surface areas.[50]

Matzger et al. also carried out research on these systems looking at the crystallisation seeding process. Seeds of MOF-5 and IRMOF-3 were grown separately under the same conditions; 100 °C in DEF for 1 day. After 15 hours, when crystals had began to form, the seed MOF-5 crystals were removed from their solution and placed in the unreacted solution of abdc and $Zn(NO_3)_2{\cdot}4H_2O$ and *vice versa*. Both samples were then heated for another 15 hours, and when viewed under the microscope, layered crystals could be observed, with either a colourless core and orange outer surface (MOF-5 core and IRMOF-3 outer surface) or an orange core and a colourless outer surface (IRMOF-3 core and MOF-5 outer surface). When the BET surface area was measured for both

samples they gave similar results of approximately 2750 m^2 g^{-1}, which is in between the surface areas observed for MOF-5 and IRMOF-3.[50]

If the synthesis of MOF-5 is carried out in DMF instead of DEF, it yields a phase impure sample, with a BET surface area of less than 1000 m^2 g^{-1}. However, when this seeding approach is used, MOF-5 can be synthesised on the surface of IRMOF-3 in DMF yielding crystals that now have a BET surface area over 2000 m^2 g^{-1}, this gives a less expensive alternative to the normal synthesis of MOF-5, as it negates the need to use the more expensive solvent DEF.[50]

1.8 Zeolitic Imidazolate Frameworks

More recently zeolitic imidazolate frameworks (ZIFs) have been designated as a new MOF class.[51] During formation of these compounds, an imidazole ligand loses a proton to form an imidazolate (IM) which then coordinates to the transition metal. The angle of the bridge between the metal-imidazolate-metal in the ZIF is close to 145°, which is similar to the angle found in many zeolites for the Si-O-Si bridge (Figure 1.28). Due to the similarity of these angles, ZIFs with zeolite based gross structures can be obtained, but the spacing between each tetrahedron will be larger, and hence larger pores will also be obtained. The pore surfaces of the ZIFs are lined with organic bridging species, rather than silicate oxide surfaces as in zeolites.

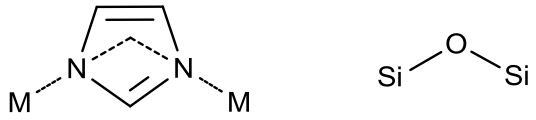

Figure 1.28: The bridges present in ZIFs (left) and zeolites (right)

An example of a highly stable ZIF is that of ZIF-8 ($[Zn(MeIM)_2]\cdot 2.3H_2O$, Figure 1.29 (MeIM = 2-methylimidazolate), first synthesised by *Yaghi et al.*. The structure of ZIF-8 consists of tetrahedrally coordinated zinc metal centres linked by 2-methylimidazolate ligands. The framework is constructed in a similar manner to the zeolite sodalite (SOD = $[Na^+_8Cl^-_2][Al_6Si_6O_{24}]$)[52] (Figure 1.29). The ZIF-8 cages are analogous to those found in sodalite, where silicon and aluminium are replaced by zinc, and the oxygens are replaced by the imidazolates, creating 4- and 6-membered rings. The Si···Al distances within sodalite are approximately 3 Å, whereas the corresponding Zn···Zn distances in ZIF-8 are close to 6 Å, owing to the production of larger pores.[51]

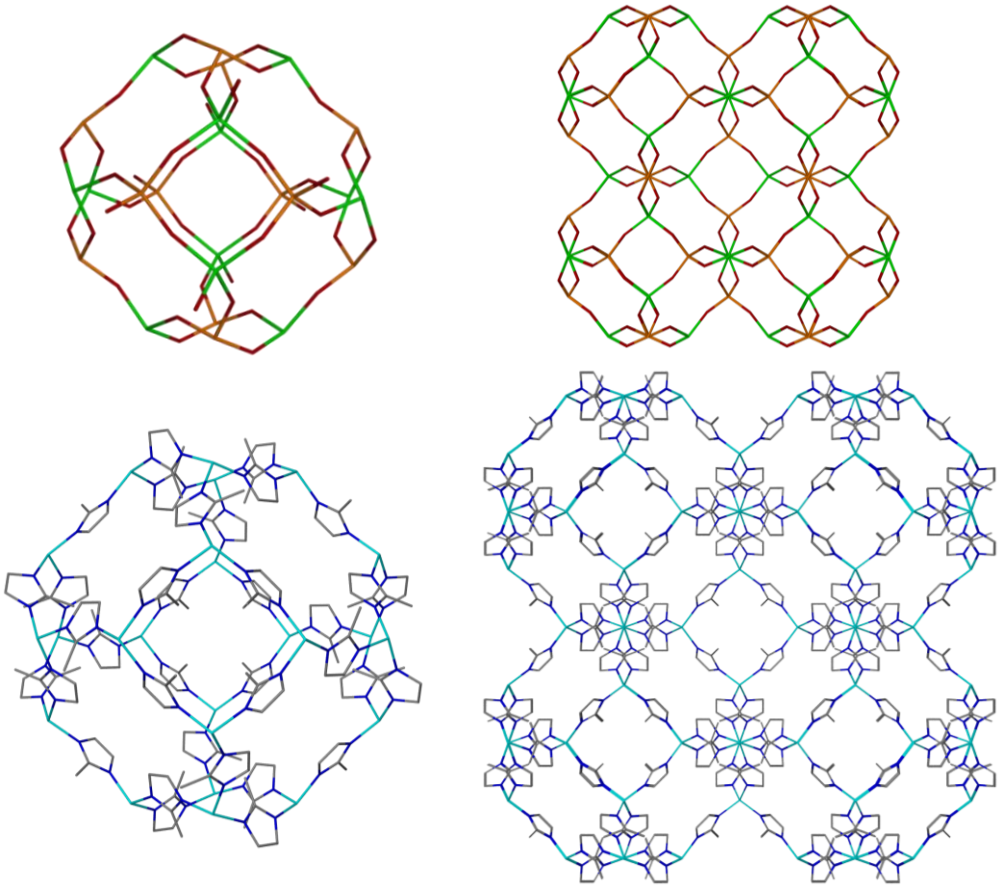

Figure 1.29: Structure of the sodalite cage (top left) and the sodalite packing (top right). The structure of the ZIF-8 cage (bottom left) and the ZIF-8 packing (bottom right). Aluminium is shown in green, silicon in orange, zinc in cyan, oxygen in red, carbon in grey and nitrogen in blue. Hydrogen atoms and solvent molecules have been omitted for clarity[51, 52]

It is possible to remove the guest solvent molecules in ZIF-8, while still maintaining a highly porous material. The TGA shows that this material is thermally stable up to 550°C, which compares favourably to other MOF structures, e.g. MOF-5, which decomposes at approximately 450°C. ZIF-8 has also shown remarkable chemical stability when placed in benzene, methanol, water or sodium hydroxide (0.1 M and 8 M) for between 1 and 7 days at ambient temperature, 50°C and at the boiling point of the medium. Powder X-ray diffraction patterns obtained at intervals, showed that ZIF-8 was unaffected by the boiling solvents, showing its high chemical stability.[51]

1.9 Post-Synthetic Modification

Most of the MOF synthesis to date has used commercially available ligands for ease of synthesis; however, recent work has used more complex linkers where there is functionality present which can be useful for specific applications. During MOF synthesis, the conditions the functional groups would be subjected to may cause the decomposition of the groups. Alternatively, the functional groups may also be involved in coordination to the metal centre. For this reason post-synthetic modification strategies have been developed, which involve formation of the desired MOF product using a 'tagged' linker that is stable during the conditions for MOF formation, but can then be transformed post-synthetically once in the MOF. This method of synthesis allows access to new MOF materials that would not otherwise be formed from the direct synthesis. Carrying out the synthesis in this manner allows the initial tag to project into the pores, and once altered the functional group will also project into the pores to aid with its application.

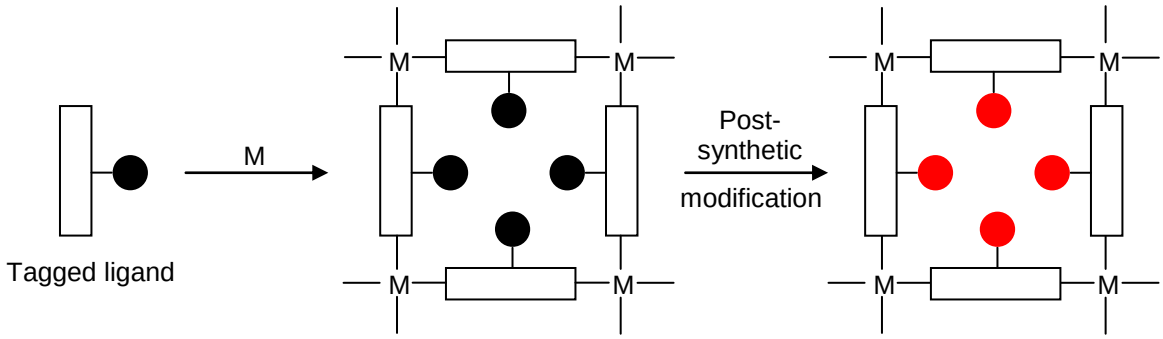

Figure 1.30: Schematic representation of post-synthetic modification

One such example of this type of modification uses an aldehyde tagged biphenyl-4,4'-dicarboxylic acid (2-formyl-biphenyl-4,4'-dicarboxylic acid = H_2fbpdc). Reaction with $Zn(NO_3)_2$ yields $[Zn_4O(fbpdc)_3(OH_2)_2]$. This structure contains the $Zn_4O(O_2CR)_6$ tetrahedral SBU, one difference is that one of the zinc atoms now has two coordinated water molecules, giving the one zinc centre distorted octahedral geometry. This structure extends into a three dimensional cubic type network which is doubly interpenetrated like IRMOF-9 ($[Zn_4O(bpdc)_3]$); the biphenyl-4,4'-dicarboxylate zinc MOF structure without the aldehyde tag present. These crystals were then placed in a DMF solution of 2,4-dinitrophenylhydrazine (DPH) for a week, after which they were isolated and examined by X-ray crystallography. It could be seen that the aldehyde groups had reacted and that the linker had been converted into 2-[(2,4-dinitrophenyl)hydrazonemethyl]biphenyl-4,4'-dicarboxylate (nhbpdc) (Figure 1.31). Through microanalysis and ^{1}H NMR spectroscopy of the digested MOF, it was

established that approximately 60 % of the aldehyde groups had been converted to the hydrazone groups giving a formula of $[Zn_4O(fbpdc)_{1.2}(nhbpdc)_{1.8}(OH_2)_2]$. Like the aldehyde tagged structure, the modified structure is also doubly interpenetrated, and due to the size of the hydrazone group, the Zn···Zn contact is 6.92 Å compared to 8.09 Å in IRMOF-9 ($[Zn_4O(bpdc)_3]$.[53]

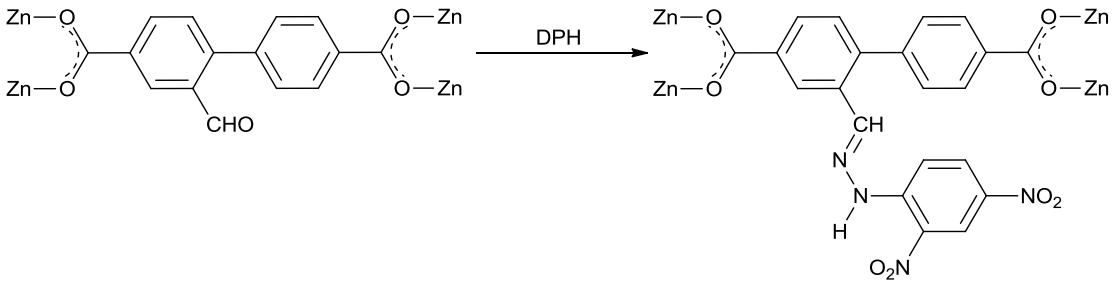

Figure 1.31: Post-synthetic modification of $[Zn_4O(fbpdc)_3(OH_2)_2]$ to the $[Zn_4O(fbpdc)_{1.2}(nhbpdc)_{1.8}(OH_2)_2]$. (fbpdc = 2-formyl-biphenyl-4,4'-dicarboxylate, nhbpdc = 2-[(2,4-dinitrophenyl) hydrazonemethyl]biphenyl-4,4'-dicarboxylate)[53]

After 4 weeks in the DPH solution, the post-synthetically modified MOF remained at 60 % conversion. The possibility of synthesising this MOF by direct reaction of H_2nhbpdc with $Zn(NO_3)_2$ was also examined. However, the product was not the same, demonstrating that this hydrazone functionalised MOF can only be synthesised through post-synthetic modification.[53]

Cohen et al. have also developed the area of post-synthetic modification, and have recently studied reactive isocyanate and isothiocyanate groups present within the framework of MIL-53(Al)-NH_2 ($[Al(OH)(NH_2bdc)]$ NH_2bdc = 2-aminoterephthalate). MIL-53 ([M(OH)(bdc)] M = aluminium(III), chromium(III), iron(III)) (Figure 1.32) is a well studied MOF first synthesised by *Férey et al*., and known with aluminium(III), chromium(III) and iron(III) all forming isostructural materials.[54, 55] The network consists of octahedral metal centres coordinated to four oxygen atoms from four carboxylates in the equatorial position, which bridge to adjacent metal ions. The metal axial positions are bridged by coordinated hydroxyl groups, which extends the motif into one dimensional chains throughout the structure. Through the linking of the bdc ligands to other one dimensional chains the structure extends into three dimensions, affording a porous material.

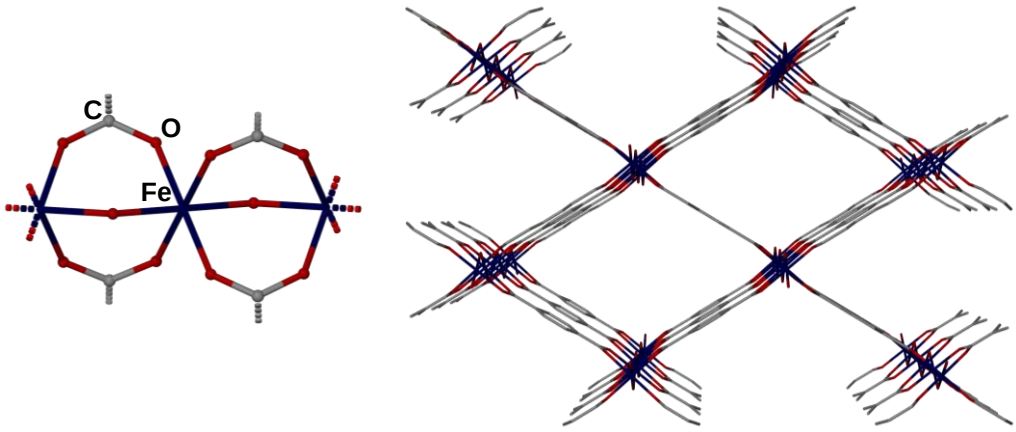

Figure 1.32: The one dimensional chain building unit (left) and the three dimensional network of MIL-53(Fe) (right). Hydrogen atoms have been omitted for clarity[56]

In *Cohen et al.*'s work, they studied the post-synthetic modification of the amino substituted bdc in MIL-53(Al).[57] They first converted these amine groups to either isocyanates (MIL-53(Al)-NCO) or isothiocyanates (MIL-53(Al)-NCS), and found that approximately 90 % of the groups were successfully changed. Due to the isolation of the post-synthetically modified materials in high yields, the frameworks were reacted further with a variety of nucleophiles to test their performance in multistep reactions (Figure 1.33).

MIL-53(Al)-NCO and MIL-53(Al)-NCS were treated with different alcohols to generate carbamate (MIL-53(Al)-CAR) and thiocarbamate (MIL-53(Al)-TCAR) modified MOFs. A range of conversions from approximately 20 % to near quantitative were noted. MIL-53(Al)-NCO and MIL-53(Al)-NCS were also reacted with a range of amines to produce urea and thiourea MOF products. Similar yields were obtained for those observed with the alcohols. These results afforded a post-synthetic approach to produce thiourea derivitised MOFs which have never been reported previously. Materials were also produced that could not otherwise be synthesised through traditional approaches.[58]

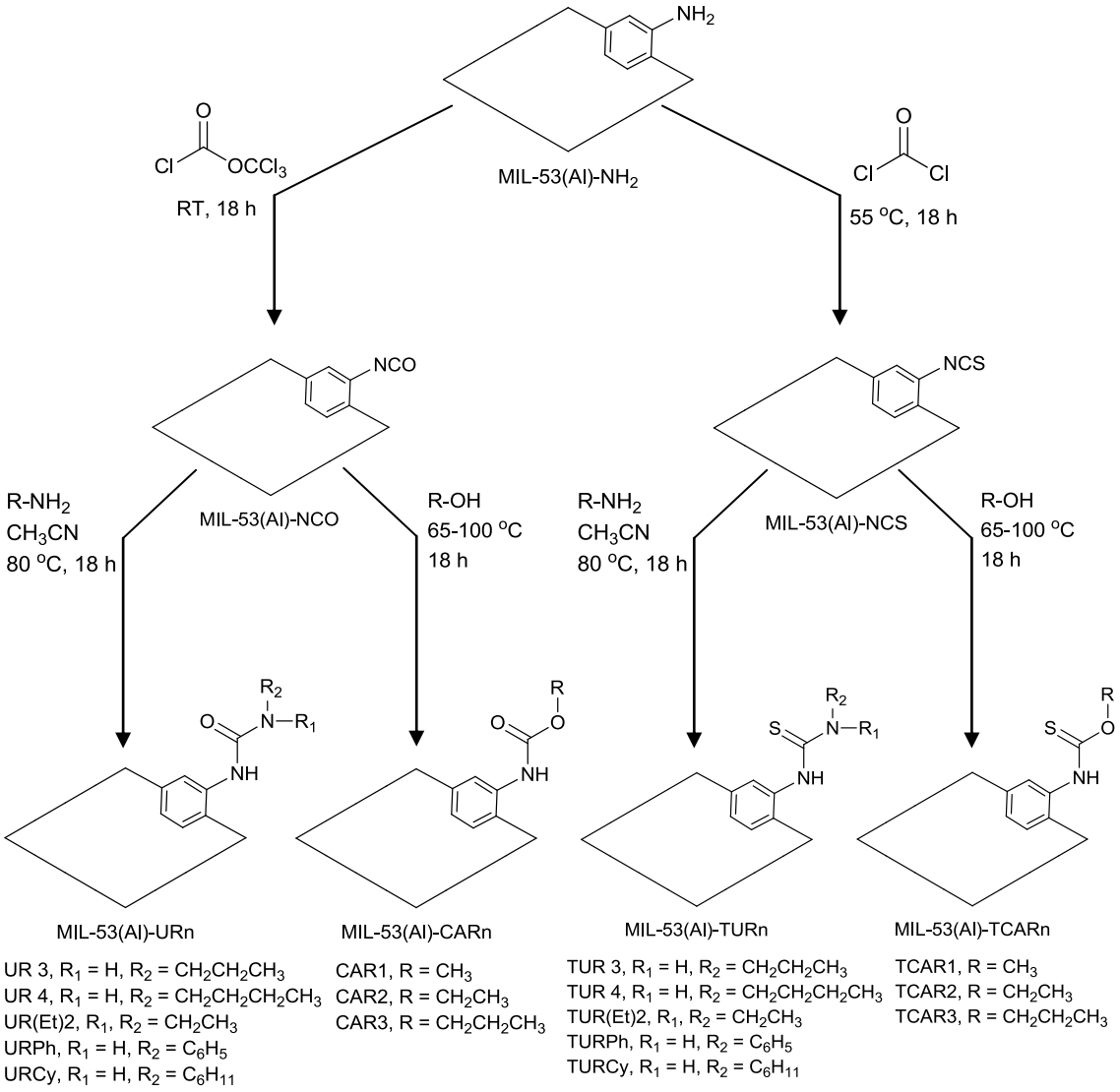

Figure 1.33: Schematic representation of the post-synthetic modifications carried out on MIL-53(Al)-NH_2[58]

Gas adsorption measurements were also carried out on the MIL-53(Al)-NCO and MIL-53(Al)-NCS materials. Neither compound demonstrated any uptake of H_2 or N_2 but showed a pronounced stepwise sorption of CO_2. These findings indicate the potential of these materials for selective adsorption of CO_2 over other gases, and their usefulness in many applications.[58]

1.10 Applications

Many of the applications of MOFs are determined by the porosity and stability of the porous frameworks and as described, many such materials have pores which contain

guest molecules. In order for the materials to be exploited, these guests must be removed leaving a crystalline product. This process is called activation.

1.10.1 Hydrogen Storage

As was mentioned previously, the need to store hydrogen is becoming more important, as fossil fuel resources begin to decrease. Hydrogen has been considered as an ideal candidate for a clean energy carrier as it contains no carbon, and the oxidation of hydrogen in fuel cells releases just water as a product. One of the main applications for storing hydrogen will be to power cars and trucks. Despite the many attractive concepts behind the hydrogen economy, there are still huge barriers to overcome - a safe, efficient and economical on-board hydrogen storage system must be developed.

The US Department of Energy (DOE) had set targets in 2005 for the storage of hydrogen, but these goals could not be met, and so in 2009 the objectives were amended for 2010 and 2015, to a more attainable goal. The targets have now been changed to 4.5 wt % (28 g/L) for 2010 and 5.5 wt % (40 g/L) for 2015, with a goal to reach an ultimate uptake of 7.5 wt % (70 g/L).[59] The mass density of hydrogen is 70.8 kg m^{-3} when it is a liquid at 20 K and 1 atm, and at ambient pressure 5 kg of hydrogen gas would fill a volume of 56 m^3.[3] This puts these targets into perspective as to the size of vessel that would be required to store hydrogen gas at ambient pressure.

MOFs seem ideal candidates for the storage of hydrogen due to their large pores and high surface areas. The DOE goals for a storage system to store hydrogen are set at near ambient pressure and high temperature, however, most of the work to date on MOFs has involved hydrogen uptake being measured at 77 K and 1 atm pressure. Nevertheless, the work carried out is instructive as to what systems may be most appropriate for hydrogen storage.

MOF-177 ($[Zn_4O(btb)_2]$, Figure 1.34, btb = 1,3,5-benzenetribenzoate) has been shown to have a high hydrogen storage capacity, with one of the highest surface areas calculated for a MOF material.[60] It is constructed from the same $Zn_4O(O_2CR)_6$ tetrahedral SBU as MOF-5 (Figure 1.7). However, instead of forming the same cubic type networks, the linker is now a tricarboxylate and extends the structure into a highly porous three dimensional framework. Due to the high porosity of the structure, there are at least fifteen DEF molecules and three H_2O housed within the pores. It is however

possible to remove these guest molecules by exchanging them with chloroform, then removing the latter under vacuum, still leaving the porous material intact.[61] This MOF has a hydrogen uptake capacity of 7.5 wt % at 77 K and 70 bar, with a Langmuir surface area above 5500 m^2 per g.[62] As such, these material types show how realistic MOFs can be at storing hydrogen according to the targets set out by the DOE.

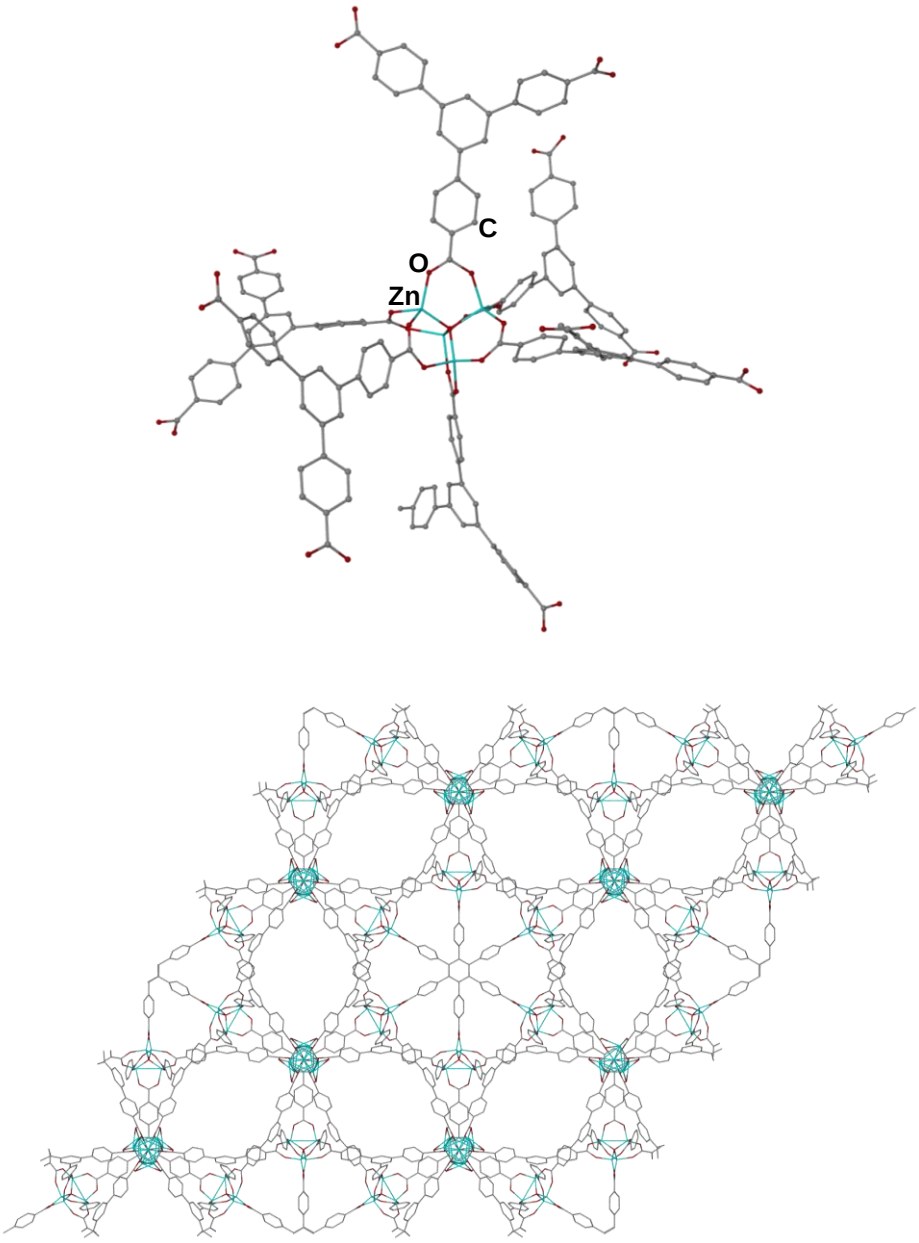

Figure 1.34: Building unit with the $Zn_4O(O_2CR)_6$ SBU (top) and packing of MOF-177 (bottom). Half the $Zn_4O(O_2CR)_6$ SBUs demonstrate disorder, hydrogen atoms and solvent molecules have been omitted for clarity[60]

1.10.2 Carbon Dioxide Capture

Carbon dioxide is released into the atmosphere as flue gas by burning fossil fuels at power plants, as well as many other sources, and is adding to global climate change. For this reason, it is important to be able to separate and recover the CO_2 from the emitted flue gas. Currently, CO_2 is removed by chemical adsorption on basic liquid solvents, such as amine solutions. However, this is highly energy consuming, and it is difficult to regenerate the solvent after the initial adsorption process. Due to this, porous materials have been suggested as an alternative to the current technology, and in particular MOF structures due to their high surface areas and tunable pore surfaces.[63]

To date one of the best MOF candidates for carbon dioxide capture is MIL-101 ($[Cr_3OX(H_2O)_2(bdc)_3]\cdot nH_2O$, X = F/OH) when treated with NH_4F. MIL-101, is a chromium based MOF, which is constructed from trimers of chromium octahedra with four coordinated oxygen atoms from the bidentate dicarboxylates, one μ_3-oxygen atom and one terminal water or fluorine ligand. Four of these chromium octahedra form the vertices of a supertetrahedron, and the organic ligands are then positioned at the six edges of the supertetrahedron (Figure 1.35).

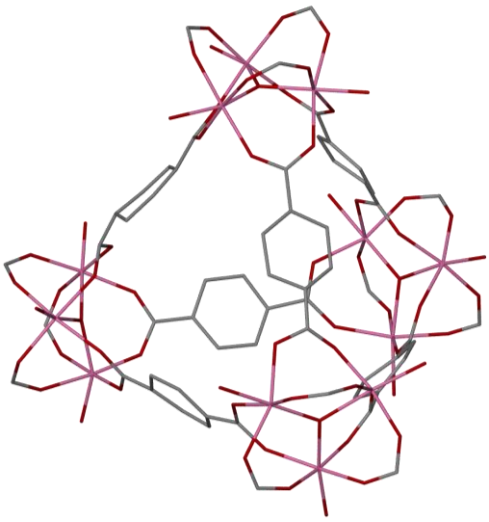

Figure 1.35: Supertetrahedra of MIL-101 with chromium trimers at the vertices. Chromium = pink, oxygen = red, carbon = grey. Hydrogen atoms have been omitted for clarity[64]

The supertetrahedra are corner sharing, forming a highly porous three dimensional structure with two different types of cages present in the system. The first cage has twelve pentagonal faces with a pore accessible diameter of 29 Å, and the second is constructed of sixteen faces (twelve pentagonal and four hexagonal), with a diameter of

34 Å. These two cages together form a mesoporous material. MIL-101 has been shown to have an excess volumetric CO_2 uptake of 390 cm^3/cm^3 and an excess gravimetric CO_2 uptake of 40 mmol/g, these are some of the highest values reported for MOF structures. They also exceed the benchmark materials zeolite 13X and activated carbon MAXSORB by a factor of 1.5.[64] These results highlight the potential of accessing new storage materials to capture carbon dioxide.

1.10.3 Gas Separation and Purification

Carbon dioxide is often found as an impurity in natural gas, which is primarily made up of methane. The presence of CO_2 within the gas can lead to pipeline corrosion and lower the energy content of the natural gas, leading to lower efficiency. The commercial value of natural gas is increased when it is of "pipeline quality methane," which is determined by the purity of the gas, when the CO_2 content is less than 2 %. The separation of CO_2 and CH_4 is typically done using solvents such as amines that remove the former. These bases are good selectively, but their regeneration afterwards is highly energy consuming. So, there is a move towards using adsorbents for this kind of process. The adsorbent needs to have the selectivity of the amines, and much of the work to date has focussed on looking at zeolites and carbon based adsorbents. However, there is now a move towards using MOFs for this same purpose, as their pore size and functionality can be tuned for CO_2 selectivity. Another positive aspect is that the MOF regeneration post separation can be conducted using milder conditions than for zeolites and is therefore more energy efficient.[65-67]

One such compound that has been good at selectively adsorbing CO_2 over CH_4 is that of $[Zn_2(ndc)_2(dpni)]$ (ndc = 2,6-napthalenedicarboxylate, dpni = N,N'-di-(4-pyridyl)-1,4,5,8-napthalene tetracarboxydiimide). This structure consists of a di-zinc paddle wheel SBU, where the carboxylates of four ndc ligands coordinate to the two zinc atoms at approximately 90° to each other. This extends the structure into a two dimensional grid, through the dpni coordinating in the axial positions of the zinc atoms the structure then extends into a three dimensional cubic type network (Figure 1.36). Adsorption measurements were carried out on this material, and it was shown to have comparable amounts of adsorption for CO_2 and CH_4. When the mixture of both gases was then subjected to the material, there were now significantly lower amounts of CH_4 adsorption compared to CO_2 uptake, showing the selectivity for CO_2.[65]

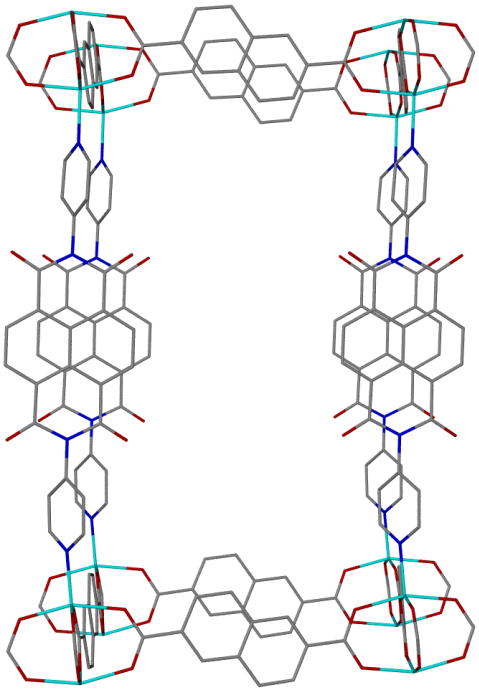

Figure 1.36: Crystal structure of [$Zn_2(ndc)_2(dpni)$] (ndc = 2,6-napthalenedicarboxylate, dpni = N,N'-di-(4-pyridyl)-1,4,5,8-napthalene tetracarboxydiimide). Hydrogen atoms have been omitted for clarity[65]

1.10.4 Catalysis

Zeolites are known to be one of the most important classes of compounds for commercial catalysis. They have high surface areas, the pores are very uniform leading to high selectivity, and they are robust to extreme conditions. Although many of these characteristics are the same for framework structures, there is one main difference; MOF structures are generally not as stable under such extreme conditions. However, this can be seen as an advantage, as they could be used for more sensitive catalysis. Heterogeneous catalysis was one of the first applications explored for MOFs[68], as well as one of the first applications tested.[69]

The cyanosilylation of aldehydes and ketones is a route to cyanohydrin derivatives.[70] The reaction involves the use of Lewis acid catalysts and for this reason [$Cu_3(tma)_2(H_2O)_3$] (tma = 1,3,5-benzenetricarboxylate) (Figure 1.6) was used to test the selectivity and catalytic activity of this MOF. The framework material was first activated by removing all guest and coordinated water molecules. The coordinated water molecules are situated in the axial positions of the copper coordination sphere, once removed the Lewis acidic copper(II) sites become accessible for the aldehyde coordination. The catalysis of benzaldehyde in trimethylsilylcyanide (TMSCN) and

pentane was studied at 313 K (Figure 1.37). After 72 hours, a yield of 57 % (88.5 % selectivity) for the product 2-phenyl-2-((trimethylsilyl)oxy)acetonitrile was found. As a comparison, the same reaction was carried out in the absence of the MOF material, and the comparative conversion was less than 10 % after 72 hours.[71] As MOFs are insoluble the reaction mixture is easy to separate at the end of catalysis, enabling the catalyst to be re-used.[72]

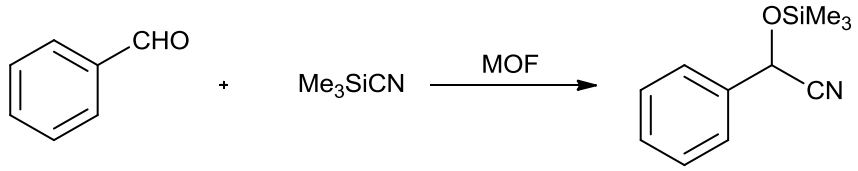

Figure 1.37: The catalysis of benzaldehyde to 2-phenyl-2-((trimethylsilyl)oxy)acetonitrile with trimethylsilylcyanide and the MOF as the catalyst

1.10.5 Drug Delivery

Controlled release of drugs for better administration is an important factor when designing materials to store drug compounds. Currently there are two main systems being used for the drug delivery process, organic and inorganic compounds. The organic compounds consist of biocompatible dendritic macromolecules or polymers and the inorganic compounds consist of zeolites or mesoporous silicates. The problems encountered with these systems are that the organic compounds can encapsulate the drugs, but the controlled release is difficult due to the ill-defined pores. With the inorganic compounds, the pores are functionalised by grafting organic molecules on to the surfaces, but this then reduces the channel size, and hence the loading capacity. Thus, researchers have begun to assess MOFs due to their high and regular porosity and the presence of organically functionalised pores, to allow for high loading and controlled release.[73]

A promising drug delivery candidate has been identified in MIL-88A ($[Fe_3O(MeOH)_3(fma)_3]\cdot CH_3CO_2^-\cdot 4.5MeOH$, fma = fumarate, Figure 1.38).[74] This structure is built up from iron octahedra coordinated to four oxygen atoms from the fma, one μ_3-oxygen atom and one oxygen atom from a terminal methanol group. The bridging oxygen atoms link each iron octahedron to two adjacent iron centres forming a trimeric SBU. The linking of these trimers through the tma to adjacent trimers causes the structure to build up into a three dimensional structure. The structure contains one dimensional chains and cages filled with solvent molecules and acetate counter ions.

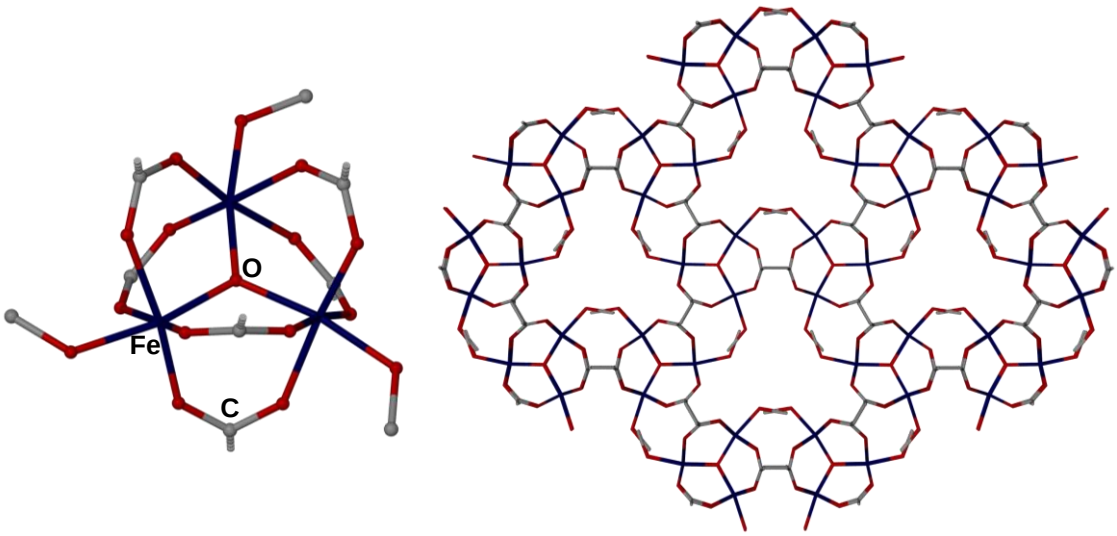

Figure 1.38: The SBU (left) and the gross packing (right) present in $[Fe_3O(MeOH)_3(fma)_3]\cdot CH_3CO_2^-\cdot 4.5MeOH$ (fma = furmarate). Hydrogen atoms, counter ions and solvent molecules have been omitted for clarity[74]

Busulfan is an antitumoural drug which is used in combination with high-dose chemotherapy to treat leukaemia in paediatrics. It possesses pore stability in aqueous solutions, and is currently encapsulated in liposomes and nanoparticles for its administration, but the loading in these compounds is approximately 5-6 wt%.[75] The weight percentage within a carrier needs to be higher to make the drug delivery more effective.[76]

MIL-88A was synthesised as nanoparticles, and soaked in a saturated solution of busulfan. The busulfan loading in MIL-88A was measured at 8 wt%, which is significantly higher than previously reported encapsulations. This means smaller amounts of solids would be necessary to deliver the required dose of the drug. Moreover, MIL-88A was tested for its degradation under physiological conditions, and showed complete breakdown after seven days at 37 ºC, with the products, iron and fumaric acid showing low toxicity.[74]

Nitric oxide is also an important delivery agent in many anti-bacterial, anti-thrombotic and wound healing applications.[77, 78] Currently there are many materials that are used to store and deliver nitric oxide such as polymers, functionalised silica nanoparticles and zeolites, however many of these agents suffer from carcinogenic or pro-inflammatory side products which can limit their use. MOFs pose an attractive alternative to these

materials as they can deliver pure nitric oxide, alleviating the problems of any side effects, and the pores can be tuned to control the amount and rate of delivery.

One such candidate is that of $[Ni_2(dhtp)(H_2O)_2]\cdot 8H_2O$ (dhtp = 2,5-dihydroxy terephthalate). The structure is built up from nickel octahedra, coordinating to five oxygen atoms from the ligand, and one oxygen from a coordinated water molecule which projects into the channels. The ligands bridge nickel atoms together forming helical chains, with the nearest neighbour helices of opposite handedness. Each helical chain is connected to three adjacent chains through the linking of the ligand, forming a three dimensional honeycomb-like network. The channel diameter is approximately 11 Å, and is filled with water molecules.[79]

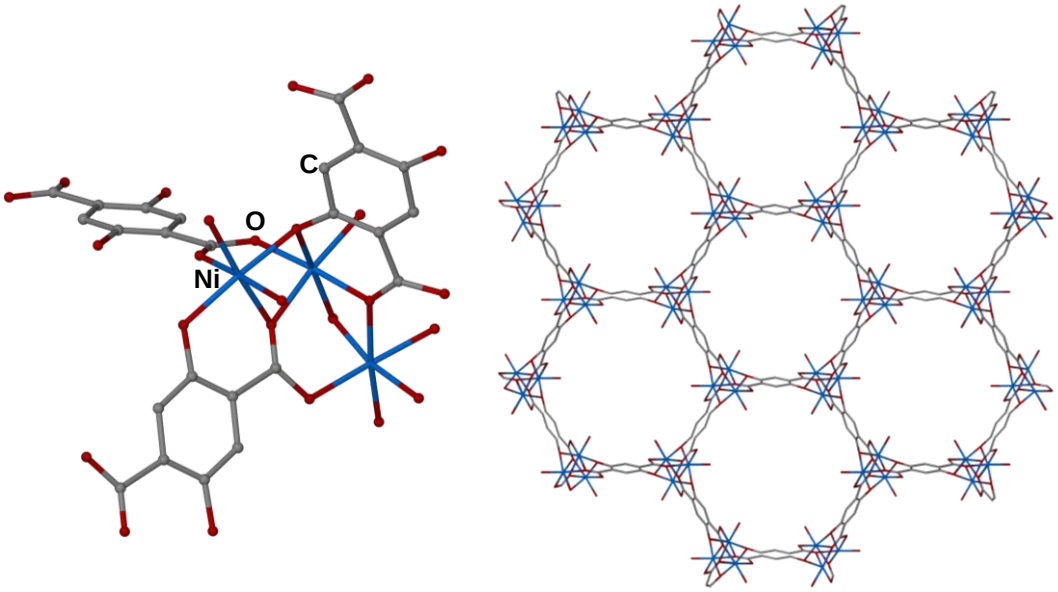

Figure 1.39: The nickel environment (left) and the gross packing (right) present in $[Ni_2(dhtp)(H_2O)_2]\cdot 8H_2O$ (dhtp = 2,5-dihydroxy terephthalate). Hydrogen atoms, and solvent molecules have been omitted for clarity[79]

It is possible to dehydrate this sample by heating to 100 ºC under vacuum, affording the removal of all guest water molecules and also the coordinated water molecules, leaving the nickel centres with coordinatively unsaturated square pyramidal geometry. It is then possible to rehydrate the sample, reforming the octahedral nickel metal centres.

This material was activated, leaving a solvent free material with coordinatively unsaturated metal sites. This was then exposed to NO gas which was accompanied by an immediate colour change from yellow to dark green, confirming the adsorption of the gas to the nickel centres. Powder X-ray diffraction also confirmed that the crystallinity

of the material had been maintained, and IR showed that a 1:1 Ni-NO adduct was obtained. It was shown that this material could be stored in a dry atmosphere, whilst maintaining the NO adsorption. When the sample was exposed to moisture, this triggered the release of the NO, with the water molecules coordinating to the nickel centre.[80]

1.11 Conclusion

MOFs are an important class of materials due to their high porosity and tuneable pore surfaces. They are extremely diverse, with a multitude of applications. The linkers within the frameworks can be functionalised either through addition of these groups to ligands prior to synthesis, or the MOFs can be post synthetically modified to obtain functionalised pore surfaces. There are also new groups of MOFs emerging which use strategies from zeolite chemistry to construct topologically similar systems, with larger pores and tuned functionality.

The remainder of this thesis will outline the synthesis and characterisation of several new MOF materials as well as the investigation of these as possible gas storage materials. These results will then be used in conjunction with previously reported framework adsorbents, to gain a better understanding behind the gas storage process.

1.12 References

1. J. L. C. Rowsell and O. M. Yaghi, *Micropor. Mesopor. Mat.*, 2004, **73**, 3.
2. C. Janiak, *Dalton Trans.*, 2003, 2781.
3. J. L. C. Rowsell and O. M. Yaghi, *Angew. Chem. Int. Ed.*, 2005, **44**, 4670.
4. D. Venkataraman, S. Lee, J. S. Moore, P. Zhang, K. A. Hirsch, G. B. Gardner, A. C. Covey and C. L. Prentice, *Chem. Mat.*, 1996, **8**, 2030.
5. A. Thirumurugan and C. N. R. Rao, *J. Mater. Chem.*, 2005, **15**, 3852.
6. M. J. Zaworotko, *Chem. Commun.*, 2001, 1.
7. B. Moulton and M. J. Zaworotko, *Chem. Rev.*, 2001, **101**, 1629.
8. G. C. Xu, Q. Hua, T. Okamura, Z. S. Bai, Y. J. Ding, Y. Q. Huang, G. X. Liu, W. Y. Sun and N. Ueyama, *CrystEngComm*, 2009, **11**, 261.
9. C. Bartolome, P. Espinet, J. M. Martin-Alvarez, K. Soulantica and J. P. H. Charmant, *Inorg. Chim. Acta*, 2010, **363**, 1864.

10. J. Ni, K. J. Wei, Y. Z. Liu, X. C. Huang and D. Li, *Cryst. Growth Des.*, 2010, **10**, 3964.
11. L. Dobrzanska, G. O. Lloyd, H. G. Raubenheimer and L. J. Barbour, *J. Am. Chem. Soc.*, 2005, **127**, 13134.
12. S. Noro, S. Kitagawa, M. Kondo and K. Seki, *Angew. Chem. Int. Ed.*, 2000, **39**, 2082.
13. S. Kitagawa, R. Kitaura and S. Noro, *Angew. Chem. Int. Ed.*, 2004, **43**, 2334.
14. S. Takamizawa, E. Nakata and H. Yokoyama, *Inorg. Chem. Commun.*, 2003, **6**, 763.
15. D. N. Dybtsev, H. Chun and K. Kim, *Angew. Chem. Int. Ed.*, 2004, **43**, 5033.
16. S. S. Y. Chui, S. M. F. Lo, J. P. H. Charmant, A. G. Orpen and I. D. Williams, *Science*, 1999, **283**, 1148.
17. M. Eddaoudi, J. Kim, N. Rosi, D. Vodak, J. Wachter, M. O'Keeffe and O. M. Yaghi, *Science*, 2002, **295**, 469.
18. M. Eddaoudi, D. B. Moler, H. L. Li, B. L. Chen, T. M. Reineke, M. O'Keeffe and O. M. Yaghi, *Acc. Chem. Res.*, 2001, **34**, 319.
19. X. B. Zhao, B. Xiao, A. J. Fletcher, K. M. Thomas, D. Bradshaw and M. J. Rosseinsky, *Science*, 2004, **306**, 1012.
20. S. R. Batten, *Curr. Opin. Solid State Mater. Sci.*, 2001, **5**, 107.
21. L. Carlucci, G. Ciani and D. M. Proserpio, *Coord. Chem. Rev.*, 2003, **246**, 247.
22. J. J. Zhang, L. Wojtas, R. W. Larsen, M. Eddaoudi and M. J. Zaworotko, *J. Am. Chem. Soc.*, 2009, **131**, 17040.
23. B. Zhai, L. Yi, H. S. Wang, B. Zhao, P. Cheng, D. Z. Liao and S. P. Yan, *Inorg. Chem.*, 2006, **45**, 8471.
24. L. Carlucci, G. Ciani, D. M. Proserpio and S. Rizzato, *Chem. Eur. J.*, 2002, **8**, 1520.
25. S. R. Batten, B. F. Hoskins, B. Moubaraki, K. S. Murray and R. Robson, *Chem. Commun.*, 2000, 1095.
26. T. Yamada and H. Kitagawa, *J. Am. Chem. Soc.*, 2009, **131**, 6312.
27. R. K. Deshpande, J. L. Minnaar and S. G. Telfer, *Angew. Chem. Int. Ed.*, 2010, **49**, 4598.
28. Y. B. Go, X. Q. Wang, E. V. Anokhina and A. J. Jacobson, *Inorg. Chem.*, 2005, **44**, 8265.
29. V. R. Pedireddi and S. Varughese, *Inorg. Chem.*, 2004, **43**, 450.
30. S. R. Halper and S. M. Cohen, *Inorg. Chem.*, 2005, **44**, 486.

31. W. Shi, X. Y. Chen, B. Zhao, A. Yu, H. B. Song, P. Cheng, H. G. Wang, D. Z. Liao and S. P. Yan, *Inorg. Chem.*, 2006, **45**, 3949.
32. J. C. Yao, J. B. Guo, J. G. Wang, Y. F. Wang, L. Zhang and C. P. Fan, *Inorg. Chem. Commun.*, 2010, **13**, 1178.
33. R. Kitaura, G. Onoyama, H. Sakamoto, R. Matsuda, S. Noro and S. Kitagawa, *Angew. Chem. Int. Ed.*, 2004, **43**, 2684.
34. T. K. Maji, R. Matsuda and S. Kitagawa, *Nature Mater.*, 2007, **6**, 142.
35. A. X. Tian, J. Ying, J. Peng, J. Q. Sha, Z. G. Han, J. F. Ma, Z. M. Su, N. H. Hu and H. Q. Jia, *Inorg. Chem.*, 2008, **47**, 3274.
36. Y. Qi, Y. X. Che, F. Luo, S. R. Batten, Y. Liu and J. M. Zheng, *Cryst. Growth Des.*, 2008, **8**, 1654.
37. P. Ren, M. L. Liu, J. Zhang, W. Shi, P. Cheng, D. Z. Liao and S. P. Yan, *Dalton Trans.*, 2008, 4711.
38. X. G. Liu, L. Y. Wang, X. Zhu, B. L. Li and Y. Zhang, *Cryst. Growth Des.*, 2009, **9**, 3997.
39. J. Tao, M. L. Tong and X. M. Chen, *Dalton Trans.*, 2000, 3669.
40. Y. C. Qiu, Z. H. Liu, Y. H. Li, H. Deng, R. H. Zeng and M. Zeller, *Inorg. Chem.*, 2008, **47**, 5122.
41. D. Y. Wu, W. Huang, C. Y. Duan and Q. J. Meng, *Inorg. Chem. Commun.*, 2007, **10**, 1009.
42. Y. Wang, P. Cheng, Y. Song, D. Z. Liao and S. P. Yanl, *Chem. Eur. J.*, 2007, **13**, 8131.
43. D. L. Reger, R. F. Semeniuc, C. A. Little and M. D. Smith, *Inorg. Chem.*, 2006, **45**, 7758.
44. C. L. Cahill, D. T. de Lill and M. Frisch, *CrystEngComm*, 2007, **9**, 15.
45. O. Angelova, J. Macicek, M. Atanasov and G. Petrov, *Inorg. Chem.*, 1991, **30**, 1943.
46. V. D. Vreshch, A. N. Chernega, J. A. K. Howard, J. Sieler and K. V. Domasevitch, *Dalton Trans.*, 2003, 1707.
47. V. D. Vreshch, A. B. Lysenko, A. N. Chernega, J. Sieler and K. V. Domasevitch, *Polyhedron*, 2005, **24**, 917.
48. H. Chun, D. N. Dybtsev, H. Kim and K. Kim, *Chem. Eur. J.*, 2005, **11**, 3521.
49. K. Koh, A. G. Wong-Foy and A. J. Matzger, *Angew. Chem. Int. Ed.*, 2008, **47**, 677.
50. K. Koh, A. G. Wong-Foy and A. J. Matzger, *Chem. Commun.*, 2009, 6162.

51. K. S. Park, Z. Ni, A. P. Cote, J. Y. Choi, R. D. Huang, F. J. Uribe-Romo, H. K. Chae, M. O'Keeffe and O. M. Yaghi, *Proc. Natl. Acad. Sci. U. S. A.*, 2006, **103**, 10186.
52. L. Pauling, *Kristallogr.*, 1930, **74**, 213.
53. A. D. Burrows, C. G. Frost, M. F. Mahon and C. Richardson, *Angew. Chem. Int. Ed.*, 2008, **47**, 8482.
54. C. Serre, F. Millange, C. Thouvenot, M. Nogues, G. Marsolier, D. Louer and G. Férey, *J. Am. Chem. Soc.*, 2002, **124**, 13519.
55. K. Barthelet, J. Marrot, D. Riou and G. Férey, *Angew. Chem. Int. Ed.*, 2002, **41**, 281.
56. S. Bauer, C. Serre, T. Devic, P. Horcajada, J. Marrot, G. Férey and N. Stock, *Inorg. Chem.*, 2008, **47**, 7568.
57. T. Ahnfeldt, D. Gunzelmann, T. Loiseau, D. Hirsemann, J. Senker, G. Férey and N. Stock, *Inorg. Chem.*, 2009, **48**, 3057.
58. C. Volkringer and S. M. Cohen, *Angew. Chem. Int. Ed.*, 2010, **49**, 4644.
59. US Department of Energy, Targets for Onboard Hydrogen Storage Systems for Light-Duty Vehicles, http://www1.eere.energy.gov/hydrogenandfuelcells/storage/pdfs/targets_onboard_hydro_storage_explanation.pdf.
60. H. K. Chae, D. Y. Siberio-Perez, J. Kim, Y. Go, M. Eddaoudi, A. J. Matzger, M. O'Keeffe and O. M. Yaghi, *Nature*, 2004, **427**, 523.
61. J. L. C. Rowsell, A. R. Millward, K. S. Park and O. M. Yaghi, *J. Am. Chem. Soc.*, 2004, **126**, 5666.
62. A. G. Wong-Foy, A. J. Matzger and O. M. Yaghi, *J. Am. Chem. Soc.*, 2006, **128**, 3494.
63. A. Wahby, J. M. Ramos-Fernandez, M. Martinez-Escandell, A. Sepulveda-Escribano, J. Silvestre-Albero and F. Rodriguez-Reinoso, *ChemSusChem*, 2010, **3**, 974.
64. G. Férey, C. Mellot-Draznieks, C. Serre, F. Millange, J. Dutour, S. Surble and I. Margiolaki, *Science*, 2005, **309**, 2040.
65. Y. S. Bae, K. L. Mulfort, H. Frost, P. Ryan, S. Punnathanam, L. J. Broadbelt, J. T. Hupp and R. Q. Snurr, *Langmuir*, 2008, **24**, 8592.
66. S. Cavenati, C. A. Grande and A. E. Rodrigues, *J. Chem. Eng. Data*, 2004, **49**, 1095.

67. L. Hamon, P. L. Llewellyn, T. Devic, A. Ghoufi, G. Clet, V. Guillerm, G. D. Pirngruber, G. Maurin, C. Serre, G. Driver, W. van Beek, E. Jolimaitre, A. Vimont, M. Daturi and G. Férey, *J. Am. Chem. Soc.*, 2009, **131**, 17490.
68. B. F. Hoskins and R. Robson, *J. Am. Chem. Soc.*, 1990, **112**, 1546.
69. M. Fujita, Y. J. Kwon, S. Washizu and K. Ogura, *J. Am. Chem. Soc.*, 1994, **116**, 1151.
70. D. A. Evans, L. K. Truesdal and G. L. Carroll, *J. Chem. Soc., Chem. Commun.*, 1973, 55.
71. K. Schlichte, T. Kratzke and S. Kaskel, *Micropor. Mesopor. Mat.*, 2004, **73**, 81.
72. J. Lee, O. K. Farha, J. Roberts, K. A. Scheidt, S. T. Nguyen and J. T. Hupp, *Chem. Soc. Rev.*, 2009, **38**, 1450.
73. P. Horcajada, C. Serre, M. Vallet-Regi, M. Sebban, F. Taulelle and G. Férey, *Angew. Chem. Int. Ed.*, 2006, **45**, 5974.
74. C. Serre, F. Millange, S. Surble and G. Férey, *Angew. Chem. Int. Ed.*, 2004, **43**, 6286.
75. G. Vassal, A. Deroussent, D. Challine, O. Hartmann, S. Koscielny, D. Valteaucouanet, J. Lemerle and A. Gouyette, *Blood*, 1992, **79**, 2475.
76. N. E. Ghermani, A. Spasojevic-de Bire, N. Bouhmaida, S. Ouharzoune, J. Bouligand, A. Layre, R. Gref and P. Couvreur, *Pharm. Res.*, 2004, **21**, 598.
77. H. F. Zhu, B. Ka and F. Murad, *World J.Surg.*, 2007, **31**, 624.
78. M. R. Miller and I. L. Megson, *Br. J. Pharmacol.*, 2007, **151**, 305.
79. P. D. C. Dietzel, B. Panella, M. Hirscher, R. Blom and H. Fjellvag, *Chem. Commun.*, 2006, 959.
80. A. C. McKinlay, B. Xiao, D. S. Wragg, P. S. Wheatley, I. L. Megson and R. E. Morris, *J. Am. Chem. Soc.*, 2008, **130**, 10440.

Chapter 2 – One Dimensional Copper and Zinc Paddle Wheel Networks using Functionalised Linkers

2.1 Introduction

The paddle wheel secondary building unit is an important feature during the construction of MOFs as noted in Chapter 1 (Figure 2.1). This motif often helps in the prediction of the topology of the materials formed. There are many examples of extended solids that incorporate this unit with metals such as copper[1], rhodium[2], zinc[3], nickel[4], chromium[5], ruthenium[6] and molybdenum.[7] The SBU consists of a dimetallic unit, in which each metal has approximate square pyramidal geometry. Four carboxylates coordinate to the metal in a bridging bidentate manner, at approximately 90º to each other. These systems have been constructed from mono-[8], di-[9] and tri-[10] carboxylates increasing the dimensionality of the MOF formed. Nitrogen donor ligands can be coordinated in the axial position of the metals. If simple donors were present here, then the extension of the structure would terminate at this point. However, use of *N*,*N*-ditopic ligands, allows the paddle wheel to be linked together. Depending on the metals used in the construction of the SBU, metal-metal bonding may also be present, and this has been observed in many systems with bond orders ranging from one to four.[11-13]

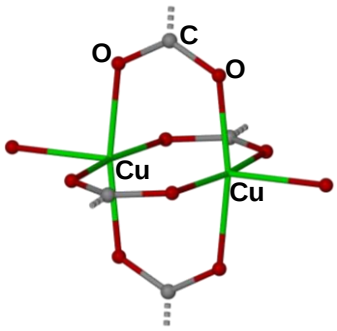

Figure 2.1: An example of a copper paddle wheel SBU. The axial positions contain coordinated water molecules. Hydrogen atoms have been omitted for clarity

MOFs can be constructed with a range of dimensionalities and paddle wheel SBUs have been included in one, two and three dimensional MOFs. For the construction of one dimensional polymer chains, *Takamizawa et al*.[14] have used benzoic acid with copper or rhodium to build the SBU. This dimeric unit does not extend into an infinite structure through the carboxylates, but is extended into a one dimensional chain by the presence of pyrazine donor ligands bonded to the metal axial positions (Figure 2.2).[14]

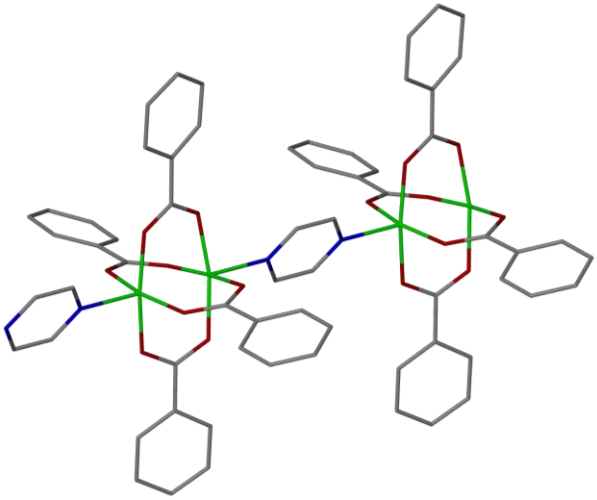

Figure 2.2: Part of the infinite chain structure in $[M_2(bza)_4(pyz)]$ (bza = benzoate, pyz = pyrazine, M = Rh(II), Cu(II). Hydrogen atoms have been omitted for clarity[14]

In order to construct a two dimensional structure from the paddle wheel moiety, a different strategy is incorporated into the MOF synthesis. In particular, a dicarboxylate ligand is used to link the dimer units together, extending the structure into a two dimensional grid. Instead of a ditopic nitrogen donor ligand in the axial position of the metal, a coordinated solvent molecule or a terminal nitrogen donor ligand such as pyridine is present which prevents the extension of the structure into three dimensions. One such example was reported by *Yang et al.*,[15] which consisted of the compound [Zn(bdc)(dma)] (bdc = 1,4-benzenedicarboxylate, dma = *N*,*N*-dimethylacetamide). The paddle wheel was based on a zinc dimer, linked via four bdc ligands which, in turn, linked paddle wheel units together to form a two dimensional square grid (Figure 2.3). A coordinated dma molecule in the axial zinc positions stopped the extension of the grid. This network is doubly interpenetrated, which reduces the pore size.[15]

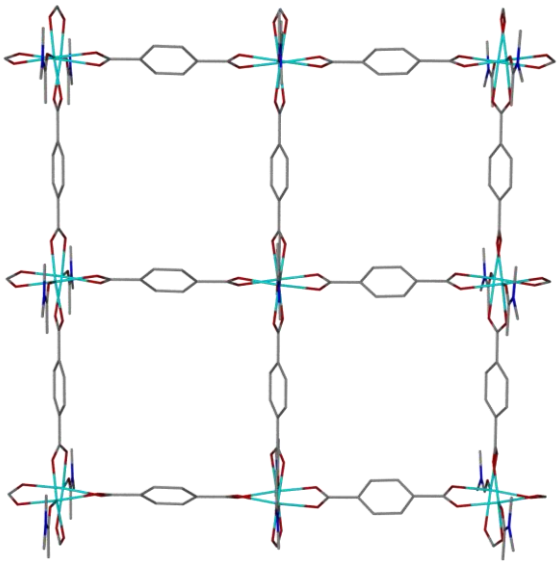

Figure 2.3: Crystal structure of [Zn(bdc)(dma)] (bdc = 1,4-benzenedicarboxylate, dma = N,N-dimethylacetamide). Hydrogen atoms have been omitted for clarity[15]

There are several ways in which three dimensional networks constructed from the paddlewheel SBU can be obtained. One approach, alluded to in Chapter 1, is to use a tricarboxylate as seen in HKUST-1 ($[Cu_3(tma)_2(H_2O)_3]$, tma = 1,3,5-benzenetricarboxylate). Another strategy is to build up from the two dimensional square grid structure shown in Figure 2.3. Instead of having a solvent molecule coordinated in the metal axial position, a ditopic nitrogen donor ligand can be coordinated which will extend the structure further into three dimensions. An example of this kind of structure was reported by *Kim et al.*[9] for the network $[Zn_2(bdc)_2(dabco)]\cdot 4DMF\cdot 0.5H_2O$ (dabco = 1,4-diazabicyclo[2.2.2]octane). In this structure the paddle wheel SBU is constructed from a zinc dimer coordinated to four bdc ligands. The latter link the SBUs together, forming a two dimensional grid. In the axial position on the zinc centres is a coordinated dabco linker, which connects the sheets into three dimensions (Figure 2.4). Within the pores of the structure are guest DMF and water molecules.[9]

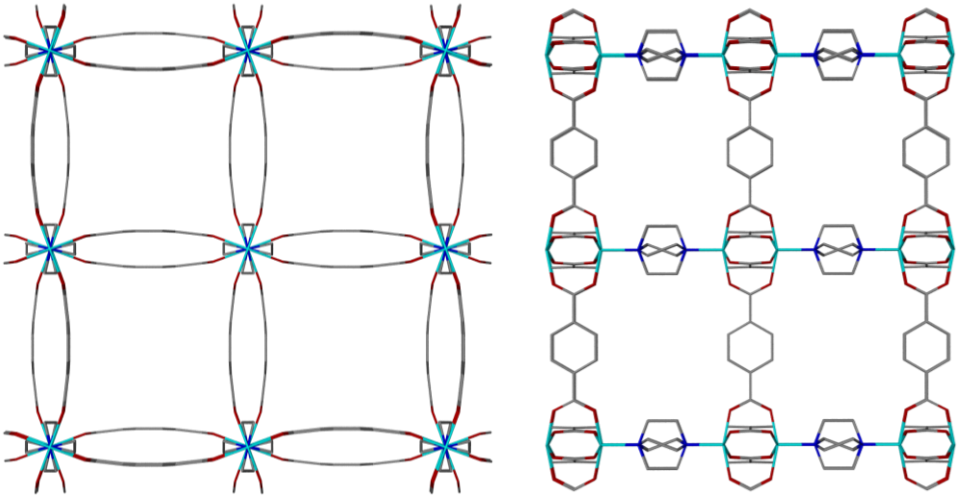

Figure 2.4: Two views of the crystal structure of [$Zn_2(bdc)_2(dabco)$] (dabco = 1,4-diazabicyclo[2.2.2] octane). Guest solvent molecules and hydrogen atoms have been omitted for clarity[9]

All three of these systems have associated advantages and disadvantages, and for applications, the pore volume and surface area of a MOF is very important. Three dimensional structures often have larger pore volumes, which makes them attractive for many applications.

The aim of the research herein was to investigate networks that could adsorb gases such as carbon dioxide, sulfur dioxide, hydrogen chloride and methane, and to monitor this process of gas uptake using *in situ* crystallography. The goal was to see if gas molecules could be located in the pores of the network, to gain an understanding of the processes surrounding gas uptake, and to identify any interactions which might be present. It was envisaged that these results would help in the synthesis of future materials with additional functionalities that would be able to incorporate greater amounts of a particular gas. A key crystallographic criterion required in order for gas molecules to be potentially located within pores was to use a system where the channels were not too large. Were the pores too large, the likelihood of the gas being crystallographically disordered over many sites would increase, giving no indication as to the preferred guest molecule location. For this reason the one dimensional systems were attractive targets.

Searches were carried out using the Cambridge Structural Database (CSD) to gain an insight into systems that had been studied previously and shown to contain CO_2, SO_2, CH_4 or HCl molecules within the pores. One series of networks that occurred

frequently was the series by *Takamizawa et al*., of the general formula $[M_2(bza)_4(pyz)]$ (bza = benzoate, pyz = pyrazine, M = Rh(II), Cu(II)) (Figure 2.2). These structures contain paddle wheel SBUs, which are linked into one dimensional chains by coordinated pyz molecules. Although the structure is one dimensional, it can be seen from Figure 2.5 that channels are nonetheless evident between the chains.

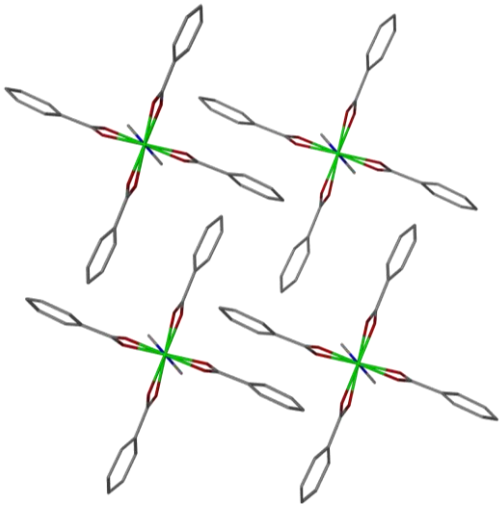

Figure 2.5: The crystal structure of $[Cu_2(bza)_4(pyz)]$ (bza = benzoate, pyz = pyrazine). Hydrogen atoms have been omitted for clarity[1]

This series of complexes have been shown to adsorb different amounts of nitrogen, sulphur dioxide, nitrogen dioxide, nitric oxide, carbon disulfide, carbon dioxide, methane, argon, oxygen, hydrogen, nitrous oxide, ethanol, propanol, butanol and pentanol. Single crystal X-ray diffraction was carried out on the gas inclusion crystals to determine the amount of gas present. Many of the crystals were shown to undergo a phase transition from a monoclinic to a triclinic crystal system on gas adsorption. X-ray crystallography is an important tool in these experiments as it allows the exact position of the gas molecules to be determined, and hence give an insight into the rationale behind high gas uptake.[1, 2, 8, 14, 16-23]

A typical structural determination on one of these types of paddle wheel structures with a gas included, is that of $[Cu_2(bza)_4(pyz)]$ with carbon dioxide. Initially, a data collection, without CO_2, was carried out at 93 K to determine the structure of the sample, this was shown to be in the monoclinic space group *C*2/*c*. A single crystal of $[Cu_2(bza)_4(pyz)]$ was then cooled to 93 K in a CO_2 atmosphere, at which point a single crystal X-ray data collection was measured. It revealed a structural transformation from the *C*2/*c* space group to the triclinic *P*-1 space group. On the uptake of CO_2 the one

dimensional channels expand and are filled with three molecules of CO_2 per copper dimer. The transformation is accompanied by an expansion of the one dimensional channels, with the void volume, if the CO_2 was removed, increasing from 16.2 % to 20.2 % after the transformation. The CO_2 molecules fit into the channels in a linear arrangement along the *b* axis, and if considering the electric quadrupole moment of CO_2 the most stable arrangement is with the CO_2 molecules aligned parallel, followed by the next stable arrangement of them lying perpendicular to each other (Figure 2.6).[1]

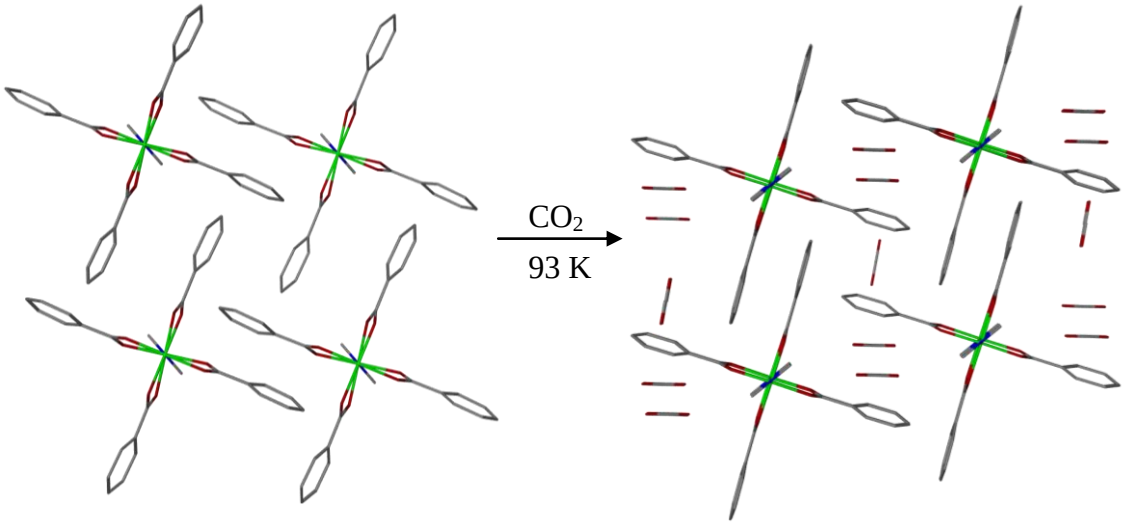

Figure 2.6: The crystal structure of [Cu_2(bza)$_4$(pyz)] (bza = benzoate, pyz = pyrazine) before and after CO_2 adsorption. Hydrogen atoms have been omitted for clarity[1]

The group also looked at the same systems with 2-methylpyrazine (Mepyz) and 2,3-dimethylpyrazine (DiMepyz), to understand the effect of the methyl groups on the adsorption process. Gas adsorption capacity measurements were first carried out on all three systems, showing that in spite of the addition of the methyl groups, the systems were still capable of adsorbing significant amounts of CO_2. [Cu_2(bza)$_4$(pyz)] and [Cu_2(bza)$_4$(Mepyz)] adsorbed similar amounts of CO_2, three molecules per copper dimer, whereas the [Cu_2(bza)$_4$(DiMepyz)] adsorbed only 0.65 molecules of CO_2 per copper dimer.[24] These two materials also remained crystalline after gas uptake so were studied crystallograpically to understand the changes involved during the adsorption process.

[Cu_2(bza)$_4$(Mepyz)], like [Cu_2(bza)$_4$(pyz)], contained three molecules of CO_2 adsorbed in the channels at 90 K. The space group of the structure before gas adsorption is *P*-1 which remains after the CO_2 adsorption. In the structure before gas uptake, due to the presence of the methyl groups, the one dimensional chains are zigzagged. Once the

CO_2 is adsorbed, the chains become completely linear. This can be seen by the change in the bend angles of the chains; before the angle is 169.88° and after gas uptake the angle becomes linear at 180° (Figure 2.7).[24]

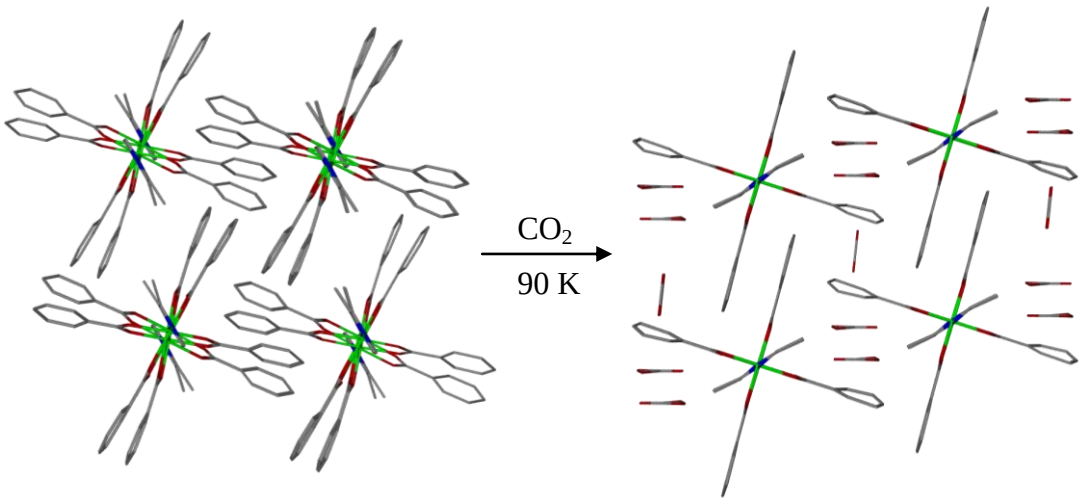

Figure 2.7: The crystal structure of [$Cu_2(bza)_4(Mepyz)$] (bza = benzoate, Mepyz = 2-methylpyrazine) before and after CO_2 adsorption. Hydrogen atoms have been omitted for clarity[24]

For [$Cu_2(bza)_4$(DiMepyz)] only a maximum of 0.65 molecules of CO_2 per copper dimer were adsorbed into the system. If this is compared to the isostructural [$Rh_2(bza)_4$(DiMepyz)] compound, the rhodium containing material was able to adsorb two molecules of CO_2 per rhodium dimer, similar to the other reported structures at 90 K. The structure is similar to that of [$Cu_2(bza)_4$(Mepyz)] where the one dimensional chains exist with a zigzag orientation. When this system adsorbs the CO_2 in contrast to [$Cu_2(bza)_4$(Mepyz)], the zigzag chains remain intact, with only a small structural change observed. The π-π stacking is maintained in the system after gas uptake, but the rings tilt and shift to accommodate the addition of the CO_2 molecules (Figure 2.8).[24]

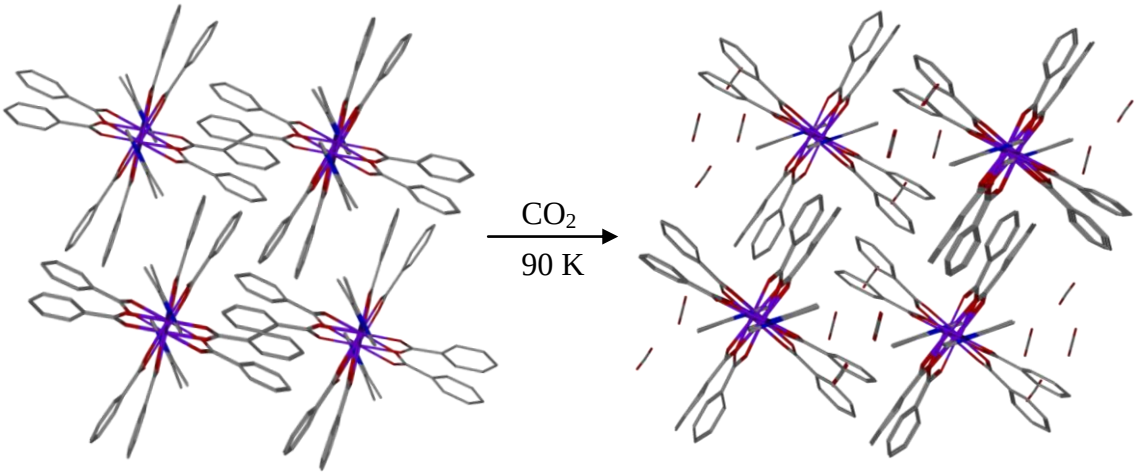

Figure 2.8: The crystal structure of [Rh_2(bza)$_4$(DiMepyz)] (bza = benzoate, DiMepyz = 2,3-dimethylpyrazine) before and after CO_2 adsorption. Hydrogen atoms have been omitted for clarity[24]

This work carried out by *Takamizawa et al.* exhibits how effective these types of materials are at adsorbing CO_2. The differences between the structures also demonstrate that the structures 'breathe' in response to the presence of CO_2, and show that it is possible to locate the gas molecules crystallographically and observe interactions that may be present.

The results from this research are promising for applications involving carbon dioxide storage and release. However, there is a need to store larger amounts of gas for them to be viable in many of these applications. Also, looking at Takamizawa's series, it was interesting to note the effect of the methyl substituent on the pyrazine, and how this affected the storage potential. The methyl groups seemed to have minimal effect in the case of [Cu_2(bza)$_4$(Mepyz)]; they affected the initial packing, but on CO_2 adsorption the network altered to take in more gas. However, when two methyl groups were present on the pyrazine rings, the amount of CO_2 adsorbed decreased from three molecules to two per metal dimer.

The aim of the research in this chapter was to investigate the gas storage potential in similar materials, using *in situ* crystallography. We reasoned that increasing the length of the carboxylate ligand could potentially increase the pore size leading to a higher storage capacity. Whilst we wanted to increase the pore size, we did not wish to extend this excessively, in order to facilitate examination of the gas storage potential using

crystallography. To be successful crystallographically, we would need to avoid gas molecule disorder.

For these reasons we used biphenyl-4-carboxylic acid (Hbiphen) and 4-iodobenzoic acid (HIbza) as ligands. We also wanted to study the effect of larger substituents on the pores obtained, and for this reason we looked at 9-anthracenecarboxylic acid (Hanthr). This ligand could also be involved in π-π interactions which might impact on the overall packing of the systems. A range of different ditopic nitrogen ligands were also studied to examine their affects on the pore size, and on gas storage potential. The linkers used were pyrazine (pyz), 1,4-diazabicyclo[2.2.2]octane (dabco), 2-aminopyrazine (NH_2pyz), 2-methylpyrazine (Mepyz) and 4,4'-bipyridine (bipy).

2.2 Results

2.2.1 Biphenylcarboxylate Paddle Wheel Structures

This first series of compounds consists of both copper and zinc paddle wheel moieties constructed from the Hbiphen ligand and a range of ditopic nitrogen donor ligands.

Green block crystals of $[Cu_2(biphen)_4(pyz)]\cdot 3.8BzOH$ (**1**) were produced from the reaction of copper(II) acetate in methanol with Hbiphen and pyz in benzyl alcohol at room temperature. In a similar reaction, green block crystals of $[Cu_2(biphen)_4(dabco)]\cdot BzOH$ (**2**) were synthesised, with dabco used in the synthesis instead of pyz. Colourless needles of $[Zn_2(biphen)_4(dabco)]\cdot 2DMF$ (**3**) were formed during the reaction of zinc(II) nitrate, biphen and dabco in DMF at 120 °C, this material is isostructural to **2**. All three materials were characterised crystallographically, and their corresponding data is shown in Table 2.1.

Compound	**1**	**2**	**3**
Empirical formula	$C_{69.30}H_{51.40}Cu_2N_2O_{9.90}$	$C_{32.50}H_{29}CuNO_{4.50}$	$C_{64}H_{62}N_4O_{10}Zn_2$
M	1197.60	569.11	1177.92
***T*/ K**	150(2)	150(2)	100(2)
Crystal system	Triclinic	Monoclinic	Monoclinic
Space group, *Z*	*P*-1, 1	*C*2/*c*, 8	*C*2/*c*, 4
***a*/ Å**	9.7080(4)	23.320(3)	23.043(10)
***b*/ Å**	14.1110(9)	9.5701(14)	9.582(4)
***c*/ Å**	16.5790(10)	26.478(4)	26.852(11)

α/ °	72.751(2)	90	90
β/ °	87.723(4)	103.799(2)	104.624(7)
γ/ °	71.095(3)	90	90
***U*/Å^3**	2048.0(2)	5738.7(14)	5737(4)
Absorption coefficient/ mm^{-1}	0.564	0.800	0.899
***F*(000)**	618	2368	2456
Theta range for data collection/ °	3.60 to 25.15	3.52 to 25.00	3.92 to 20.65
Reflections collected/ observed [$I>2\sigma(I)$]	25559/ 4798	22246/ 3400	10340/ 1557
Data Completeness	0.984	0.994	0.989
Goodness-of-fit on F^2	1.028	1.039	1.032
Final *R* indices [$I>2\sigma(I)$]	$R1$ = 0.0751, $wR2$ = 0.1955	$R1$ = 0.0768, $wR2$ = 0.2140	$R1$ = 0.0423, $wR2$ = 0.0781
***R* indices (all data)**	$R1$ = 0.1103, $wR2$ = 0.2095	$R1$ = 0.1143, $wR2$ = 0.2340	$R1$ = 0.0804, $wR2$ = 0.0866
Largest diff. peak and hole Å^{-3}	1.900 and -0.514	0.916 and -0.497	0.296 and -0.221

*Table 2.1: Crystallographic data for compounds $[Cu_2(biphen)_4(pyz)]\cdot 3.8BzOH$ (**1**), $[Cu_2(biphen)_4(dabco)]\cdot BzOH$ (**2**) and $[Zn_2(biphen)_4(dabco)]\cdot 2DMF$ (**3**)*

The asymmetric unit for **1** consists of one copper atom, two biphen ligands and half a pyz molecule. Within the asymmetric unit there is 90 % of a molecule of benzyl alcohol which was located crystallographically, the oxygen atom of this was equally disordered over two positions. There was also some highly disordered solvent which was approximated to one molecule of benzyl alcohol per asymmetric unit using PLATON SQUEEZE. Through a space group inversion centre, the structure extends into the typical copper dimer paddle wheel SBU (Figure 2.9).

Compounds **2** and **3** form isostructural materials, and their asymmetric units consist of two half-occupancy metal centres, two biphen ligands and one half occupancy dabco ligand. For **2**, a fragment of highly disordered solvent was also present, and this was approximated to half a benzyl alcohol per asymmetric unit using the PLATON SQUEEZE function. In **3**, there was an ordered DMF molecule located within the channels. In a similar manner to **1**, metal dimer paddle wheel SBUs are formed (Figure 2.9).

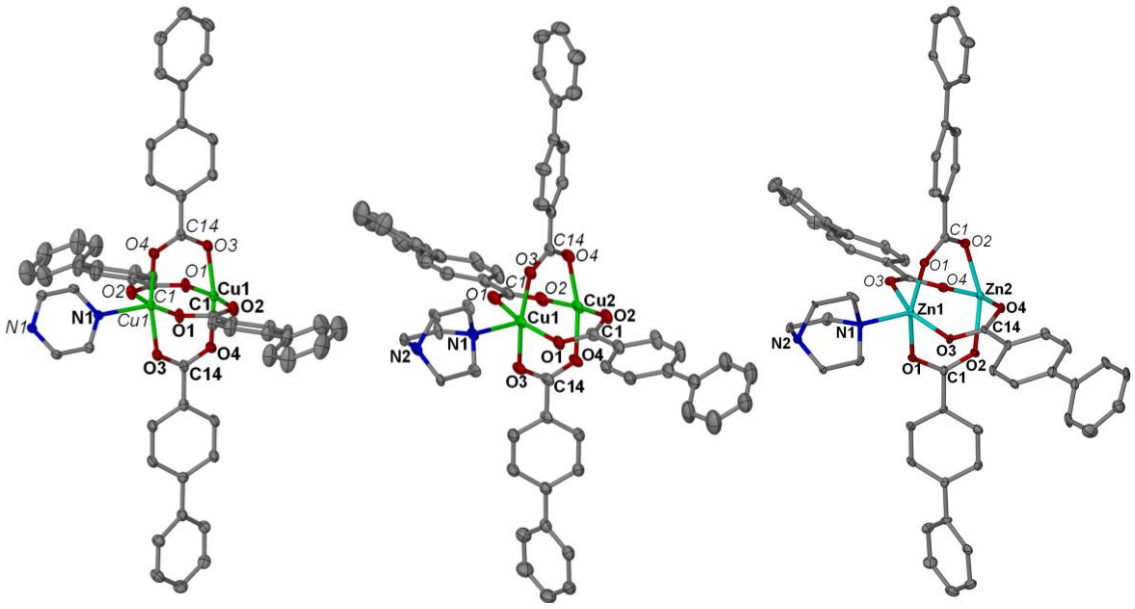

*Figure 2.9: The crystal structures of [Cu_2(biphen)$_4$(pyz)]·3.8BzOH (**1**) (left), [Cu_2(biphen)$_4$(dabco)]·BzOH (**2**) (middle) and [Zn_2(biphen)$_4$(dabco)]·2DMF (**3**) (right) with thermal ellipsoids at the 30 % probability level. Symmetry equivalent atom labels are displayed in italics. Hydrogen atoms and solvent molecules have been omitted for clarity*

In all these structures each metal centre has approximate square pyramidal geometry, with four coordinated biphen ligands at 90° to each other, bridging the metal centres into M_2 dimers. In the axial position of the metal centres is either a coordinated pyz ligand (**1**) or a dabco ligand (**2**, **3**), and these extend the structures into one dimensional chains (Figure 2.10).

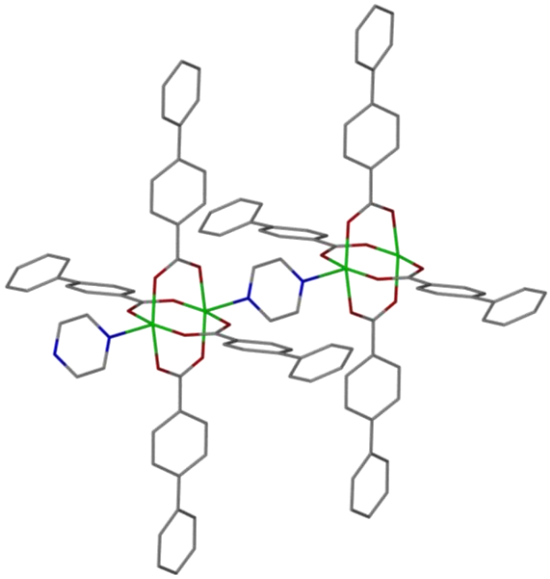

*Figure 2.10: Infinite chain structure of compound **1**. Hydrogen atoms and solvent molecules have been omitted for clarity*

Table 2.2 shows a comparison of bond lengths for compounds **1**, **2** and **3**. For **1** and **2**, the Cu-O bond lengths are comparable to those in $[Cu_2(bza)_4(pyz)]$.[14] The Cu-N distance in **1** is also comparable to this literature compound, but the bond distances in **2** are longer due to the presence of dabco instead of pyz. In compound **3** the Zn-O and Zn-N bond distances are similar to those reported for similar paddle wheel SBU type materials.[25] If these are compared to the bond lengths for the isostructural compound **2**, variations can be observed. Due to the Jahn-Teller effect of the d^9 copper(II) centres, **2** exhibits a shortening of the equatorial bond lengths and lengthening of the axial bond lengths, relative to **3**.

Compound	Cu-O (Å)	Cu-N (Å)	Zn-O (Å)	Zn-N (Å)
1	1.952(3)-1.965(3)	2.172(3)		
2	1.960(5)-1.989(4)	2.187(5)-2.191(5)		
3			2.020(5)-2.079(4)	2.039(7)-2.081(7)

*Table 2.2: Comparison of bond lengths for compounds **1**, **2** and **3***

Through the packing of the one dimensional chains, channels are created within these systems which are larger than those seen in $[Cu_2(bza)_4(pyz)]$, which are approximately 3.9 x 8.8 Å (Figure 2.11). For compound **1** the pore size is approximately 11.3 x 13.3 Å. The void volume and hence percentage void space within the structure can also be calculated using PLATON SQUEEZE. For **1** the percentage void volume is 52.1 % when all solvent has been removed, compared to 16.2 % for $[Cu_2(bza)_4(pyz)]$. The pore sizes in **2** and **3** are approximately 6.8 x 9.2 Å, with a void volume calculated at 19.1 %. The void volume of **2** and **3** is smaller than observed for **1** due to the packing of the biphen ligands, these are interdigitated in **2** and **3** reducing the pore size. Due to the increase in pore size compared to $[Cu_2(bza)_4(pyz)]$, these materials look like excellent candidates for gas adsorption studies. However, the pores of these structures are filled with guest solvent molecules, which will need removing prior to gas adsorption without any decomposition of the materials.[14]

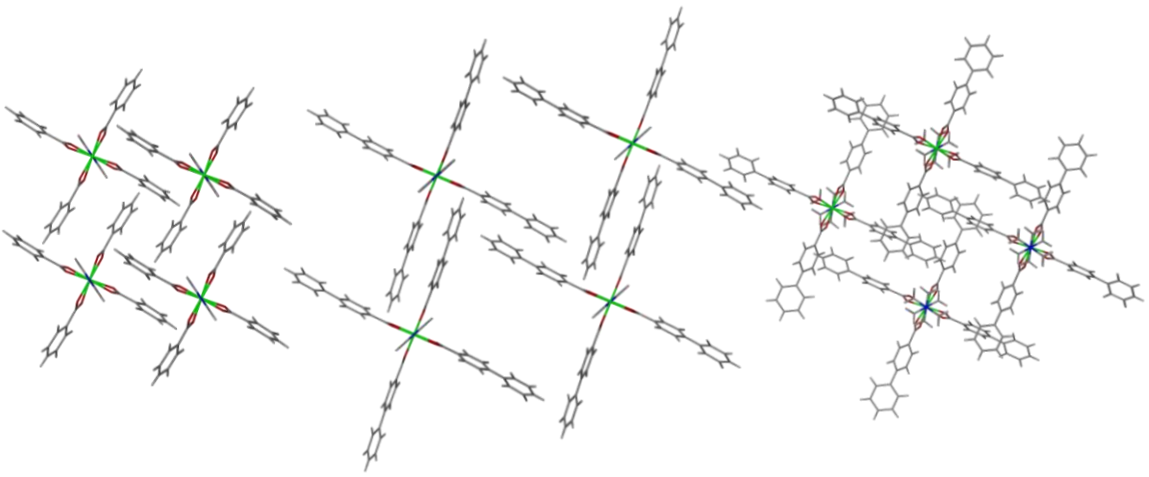

*Figure 2.11: The infinite channels of [$Cu_2(bza)_4(pyz)$] (left) compared to those in **1** (middle) and **2/3** (right). Solvent molecules have been omitted for clarity*[14]

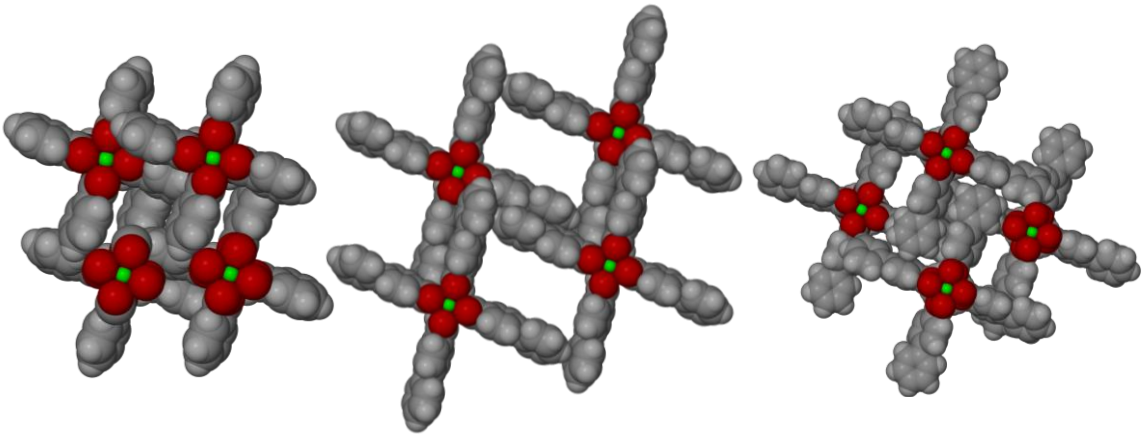

*Figure 2.12: Space filling representation of the infinite channels of [$Cu_2(bza)_4(pyz)$] (left) compared to those in **1** (middle) and **2/3** (right). Solvent molecules have been omitted for clarity*[14]

From the space filling comparison of the structures (Figure 2.12) it is obvious that the pores in compounds **1**, **2** and **3** are much larger than those seen for [$Cu_2(bza)_4(pyz)$]. As would be expected for such large pores the channels are filled with solvent molecules.[14] Powder X-ray diffraction, elemental analysis and Thermogravimetric analysis (TGA) was carried out on **1**. The powder X-ray diffraction trace and elemental analysis showed the material to be phase impure, and so the TGA could not be analysed in order to make deductions about the process of solvent loss. Attempts were made to isolate **1** from the mixture of products, using density separations,[26] but these proved unsuccessful. Single crystals of **1** were placed under vacuum to remove the benzyl alcohol solvent, however during this process the crystals of **1** degraded, owing to the loss in crystallinity of the sample.

TGA was carried out on compound **2**. The TGA had a 9-9.5 % weight loss up to 150-160 °C which can be attributed to the loss of the benzyl alcohol, which was calculated as 9.5 % per copper dimer. Above this temperature there is a gradual decrease in mass up to 350 °C where the percentage weight left decreases to approximately 30 %, this can be assigned to the slow decomposition of the compound. After loss of the benzyl alcohol, there is no plateau of the curve, suggesting that after the removal of the solvent, the structure immediately begins to decompose.

Crystals of **2** also appeared to degrade when left in air for several hours. Typically, a batch of crystals was observed under the microscope to be highly crystalline. When left out in the air for an hour and viewed again under the microscope, cracks had appeared in the crystals. Although the sample appeared to be highly porous from the crystal data, it was not a suitable candidate to follow the adsorption potential due to its loss of crystallinity and decomposition on activation.

The results from the powder X-ray diffraction and elemental analysis for **3** show the material to be phase pure. The TGA for compound **3** exhibits an initial 13 % weight loss up to 170 °C which can be compared to a calculated value of 12.4 % for the loss of two molecules of guest DMF. After this temperature there is a small plateau up until 250 °C. This is followed by another weight loss of approximately 7.5 % up to 290 °C which can be attributed to the loss of the dabco linker. Above this temperature there is a slow decomposition evident up to 550 °C where 25 % of the initial compound mass remains. Attempts to activate this sample by placing under vacuum, caused a loss in crystallinity when monitored by powder X-ray diffraction.

1, **2** and **3** were attempted to be synthesised under a number of reaction conditions. A range of other solvents were tested including methanol, ethanol, THF and DMF, but these all formed products which could not be successfully characterised. Compounds **1** and **2** were also produced at room temperature. Attempts were made to synthesise these at elevated temperatures, but again different uncharacterised products were made.

These results have shown that the use of the longer biphen ligand in comparison to bza produces similar structures to that of $[Cu_2(bza)_4(pyz)]$,[14] but with larger pores present. However, due to the presence of these expanded channels, the structures are less stable and loss of crystallinity is observed on removal of solvent.

The difference between the structure of $[Cu_2(biphen)_4(pyz)_2]\cdot 2BzOH$ (**1**) and $[Cu_2(biphen)_4(dabco)_2]\cdot BzOH$ (**2**) is the nitrogen donor linker. In **2**, the void size is reduced due to the packing of the biphen ligands when compared to **1**; this can also be seen from the amount of solvent present in these pores.

The compounds $[Cu_2(biphen)_4(dabco)_2]\cdot BzOH$ (**2**), and $[Zn_2(biphen)_4(dabco)_2]\cdot 2DMF$ (**3**), produced isostructural materials even with the use of different metals, showing that this structural arrangement is energetically favourable with the use of dabco and Hbiphen.

2.2.2 Iodobenzoate Paddle Wheel Structures

This series of structures are constructed from copper and zinc dimer paddle wheel motifs, coordinated via HIbza ligands. The ditopic nitrogen donor ligands used were pyz, dabco and NH_2pyz. These materials were synthesised to assess structural changes upon alteration of the carboxylate ligands.

The first compound synthesised was $[Cu_2(Ibza)_4(MeOH)_2]$ (**4**), which produced green plate-like crystals from the reaction of copper(II) acetate and HIbza in methanol. Green crystals of $[Cu_2(Ibza)_4(pyz)]$ (**5**) and $[Cu_2(Ibza)_4(NH_2pyz)]\cdot 2BzOH$ (**6**) were formed from the reaction of copper(II) acetate in methanol and HIbza and either pyz or NH_2pyz in benzyl alcohol. Finally colourless needles of the zinc analogue $[Zn_2(Ibza)_4(dabco)]\cdot 3.25DMF$ (**7**) were synthesised from the reaction of zinc(II) nitrate with HIbza and dabco in DMF at 120 °C. All of these reactions produced crystals of suitable size for single crystal X-ray analysis, and the data from these experiments are shown in Table 2.3.

Compound	**4**	**5**	**6**	**7**
Empirical formula	$C_{30}H_{22}Cu_2I_4O_{10}$	$C_{16}H_{10}CuNO_4I_2$	$C_{46}H_{38}Cu_2N_3O_{10}I_4$	$C_{87.50}H_{101.50}N_{10.50}O_{22.50}Zn_4I_8$
M	1177.16	597.59	1427.47	2936.97
***T*/ K**	150(2)	150(2)	150(2)	150(2)
Crystal system	Triclinic	Tetragonal	Tetragonal	Triclinic
Space group, *Z*	*P*-1, 2	$I4_1/a$, 16	$P4_1$, 4	*P*-1, 2
***a*/ Å**	12.0340(2)	18.775(1)	12.7970(5)	12.4072(8)
***b*/ Å**	13.0260(3)	18.775(1)	12.7970(5)	12.4082(7)
***c*/ Å**	13.1030(3)	19.672(3)	39.0980(18)	33.608(2)

α/ °	74.414(1)	90	90	87.891(2)
β/ °	68.037(1)	90	90	88.473(2)
γ/ °	86.525(1)	90	90	83.785(2)
***U*/Å^3**	1833.02(7)	6934.4(10)	6402.8(5)	5138.8(5)
Absorption coefficient/ mm^{-1}	4.579	4.841	2.637	3.397
***F*(000)**	1104	4480	2740	2848
Theta range for data collection/ °	3.62 to 27.52	3.70 to 32.94	3.55 to 23.97	3.85 to 32.00
Reflections collected/ observed [$I>2\sigma(I)$]	20746/ 5498	12737/ 5843	6739/ 2490	52084/ 17405
Data Completeness	0.967	0.998	0.433	0.978
Goodness-of-fit on F^2	1.018	1.060	1.078	1.032
Final *R* indices [$I>2\sigma(I)$]	$R1$ = 0.0497, $wR2$ = 0.1178	$R1$ = 0.0668, $wR2$ = 0.1750	$R1$ = 0.0786, $wR2$ = 0.2418	$R1$ = 0.0764, $wR2$ = 0.1937
***R* indices (all data)**	$R1$ = 0.0816, $wR2$ = 0.1359	$R1$ = 0.1125, $wR2$ = 0.1890	$R1$ = 0.1056, $wR2$ = 0.2617	$R1$ = 0.1137, $wR2$ = 0.2210
Largest diff. peak and hole Å^{-3}	1.197 and -0.293	4.985 and -3.155	0.745 and -1.405	6.503 and -4.242

*Table 2.3: Crystallographic data for compounds $[Cu_2(Ibza)_4(MeOH)_2]$ (**4**), $[Cu_2(Ibza)_4(pyz)]$ (**5**), $[Cu_2(Ibza)_4(NH_2pyz)]\cdot 2BzOH$ (**6**) and $[Zn_2(Ibza)_4(dabco)]\cdot 3.25DMF$ (**7**)*

The asymmetric unit for **4** consists of two full occupancy copper atoms, four Ibza ligands, and two methanol solvent molecules coordinated to the axial positions of the copper atoms (Figure 2.13).

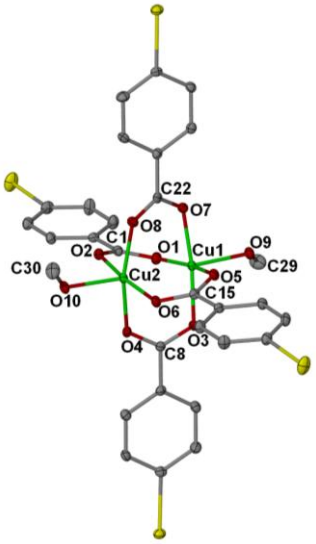

*Figure 2.13: The asymmetric unit of $[Cu_2(Ibza)_4(MeOH)_2]$ (**4**) showing thermal ellipsoids at the 30% probability level. Hydrogen atoms have been omitted for clarity*

Each copper atom has approximate square pyramidal geometry, with four bonds to oxygen atoms from each of the four bridging carboxylates [Cu-O 1.948(4) – 1.992(3) Å], forming the paddle wheel SBU. A methanol molecule is coordinated in the axial position of the copper centres [Cu-O 2.126(3) – 2.129(3) Å]. The Cu-O bond distances correspond well with the literature,[14] and the copper-oxygen bond lengths for the coordinated methanol relate well with similar structures within the CSD.[27]

Although the axial positions of each copper are occupied by a coordinated methanol molecule, the paddle wheels still link into one dimensional chains through hydrogen bonding. The hydrogen atom of the methanol hydroxyl group hydrogen bonds to a coordinated oxygen from a carboxylate on an adjacent paddle wheel, as seen in Figure 2.14. These hydrogen bonds correspond to O-H···O interactions [O(10)···O(8)^{i} 2.80 Å, H(43)···O(8)^{i} 2.03 Å, O(10)–H(43)···O(8)^{i} 141°]. Due to this staggered hydrogen bonding along the chains, only very small channels are present within the gross structure.

Symmetry transformations used to generate equivalent atoms:
^{i} 2 -x, 1 -y, -z

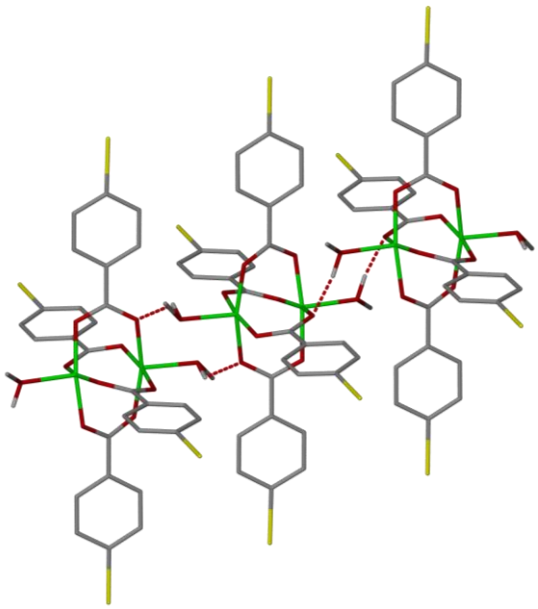

*Figure 2.14: Hydrogen bonding present in compound **4** showing the construction of the one dimensional chains. All hydrogen atoms, except those involved in hydrogen bonding have been omitted for clarity*

Compounds **5**, **6** and **7** (unlike **4**), contain a nitrogen donor ligand coordinated in the axial position of the metal centre, instead of a coordinated methanol molecule. Therefore, these three compounds all produce one dimensional chains.

The asymmetric unit for $[Cu_2(Ibza)_4(pyz)]$ (**5**) consists of two half occupancy copper centres, half a pyz molecule and two Ibza ligands. The phenyl ring of the Ibza containing I(2) is positionally disordered, with the two rings approximately 90° to each other in a 65:35 occupancy ratio (Figure 2.15).

$[Cu_2(Ibza)_4(NH_2pyz)]\cdot 2BzOH$ (**6**) forms a similar paddle wheel moiety; however the asymmetric unit is slightly different, consisting of two copper centres bridged by four coordinated Ibza ligands, and a coordinated NH_2pyz linker. The amino group of this linker is disordered over three sites in a 50:25:25 ratio. There was also an area of diffuse solvent, and when PLATON SQUEEZE was used, two molecules of benzyl alcohol were assigned to the asymmetric unit (Figure 2.15).

Finally, $[Zn_2(Ibza)_4(dabco)]\cdot 3.25DMF$ (**7**) was characterised and shown to exist with the same paddle wheel geometry. The asymmetric unit for **7** consists of four independent zinc atoms, two of which make up a complete paddle wheel moiety with the other two zinc centres forming two halves of paddle wheel units. There are a total of eight Ibza

ligands per asymmetric unit and two dabco ligands. One of the dabco ligands is disordered in 60:40 ratio. The asymmetric unit also houses six and a half solvent DMF molecules (Figure 2.16).

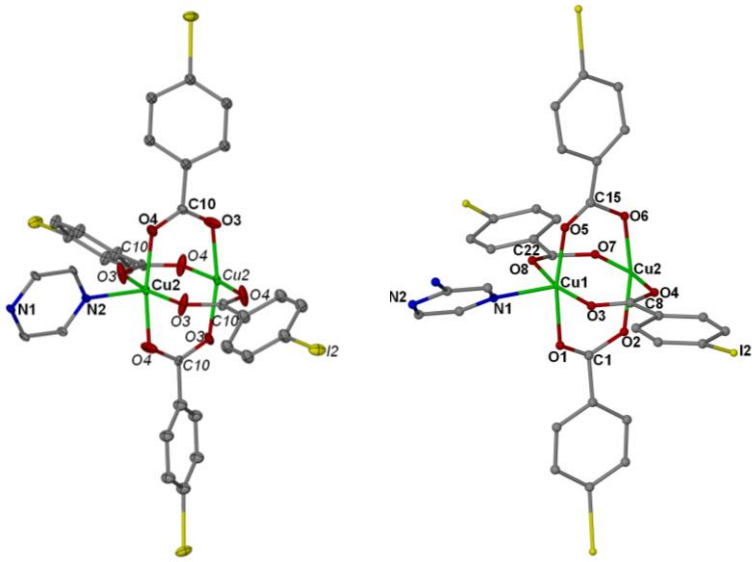

*Figure 2.15: The crystal structure of [Cu_2(Ibza)$_4$(pyz)] (**5**) (left) and [Cu_2(Ibza)$_4$(NH_2pyz)]·2BzOH (**6**) (right). Thermal ellipsoids have been displayed at the 30 % probability level on **5** only. Symmetry equivalent atom labels are displayed in italics. Hydrogen atoms, minor disordered components and solvent molecules have been omitted for clarity*

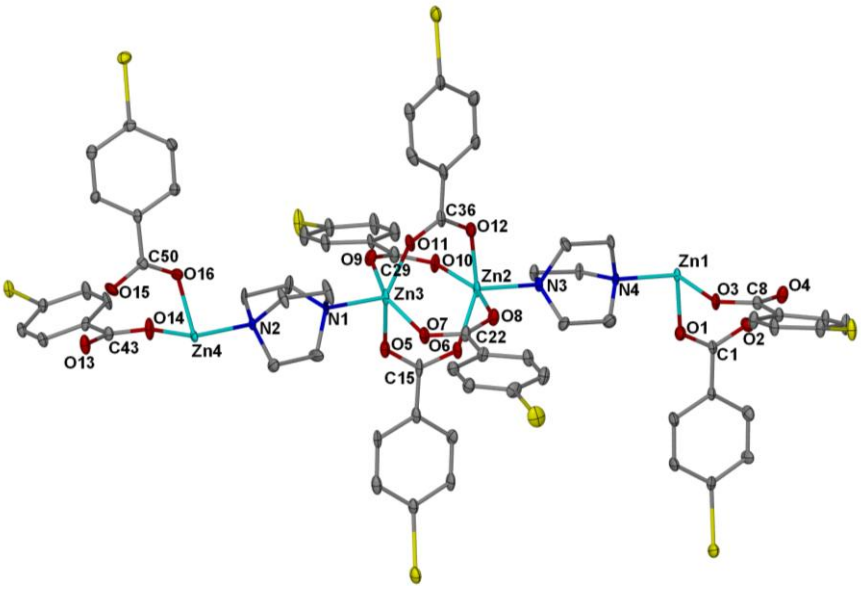

*Figure 2.16: Asymmetric unit of [Zn_2(Ibza)$_4$(dabco)]·3.25DMF (**7**) with thermal ellipsoids at the 30 % probability level. Hydrogen atoms, minor disordered components and solvent molecules have been omitted for clarity*

In a similar manner to **1-4**, the metal centres in **5-7** exhibit approximate square pyramidal geometry, with four coordinated oxygen atoms in the equatorial position from the carboxylate, which bridge the two metal atoms of the SBU together. In the axial position of the metal is a coordinated nitrogen atom from either a pyz, NH_2pyz or dabco ligand, which serves to link the dimers into one dimensional chains.

The bond lengths for compounds **5** and **7** are given in Table 2.4. Those for compound **6** will not be discussed in detail, due to the poor quality of the data. The values observed for compound **5** correspond well with those in $[Cu_2(bza)_4(pyz)]$.[14] The distances seen for **7** are consistent with those for compound **3**, and also relate well to similar compounds within the CSD.[25]

Compound	Cu-O (Å)	Cu-N (Å)	Zn-O (Å)	Zn-N (Å)
5	1.947(5)-1.978(4)	2.204(7)-2.212(7)		
7			2.030(7)-2.067(6)	2.069(6)-2.090(6)

*Table 2.4: Comparison of bond lengths for compounds **5** and **7***

Differences are observed in the one dimensional frameworks of **6** and **7**. The chains in these structures are no longer linear, but have now formed zigzagged chains relative to those in **5**. The bend angles along the Cu-N chain have become less than 180°, in **6**, the angles are between 174-179° and in **7** between 173.95(19)-178.20(20)°.

In **7** there is halogen bonding present between the iodine atoms of the Ibza ligand and the oxygen atoms of the DMF solvates [I···O 2.981 - 3.227 Å, C-I···O 158-168°]. These distances and angles correspond well with other structures in the database.[28] These favourable contacts pull the Ibza ligand away from the paddle wheel dimer, causing the distortion observed in the chains. Halogen bonding is defined as the non-covalent interaction, R-X···B, between a covalently bonded halogen atom (X) and an electron rich species (B). R can be defined as a number of atoms, including other halogen atoms, or C and O atoms for example. The contacts observed in **7** are below the sum of the van der Waals radii for iodine and oxygen (3.50 Å), and the angles are close to 180° indicating the presence of halogen bonding.[29]

Compared to the structures **1**-**3**, the one dimensional chains in **5**-**7** pack similarly, to produce channels throughout the structures. The channels in $[Cu_2(bza)_4(pyz)]$ are measured at approximately 3.9 x 8.8 Å, and the percentage void volume using PLATON SQUEEZE is calculated at 16.2 %. The pore volume for compound **5** (Figure 2.17) was calculated using SQUEEZE, and there are no accessible voids present within the structure, showing a significant reduction in the pore size present when compared to $[Cu_2(bza)_4(pyz)]$. Compound **6** has larger pores than $[Cu_2(bza)_4(pyz)]$ with approximate dimensions 8.1 x 8.4 Å (Figure 2.18), and has a calculated void volume of 51.0 % once all the solvent has been removed. In a similar manner, **7** also has larger channels, with values of approximately 5.7 x 8.5 Å (Figure 2.18) with a void space calculated as 33.1 % of the total volume for the material. We reasoned that if it was possible to remove the guest solvent molecules and maintain the structural integrity in **6** and **7**, these materials might prove to be promising gas adsorption candidates.[14]

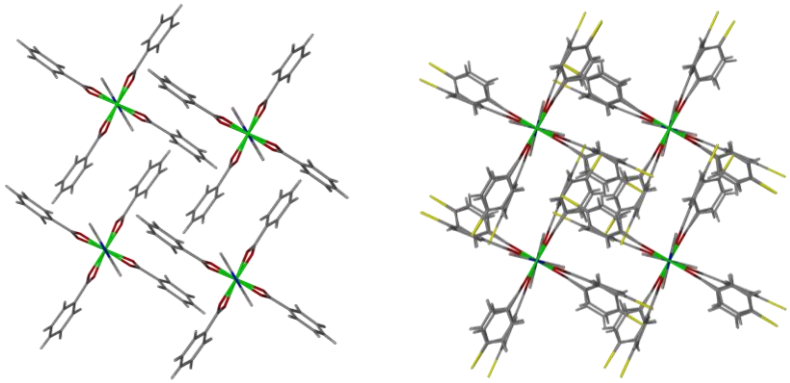

*Figure 2.17: The infinite channels of $[Cu_2(bza)_4(pyz)]$ (left) compared to those in **5** (right). Minor disordered components and solvent molecules have been omitted for clarity*[14]

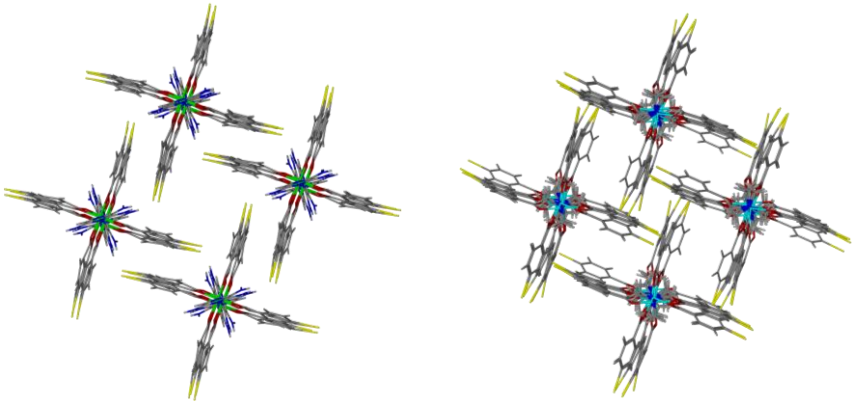

*Figure 2.18: The infinite channels of **6** (left) and **7** (right). Minor disordered components and solvent molecules have been omitted for clarity*

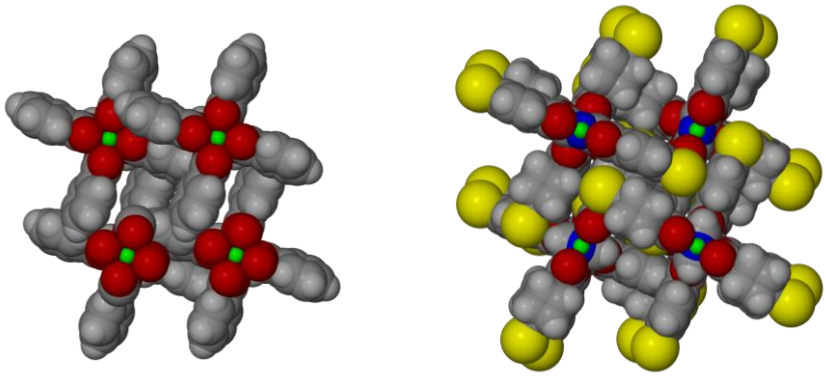

*Figure 2.19: Space filling representation of the infinite channels of [$Cu_2(bza)_4(pyz)$] (left) compared to those in **5** (right). Minor disordered components and solvent molecules have been omitted for clarity*[14]

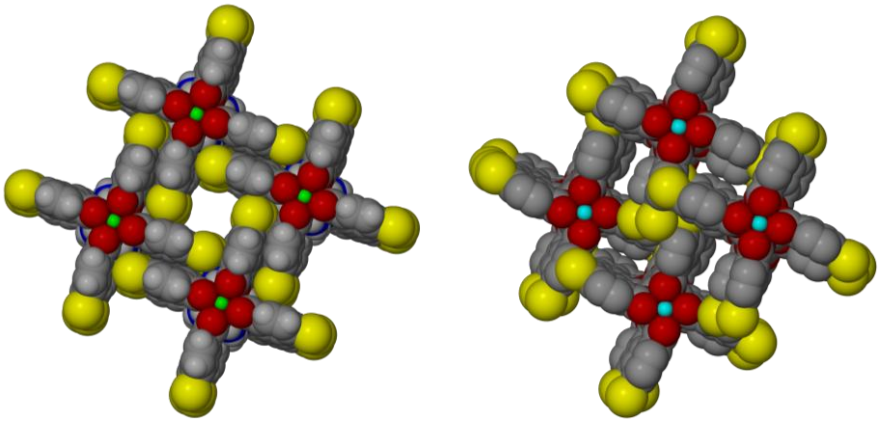

*Figure 2.20: Space filling representation of the infinite channels of **6** (left) and **7** (right). Minor disordered components and solvent molecules have been omitted for clarity*

From the calculations of the void volume and viewing the space filling diagrams of the structures (Figures 2.19 and 2.20) the channels created in **6** and **7** are larger than those observed in [$Cu_2(bza)_4(pyz)$].[14] These channels house solvent guest molecules, and TGA has been carried out on the samples to investigate the solvent loss process.

The X-ray powder diffraction trace for **6** showed a good match to that simulated from the crystal data, confirming the phase purity of the sample. The TGA trace for **6** showed a weight loss of approximately 23 % up to 140 °C, this can be attributed to the loss of three molecules of benzyl alcohol, which was calculated as 23 % per copper dimer. From this temperature there is a plateau up until 260 °C where the compound decomposes. On attempted activation of this material under heat and vacuum, the resultant powder X-ray diffraction trace showed the compound to be amorphous.

For compound **7**, the TGA shows a gradual weight loss of approximately 19 % up to 300 °C, which can be attributed to the loss of four solvent DMF molecules which was calculated at 20 % per zinc dimer. After this temperature there is a slow decomposition of the compound up to 450 °C. After activation, there is no plateau in the TGA trace, suggesting that after guest removal the network is no longer stable and begins to decompose.

Several attempts were made at synthesising materials **5-7** prior to their successful syntheses. These included using a range of solvent such as methanol, ethanol, THF and acetone. The reaction carried out in methanol to try and produce the pyz substituted copper paddle wheel instead formed compound **4**, where there was a coordinated methanol molecule as opposed to a pyz linker.

Similar synthetic approaches were adopted for $[Cu_2(Ibza)_4(pyz)_2]$ (**5**) and $[Cu_2(Ibza)_4(NH_2pyz)_2]\cdot 2BzOH$ (**6**), with the exception of the nitrogen donor ligand used. When pyz is present in the system, linear one dimensional chains are observed, but when the bulkier NH_2pyz linker is used then one dimensional zigzagged chains are produced. This suggests that the amine group presence alters the packing of the one dimensional chains.

Compounds $[Zn_2(biphen)_4(dabco)_2]\cdot 2DMF$ (**3**) and $[Zn_2(Ibza)_4(dabco)_2]\cdot 2.25DMF$ (**7**) were also synthesised in the same manner, just with a different carboxylic acid. From comparing these two structures the effect of the Ibza on structure formation can be seen. **3** forms the expected one dimensional linear chains, however when Ibza is present, **7** is formed wherein the chains are no longer linear but slightly zigzagged. This is due to the presence of halogen bonding between the iodine atoms of the ligand and the oxygen atoms of the solvent DMF molecules.

2.2.3 Bipyridine Containing Structures

The next series of compounds examined involved the incorporation of the 4,4'-bipy ligand into the materials. This was to investigate the change in the structures as the linker length was increased. Bipy was used in reactions in combination with copper and zinc, and Hbiphen and HIbza.

[Cu(biphen)$_2$(bipy)]·4BzOH (**8**) was produced from the reaction of copper(II) acetate in methanol and Hbiphen and bipy in benzyl alcohol. Colourless tabloid crystals were isolated for [Zn$_2$(biphen)$_4$(bipy)$_2$] (**9**) and [Zn(Ibza)$_2$(bipy)] (**10**), from the reaction of zinc(II) nitrate, bipy and either Hbiphen or HIbza respectively, in DMF. All three materials had their structures determined via single crystal X-ray diffraction and these data are summarised in Table 2.5.

Compound	**8**	**9**	**10**
Empirical formula	$C_{64}H_{58}CuN_2O_8$	$C_{72}H_{52}N_4O_8Zn_2$	$C_{48}H_{32}N_4O_8Zn_2I_4$
M	1046.66	1231.92	1431.12
***T*/ K**	150(2)	150(2)	150(2)
Crystal system	Monoclinic	Monoclinic	Monoclinic
Space group, *Z*	*C*2/*c*, 4	*C*2, 4	*C*2/*c*, 4
***a*/ Å**	15.6030(2)	25.7330(6)	26.7860(7)
***b*/ Å**	11.1260(1)	13.5820(3)	24.7060(7)
***c*/ Å**	29.8590(3)	17.2990(4)	7.4370(2)
α/ °	90	90	90
β/ °	90.711(1)	106.939(1)	104.858(2)
γ/ °	90	90	90
***U*/Å^3**	5183.09(10)	5783.8(2)	4757.1(2)
Absorption coefficient/ mm^{-1}	0.482	0.893	3.662
***F*(000)**	2196	2544	2736
Theta range for data collection/ º	3.52 to 27.48	3.80 to 27.49	3.55 to 27.50
Reflections collected/ observed [$I>2\sigma(I)$]	32492/ 4877	51278/8592	35694/3640
Data Completeness	0.979	0.994	0.995
Goodness-of-fit on F^2	1.040	1.022	1.080
Final *R* indices [$I>2\sigma(I)$]	$R1$ = 0.0391, $wR2$ = 0.0837	$R1$ = 0.0561, $wR2$ = 0.1289	$R1$ = 0.0591, $wR2$ = 0.1590
***R* indices (all data)**	$R1$ = 0.0532, $wR2$ = 0.0906	$R1$ = 0.1073, $wR2$ = 0.1506	$R1$ = 0.0965, $wR2$ = 0.1728
Largest diff. peak and hole Å^{-3}	0.334 and -0.701	0.912 and -0.893	1.660 and -1.781

*Table 2.5: Crystallographic data for compounds [Cu(biphen)$_2$(bipy)]·4BzOH (**8**), [Zn$_2$(biphen)$_4$(bipy)$_2$] (**9**) and [Zn(Ibza)$_2$(bipy)] (**10**)*

The asymmetric unit for compound **8** consists of half a copper atom, one biphen ligand, half a bipy ligand and two solvent benzyl alcohol molecules within the channels (Figure 2.21).

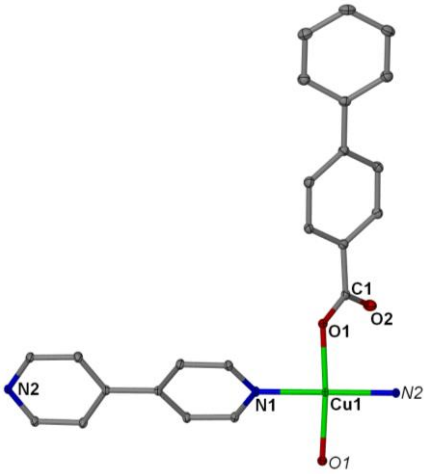

*Figure 2.21: The crystal structure of [Cu(biphen)$_2$(bipy)]·4BzOH (**8**) with thermal ellipsoids at the 30 % probability level. Symmetry equivalent atom labels are displayed in italics. Hydrogen atoms and solvent molecules have been omitted for clarity*

In **8** the copper atoms exhibit approximate square planar geometry, and coordinate to two bipy ligands and to two biphen ligands in a monodentate manner [Cu(1)-N(1) 1.9986(19), Cu(1)-N(2)[ii] 2.0222(18) Å, Cu(1)-O(1) 1.9609(11) Å]. The bipy ligands link the coppers linearly to form one dimensional chains. Although the Cu-O bonding in this complex is monodentate compared to bridging bidentate as is observed in the paddle wheel complexes, this bond length is still in the range observed for these compounds. The Cu-N distances however are shorter than those previously observed; this is due to the presence of the bipy ligand instead of pyz or dabco. The –OH groups of the two molecules of benzyl alcohol within the pores of the structure are involved in O-H···O hydrogen bonding to the free oxygen of the carboxylate groups.

Figure 2.22 demonstrates the packing that is present in **8**. The biphen ligands project from the copper-bipy backbone into the channel. The biphen ligands from adjacent chains then stack in a parallel fashion with these, along the crystallographic *a* axis.

[ii] Symmetry transformations used to generate equivalent atoms:
x, y +1, z

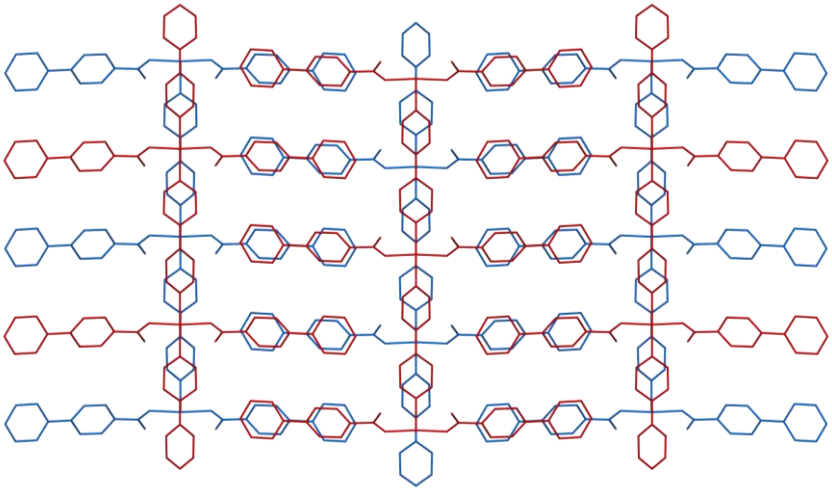

*Figure 2.22: The packing displayed in compound **8**, with different chains shown in red and blue. Hydrogen atoms and solvent molecules have been omitted for clarity*

Compound **8** does not contain the expected paddle wheel dimer that was observed in the other structures, this is due to the presence of the bipy ligand. Under the same conditions with dabco and pyrazine, compounds **2** and **3** were formed; this shows the effect of the nitrogen containing linker size on the frameworks formed. Under these reaction conditions when the longer bipy linker is used it is no longer preferential to form the paddle wheel moiety.

The next compound synthesised used zinc(II) nitrate as the metal salt to observe any differences between copper and zinc metal centres. Compound **9** contains two zinc metal centres, four biphen ligands and two bipy linkers within the asymmetric unit (Figure 2.23).

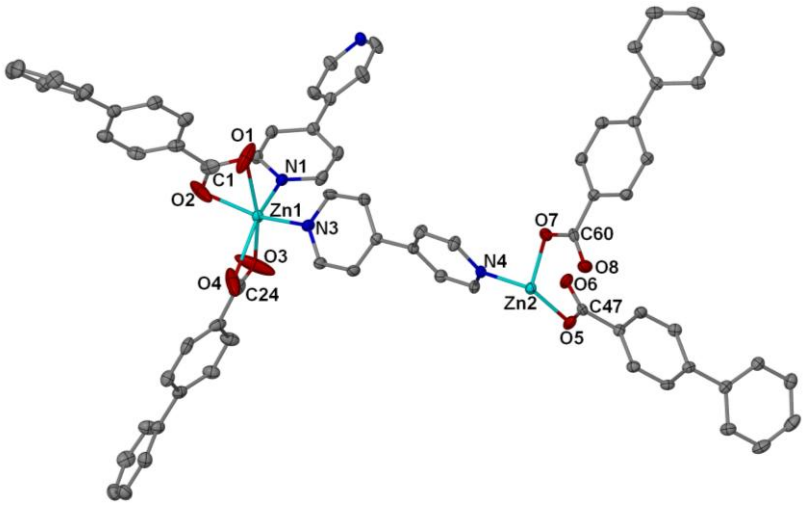

*Figure 2.23: The crystal structure of $[Zn_2(biphen)_4(bipy)_2]$ (**9**) with thermal ellipsoids at the 30 % probability level. Hydrogen atoms have been omitted for clarity*

Zn(2) in **9** has approximate tetrahedral geometry and is coordinated to two monodentate biphen ligands, and two bipy ligands. The bipy ligands then extend the structure into one dimensional chains through coordination to Zn(1) which has distorted octahedral geometry, coordinating to two bipy linkers and two chelating bidentate biphen ligands. Due to the chelating role of the biphen ligands attached to Zn(1), the coordination about the metal centre is octahedral although the projection of the four ligands from the metal is approximately tetrahedral.

The Zn-O bond lengths for compound **9** exhibit a wide variety of distances due to the nature of their coordination. Zn(2) coordinates to the oxygen atoms in a monodentate manner, and here two types of C-O bond length are observed, a shorter and longer length. This suggests the longer of the C-O lengths indicates more single bond character [C(47)-O(5) 1.283(5) Å and C(60)-O(7) 1.293(5) Å], while the shorter of the two has more double bond character [C(47)-O(6) 1.234(5) Å and C(60)-O(8) 1.224(5) Å]. Overall this observation suggests that there is little delocalisation of the carboxylate electrons. Although most of the examples of similar structures in the CSD show these lengths often to be similar, there are also a few examples where there are two different ranges of bond length present suggesting single and double bond character.[30]

For Zn(1) the oxygen atoms coordinate in a chelating bidentate manner, so only one type of C-O bond length is observed [C-O 1.147-1.237 Å], this suggests delocalisation of the electrons round the –COO chelate ring. Both zinc centres coordinate to bipy ligands, and the bond lengths for these are similar for both [Zn(1)-N(2) 2.045(4), Zn(1)-N(4) 2.061(4) Å, Zn(2)-N(1) 2.061(4), Zn(2)-N(2) 2.073(4) Å]. These distances are consistent with other Zn-N bond lengths observed in **7**.

Due to the *bis*-coordination of the bipy ligands, the structure extends into one dimensional chains. The projection of the ligands from each zinc centre is approximately tetrahedral, and therefore zigzag chains are formed (Figure 2.24). This differs from the structure of **8**, as the copper centres exhibit square planar geometry and hence the chains formed are linear.

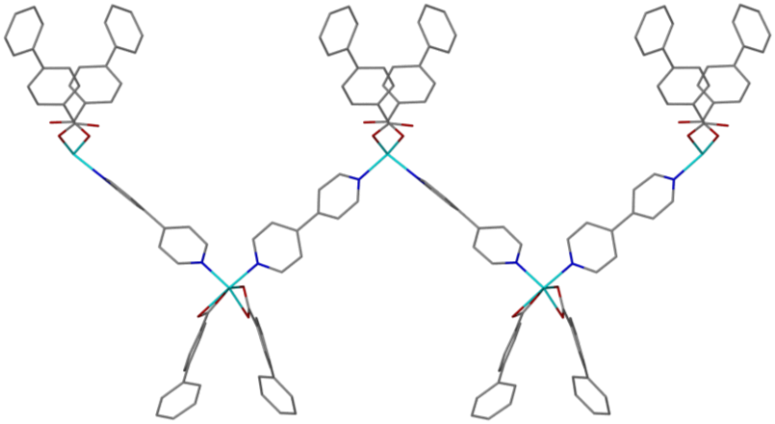

*Figure 2.24: Zigzag chains present in **9**. Hydrogen atoms have been omitted for clarity*

Despite the zigzag nature of the chains they pack in a similar manner to those in **8**. The biphen ligands project from the backbone of the chain into the pore space created by adjacent chains (Figure 2.25). Due to the nature of the chains, they stack directly above each other, and are not offset like in compound **8**.

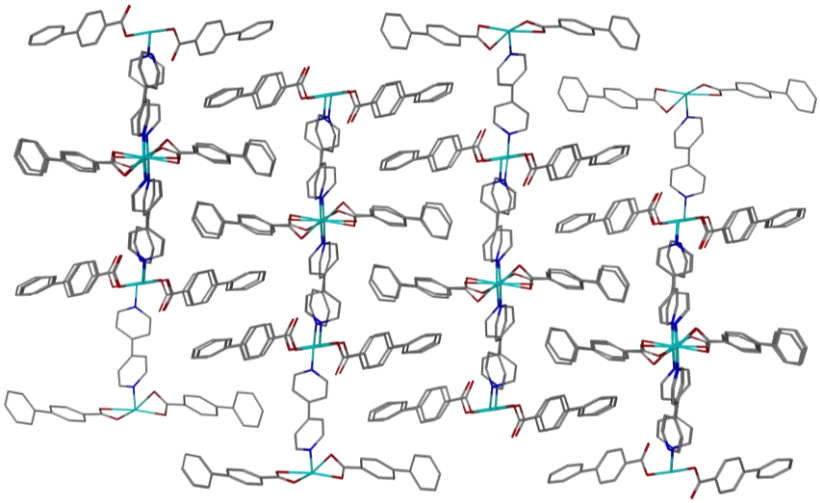

*Figure 2.25: Packing of **9** viewed down the crystallographic b axis. Hydrogen atoms have been omitted for clarity*

Finally, compound **10** is constructed in the same manner as **9**, with the biphen ligand replaced for Ibza. One zinc centre, two Ibza ligands and one bipy ligand make up the asymmetric unit (Figure 2.26).

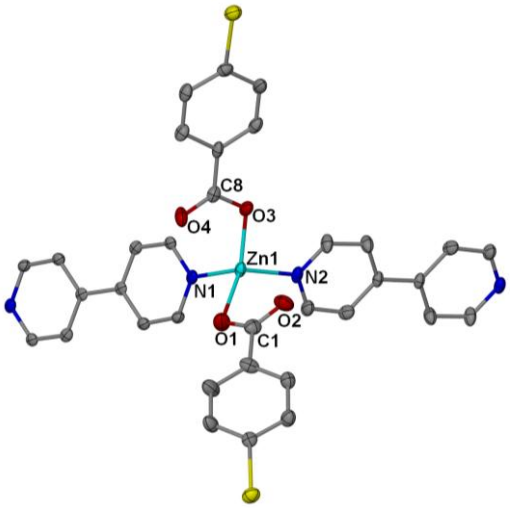

*Figure 2.26: The crystal structure of [Zn(Ibza)$_2$(bipy)] (**10**) with thermal ellipsoids at the 30 % probability level. Hydrogen atoms have been omitted for clarity*

The zinc centres exist with approximate tetrahedral geometry in which the two Ibza ligands coordinate in a monodentate manner [Zn(1)-O(1) 2.007(6) Å, Zn(1)-O(3) 1.942(5) Å]. The other two positions of the zinc coordination sphere are completed by coordination of two nitrogen atoms from the bipy ligands [Zn(1)-N(1) 2.067(6) Å, Zn(1)-N(2) 2.062(5) Å]. The bond distances correspond well with those observed for compound **7** and **9**. The bipy ligands coordinate adjacent zinc atoms together and due to the tetrahedral nature of the metal, the structure forms one dimensional zigzag chains (Figure 2.27).

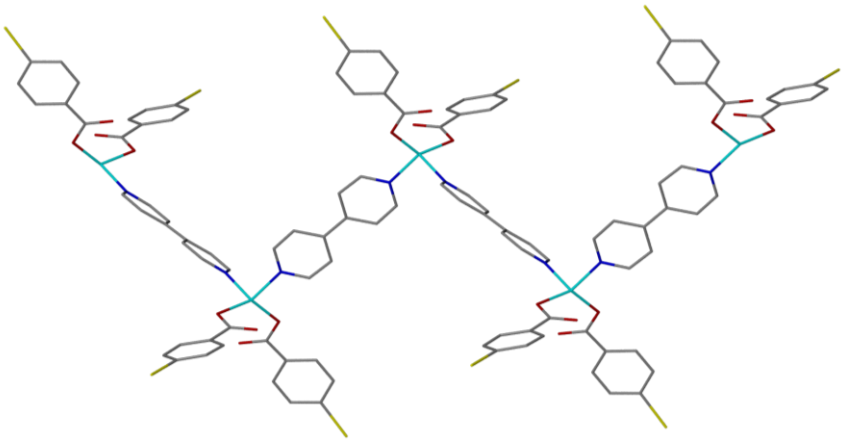

*Figure 2.27: One dimensional zigzag chains of **10**. Hydrogen atoms have been omitted for clarity*

These chains pack through the interaction of a bipy ligand of one chain and the benzene ring of an Ibza ligand from an adjacent chain, through π-π stacking. The distance

between the centroids of each Ibza benzene ring and the bipy ligand was calculated at approximately 3.636 Å, consistent with the presence of a π-π interaction (Figure 2.28).

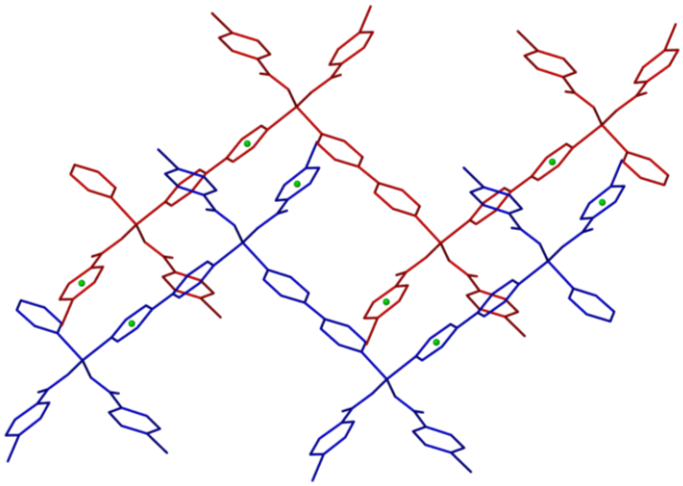

*Figure 2.28: π-π stacking of two chains of **10**. Centroids are shown in green. Hydrogen atoms have been omitted for clarity*

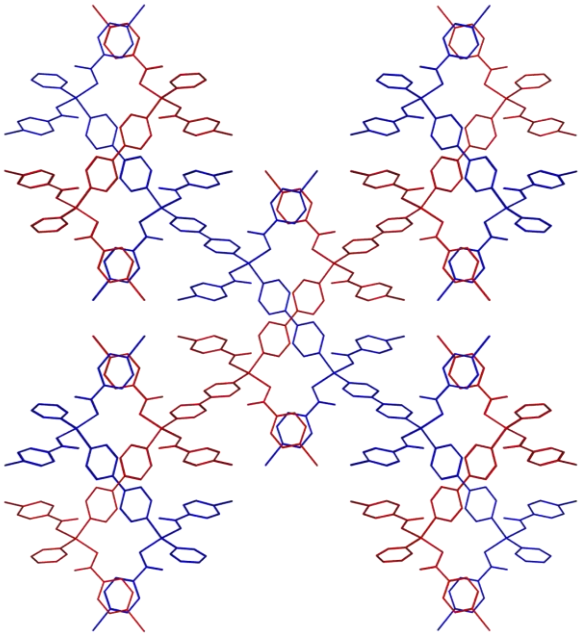

*Figure 2.29: The packing of the chains in **10**, with different chains shown in red and blue. Hydrogen atoms have been omitted for clarity*

The structures of **8**-**10** reveal that in presence of the bipy ligand there is no longer a preference to form the paddle wheel dimer.

$[Cu(biphen)_2(bipy)]\cdot 4BzOH$ (**8**) and $[Zn_2(biphen)_4(bipy)_2]$ (**9**) show the differences when the metal centres are altered, although to synthesise these materials different reaction conditions were used. In **8**, the copper centres exist with approximate square planar geometry forming linear one dimensional chains. In **9** there are two types of zinc

centre, one with approximate octahedral geometry and one with approximate tetrahedral geometry, this causes the one dimensional chains to become zigzagged.

$[Zn(Ibza)_2(bipy)]$ (**10**) was synthesised in the same manner as **9**, but with HIbza. In this structure there is only one type of zinc centre with approximate tetrahedral geometry, causing formation of zigzagged chains similar to those in **9**. However, the individual chains present in **9** and **10** appear very similar but the packing of these is very different. Due to π-π stacking present in **10**, the chains stack at 90° degrees to each other, whereas in **9** one dimensional interdigitated layers are formed.

2.2.4 Anthracenecarboxylate Paddle Wheel Structures

The final set of materials in this chapter involve the copper dimer paddle wheel synthesised with the Hanthr ligand. This ligand was used to study the effect of the larger substituent on the products and pore sizes obtained. Anthracene compounds are also known to be involved in π-π stacking, and so it was deemed interesting to observe the effects of this within a MOF context.

Three of the materials synthesised were shown to be suitable for single crystal X-ray diffraction, $[Cu_2(anthr)_4(Mepyz)]\cdot 0.5MeOH$ (**11**), $[Cu_2(anthr)_4(dabco)]$ (**12**) and $[Cu_2(anthr)_4(pyz)]$ (**13**). Each reaction produced yellow needles suitable from the reaction of copper(II) acetate in methanol, and Hanthr and either Mepyz, dabco or pyz in benzyl alcohol. The crystallographic data for the resultant materials is shown in Table 2.6.

Compound	**11**	**12**	**13**
Empirical formula	$C_{65.5}H_{44}N_2O_{8.5}Cu_2$	$C_{33}H_{24}NO_4Cu$	$C_{33}H_{24}NO_4Cu$
M	1122.17	562.07	562.07
***T*/ K**	150(2)	150(2)	150(2)
Crystal system	Monoclinic	Tetragonal	Tetragonal
Space group, *Z*	$P2_1/n$, 4	$P4/nnc$, 4	$P4/nnc$, 4
***a*/ Å**	14.057(5)	16.7000(3)	16.822(10)
***b*/ Å**	21.260(5)	16.7000(3)	16.822(10)
***c*/ Å**	17.965(5)	9.6300(3)	9.529(7)
***α*/ °**	90	90	90
***β*/ °**	106.272(5)	90	90

γ / °	90	90	90
U/Å^3	5154(3)	2685.71(11)	2697(3)
Absorption coefficient/ mm^{-1}	0.887	0.853	0.849
F(000)	2308	1160	1160
Theta range for data collection/ °	1.79 to 24.07	2.44 to 24.99	4.92 to 25.00
Reflections collected/ observed [I>2σ(I)]	15413/5110	19247/1034	16919/937
Data Completeness	0.964	0.970	0.934
Goodness-of-fit on F^2	0.937	1.177	1.109
Final R indices [I>2σ(I)]	R1 = 0.0582, wR2 = 0.1530	R1 = 0.0465, wR2 = 0.1202	R1 = 0.0575, wR2 = 0.1381
R indices (all data)	R1 = 0.0886, wR2 = 0.1638	R1 = 0.0532, wR2 = 0.1242	R1 = 0.0669, wR2 = 0.1456
Largest diff. peak and hole Å^{-3}	0.529 and -0.800	0.882 and -0.640	0.643 and -0.353

*Table 2.6: Crystallographic data for compounds [Cu_2(anthr)$_4$(Mepyz)]·0.5MeOH (**11**), [Cu_2(anthr)$_4$(dabco)] (**12**) and [Cu_2(anthr)$_4$(pyz)] (**13**)*

The asymmetric unit for compound **11** consists of two copper centres bridged by four coordinated anthr ligands and a coordinated Mepyz linker. The non-nitrogen atoms of the Mepyz are disordered over two sites in a 70:30 ratio. There is also an area of diffuse solvent within the lattice that was treated using the PLATON SQUEEZE algorithm and assigned to half a molecule of methanol per asymmetric unit (Figure 2.30).

Compounds **12** and **13** form isostructural materials, and their asymmetric units consist of a quarter of a copper atom, half an anthr ligand and quarter of a molecule of either a coordinated dabco or pyz linker. Due to the crystallographic four-fold rotation axis, the dabco ligand is inherently disordered (Figure 2.30).

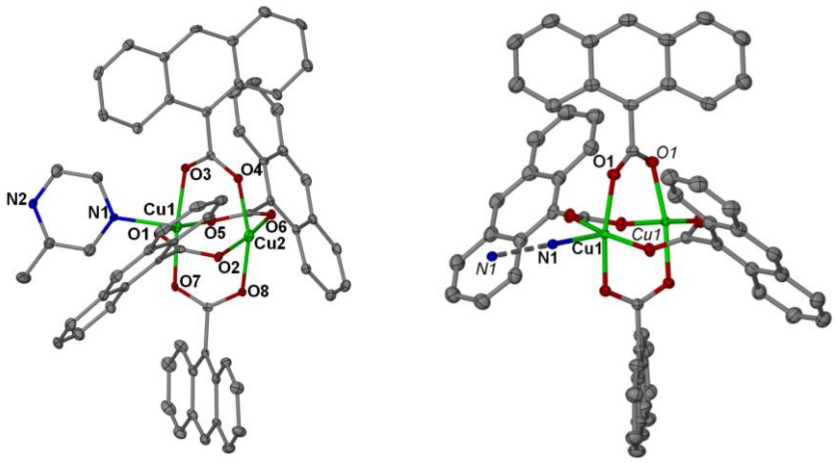

*Figure 2.30: [$Cu_2(anthr)_4(Mepyz)]\cdot 0.5MeOH$ (**11**) (left) and [$Cu_2(anthr)_4(dabco)$] (**12**) (right) with thermal ellipsoids at the 30 % probability level. Symmetry equivalent atom labels are displayed in italics. Hydrogen atoms, minor disordered components and solvent molecules have been omitted for clarity. The dabco moiety in **12** has not been fully displayed due to the disorder*

In this series of compounds, all the copper centres exist with approximate square pyramidal geometry, coordinating to four oxygen atoms in the equatorial plane from the anthr ligand, and in the axial position is a coordinated nitrogen atom from the nitrogen donor linker, which extends the structures into one dimensional chains.

Bond lengths for compounds **11**-**13** are given in Table 2.7. The Cu-O distances correspond well to those for [$Cu_2(bza)_4(pyz)$].[14] Variations are observed in the Cu-N distances due to the presence of different ditopic nitrogen linkers. Compound **12** contains dabco and the Cu-N bond length corresponds well with that in [$Cu_2(biphen)_4(dabco)]\cdot$BzOH (**2**). Similarly, the pyz containing compounds **13** and [$Cu_2(biphen)_4(pyz)]\cdot 1.9$BzOH (**1**) have similar Cu-N bond lengths.

Compound	Cu-O (Å)	Cu-N (Å)
11	1.948(3)-1.998(3)	2.200(2)-2.222(3)
12	1.984(3)	2.196(5)
13	1.974(2)	2.175(6)

*Table 2.7: Comparison of bond lengths for compounds **11**, **12** and **13***

Compounds **12** and **13** form linear chains, whereas compound **11** forms zigzag chains. The bend angles along the Cu-N chain of **11** are no longer 180° but are now in the range of 170-176°. When **11** is viewed along the chains, due to presence of the bulkier anthr ligand, and the zigzag chains, it is not apparent that any pores are present within the compound (Figure 2.31). PLATON SQUEEZE was used to estimate the void space, and this was shown to have only 5.0 % accessible voids, which is also confirmed by the small amount of guest methanol housed in this material.

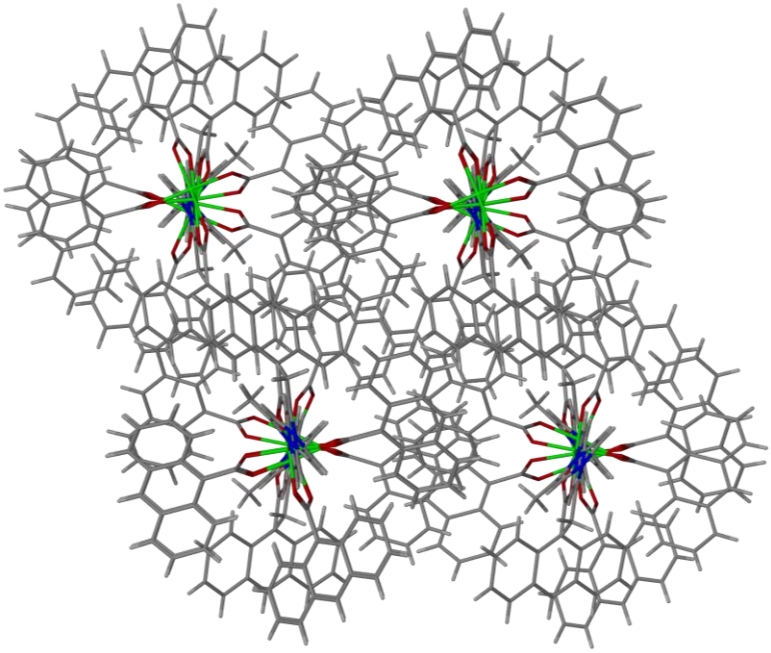

*Figure 2.31: The packing of **11** viewed along the one dimensional chains. Solvent molecules have been omitted for clarity*

Two of the anthr rings in **11** are involved in π-π stacking to adjacent rings. The centroids of the central anthr rings are separated by a distance of approximately 3.391 Å, and the angle between the planes of the two rings is 2.62°, indicative of an interaction being present.

Compounds **12** and **13** form one dimensional chains and pack similarly to $[Cu_2(bza)_4(pyz)]$, however due to the presence of the bulkier anthr ligands the pore size is reduced dramatically to approximately 5.5 x 5.5 Å (Figure 2.32). When using PLATON SQUEEZE the structure was shown to have a solvent accessible void volume of 10.6 %, as compared to a void volume of 16.2 % for $[Cu_2(bza)_4(pyz)]$.[14] Due to the interactions between the anthr ligands, the structures are extended further into three dimensions through parallel π···π stacking of all the benzene rings at a separation between centroids of the central ring of approximately 3.406 Å.

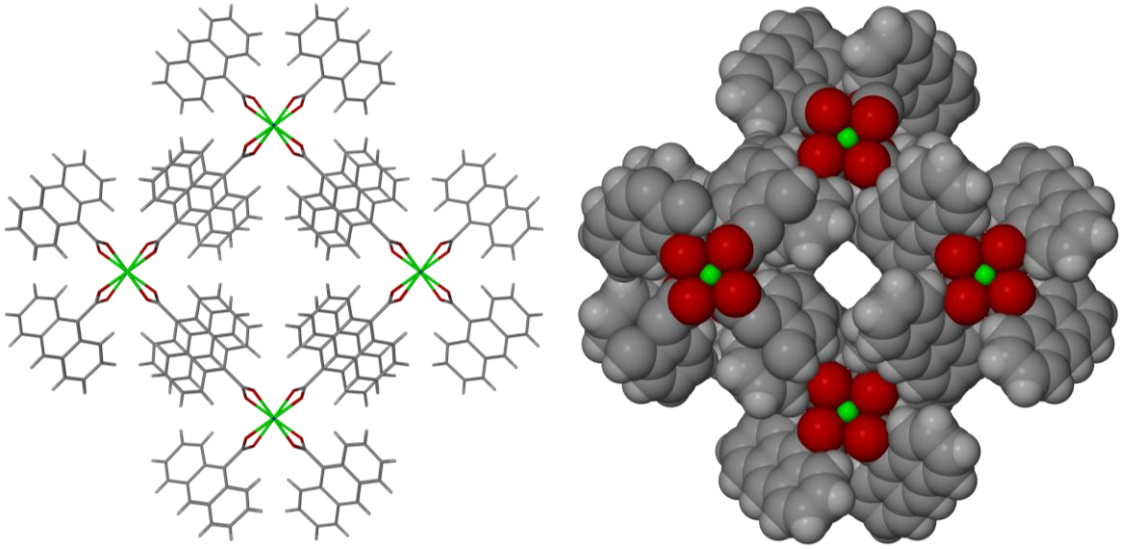

*Figure 2.32: The infinite channels (left) and space filling representation of the channels (right) present in **12** and **13***

Compound **12** has been reported previously in a solvated form. *Bu et al.* report the synthesis of $[Cu_2(anthr)_4(dabco)]\cdot 0.25MeOH$ synthesised using a different method, with the same gross structure obtained as **12**, but with 0.25 molecules of methanol situated within the one dimensional channels.[31]

The three compounds, **11**, **12** and **13** reported here demonstrate that the paddle wheel dimer is still formed even with the use of the bulkier anthr ligand. However, due to the presence of this large group, all the pore sizes are reduced in comparison to $[Cu_2(bza)_4(pyz)]$. Compounds **[**$Cu_2(anthr)_4(Mepyz)]\cdot 0.5MeOH$ (**11**), $[Cu_2(anthr)_4(dabco)]$ (**12**) and $[Cu_2(anthr)_4(pyz)]$ (**13**) were all synthesised in the same manner, each containing different nitrogen donor linkers. When pyz and dabco were used, the same structures were obtained, with linear one dimensional chains. However, when the bulkier Mepyz linker was used, this caused the one dimensional chains to become zigzagged, which reduced the pore size.

2.3 Conclusion

Thirteen new compounds using a variety of carboxylate ligands, ditopic nitrogen donor linkers and metal salts have been successfully synthesised and characterised. Compounds **1-7** and **11-13** contain the metal dimer paddle wheel moiety, and are linked into one dimensional chains through the use of pyz, NH_2pyz, Mepyz or dabco. These chains pack in a similar manner to those in $[Cu_2(bza)_4(pyz)]$,[14] with the majority having

larger pores than reported for this structure. However, when increasing the size of the nitrogen donor linker to bipy, compounds **8-10** were obtained. These all contain one dimensional chains, but contain single metal centres as opposed to the expected paddle wheel SBUs. These three structures pack such that channels are not created within the systems.

Compound **2**, $[Cu_2(biphen)_4(pyz)_2]\cdot 1.9BzOH$ was shown to have the largest pores in this series. Using PLATON SQUEEZE this void volume was calculated as 52.1 % of the structure. However on attempting to activate this material, the crystallinity was lost, owing to the collapse of the framework.

Similarly many of the other structures from this series also contained larger pores than $[Cu_2(bza)_4(pyz)]$.[14] Like compound **2** these materials also lost crystallinity on efforts to remove the guest solvent molecules, therefore no further diffraction experiments could be carried out on these materials. This also meant that crystals could not be exposed to gases to look at their adsorption properties. Overall, it was concluded that these compounds were not suitable candidates for assessing our initial goal.

2.4 Experimental

2.4.1 General

All reagents used for the synthesis of compounds **1-13** were obtained commercially and used without further purification.

Powder diffraction measurements were recorded using a Bruker D8 powder diffractometer, fitted with Goebel mirrors, and using CuK_α radiation of wavelength 1.5414 Å. Samples were placed in 0.3, 0.5 or 0.7 mm diameter Lindemann capillaries, and measured with a 2θ range of 4 - 60°. The step size was 0.02° with time per step of 1.00s.

Elemental analyses were conducted by Alan Carver (University of Bath).

Thermogravimetric analyses were recorded on a Perkin Elmer TGA 4000 Thermogravimetric analyzer, with a temperature range of 40-600 °C at 5 °C per minute under an atmosphere of nitrogen.

2.4.2 Crystallography

X-ray data for compounds **1**, **4**, **6** and **8-10** were collected on a Nonius Kappa CCD diffractometer using Mo-K_α radiation, while those for compound **2** were measured on a Bruker APEX II diffractometer using synchrotron radiation (λ = 0.69450 Å) at Station 9.8 of the SRS Daresbury Laboratory. A Bruker Apex II diffractometer using synchrotron radiation (λ = 0.7749 Å) at Station 11.3.1 of the ALS Lawrence Berkeley National Laboratory was used to collect the single crystal data for compounds **3** and **7**. X-ray data for compounds **5** and **11** were collected on an Oxford Diffraction Gemini diffractometer fitted with an Atlas CCD detector, using Mo-K_α radiation. Finally, beamline I19 of Diamond Light Source using a Crystal Logic 4-circle kappa goniometer fitted with a Rigaku Saturn 724 CCD detector employing synchrotron radiation (λ = 0.6889 Å) was used to collect the single crystal data for compounds **12** and **13**. Unless noted, all non-hydrogen atoms were refined anisotropically in the final least squares run, and hydrogen atoms were included at calculated positions. The structures were solved using SHELXS-97[32] and refined using full-matrix least squares in SHELXL-97.[32] Refinements were generally straightforward with the following exceptions and points of note.

For **1**, the oxygen of the benzyl alcohol solvent moiety was disordered equally over two proximate sites. The associated hydrogens could not be reliably located so were omitted from the final refinement.

Compound **3** contained a solvent DMF molecule which was disordered over two sites (55:45). The dabco CH_2 groups were equally disordered due to the nitrogen atoms being located on a crystallographic 2-fold rotation axis. Due to the poor diffracting ability of the crystal at higher Bragg angles, the data was truncated at 20°.

The crystallographic data for **6** were poor, as the intensity of the reflections dropped off above Bragg angles of 14°. Nonetheless, an unambiguous structural model was still obtained.

The asymmetric unit for compound **7** contained six full occupancy DMF molecules, and an additional half molecule of DMF located on an inversion centre. Some distance restraints were applied to the solvent molecules, and atomic displacement parameter

restraints were applied to the dabco carbon atoms. All fragments with less than 50 % occupancy were treated isotropically.

For compounds **4-7**, the largest residual difference peak and hole remain high, due to the presence of the iodine atoms in each of these structures.

Large atomic displacement parameters were observed for the chelating carboxylate groups attached to Zn(1) in **9**. There is also residual electron density positioned here in the Fourier map. This indicates some disorder, however attempts to refine a sensible model where the carboxylate is disordered between monodentate and bidentate coordination were unsuccessful.

The non-nitrogen atoms of the Mepyz were disordered over two sites in a 70:30 ratio for **11**. For the minor component, distance restraints and planarity restraints had to be applied. Data were also truncated to a Bragg angle of 24°, due to the diffracting ability of the small crystal.

In compound **12**, the copper centres were located on a four-fold rotation axis, as were the nitrogen atoms in the dabco, causing the associated carbons in this ligand to also be disordered. As the dabco nitrogens each exhibit 25 % occupancy, there must be 75 % occupancy of the carbon atoms within the dabco moiety, to maintain the overall 1:3 ratio of nitrogen to carbon. However, the carbons in the dabco were also disordered over two sites, but the refinement became stable when this disorder was modelled in a 46:29 ratio.

2.4.3 Synthesis of $[Cu_2(biphen)_4(pyz)]\cdot 3.8BzOH$, 1

Hbiphen (0.099 g, 0.50 mmol) and pyz (0.041 g, 0.50 mmol) were dissolved in benzyl alcohol (BzOH) (6 cm^3) with gentle heating and stirring. Once cooled, benzyl alcohol (2 cm^3) was gently layered on top of this solution. Layered on top of this was a solution of $Cu(OAc)_2\cdot H_2O$ (0.037 g, 0.19 mmol) dissolved in methanol (6 cm^3), with the aid of sonication. The vial was sealed with a lid, and the solution left for several days for crystallisation to occur. Crystals of suitable size were produced for single crystal X-ray diffraction. Yield 0.0564 g. The X-ray powder diffraction trace (Figure 2.33) and elemental analysis showed evidence for the sample being phase impure, and so the TGA was not analysed for information about the solvent loss of the compound.

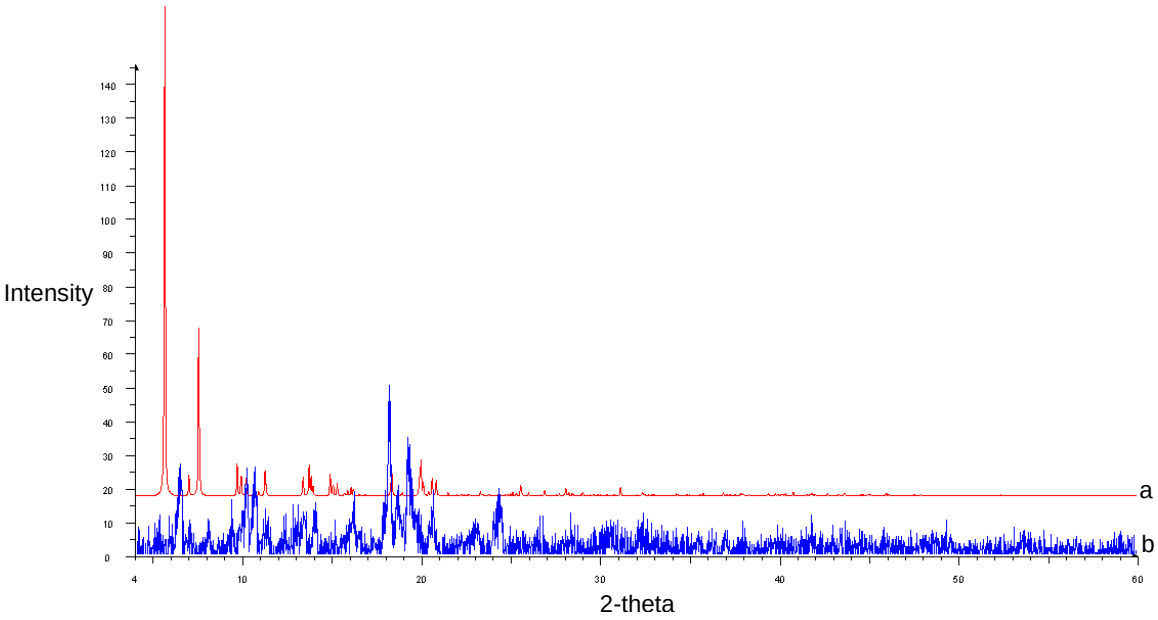

*Figure 2.33: The X-ray powder diffraction trace for **1** (b) and that simulated from the crystal data of **1** (a)*

2.4.4 Synthesis of $[Cu_2(biphen)_4(dabco)]\cdot BzOH$, 2

Hbiphen (0.099 g, 0.50 mmol) and dabco (0.056 g, 0.50 mmol) were dissolved in benzyl alcohol (BzOH) (6 cm^3) with gentle heating and stirring. Once cooled, benzyl alcohol (2 cm^3) was gently layered on top of this solution. Layered on top of this was a solution of $Cu(OAc)_2\cdot H_2O$ (0.038 g, 0.19 mmol) dissolved in methanol (6 cm^3), with the aid of sonication. The vial was sealed with a lid, and the solution left for several days for crystallisation to occur. Crystals of suitable size were produced for single crystal X-ray diffraction. Yield 0.0818 g. Found: C, 65.7; H, 5.17; N, 2.52. $C_{58}H_{48}Cu_2N_2O_8$ requires C, 67.7; H, 4.71; N, 2.73%. The X-ray powder diffraction pattern (Figure 2.34) showed the sample to be impure, with an unidentified by-product present; this result is in line with those observed for the elemental analysis. The TGA shows a percentage weight loss of approximately 9.5 % at 170 °C which can be attributed to the loss of the guest benzyl alcohol molecule. After this, there is a rapid weight loss between 200-350 °C, followed by a gradual weight loss up to 600 °C, leaving about 20 % of the initial weight, which signifies the decomposition of **2** (Figure 2.35). However, not too many conclusions can be drawn from these results as the bulk material is shown to be phase impure.

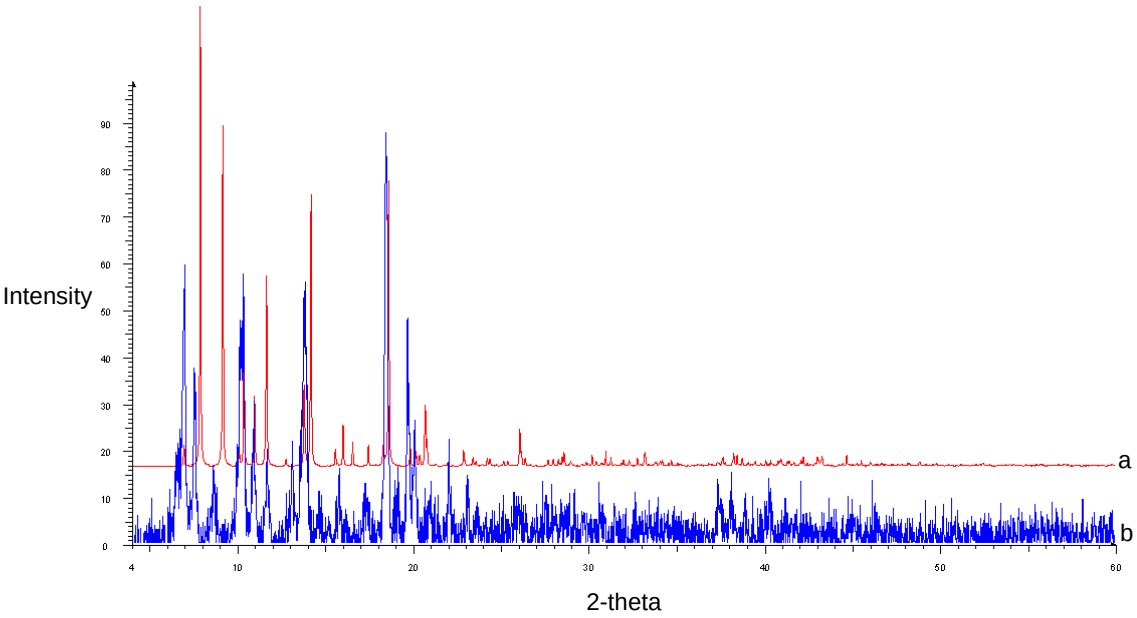

*Figure 2.34: The X-ray powder diffraction trace for **2** (b) and that simulated from the crystal data of **2** (a)*

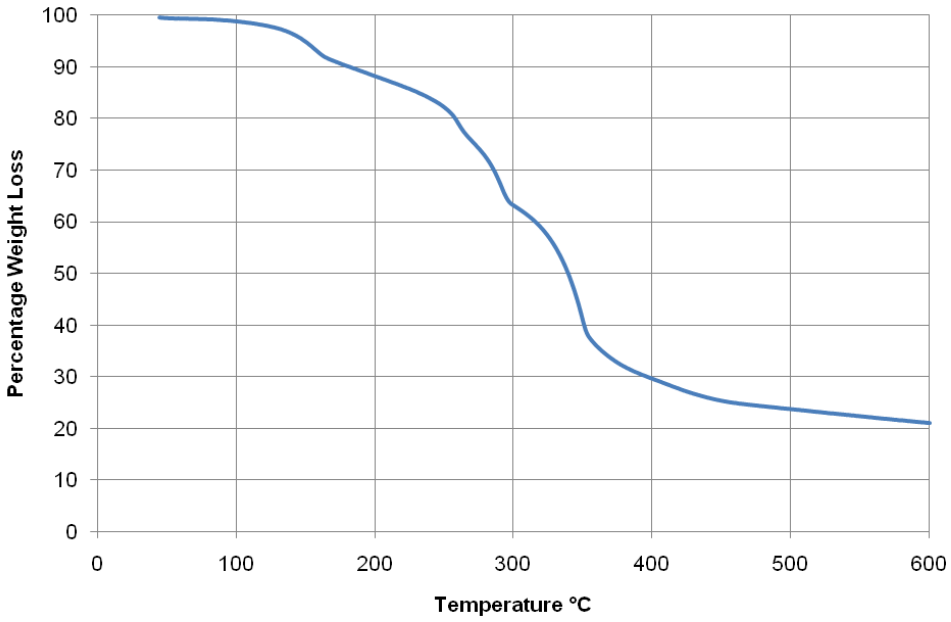

*Figure 2.35: TGA trace for compound **2***

2.4.5 Synthesis of $[Zn_2(biphen)_4(dabco)]\cdot 2DMF$, 3

Hbiphen (0.334 g, 1.68mmol), $Zn(NO_3)_2\cdot 6H_2O$ (0.250 g, 0.84 mmol) and dabco (0.093 g, 0.83 mmol) were dissolved in DMF (10 cm^3), and placed in a 20 cm^3 pressure tube. The tube was sealed and heated to 120°C for 2 days. Once removed from the oven crystals of suitable size were produced for single crystal X-ray diffraction after several days. Yield 0.334 g (63 %). Found: C, 64.8; H, 5.25; N, 4.68. $C_{64}H_{62}N_4O_{10}Zn_2$ requires

C, 65.2; H, 5.31; N,4.76%. The X-ray powder diffraction pattern of **3** was a good match to that simulated from the single crystal data (Figure 2.36). The TGA shows a percentage weight loss of approximately 13 % up to 170 °C which can be attributed to the release of two molecules of DMF from the pores. After this temperature there is a small plateau up until 250 °C. This is followed by another weight loss of approximately 7.5 % up to 290 °C which can be attributed to the loss of the dabco linker. Above this temperature there is a slow decomposition evident up to 550 °C where 25 % of the initial compound mass remains. (Figure 2.37).

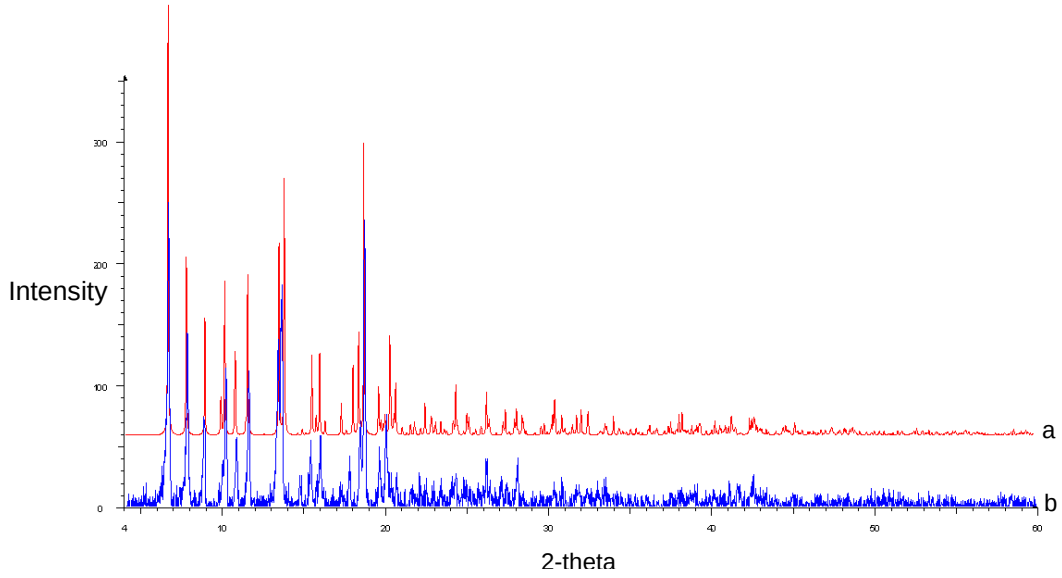

*Figure 2.36: The X-ray powder diffraction trace for **3** (b) and that simulated from the crystal data of **3** (a)*

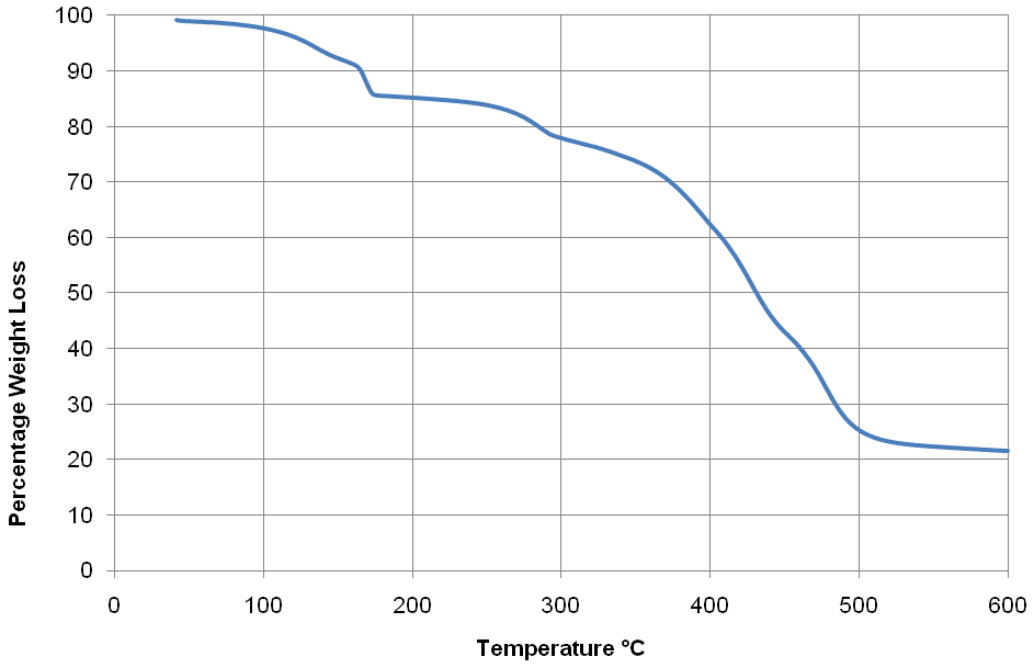

*Figure 2.37: TGA trace for compound **3***

2.4.6 Synthesis of $[Cu_2(Ibza)_4(MeOH)_2]$, 4

$Cu(OAc)_2 \cdot H_2O$ (0.250 g, 1.25 mmol) was dissolved in methanol (15 cm^3) with gentle heating and stirring. To this, a solution of HIbza (1.241 g, 5.01 mmol) dissolved in methanol (15 cm^3) and pyz (0.100 g, 1.2 mmol) dissolved in methanol (5 cm^3) was added. The solution was left for crystallisation to occur, with very slow evaporation of the solvent over two days. Crystals of suitable size for single crystal X-ray diffraction were grown from this solution. Yield 0.612 g. The crystal structure showed that the pyrazine had not been incorporated into the axial position of the copper, and instead a methanol solvent molecule was coordinated here. The powder X-ray diffraction trace showed the sample to be impure and elemental analysis was not consistent with the product expected.

2.4.7 Synthesis of $[Cu_2(Ibza)_4(pyz)]$, 5

HIbza (0.124 g, 0.50 mmol) and pyz (0.041 g, 0.50 mmol) were dissolved in benzyl alcohol (6 cm^3) with gently heating and stirring. Once cooled, benzyl alcohol (2 cm^3) was gentle layered on top of this solution. Layered on top of this was a solution of $Cu(OAc)_2 \cdot H_2O$ (0.038 g, 0.19 mmol) dissolved in methanol (6 cm^3), with the aid of sonication. The vial was sealed with a lid, and the solution left for several days for crystallisation to occur. Crystals of suitable size were produced for single crystal X-ray diffraction. Yield 0.0794 g (70 %). Found: C, 32.5; H, 1.81; N, 2.46. $C_{32}H_{20}Cu_2N_2O_8I_4$ requires C, 32.1; H, 1.69; N, 2.34%. The X-ray powder diffraction pattern confirmed that **5** was the only product present (Figure 2.38). The TGA exhibits only a decomposition of the complex at around 250 °C, confirming no solvent to be present in the pores (Figure 2.39).

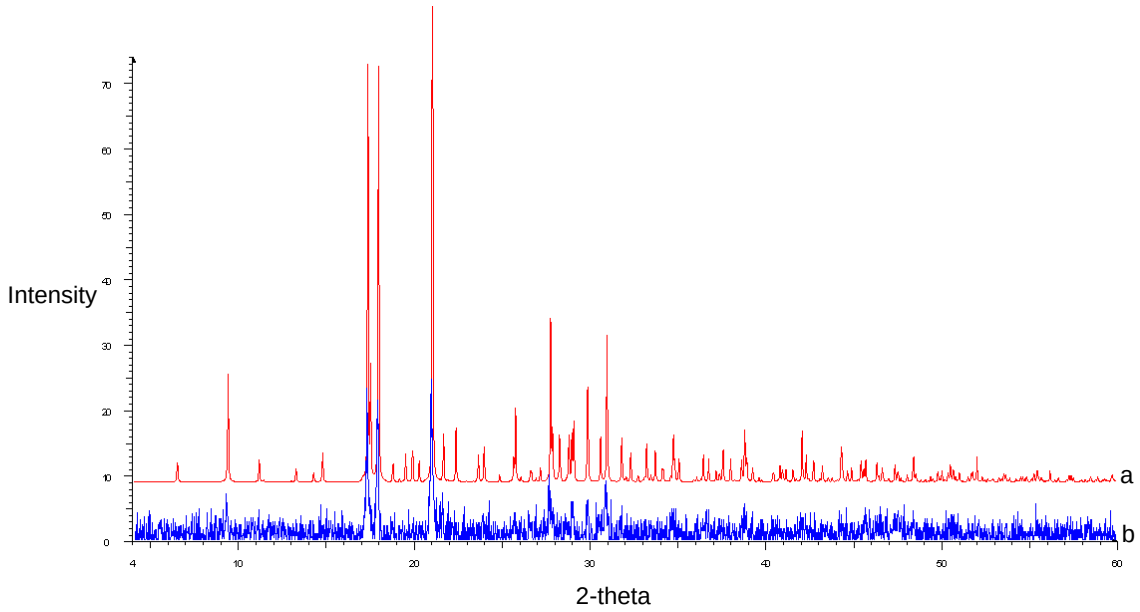

*Figure 2.38: The X-ray powder diffraction trace for **5** (b) and that simulated from the crystal data of **5** (a)*

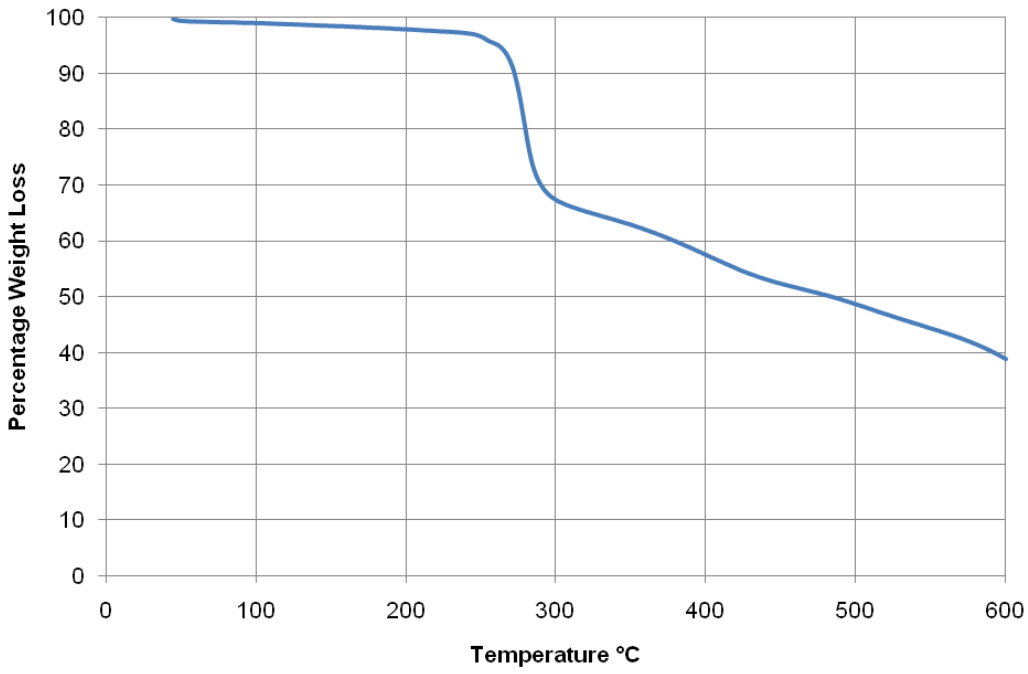

*Figure 2.39: TGA trace for compound **5***

2.4.8 Synthesis of $[Cu_2(Ibza)_4(NH_2pyz)]\cdot 2BzOH$, 6

HIbza (0.125 g, 0.50 mmol) and NH_2pyz (0.049 g, 0.51 mmol) were dissolved in benzyl alcohol (6 cm^3) with gentle heating and stirring. Once cooled, benzyl alcohol (2 cm^3) was gently layered on top of this solution. Layered on top of this was a solution of $Cu(OAc)_2\cdot H_2O$ (0.038 g, 0.19 mmol) dissolved in methanol (6 cm^3), with the aid of sonication. The vial was sealed with a lid, and the solution left for several days for

crystallisation to occur. Crystals of suitable size were produced for single crystal X-ray diffraction. Yield 0.0971 g (72 %). The X-ray powder diffraction pattern of **6** showed a good match to the pattern simulated from the crystal data, however, due to the weak diffraction of the sample it is hard to tell whether the sample is phase pure (Figure 2.40). The elemental analysis was also not a match for the calculated value, confirming the presence of an unidentified material. The TGA for **6** showed a weight loss of approximately 23 % up to 140 °C, this can be attributed to the loss of three molecules of benzyl alcohol. From this temperature there is a plateau up until 260 °C where there is a decomposition of the compound (Figure 2.41).

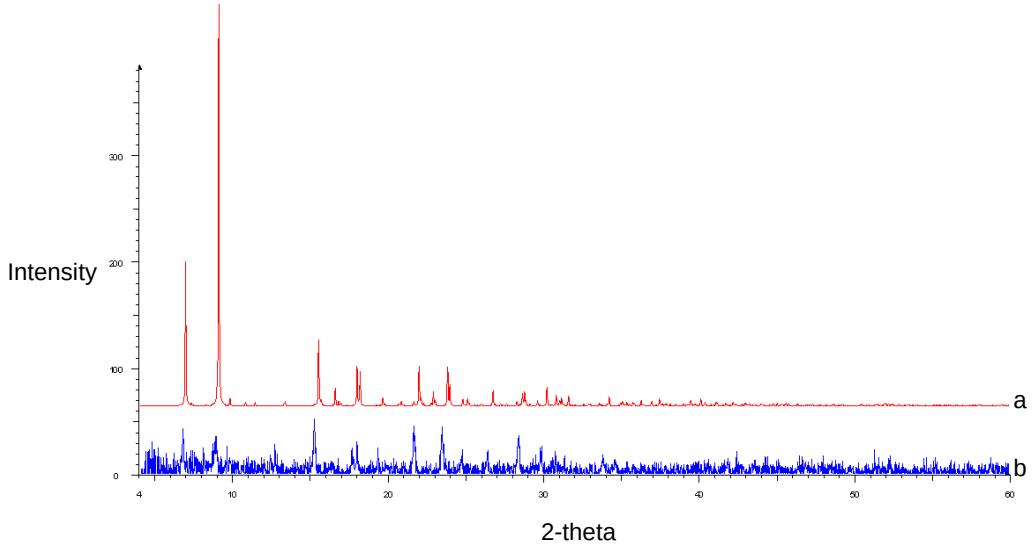

*Figure 2.40: The X-ray powder diffraction trace for **6** (b) and that simulated from the crystal data of **6** (a)*

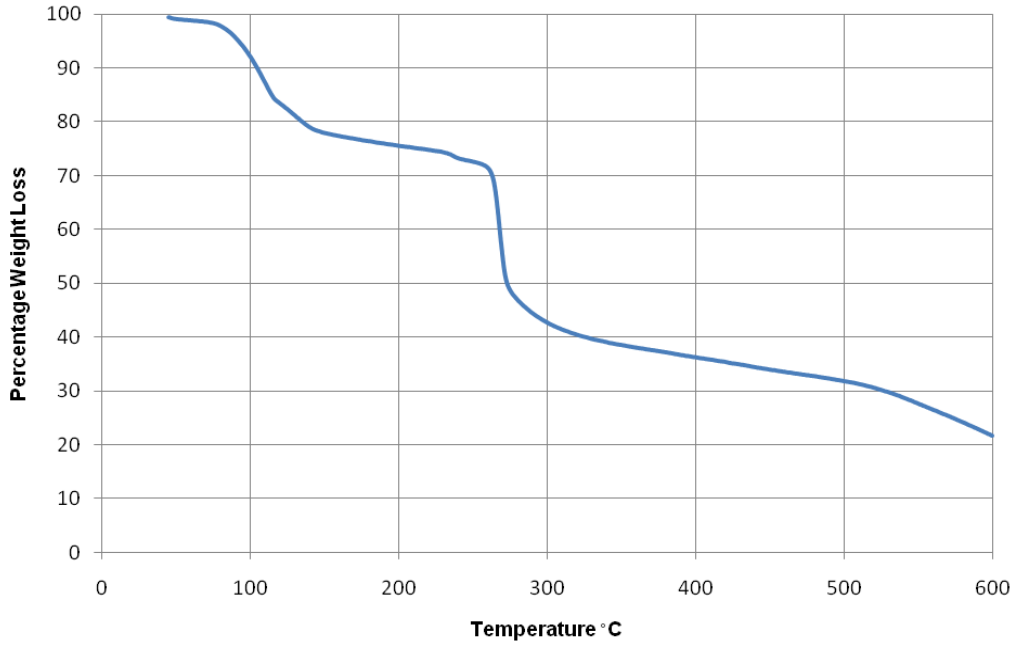

*Figure 2.41: TGA trace for compound **6***

2.4.9 Synthesis of $[Zn_2(Ibza)_4(dabco)]\cdot 3.25DMF$, 7

HIbza (0.422 g, 1.70 mmol), $Zn(NO_3)_2\cdot 6H_2O$ (0.248 g, 0.84 mmol) and dabco (0.092 g, 0.82 mmol) were dissolved in DMF (10 cm^3), and placed in a 20 cm^3 pressure tube. The tube was sealed and heated to 120°C for 2 days. Once removed from the oven crystals of suitable size were produced for single crystal X-ray diffraction after several days. Yield 0.1999 g. Found: C, 36.0; H, 3.12; N, 4.46. $C_{43}H_{49}I_4N_5O_{11}Zn_2$ requires C, 35.6; H, 3.41; N, 4.83%. The X-ray powder diffraction pattern for **7** shows there to be a poor match with those calculated from the crystal data. There are several peaks at high 2θ values suggesting the presence of an unidentified material (Figure 2.42). The TGA shows a percentage weight loss of approximately 20 % up to 300 °C which can be attributed to the slow release of four molecules of DMF from the pores. Above this temperature there is a slow decrease to about 5 % of the weight, which corresponds to the decomposition of **7** (Figure 2.43). However, not too many conclusions can be drawn from these results as the bulk material is shown to be phase impure.

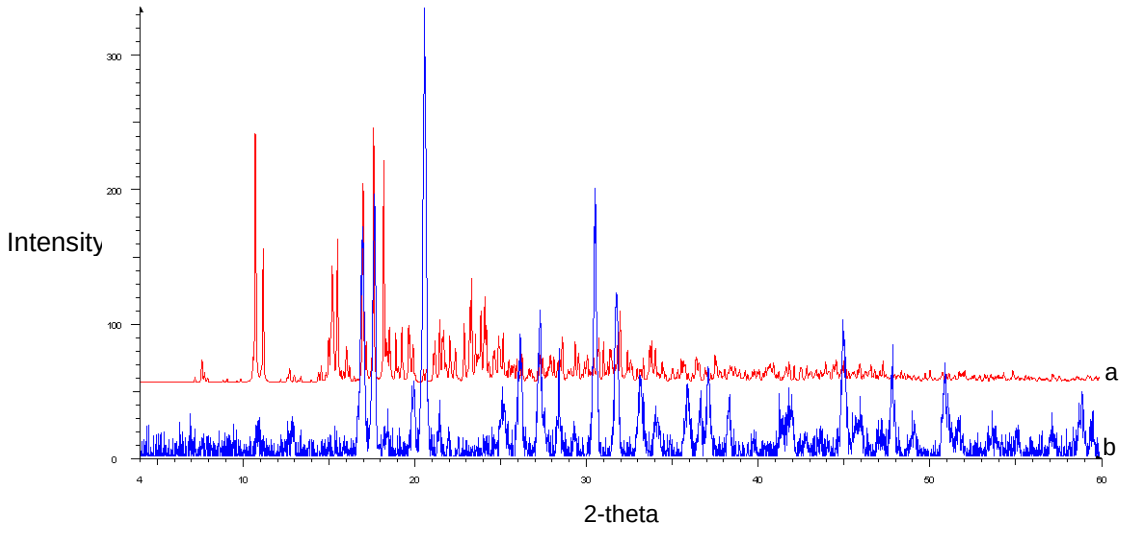

*Figure 2.42: The X-ray powder diffraction trace for **7** (b) and that simulated from the crystal data of **7** (a)*

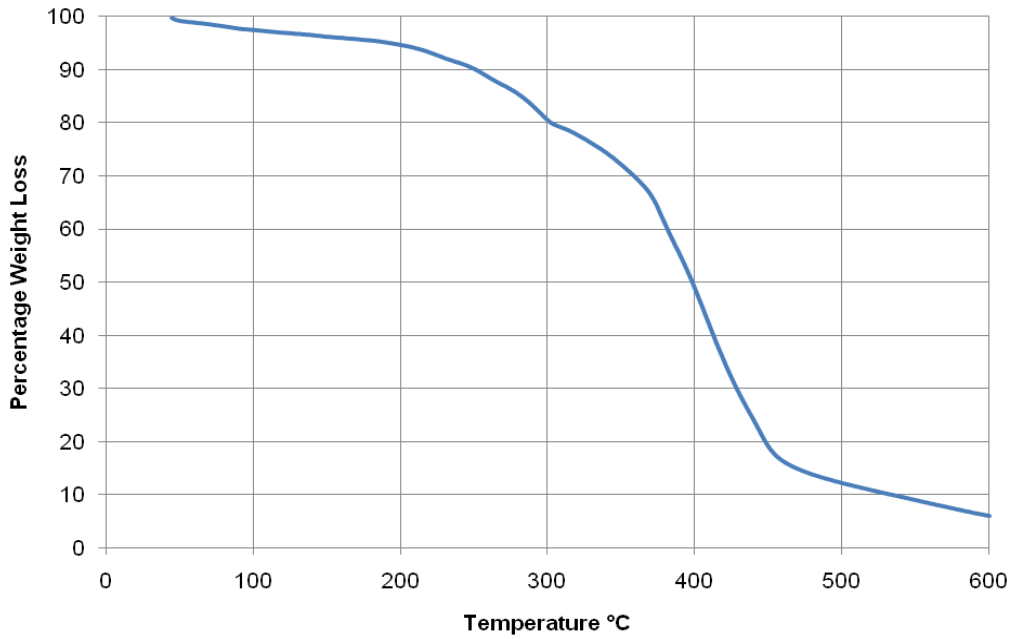

*Figure 2.43: TGA trace for compound **7***

2.4.10 Synthesis of [Cu(biphen)$_2$(bipy)]·4BzOH, 8

Hbiphen (0.099 g, 0.50 mmol) and bipy(0.078 g, 0.50 mmol) were dissolved in benzyl alcohol (BnOH) (6 cm^3) with gentle heating and stirring. Once cooled, benzyl alcohol (2 cm^3) was gently layered on top of this solution. Layered on top of this was a solution of Cu(OAc)$_2$·H$_2$O (0.050 g, 0.25 mmol) dissolved in methanol (6 cm^3), with the aid of sonication. The vial was sealed with a lid, and the solution left for several days for crystallisation to occur. Crystals of suitable size were produced for single crystal X-ray diffraction. The reaction produced blue crystals of **8**, and a green unidentified product. The blue crystals were selected from this mixture to measure the X-ray powder diffraction, which showed **8** to be the major product (Figure 2.44), and this sample also had the elemental analysis carried out on it. Found: C, 73.1; H, 5.50; N, 2.71. $C_{64}H_{58}Cu_1N_2O_8$ requires C, 73.4; H, 5.59; N, 2.68%.

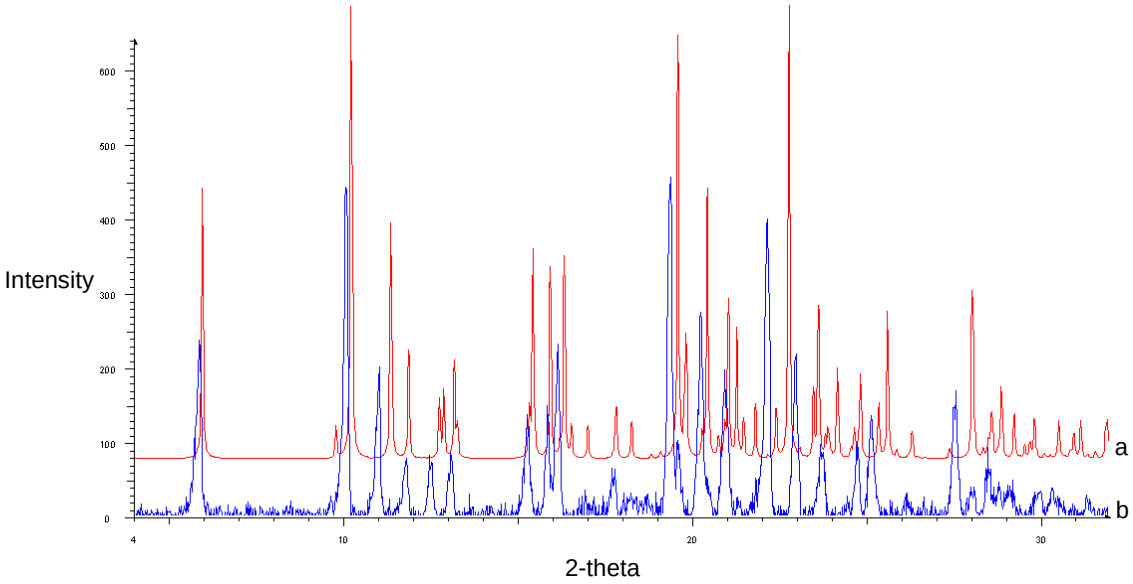

*Figure 2.44: The X-ray powder diffraction trace for **8** (b) and that simulated from the crystal data of **8** (a)*

2.4.11 Synthesis of $[Zn_2(biphen)_4(bipy)_2]$, 9

Hbiphen (0.327 g, 1.65mmol), $Zn(NO_3)_2 \cdot 6H_2O$ (0.252 g, 0.85 mmol) and bipy (0.063 g, 0.40 mmol) were dissolved in DMF (10 cm^3), and placed in a 20 cm^3 pressure tube. The tube was sealed and heated to 120°C for 2 days. Once removed from the oven crystals of suitable size were produced for single crystal X-ray diffraction after several days. Yield 0.1949 g (79 %). Found: C, 64.8; H, 5.25; N, 4.68. $C_{64}H_{62}N_4O_{10}Zn_2$ requires C, 65.2; H, 5.31; N,4.76%. The X-ray powder diffraction pattern confirms that the bulk material is compound **9** (Figure 2.45).

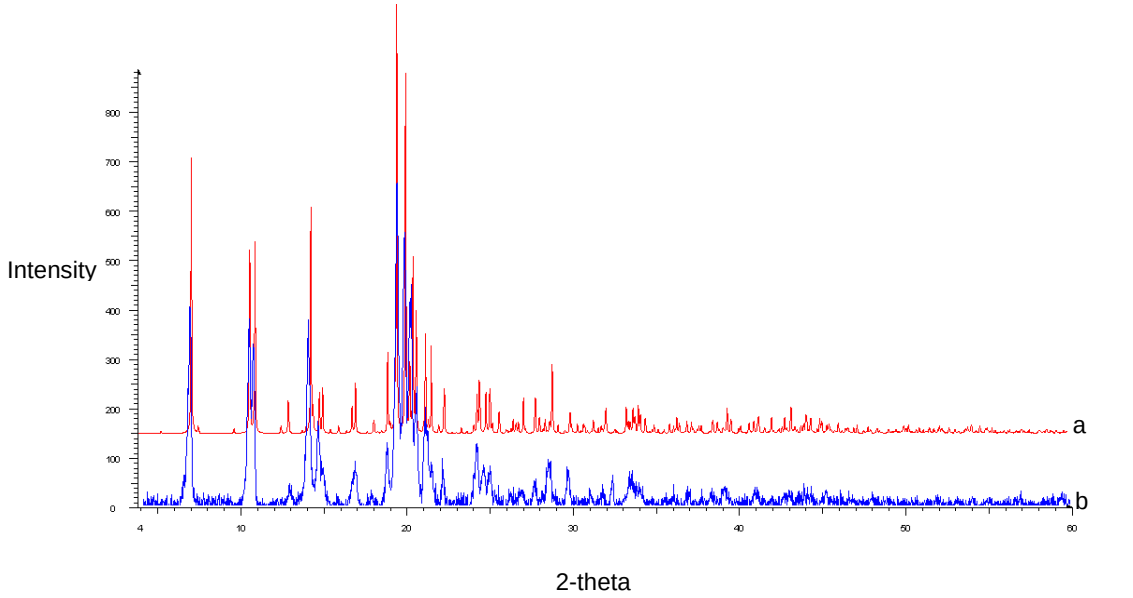

*Figure 2.45: The X-ray powder diffraction trace for **9** (b) and that simulated from the crystal data of **9** (a)*

2.4.12 Synthesis of [Zn(Ibza)$_2$(bipy)], 10

HIbza (0.416 g, 1.68mmol), $Zn(NO_3)_2 \cdot 6H_2O$ (0.248 g, 0.84 mmol) and bipy (0.144 g, 0.92 mmol) were dissolved in DMF (10 cm^3), and placed in a 20 cm^3 pressure tube. The tube was sealed and heated to 120°C for 2 days. Once removed from the oven crystals of suitable size were produced for single crystal X-ray diffraction after several days. Yield 0.3067 g (51 %). Found: C, 40.1; H, 2.28; N, 4.01. $C_{48}H_{32}N_4O_8Zn_2I_4$ requires C, 40.3; H, 2.25; N, 3.92%. The X-ray powder diffraction for compound **10** was carried out and confirms the phase purity of this sample (Figure 2.46).

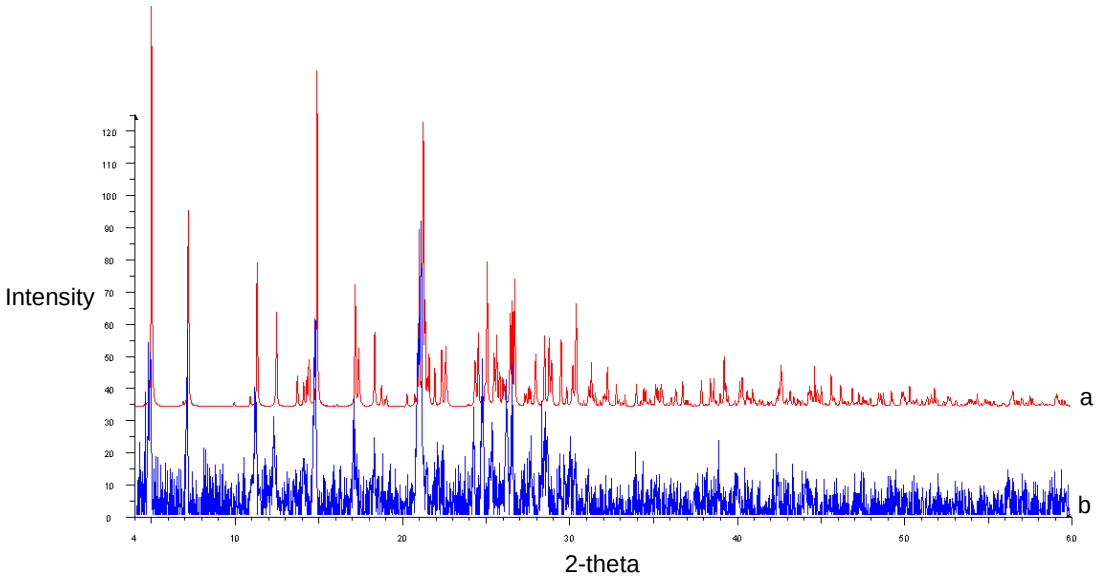

*Figure 2.46: The X-ray powder diffraction trace for **10** (b) and that simulated from the crystal data of **10** (a)*

2.4.13 [Cu$_2$(anthr)$_4$(Mepyz)]·0.5MeOH, 11

Hanthr (0.111 g, 0.50 mmol) and Mepyz (0.047 g, 0.50 mmol) were dissolved in benzyl alcohol (6 cm^3) with gentle heating and stirring. Once cooled, benzyl alcohol (2 cm^3) was gently layered on top of this solution. Layered on top of this was a solution of $Cu(OAc)_2 \cdot H_2O$ (0.038 g, 0.19 mmol) dissolved in methanol (6 cm^3), with the aid of sonication. The vial was sealed with a lid, and the solution left for several days for crystallisation to occur. Crystals of suitable size were produced for single crystal X-ray diffraction. Yield 0.0595 g (57 %). Found: C, 70.1; H, 3.95; N, 2.50. $C_{131}H_{88}Cu_4N_4O_{17}$ requires C, 70.6; H, 3.83; N, 2.53 %. The X-ray powder diffraction pattern confirmed that **11** was the only product present (Figure 2.47). The TGA shows only a decomposition of the complex at around 250 °C, showing no solvent to be present in the pores.

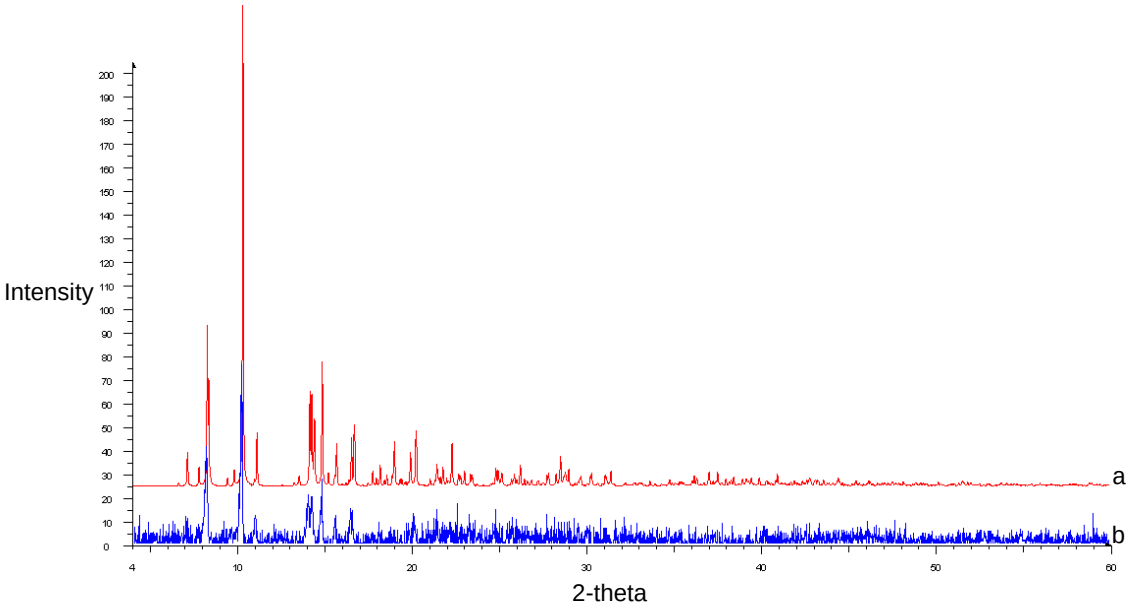

*Figure 2.47: The X-ray powder diffraction trace for **11** (b) and that simulated from the crystal data of **11** (a)*

2.4.14 [Cu_2(anthr)$_4$(dabco)], 12

Hanthr (0.111 g, 0.50 mmol) and dabco (0.056 g, 0.50 mmol) were dissolved in benzyl alcohol (6 cm^3) with gentle heating and stirring. Once cooled, benzyl alcohol (2 cm^3) was gently layered on top of this solution. Layered on top of this was a solution of $Cu(OAc)_2{\cdot}H_2O$ (0.038 g, 0.19 mmol) dissolved in methanol (6 cm^3), with the aid of sonication. The vial was sealed with a lid, and the solution left for several days for crystallisation to occur. Crystals of suitable size were produced for single crystal X-ray diffraction. Yield 0.0643 g (61 %). Found: C, 70.3; H, 4.18; N, 2.18. $C_{64}H_{40}Cu_2N_2O_8$ requires C, 70.4; H, 3.69; N, 2.57 %. The X-ray powder diffraction pattern for 12 showed the material to be phase pure (Figure 2.48). The TGA shows an initial weight loss of approximately 12 % under 100 °C, which corresponds to the loss of four methanol molecules. After this temperature there is a small plateau before a further weight loss of 12 % up to 150 °C. Up to 300 °C there is a rapid weight loss which corresponds to the sample decomposition (Figure 2.49).

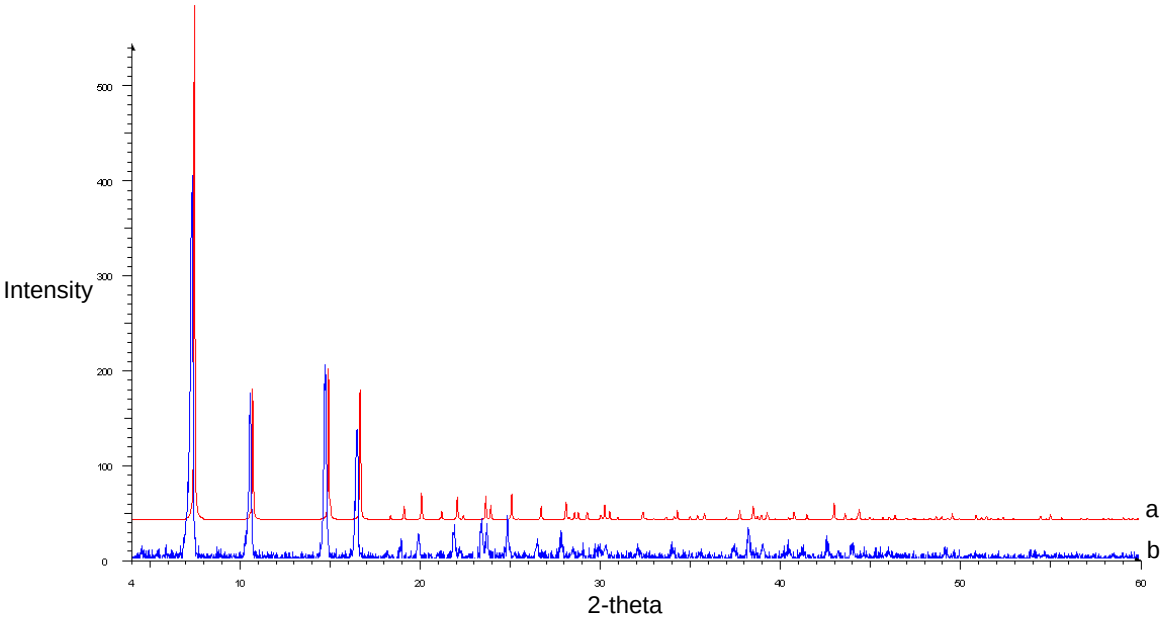

*Figure 2.48: The X-ray powder diffraction trace for **12** (b) and that simulated from the crystal data of **12** (a)*

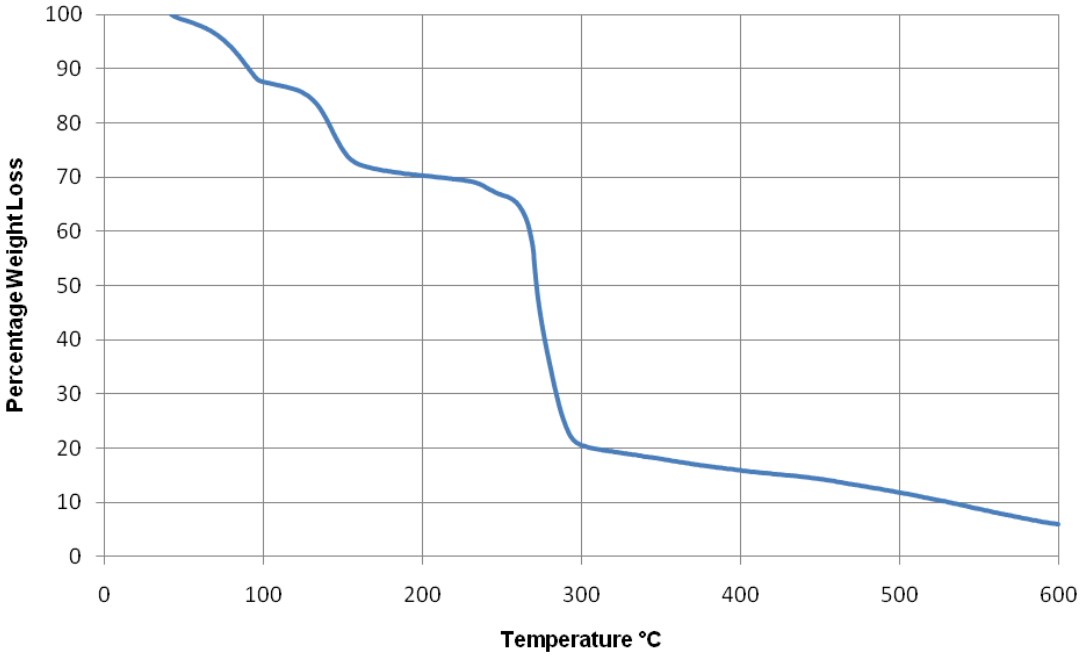

*Figure 2.49: TGA trace for compound **12***

2.4.15 $[Cu_2(anthre)_4(pyz)]$, 13

Hanthr (0.111 g, 0.50 mmol) and pyz (0.040 g, 0.50 mmol) was dissolved in benzyl alcohol (6 cm^3) with gentle heating and stirring. Once cooled, benzyl alcohol (2 cm^3) was gently layered on top of this solution. Layered on top of this was a solution of $Cu(OAc)_2 \cdot H_2O$ (0.038 g, 0.19 mmol) dissolved in methanol (6 cm^3), with the aid of sonication. The vial was sealed with a lid, and the solution left for several days for

crystallisation to occur. Crystals of suitable size were produced for single crystal X-ray diffraction. Yield 0.0694 g. The elemental analysis and X-ray powder diffraction trace (Figure 2.50) show the product to be phase impure, and therefore the TGA could not be analysed.

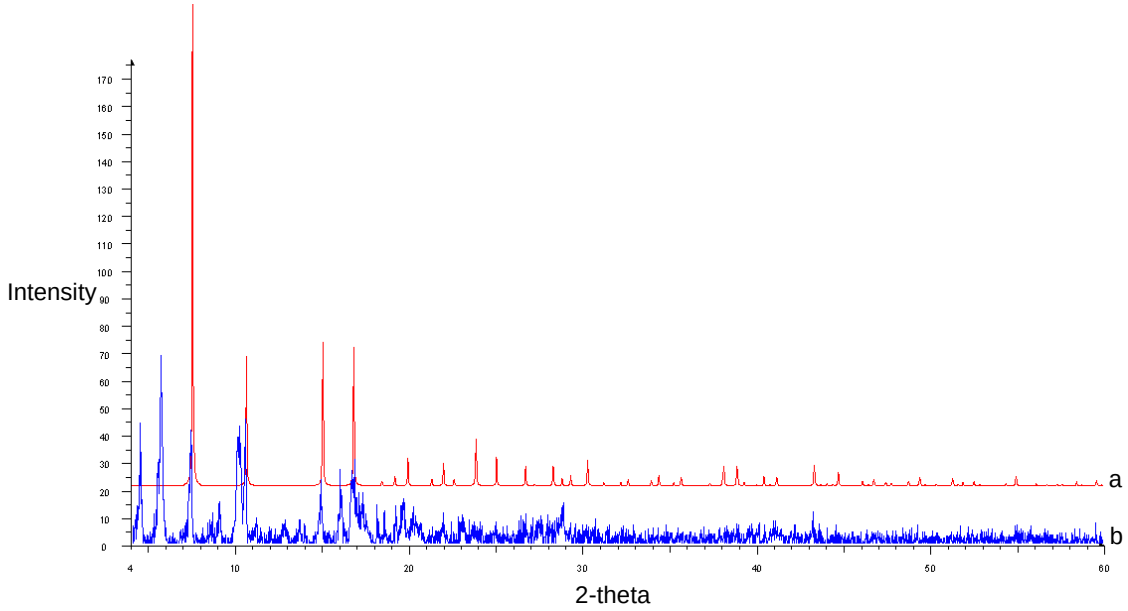

*Figure 2.50: The X-ray powder diffraction trace for **13** (b) and that simulated from the crystal data of **13** (a)*

2.5 References

1. S. Takamizawa, E. I. Nakata and T. Saito, *Inorg. Chem. Commun.*, 2004, **7**, 1.
2. S. Takamizawa, E. Nakata, H. Yokoyama, K. Mochizuki and W. Mori, *Angew. Chem. Int. Ed.*, 2003, **42**, 4331.
3. H. Kwak, S. H. Lee, S. H. Kim, Y. M. Lee, B. K. Park, E. Y. Lee, Y. J. Lee, C. Kim, S. J. Kim and Y. Kim, *Polyhedron*, 2008, **27**, 3484.
4. L. Zhang, *Acta Crystallogr.*, 2007, **E63**, m2950.
5. E. Y. Choi, K. Park, C. M. Yang, H. Kim, J. H. Son, S. W. Lee, Y. H. Lee, D. Min and Y. U. Kwon, *Chem. Eur. J.*, 2004, **10**, 5535.
6. F. A. Cotton, J. Lu and A. Yokochi, *Inorg. Chim. Acta*, 1998, **276**, 447.
7. B. W. Eichhorn, M. C. Kerby, K. J. Ahmed and J. C. Huffman, *Polyhedron*, 1991, **10**, 2573.
8. S. Takamizawa, T. Hiroki, E. Nakata, K. Mochizuki and W. Mori, *Chem. Lett.*, 2002, 1208.
9. D. N. Dybtsev, H. Chun and K. Kim, *Angew. Chem. Int. Ed.*, 2004, **43**, 5033.

10. S. S. Y. Chui, S. M. F. Lo, J. P. H. Charmant, A. G. Orpen and I. D. Williams, *Science*, 1999, **283**, 1148.
11. F. R. L. Schoening, J. N. van Niekerk and J. F. de Wet, *Acta Crystallogr.*, 1953, **6**, 501.
12. A. Bino, F. A. Cotton and T. R. Felthouse, *Inorg. Chem.*, 1979, **18**, 2599.
13. F. R. L. Schoening and J. N. Van Niekerk, *Acta Crystallogr.*, 1953, **6**, 227.
14. S. Takamizawa, E. Nakata and H. Yokoyama, *Inorg. Chem. Commun.*, 2003, **6**, 763.
15. F. K. Wang, S. Y. Yang, R. B. Huang, L. S. Zheng and S. R. Batten, *CrystEngComm*, 2008, **10**, 1211.
16. S. Takamizawa, T. Saito, T. Akatsuka and E. Nakata, *Inorg. Chem.*, 2005, **44**, 1421.
17. S. Takamizawa, E. Nakata, T. Saito and K. Kojima, *CrystEngComm*, 2003, **5**, 411.
18. S. Takamizawa, E. Nakata, T. Saito, T. Akatsuka and K. Kojima, *CrystEngComm*, 2004, **6**, 197.
19. S. Takamizawa, E. Nakata, T. Saito and T. Akatsuka, *Inorg. Chem.*, 2005, **44**, 1362.
20. S. Takamizawa, E. Nakata and T. Saito, *Chem. Lett.*, 2004, **33**, 538.
21. S. Takamizawa, E. Nakata and T. Saito, *CrystEngComm*, 2004, **6**, 39.
22. S. Takamizawa, E. Nakata and T. Saito, *Inorg. Chem. Commun.*, 2003, **6**, 1415.
23. S. Takamizawa, C. Kachi-Terajima, M. A. Kohbara, T. Akatsuka and T. Jin, *Chem. Asian J.*, 2007, **2**, 837.
24. S. Takamizawa, E. Nataka, T. Akatsuka, R. Miyake, Y. Kakizaki, H. Takeuchi, G. Maruta and S. Takeda, *J. Am. Chem. Soc.*, 2010, **132**, 3783.
25. T. Gadzikwa, B. S. Zeng, J. T. Hupp and S. T. Nguyen, *Chem. Commun.*, 2008, 3672.
26. O. K. Farha, K. L. Mulfort, A. M. Thorsness and J. T. Hupp, *J. Am. Chem. Soc.*, 2008, **130**, 8598.
27. L. Benisvy, I. Mutikainen, M. Quesada, U. Turpeinen, P. Gamez and J. Reedijk, *Chem. Commun.*, 2006, 3723.
28. J. Bauer, D. Milic and M. Modric, *Acta Crystallogr. Sect. C-Cryst. Struct. Commun.*, 2009, **65**, O512.
29. P. Politzer, J. S. Murray and T. Clark, *Phys. Chem. Chem. Phys.*, 2010, **12**, 7748.

30. O. R. Evans and W. B. Lin, *Chem. Mat.*, 2001, **13**, 3009.
31. C. S. Liu, J. J. Wang, L. F. Yan, Z. Chang, X. H. Bu, E. C. Sanudo and J. Ribas, *Inorg. Chem.*, 2007, **46**, 6299.
32. G. M. Sheldrick, *Acta Crystallogr. Sect. A*, 2008, **64**, 112.

Chapter 3 – *In Situ* Gas Storage Experiments using an Environmental Gas Cell

3.1 Introduction

The storage of gases is a very important topic with applications in many environmental issues, gas separations and gaseous drug delivery. There are many examples of materials for these uses such as activated carbons and metal oxides, but the surface area of these structures are often not large enough to store as much gas as required. For this reason zeolites and MOFs have become important classes of compounds due to their larger surface areas.

The work in this chapter focuses on using MOFs as gas storage materials. When frameworks are synthesised, the pores are often filled with solvent guest molecules. Before adsorption is possible these guest molecules must be removed from the pores, to allow space for the gas to enter the MOF. There are also a number of materials that contain solvent molecules coordinated to the metal centres. If these coordinated molecules can be removed without a change in the network, the resultant coordinatively unsaturated metal centres would be beneficial for gas adsorption. The removal of guest solvent molecules is known as activation, and this can be achieved through heating the material under vacuum to remove any solvent that may be present. It is important at this point to make sure that complete removal of the solvent is achieved, otherwise the maximum adsorption capacities may not be observed.[1] Many MOF materials are unstable to the removal of solvent, leading to a collapse of the framework, whereas some have shown to retain their crystallinity and are capable of 'breathing' after the removal of solvent.[2, 3]

HKUST-1 ($[Cu_3(tma)_2(H_2O)_3]$, tma = trimesate) is a highly studied material that remains crystalline and contains free metal sites once dehydration has occurred. These sites contribute significantly to the adsorption behaviour of this material due to a partial positive charge existing on the metals which is compensated by a partial negative charge on the carboxylates. These characteristics as well as the van der Waals surface interactions cause this material to adsorb large amounts of gases.[1]

There are also materials that do not contain coordinatively unsaturated metal centres but still show significant amounts of adsorption. For example, MOF-5 ($[Zn_4O(bdc)_3]$) (bdc = 1,4-benzenedicarboxylate) containing the $Zn_4O(O_2CR)_6$ SBU. This compound has been shown to have a high BET surface area of 3170 m^2 g^{-1}, yet it contains no coordinatively unsaturated metal centres.[4]

There are two principal mechanisms in which gases can be stored in solids, chemisorption and physisorption. Chemisorption involves the formation of weak chemical bonds between the gas molecules and the solid surface. This relates to the adsorption of gas molecules to coordinatively unsaturated metal sites. Physisorption however involves the formation of weaker van der Waals forces between the gas molecules and the solid surface, as is seen in MOF-5. The energy of chemisorption is of the magnitude 40-200 kJ mol^{-1} and higher than physisorption, so higher temperatures may be required to remove the gases after adsorption. Generally with chemisorbed species only monolayer formation occurs, as once the adsorbing sites are filled no more adsorption can occur. Physisorption however, under the appropriate temperatures and pressures can result in multilayered adsorption.

There are many reported MOF materials in the literature that have been shown to be good adsorbents, but much of this occurs at higher pressures, making them unsuitable for many applications. It is also unclear the points of contact where the gas molecules interact within the framework, and the processes behind the gas adsorption. It is important to understand how gases interact with framework materials if new materials are to be designed with higher adsorption capacities. For this reason, more recently research has focussed on *in situ* experiments, locating the position of gas molecules within frameworks crystallographically.

Much of this research involves single crystal X-ray techniques, locating the atom positions of the gas molecules within the frameworks. In these cases, the position of gases such as sulfur dioxide, carbon dioxide, nitrogen and the noble gases have been investigated. As noted above, it is often necessary for solvent guest molecules to be removed before gas adsorption is possible. For the success of *in situ* experiments, these molecules have to be removed whilst maintaining the crystallinity of the material.

One such material that has been studied in this way is $Cu_2(OH)(SIP)(H_2O)\cdot 2H_2O$ (Cu-SIP-3, SIP = 5-sulfoisophthalate) (Figure 3.1).[5] The structure consists of a copper tetramer SBU, where each copper centre has square based pyramidal geometry. The copper centres are linked together by two three-coordinate hydroxyl groups in the centre. The 5-sulfoisophthalate ligands bridge copper centres, and then connect to adjacent SBUs forming two dimensional layers. The structure is extended into three dimensions through the coordination of two of the three oxygen atoms of the sulfonate group to adjacent layers.[5]

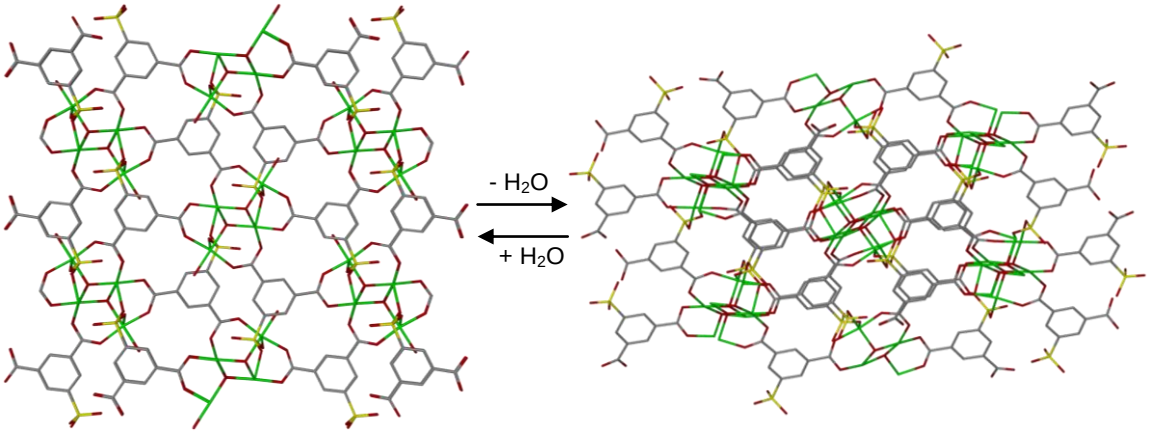

Figure 3.1: The structure of hydrated Cu-SIP-3 (left) and dehydrated (right). Guest water molecules and hydrogen atoms have been omitted for clarity[6]

This material was placed under a dynamic vacuum at varying temperatures to remove the guest and coordinated water molecules. At temperatures in the range of 150-365 K the hydrated form of Cu-SIP-3 was obtained. Above 365 K the Bragg scattering deteriorated, and a unit cell determination could not be obtained. However, above 405 K, the Bragg reflections reappeared, and at 430 K it was possible to determine both the unit cell and structure, yielding the dehydrated Cu-SIP-3 material. In this high temperature form, all guest and coordinated water molecules were completely removed, causing the now vacant site on the copper to be coordinated by the third sulfonate ligand oxygen.[6]

After this dehydration, the single crystal of Cu-SIP-3 was exposed to nitric oxide. Cu-SIP-3 has previously been shown to be highly selective at adsorbing NO, through a coordination-driven gating mechanism.[5] Low pressures of NO (<275 mbar) were exposed to the dehydrated sample, and no change was observed. However, when the pressure was increased above the gate opening pressure of 275 mbar, an immediate

change was observed, with a loss of Bragg diffraction. It was suggested that at these pressures some of the NO has become coordinated to the copper ions, whilst some has not, resulting in the loss of long range order.[6]

MOF-5 is a material that does not contain any unsaturated metal sites; however it still facilitates a significant amount of adsorption. Precise determination of the adsorption sites in MOF-5 is important due to the large pores and the possibility of many adsorption sites existing. For this reason *Yaghi et al*. used single crystal X-ray diffraction to study argon and nitrogen adsorption within MOF-5. Crystals of MOF-5 were evacuated and then placed in glass capillaries and backfilled with either Ar or N_2 and then flame-sealed.[7]

Several datasets were collected with both Ar and N_2 between the temperature range 30-293 K. No significant electron density peaks were observed at 293 K, but as the temperature was lowered, considerable electron density was identified in the Fourier map. The data collected at 30 K showed the most apparent localisation of gas molecules proximal to the $Zn_4O(CO_2)_6$ unit. The first lies on a triangular face of the octahedron whose vertices are defined by the carboxylate C atoms. Of all the sites observed, this shows the greatest occupancy, and hence is referred to as the primary adsorption site. From the electron density maps, a total of seven adsorption sites were located, five primary adsorption sites, which are closest to the framework, and three secondary sites which form a second layer of adsorption in the pores (Figure 3.2).[7]

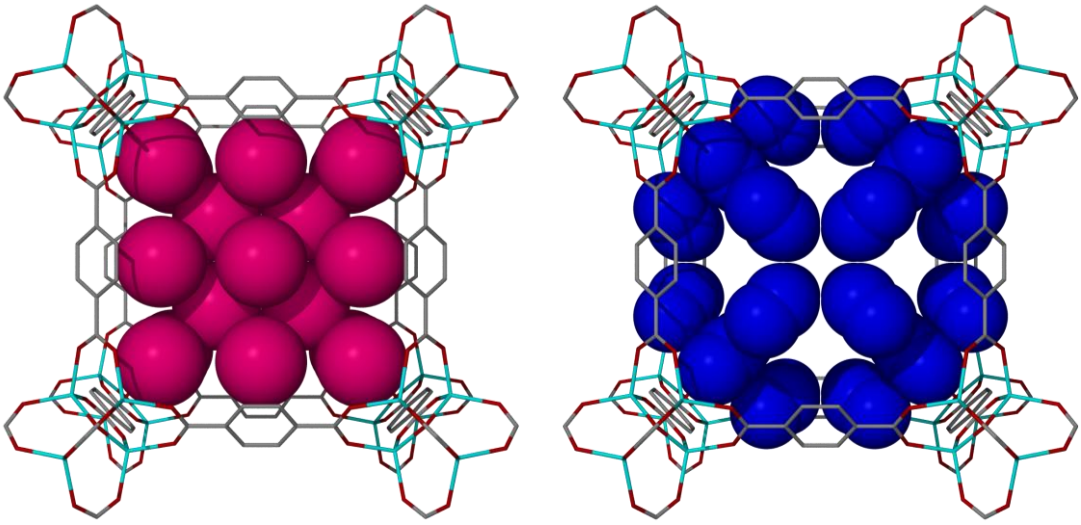

Figure 3.2: The crystal structure of MOF-5 loaded with argon (left) and nitrogen (right). Hydrogen atoms have been omitted for clarity[7]

Another material that has shown a great affinity of adsorbing CO_2 over CH_4, and so could potentially be used for separating mixtures of CO_2 and CH_4 is $(Me_2NH_2)(HDMF)[Co_3Cl_4(ppt)_2]\cdot 2H_2O\cdot DMF$ (MAF-X7, H_2ppt = 3-(2-phenol)-5-(4-pyridyl)-1,2,4-triazole) (Figure 3.3). There are two crystallographically different cobalt centres within the structure, one with octahedral geometry and one with tetrahedral geometry. Three cobalt centres are bridged together through the coordination of the ppt ligand μ-phenolate oxygen and the triazolate 1- and 2-nitrogens. The tetrahedral cobalt coordination sphere is completed by the coordination of two chloride ions, and the octahedral metal centre has two coordinated nitrogen atoms from the 4-pyridyl group of adjacent ppt ligands. This extends the structure into a two dimensional grid. The triazolate 4-nitrogen remains uncoordinated and is exposed to the pore surface, enhancing the adsorption potential of CO_2. The pores of the structure are filled with water, DMF and $HDMF^+$ as well as $Me_2NH_2^+$ cations. These reside between the two dimensional grids, and are involved in hydrogen bonding, forming a three dimensional net. It is possible to remove these solvent guest molecules from the framework whilst maintaining its crystallinity.[8]

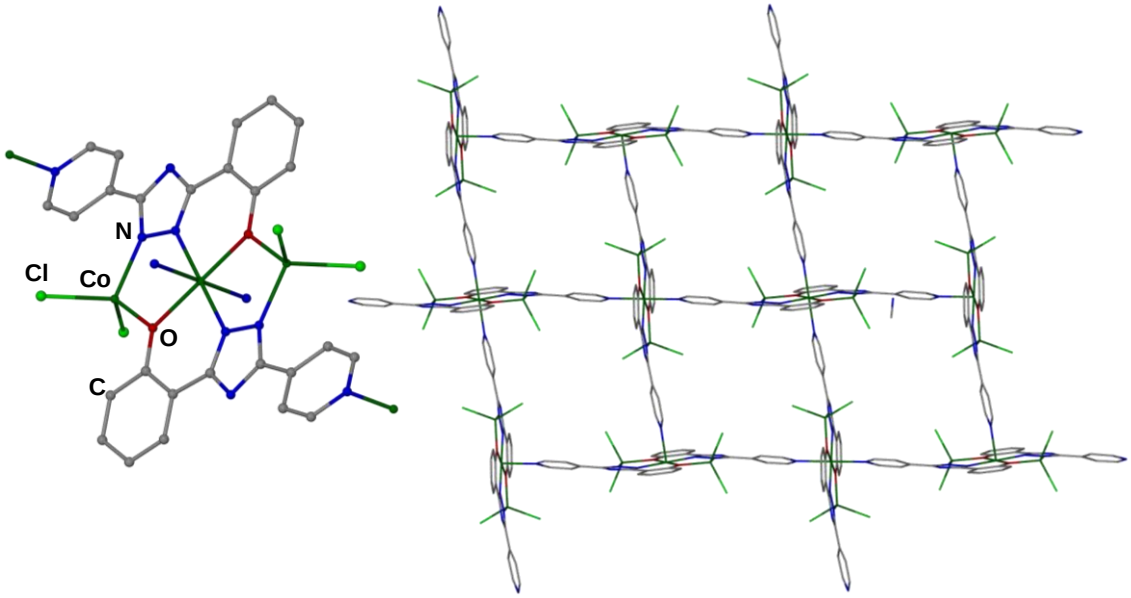

Figure 3.3: The structure of $(Me_2NH_2)(HDMF)[Co_3Cl_4(ppt)_2]\cdot 2H_2O\cdot DMF$ (MAF-X7, H_2ppt = 3-(2-phenol)-5-(4-pyridyl)-1,2,4-triazole) (left) and the two dimensional grid (right). Hydrogen atoms and guest molecules have been omitted for clarity[8]

The activated sample was then loaded with CO_2 and characterised by single crystal X-ray diffraction. Thus, it was possible to locate a CO_2 molecule within the pores of the structure, where it forms a short contact with the triazolate 4-nitrogen, and a longer

contact to the phenyl carbon atoms, confirming the attractive interaction with the exposed ligand nitrogen atom. The CO_2 also forms a contact with the $HDMF^+$ cation, suggesting that both the ligand nitrogen atom and the cations within the channels help stabilise the presence of CO_2 within the pores.[8]

It is also possible to study gas uptake within MOFs using powder X-ray diffraction. *Blom et al*. studied the microporous framework CPO-27-Ni ($[Ni_2(dhtp)(H_2O)_2]\cdot 8H_2O$, dhtp = 2,5-dihydroxoterephthalate).[9] In this structure the nickel metal centres are octahedrally bound by five oxygen atoms from four ligands, and an oxygen atom from a coordinated water molecule. The gross structure is a three dimensional honeycomb network. Once the material has been dehydrated, the guest water, and also coordinated water molecules are removed, leaving the nickel centre as coordinatively unsaturated, whilst maintaining the gross structure. The powdered sample was placed in a capillary tube, exposed to carbon dioxide in the pressure range 0.2-0.5 atm, and then flame sealed; a data collection was then carried out at 100 K. Through Rietveld refinement, it was possible to solve the structure and locate the carbon dioxide molecules, which were coordinated to the nickel centre in an end-on manner (Figure 3.4).[10]

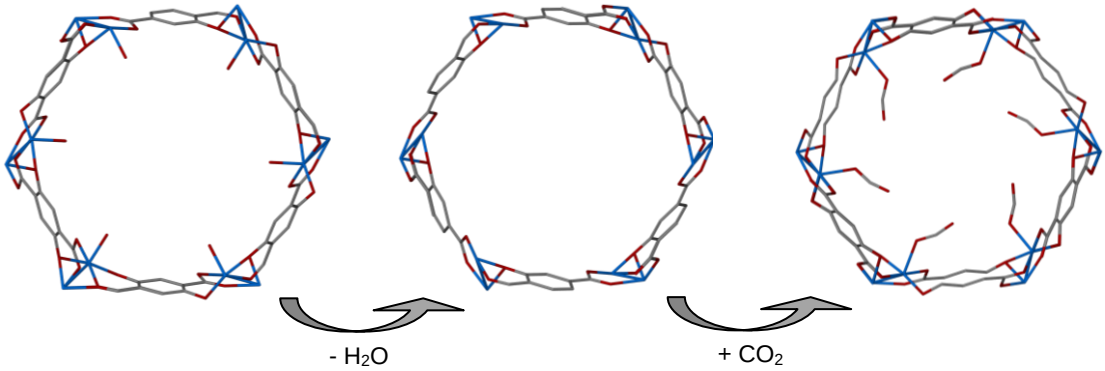

Figure 3.4: The crystal structure of CPO-27-Ni (left), dehydrated (middle) and CO_2 loaded (right). Hydrogen atoms have been omitted for clarity[10]

The aim of the work in this chapter was to investigate a range of MOF materials using *in situ* single crystal X-ray diffraction to determine sites where gases interact with the frameworks, in order to better understand the processes underpinning gas adsorption.

The gases focussed upon in this study are carbon dioxide and sulfur dioxide. Carbon dioxide is a known pollutant from the burning of fossil fuels, adding to the global climate change. Sulfur dioxide is also a greenhouse gas, identified to have harmful

effects on plants and wildlife through its reaction with atmospheric water forming acid rain. As well as their implications in worldwide climate change, there are also practical reasons to testing these gases. As X-ray crystallography is used as the main tool for determining the gas location, the molecules have reasonable electron density for their location to be identified. Sulfur dioxide, for this reason appears to be a better candidate due to the increase in the X-ray scattering power of the sulfur atom over carbon. However, crystal decomposition whilst in the presence of this gas may also be observed.

These gases were studied with a range of materials within the environmental gas cell, to gain an understanding from a variety of frameworks. The first materials studied were the newly synthesised paddle wheel structures outlined in Chapter 2. A literature search was also conducted to source MOFs that might be promising adsorbing materials, but had not yet had gas molecules located within their pores.

3.2 The Crystallographic Experiment

In situ X-ray measurements of gas inclusion within materials have been carried out using the environmental gas cell (EGC) on Station 11.3.1 of the ALS, Berkeley, California (Figure 3.5).[11] This set up allows a single crystal to be placed under a vacuum, for either dehydration or removal of guest solvent, or to be exposed to a pure gas or mixture of gases. It is beneficial to use the EGC in combination with an X-ray synchrotron source. The higher flux of the source allows the observation of higher diffraction intensities, owing to the use of smaller crystals which also maximises the gas penetration. The borosilicate capillary also produces a vast amount of amorphous scattering, reducing I/σ, often resulting in longer collection times. If standard X-ray diffractometers were used, even with large crystals, data collections would be in the range of several hours, whereas at a synchrotron source these collection times can be reduced to approximately one hour. This is invaluable when carrying out *in situ* measurements, as the continuous evaluation of the crystal is necessary under a variety of conditions. Thus, even at a synchrotron source this can take several days.

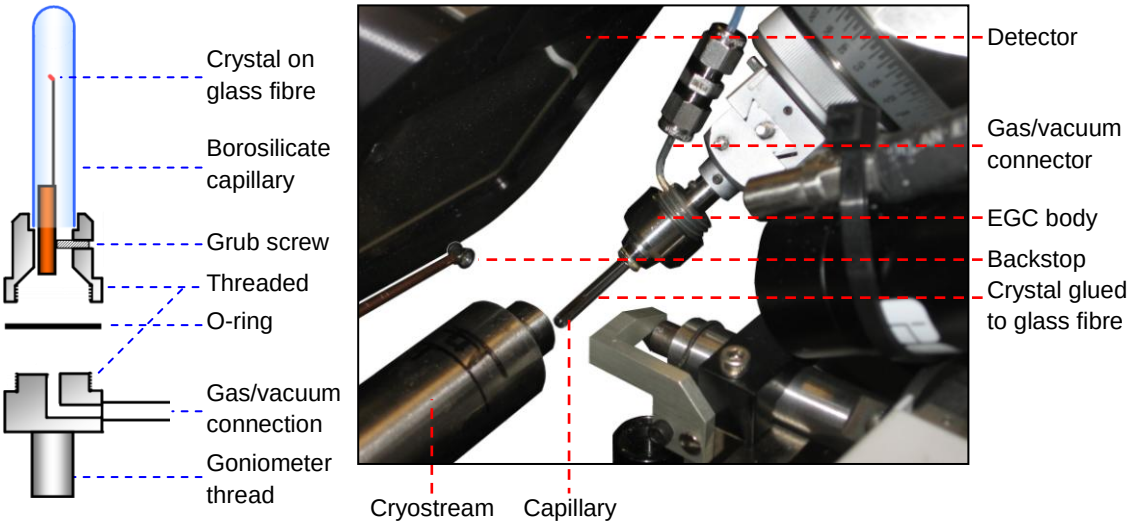

Figure 3.5: Schematic of the environmental gas cell[11] (left) and a photograph of the EGC on Station 11.3.1 at the ALS

For the experimental procedure, the crystal is manipulated under solvent and mounted to the glass fibre with the minimum amount of epoxy glue, taking care not to coat the entire crystal with glue. The EGC is assembled and tested to confirm that there are no leaks within the system. An initial X-ray data collection is carried out on the crystal to confirm the data quality before the crystal environment is changed. Many of the samples tested within this chapter contain guest solvent molecules within the pores and for this reason the crystals would be exposed to a vacuum before any gas was applied, to remove this solvent.

The vacuum is first applied to the EGC at 283 K and maintained during the next data collection. After the collection, the data are analysed to determine how much of the guest molecules have been removed from the pores. If all the solvent has not been removed at this temperature, the temperature would be increased for each concurrent data collection, whilst still maintaining the vacuum. After each rise in temperature a new dataset would be collected, examining the loss of the solvent by allowing the occupancy of the guest molecules to refine freely. Once the solvents have been completely removed, the temperature can be reduced back to 283 K, and data can be collected again, prior to any gas exposure, and compared to the results from the initial data set.

After complete guest removal it is then possible to expose the crystal to the specified gas. The gas (CO_2/SO_2) is first mixed with nitrogen and then slowly introduced to the cell. The crystal is left to equilibrate before data is collected and analysed. For the next few data collections a similar procedure is followed, increasing the concentration of CO_2 or SO_2 in the mixture with N_2. For the analysis of the data, it is often the case that once the gas is taken into the system there is a large amount of disorder, this means the location of the gas is difficult to find. For this reason PLATON SQUEEZE is used as a tool for identifying the residual electron density within the pores of the structures.

After the maximum amount of gas has been adsorbed, the crystal is again placed under a dynamic vacuum to show the gas could be released from the framework. This was first conducted at 283 K, but if removal was slow the temperature was increased to aid with the release. This process generally occurred much quicker than the removal of the guest solvent molecules. It is then possible to test the same crystal with different gases in a similar manner to previously stated.

PLATON SQUEEZE is an algorithm used to take into account the contributions from disordered guest molecules, by using the electron density found in the solvent accessible volume outside the ordered part of the structure. The solvent accessible void is a defined region where a sphere with a 1.2 Å radius can be accommodated, whilst not intersecting the van der Waals radii of any of the atoms present within the structure. The electron density within this region is then calculated and used as a contribution towards the disordered guest. Once SQUEEZE has been carried out, a new reflection file is produced where the disordered guest contribution has been eliminated. This can then be refined against the old structural model, producing a refinement based on data with excess electron density removed. The latter is then assigned to disordered guest molecules.[12, 13]

3.3 Paddle Wheel Structures

In Chapter 2 several compounds were synthesised which were based on the paddle wheel SBU. These compounds were prepared as the related structures by *Takamizawa et al.*[14] had been shown crystallographically to adsorb a variety of gases. Of the compounds synthesised, two of these were studied within the EGC, as they had produced crystals of suitable size for this study. These compounds were:

- $[Cu_2(biphen)_4(pyz)]\cdot 1.9BzOH$, **1** (biphen = biphenyl-4carboxylate, pyz = pyrazine)
- $[Cu_2(Ibza)_4(NH_2pyz)]\cdot 2BzOH$, **2** (Ibza = 4-iodobenzoate, NH_2pyz = 2-aminopyrazine)

Compounds **1** and **2** looked to be promising candidates, both containing large pores, with the largest pore present in **1**, of approximate dimensions 11.3 x 13.3 Å. However, when these were placed in the EGC and subjected to a dynamic vacuum at 283 K, they both immediately lost crystallinity. Although both of these structures contain benzyl alcohol within the pores, these solvent molecules could not be located crystallographically, and PLATON SQUEEZE was used to locate residual electron density within the structure which was assigned to the benzyl alcohol guest. The reactions were also carried out in methanol, and so some of the solvent designated as disordered benzyl alcohol could be arising from guest methanol within the pores. This could explain the loss of solvent at lower temperatures, and perhaps this loss in crystallinity. This may have been because the pores were too large to support the framework once the solvent was removed.

3.4 MOFs from within the Literature

After these new materials had been studied, a search on compounds within the literature that looked to be promising adsorbents was conducted. These materials had to produce good quality crystals for the diffraction experiments, contain pores that could adsorb the gases, whilst limiting the size of this pore, so highly disordered gas molecules would not be present, and if they contained solvents within the pores, that these could be removed without a loss of crystallinity. From this search, two suitable materials were identified:

- $[Zn(bdc)(bipy)_{0.5}]\cdot DMF\cdot 0.5H_2O$ (bdc = 1,4-benzenedicarboxylate, bipy = 4,4'-bipyridine)[15]
- $[Zn_2(ox)(atz)_2]\cdot 2MeOH$ (ox = oxalate, atz = 3-amino-1,2,4-triazolate)[16]

3.4.1 $[Zn(bdc)(bipy)_{0.5}]\cdot DMF\cdot 0.5H_2O$

$[Zn(bdc)(bipy)_{0.5}]$ has a structure constructed from a $Zn_2(O_2CR)_4$ paddle wheel SBU, where the bdc ligands link the zinc paddle wheels into a two dimensional square grid.

The bipy ligand coordinates in the axial position of the zinc, and acts as a pillar to link the square grids together, extending the structure into three dimensions. The framework is doubly interpenetrated, reducing the pore size (Figure 3.6).[15]

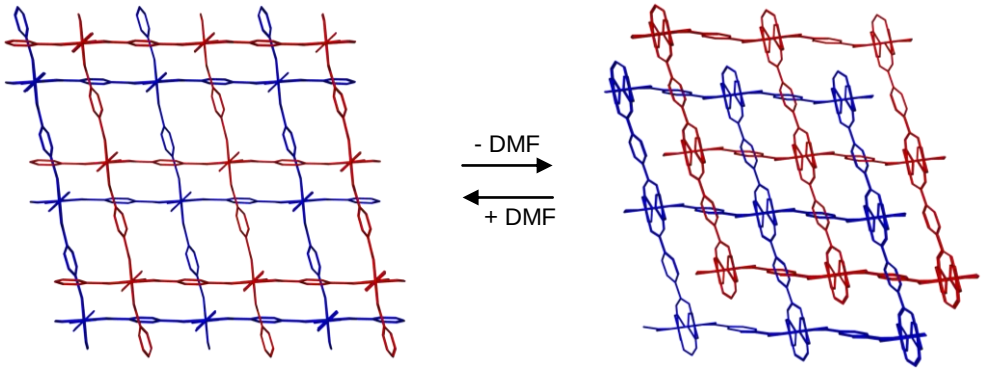

Figure 3.6: The solvated structure of $[Zn(bdc)(bipy)_{0.5}]\cdot DMF\cdot 0.5H_2O$ (left) and desolvated (right). Guest solvent molecules and hydrogen atoms have been omitted for clarity[17]

From previous work carried out on this material, the TGA data indicated that the solvent could be removed from the material over the temperature range 25-145 °C, and that it is thermally stable up to 360 °C. The structures of both the solvated and desolvated forms have previously been reported, showing the crystallinity of the material is maintained after activation. It is also possible to soak the desolvated sample in a mixture of DMF and ethanol to reform the solvated structure, and this activation/solvation process can be repeated several times. These results suggest that this material would be a suitable candidate to study within the EGC as the crystallinity of the sample is maintained after solvent removal. Also, the structures can be interconverted several times, suggesting the structure can 'breathe' on removal and addition of solvents. The N_2, H_2 and CO_2 isotherms were also carried out on the material, and the Langmuir surface area calculated from the N_2 sorption was found to be 946 $m^2\ g^{-1}$.[17]

The crystal structure of the guest free structure reveals that the overall connectivity is maintained, but the paddle wheel SBU is distorted and the bipy linkers are bent. These changes cause the network to compress considerably forming a densely packed doubly interpenetrated framework.[17]

The crystal was first placed into the gas cell and a ground state dataset was collected, to determine the overall quality of the sample. The crystal was then placed under a vacuum and the temperature was gradually increased. Each dataset was analysed, and PLATON SQUEEZE was used to determine the change in electron density within the pores of the structure, and hence offer a means of monitoring solvent loss. Results indicated that a small decrease in electron density had occurred, suggesting a slow removal of the solvent. However, when the cryostream was ramped to 353 K, the crystallinity of the sample was lost. The same experiment was repeated several times, and the same result was obtained. From previous work carried out on this sample, the TGA showed that the solvent loss occurred up to a temperature of 145 °C. In the experimental work, the crystal decomposed at 80 °C, suggesting that all the solvent may not have been lost up to this point. Consequently, no experiments were carried out testing the adsorption potential of this material.

Although this material looked to be a promising candidate to follow with *in situ* crystallographic gas studies, the single crystallinity of the material could not be maintained during solvent loss. As reported by *Morris et al.*, it is possible to continue desolvating a material at higher temperatures, and for the crystallinity of the material to return.[6] As the solvent is initially removed from the pores, the remainder of the solvent becomes disordered, which causes the Bragg scattering to decrease. Once the solvent is fully removed, there is no disorder and so the Bragg reflections reappear. Due to time restraints on the experiment, it was not possible to test out this theory on the sample, but this could be a basis for future work on this material.

3.4.2 $[Zn_2(ox)(atz)_2]\cdot 2MeOH$

The structure of $[Zn_2(ox)(atz)_2]\cdot 2MeOH$ is constructed from two zinc centres each with distorted trigonal bipyramidal geometry. Three of these coordination nodes are filled by coordination to the aminotriazolate through the three N-atoms of the ring, the amino groups remain uncoordinated. One of these rings is disordered over two sites in a 40:60 ratio. The oxalate completes the zinc coordination sphere through the coordination of bidentate oxygen atoms from the different carboxylate groups. The zinc centres and aminotriazolate form two dimensional layers which are pillared by the oxalate groups, forming a three dimensional porous framework (Figure 3.7). The free amino groups project into the pores, and the remainder of the pore space is filled with two molecules

of methanol. Each methanol is positionally disordered, with both sites being located crystallographically. One methanol is disordered in a 25:75 ratio and the other is disordered in a 46:54 ratio.[16]

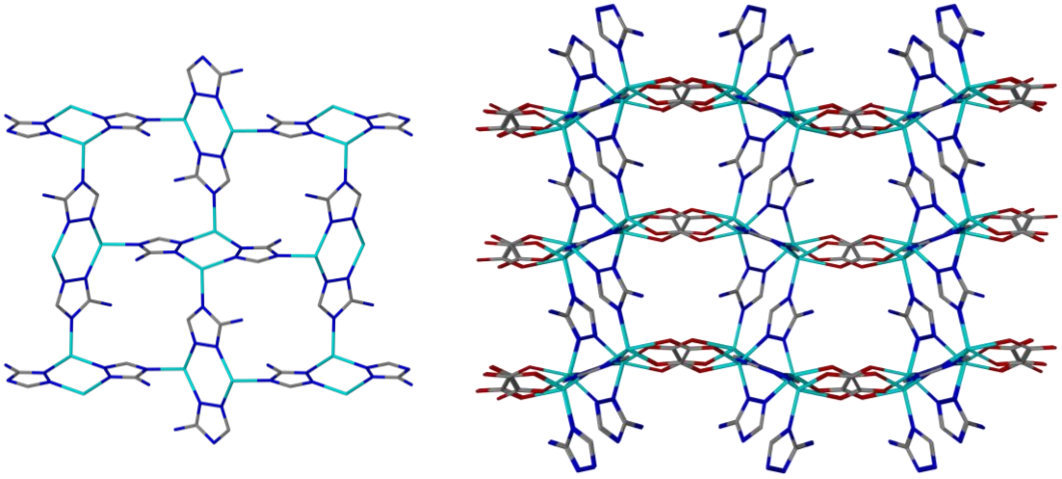

Figure 3.7: The crystal structure of the Zn-atz layer (left) and the three dimensional structure of [Zn_2(ox)(atz)$_2$] (right). Hydrogen atoms, minor disordered components and solvent molecules have been omitted for clarity

The TGA data from previous studies showed that this material was able to lose the guest solvent in the temperature range 30-130 °C, with a decomposition temperature of 300 °C. After the solvent was lost and before the decomposition, the powder X-ray diffraction pattern showed a comparable trace to that seen for the solvated form. Adsorption of CO_2 was also measured at 273 K, giving a surface area of 782 m^2 g^{-1}, with notable uptake at lower pressures. The adsorption and desorption cycles were also repeated several times on the same sample, showing complete reversibility, with supporting data obtained through powder X-ray diffraction and TGA. Gas adsorption measurements were also carried out with N_2, Ar and H_2 under the same conditions, with no appreciable uptake. This demonstrates the selectivity of this material to adsorb CO_2 over the other gases, possibly due to the presence of the free amino groups to be involved in host-guest interactions.[16]

This previous work suggests that this material is an ideal candidate for studies within the EGC. It demonstrates selective gas uptake, and if it can be understood whether the amino functionalities play a role in CO_2 adsorption, this may inform the design of new framework materials in the future.

The sample was first activated under vacuum by collecting several datasets whilst increasing the temperature from 283 K to 400 K. The occupancy of the methanol molecules was monitored until complete desolvation was achieved after 22 hours. SQUEEZE was also used to monitor the reduction in electron density as the sample was desolvated. After the methanol had been successfully removed, the crystal was cooled to 283 K and carbon dioxide gas was then administered to the EGC, with varying pressures of CO_2, but not exceeding 900 Torr. After each administration, the cell was left to equilibrate for 30 minutes before a dataset was collected. Once it was established maximum adsorption had occurred, the cell was purged with N_2 and then heated under vacuum to assess the reversibility of the CO_2 adsorption. The CO_2 was not visible within the Fourier maps of the datasets collected, so PLATON SQUEEZE was used to see if an increase in electron density was occurring as CO_2 was administered to the cell.

After complete removal of the CO_2 the temperature was lowered to 283 K, and sulfur dioxide was administered to the EGC in a similar manner to before, with several datasets being collected. Due to time restrictions on the experiment, and degradation of the crystal quality due to the addition of the SO_2, the gas was removed after 10 hours of exposure to the crystal. This was achieved by purging the EGC with N_2 and heating the sample to 400 K under vacuum. For many of the SO_2 loaded datasets, the gas was not visible within the Fourier map, due to disorder within the structure. However, the final dataset had a significant amount of SO_2 present, and the sulfur atom was refined freely within this refinement. Details for all data collections are given in Tables 3.1 and 3.2.

Dataset	**1 - Solvated**	**2 – 85 % MeOH**	**3 – 68 % MeOH**	**4 – 50 % MeOH**	**5 – 40 % MeOH**	**6 - deoslvated**	**7 – CO_2 1 hr**	**8 – CO_2 2 hrs**
Empirical formula	$C_8H_{14}N_8O_6Zn_2$	$C_{7.7}H_{12.8}N_8O_{5.7}Zn_2$	$C_{7.36}H_{11.44}N_8O_{5.36}Zn_2$	$C_7H_{10}N_8O_5Zn_2$	$C_{6.8}H_{9.2}N_8O_{4.8}Zn_2$	$C_6H_6N_8O_4Zn_2$	$C_6H_6N_8O_4Zn_2$	$C_{6.13}H_6N_8O_{4.25}Zn_2$
M	449.01	439.40	428.51	416.97	410.56	384.93	384.93	390.43
***T*/ K**	283(2)	283(2)	323(2)	343(2)	343(2)	400(2)	283(2)	283(2)
Crystal system	Orthorhombic	Orthorhombic	Orthorhombic	Orthorhombic	Orthorhombic	Orthorhombic	Orthorhombic	Orthorhombic
Space group, *Z*	*Pbca*, 8	*Pbca*, 8	*Pbca*, 8	*Pbca*, 8	*Pbca*, 8	*Pbca*, 8	*Pbca*, 8	*Pbca*, 8
***a*/ Å**	13.7758(15)	13.7810(7)	13.8089(6)	13.8337(7)	13.8369(5)	13.8544(6)	13.8525(6)	13.8504(7)
***b*/ Å**	13.0846(14)	13.0844(7)	13.0736(6)	13.0065(7)	12.9593(5)	12.8869(5)	12.8846(6)	12.8675(6)
***c*/ Å**	16.9530(18)	16.9186(9)	16.8754(8)	16.8745(9)	16.8725(7)	16.8899(7)	16.8846(8)	16.8849(8)
***U*/ Å ^{3}**	3055.8(6)	3050.7(3)	3046.6(2)	3036.2(3)	3025.5(2)	3015.5(2)	3013.6(2)	3009.2(3)
***F*(000)**	1808	1765	1716	1664	1635	1520	1520	1542
Theta range for data collection/ º	4.49 to 33.75	4.58 to 33.69	4.21 to 30.55	4.59 to 33.73	4.60 to 32.56	4.60 to 33.63	4.60 to 33.63	4.60 to 33.63
Reflections collected/ observed [*I*>2σ(*I*)]	31670/3027	31461/3037	31423/2945	31453/2977	29560/2920	31089/3060	30974/2907	30878/2959
Data Completeness	0.987	0.992	0.992	0.990	0.995	0.992	0.992	0.992
Goodness-of-fit on F^2	1.009	1.002	1.001	0.931	0.940	0.933	0.985	0.928
Final *R* indices [*I*>2σ(*I*)]	*R*1 = 0.0426, *wR*2 = 0.1028	*R*1 = 0.0409, *wR*2 = 0.0978	*R*1 = 0.0410, *wR*2 = 0.0928	*R*1 = 0.0405, *wR*2 = 0.0908	*R*1 = 0.0367, *wR*2 = 0.0824	*R*1 = 0.0378, *wR*2 = 0.0813	*R*1 = 0.0405, *wR*2 = 0.0920	*R*1 = 0.0401, *wR*2 = 0.0878
***R* indices (all data)**	*R*1 = 0.0802, *wR*2 = 0.1211	*R*1 = 0.0793, *wR*2 = 0.1162	*R*1 = 0.0839, *wR*2 = 0.1116	*R*1 = 0.0770, *wR*2 = 0.1015	*R*1 = 0.0640, *wR*2 = 0.0902	*R*1 = 0.0685, *wR*2 = 0.0898	*R*1 = 0.0811, *wR*2 = 0.1096	*R*1 = 0.0745, *wR*2 = 0.0974
Largest diff. peak and hole Å $^{-3}$	0.679 and -0.633	0.755 and -0.594	0.497 and -0.433	0.472 and -0.595	0.508 and -0.420	0.555 and -0.592	0.588 and -0.658	0.511 and -0.645

Table 3.1: Crystallographic data for datasets 1-8 of [Zn_2(ox)(atz)$_2$]

Dataset	**9 – CO_2 4 hrs**	**10 – CO_2 5 hrs**	**11 – CO_2 8 hrs**	**12 - evacuated**	**13 – SO_2 1 hr**	**14 – SO_2 4 hrs**	**15 – SO_2 10 hrs**	**16 - evacuated**
Empirical formula	$C_{6.25}H_6N_8O_{4.5}Zn_2$	$C_{6.31}H_6N_8O_{4.63}Zn_2$	$C_{6.44}H_6N_8O_{4.88}Zn_2$	$C_6H_6N_8O_4Zn_2$	$C_6H_6N_8O_{4.2}S_{0.1}Zn_2$	$C_6H_6N_8O_{4.92}S_{0.46}Zn_2$	$C_6H_6N_8O_6SZn_2$	$C_6H_6N_8O_4Zn_2$
M	395.93	398.68	404.18	384.93	391.33	414.40	448.99	384.93
***T*/ K**	283(2)	283(2)	283(2)	283(2)	283(2)	283(2)	283(2)	400(2)
Crystal system	Orthorhombic	Orthorhombic	Orthorhombic	Orthorhombic	Orthorhombic	Orthorhombic	Orthorhombic	Orthorhombic
Space group, *Z*	*Pbca*, 8	*Pbca*, 8	*Pbca*, 8	*Pbca*, 8	*Pbca*, 8	*Pbca*, 8	*Pbca*, 8	*Pbca*, 8
***a*/ Å**	13.8487(7)	13.8511(6)	13.8487(6)	13.8458(6)	13.860(3)	13.8526(10)	13.808(7)	13.8403(6)
***b*/ Å**	12.8412(7)	12.7388(5)	12.7375(5)	12.8529(5)	12.806(3)	12.7030(9)	12.803(7)	12.8428(6)
***c*/ Å**	16.8873(9)	16.9125(7)	16.9101(7)	16.8925(7)	16.902(4)	16.8928(12)	16.858(9)	16.8654(8)
***U*/ Å ^{3}**	3003.1(3)	2984.1(2)	2982.9(2)	3006.2(2)	3000.0(11)	2972.6(4)	2980(3)	2997.8(2)
***F*(000)**	1564	1575	1597	1520	1546	1638	1776	1520
Theta range for data collection/ º	4.60 to 33.65	4.60 to 33.64	4.60 to 33.65	4.60 to 33.68	4.60 to 33.70	4.61 to 33.62	4.51 to 33.67	4.60 to 28.98
Reflections collected/ observed [$I>2\sigma(I)$]	30904/2927	30880/2815	30870/2786	27448/2896	30960/2753	30441/2285	30349/2236	23222/2217
Data Completeness	0.990	0.992	0.992	0.991	0.990	0.993	0.993	0.993
Goodness-of-fit on F^2	0.920	0.958	0.942	0.992	0.915	0.871	1.035	01.033
Final R indices [$I>2\sigma(I)$]	$R1$ = 0.0404, $wR2$ = 0.0887	$R1$ = 0.0433, $wR2$ = 0.1038	$R1$ = 0.0432, $wR2$ = 0.1048	$R1$ = 0.0398, $wR2$ = 0.0906	$R1$ = 0.0451, $wR2$ = 0.0991	$R1$ = 0.0517, $wR2$ = 0.1186	$R1$ = 0.1028, $wR2$ = 0.2781	$R1$ = 0.0396, $wR2$ = 0.0925
***R* indices (all data)**	$R1$ = 0.0750, $wR2$ = 0.0986	$R1$ = 0.0791, $wR2$ = 0.1149	$R1$ = 0.0801, $wR2$ = 0.1167	$R1$ = 0.0796, $wR2$ = 0.1061	$R1$ = 0.0878, $wR2$ = 0.1123	$R1$ = 0.1189, $wR2$ = 0.1378	$R1$ = 0.1733, $wR2$ = 0.3088	$R1$ = 0.0646, $wR2$ = 0.1044
Largest diff. peak and hole Å $^{-3}$	0.527 and -0.572	0.662 and -0.537	0.597 and -0.602	0.660 and -0.645	0.807 and -0.599	0.691 and -0.594	1.443 and -0.767	0.803 and -0.393

Table 3.2: Crystallographic data for datasets 9-16 of $[Zn_2(ox)(atz)_2]$

Table 3.3 shows the conditions the EGC was subjected to, and the temperature at which each dataset was collected. It also shows the final *R* factor for the fully refined structure, giving some indication of the crystal quality. In addition, the occupancy of the methanol and sulfur dioxide are included, where applicable, and the SQUEEZE electron count, in the number of electrons per unit cell is added to indicate the electron density change within the pores of the structure.

Dataset	Conditions	Temp. (K)	*R* (%)	Occupancy (%)	SQUEEZE Number of Electrons per Unit Cell
1		283	4.26	MeOH 100	197
2	Vacuum 3 hours	283	4.11	MeOH 85	173
3	Vacuum 9 hours	323	4.10	MeOH 68	145
4	Vacuum 11 hours	343	4.05	MeOH 50	112
5	Vacuum 16 hours	343	3.67	MeOH 40	89
6	Vacuum 22 hours	400	3.78	MeOH 0	67
7	CO_2 1 hour 655 Torr	283	4.05		80
8	CO_2 2 hours 717 Torr	283	4.01		90
9	CO_2 4 hours 677 Torr	283	4.04		108
10	CO_2 5 hours 660 Torr	283	4.33		122
11	CO_2 8 hours 862 Torr	283	4.32		144
12	Vacuum 2.5 hours	400	3.98		65
13	SO_2 1 hour 831 Torr	283	4.51		92
14	SO_2 4 hours 836 Torr	283	5.17		183
15	SO_2 10 hours 834 Torr	283	10.27	SO_2 42	308
16	Vacuum 4 hours	400	3.96		64

Table 3.3: The conditions applied to $[Zn_2(ox)(atz)_2]$ during desolvation, CO_2 and SO_2 adsorption

Figure 3.8 shows a graph of the change in electron count using SQUEEZE when compared to all the datasets collected. There are clear cut off points in the graph where the start of each change of environment occur. From datasets 1-6, the sample is under a dynamic vacuum, and as expected the number of electrons decreases gradually throughout this, to a minimum of 67 electrons. At this point, the occupancy of the methanol was 0 %, and the Fourier map showed no indication of the presence of any

residual electron density. Therefore this value of 67 electrons was used as the baseline value for a completely guest free structure.

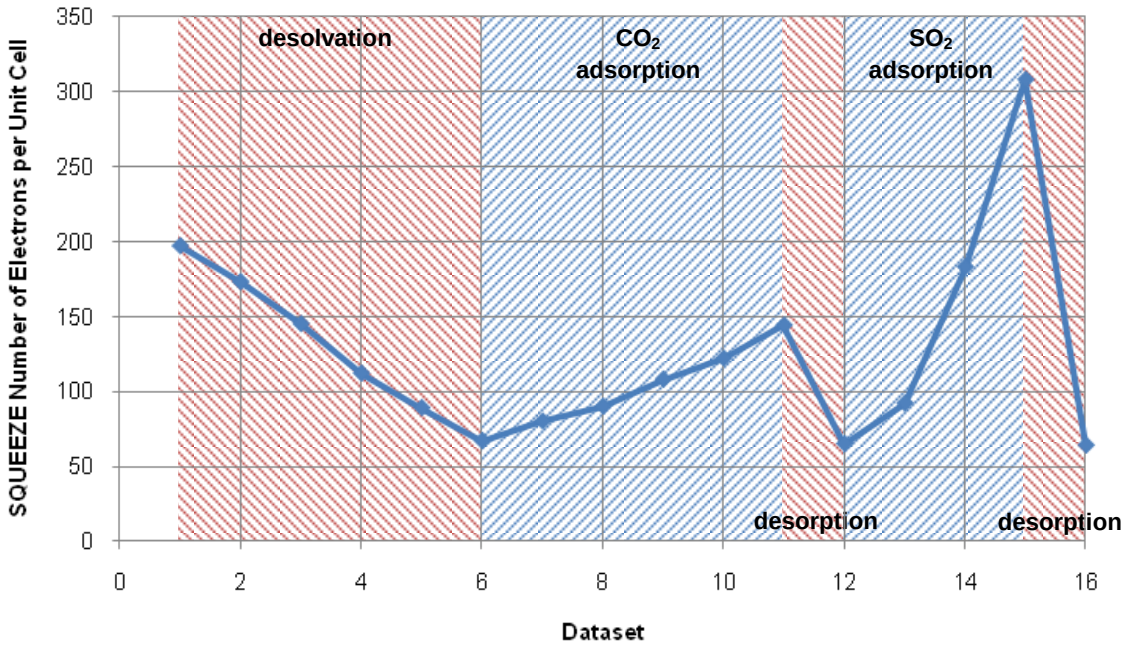

Figure 3.8: A graph of the change in electron count using SQUEEZE as the datasets for $[Zn_2(ox)(atz)_2]$ proceed through desolvation, CO_2 and SO_2 adsorption

Datasets 7-11 show the addition of CO_2 to the EGC, with a slow increase in the pressure of gas from 655 to 862 Torr. It is clear from the graph that the increase in the pressure of CO_2 within the cell causes the number of electrons within the unit cell to increase accordingly. This increase suggests the adsorption of CO_2 into the framework structure. Using PLATON SQEUEEZE to gain an estimation of the number of electrons present within the unit cell, the formula for dataset 11 can be estimated as $[Zn_2(ox)(atz)_2]\cdot 0.44CO_2$.

The pressure after dataset 11 could not be increased any further, due to the capabilities of the EGC, and a maximum electron count was reached at this point. Therefore, dataset 12 shows the results after the cell was placed under vacuum for two and a half hours at 400 K. It is evident from Figure 3.8 that after this experiment complete removal of the CO_2 had occurred, returning the electron count to 65; approximately the baseline value.

Sulfur dioxide was then loaded into the EGC, and datasets 13-15 show the results obtained from these runs. There is a dramatic increase in the number of electrons once SO_2 starts to be adsorbed. This is not surprising when compared to CO_2 due to the increase in the scattering power of sulfur over carbon. In datasets 13 and 14 SQUEEZE was used to determine the increase in the number of electrons, however, in 15 due to the presence of an increased amount of electron density it was possible to locate two sulfur atom sites (Figure 3.9). Due to the decrease in scattering power of the oxygen atoms however, these could not be located. The two sulfur atoms were refined freely giving the formula $[Zn_2(ox)(atz)_2]\cdot 0.42SO_2$.

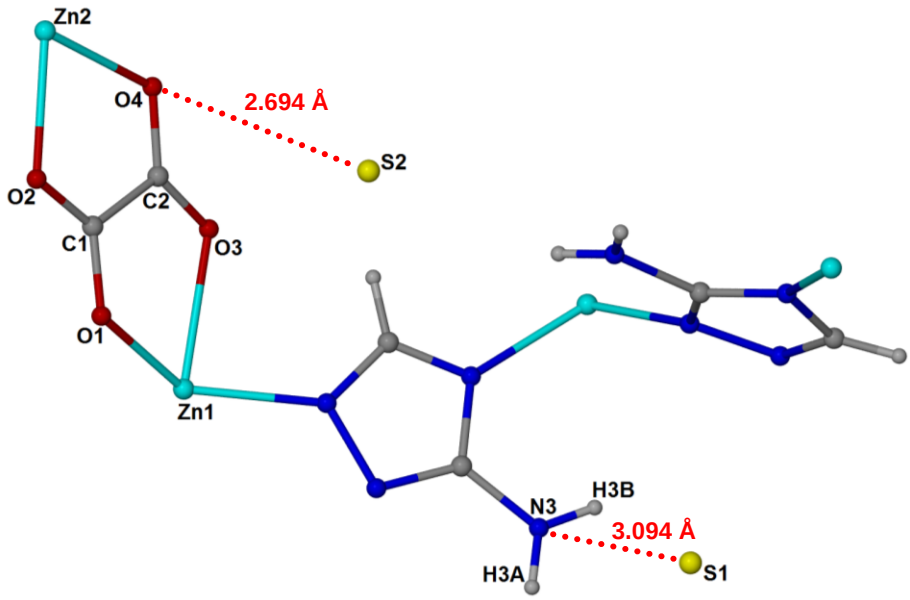

Figure 3.9: Crystal structure of $[Zn_2(ox)(atz)_2]\cdot 0.42SO_2$, indicating the sulfur positions within the pores. The bond distances between closest neighbours have been indicated in red

The two SO_2 binding sites within the framework are indicated in Figure 3.9. S1 is located near the amine group which is directed into the pore with approximately 32 % occupancy, and S2 is positioned near one of the oxalate groups with approximately 10 % occupancy. The higher occupancy of S1 is expected due to its proximity to the amine group.

With S1 positioned near the amine group, it is possible for there to be an interaction between the SO_2 and the amine functionality. It would be expected that if the oxygen atoms could be located on the SO_2, that these would hydrogen bond to the hydrogen atoms of the amine group. If the oxygen atom was located in the correct orientation for

a hydrogen bond to occur, then this atom separation would be of the appropriate length for this contact. The amine group is also involved in hydrogen bonding to adjacent oxygen atoms from the oxalate groups [N(3)···O(1) 2.858 Å, H(3A)···O(1) 2.218 Å, N(3)-H(3A)···O(1) 129° and N(3)···O(4) 3.012 Å, H(3B)···O(4) 2.260 Å, N(3)-H(3B)···O(4) 143°].

S2 is located between two oxalate groups, and the sulfur atom is in close proximity to the partially negative oxygen atoms of the oxalate [S(2)···O(4) 2.694 Å]. Due to this distance, it is possible that these two atoms could be involved in an interaction. The occupancy of this sulfur atom is lower than for S1, owing to the presence of a potentially weaker interaction, suggesting a preferential location near the amine group.

Figure 3.10 charts the change in the *b* axis length and volume of the unit cell when compared to all the datasets collected. Datasets 1-6 show the changes when the sample is placed under a vacuum at varying temperatures to remove the methanol solvent. As the methanol is removed, the unit cell volume and *b* axis decrease, which is expected, as the cell contracts on the removal of solvent. After desolvation, the crystal is placed under an environment of CO_2 (datasets 7-11). It would be expected that the cell would expand as the CO_2 was adsorbed into the pores, however the cell actually contracts. It is presumed that the adsorption of the CO_2 behaves in a similar fashion to the SO_2 described above, with a strong interaction between the amine group of the framework and the absorbed gas. This would cause the amine group and CO_2 to be drawn closer to each other, causing a contraction in the unit cell.

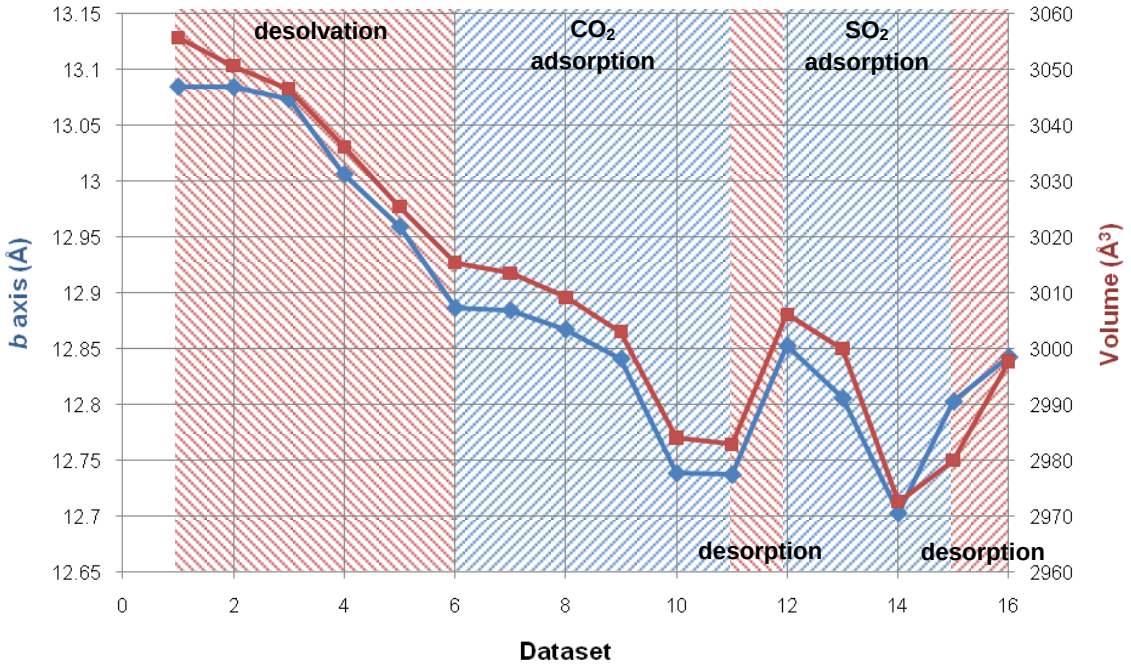

Figure 3.10: Change in the b axis cell length (blue) and volume (red) as the datasets for [Zn_2(ox)(atz)$_2$] proceed through desolvation, CO_2 and SO_2 adsorption

After CO_2 adsorption it is possible to completely remove this gas from the pores of the structure, by placing the sample under a vacuum. Dataset 12 shows how once the CO_2 is removed the unit cell *b* axis and volume return to similar values than before CO_2 was adsorbed. SO_2 is then adsorbed into the pores in a similar manner to the CO_2 loading (datasets 13-15). The cell begins to contract due to the presence of the interaction with the amine functionality. However, when a large amount of SO_2 is adsorbed into the pores (dataset 15), there is an increase in the cell size. It is important to note for this dataset that there was also a large decrease in the crystal quality, as is seen in the *R* factors (Table 3.3). Therefore, it is not possible to draw many conclusions from this result, as it may be due to the collection of poor data. Once the SO_2 gas is removed (dataset 16), the crystal quality is returned, and the *b* axis and cell volume produce values similar to those seen for the desolvated structure. This suggests a similar process may be occurring to Cu-SIP-3,[6] in which when the gas is applied to the cell and the gas begins to be adsorbed, there is a loss in the Bragg diffraction, owing to the poorer quality of the data collected.

After the experimental work using this network, *Science* published similar results with CO_2. This work had studied the temperature variations on gas uptake, and therefore due

to the lower temperatures studied, CO_2 was able to be crystallographically located within the pores.[18]

However, when the published results are compared to the results obtained here with sulfur dioxide there are many similarities that can be drawn. The highest proportion of CO_2 uptake was obtained at 173 K, giving the formula $[Zn_2(ox)(atz)_2]\cdot 1.3CO_2$. In a similar manner, two CO_2 sites were found, one with 80 % occupancy near the amine functionality, and one with 50 % occupancy located between two oxalate groups. This compares well with the locations of the sulfur atoms found in this study. It also agrees that the higher occupancy fragment was located near the amine functionality, due to stronger interactions (Figure 3.11).

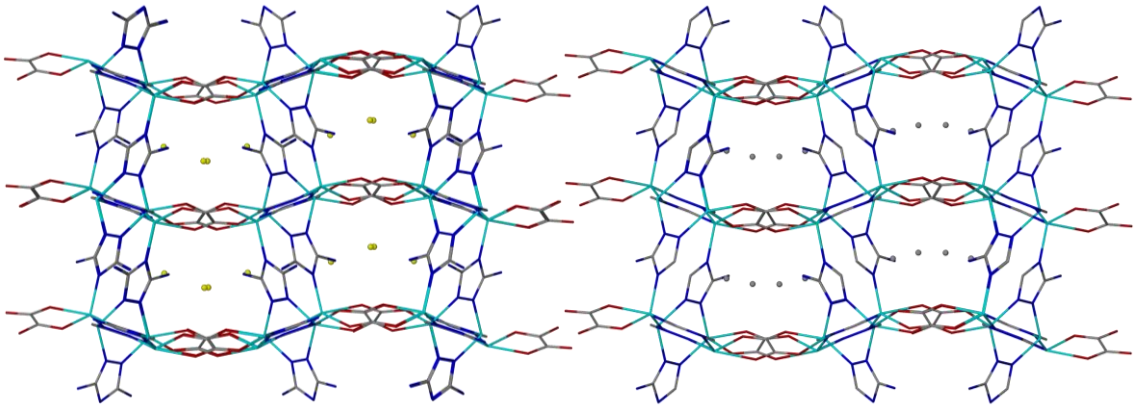

Figure 3.11: Crystal structure of $[Zn_2(ox)(atz)_2]\cdot 0.42SO_2$ (left) and the comparison with $[Zn_2(ox)(atz)_2]\cdot 1.3CO_2$[18] (right). Hydrogen atoms and carbon dioxide oxygen atoms have been omitted for clarity[18]

The unit cell for this published structure has the cell lengths 13.8034, 12.9639 and 16.8318 Å. If these are compared to dataset 15, which contained the most amount of adsorbed SO_2, then these relate well. The biggest difference is observed in the length of the *b* axis, but as was seen in Figure 3.10, this axis changed the most significantly during all the data collections. These differences in cell length may also be due to the amount of gas adsorbed. Although during initial gas adsorption there is a decrease in the *b* axis cell length, as more gas is adsorbed, the cell length begins to increase again, which may agree with the findings for $[Zn_2(ox)(atz)_2]\cdot 1.3CO_2$.

The CO_2 molecules in $[Zn_2(ox)(atz)_2]\cdot 1.3CO_2$ also adopt a T-shaped conformation, where one of the O atoms forms a contact with the C atom of an adjacent molecule

[3.014 Å]. The separation of the CO_2 C atoms in this structure is 4.120 Å. This can be compared to the S-S distance of the SO_2 molecules in $[Zn_2(ox)(atz)_2]\cdot 0.42SO_2$ which is approximately 4.423 Å. Although the oxygen could not be located in this structure, this distance between sulfur atoms indicates that a contact could be present between SO_2 molecules in a similar manner to the CO_2 molecules in $[Zn_2(ox)(atz)_2]\cdot 1.3CO_2$.

The data collections carried out in the gas cell were conducted at 283 K. At this temperature more movement occurs at atomic level, and so the gas loaded materials contain molecules which are highly disordered. If small amounts of gas are taken into the systems they are hard to locate due to this disorder. It would also be expected that less gas would be taken into the MOF at higher temperatures. If the temperature of the experiment was decreased, it would be likely that more gas would be adsorbed into the material, and that this gas would have less disorder, making it easier to locate the gas molecules.

The results obtained here for $[Zn_2(ox)(atz)_2]$ show that adsorption within MOFs can be obtained even at low pressures and 10 °C. The structure shows that a higher gas adsorption is observed perhaps due to the presence of the amine group within the network. This gives evidence to the preferential adsorption sites within MOFs, and will inform the construction of future materials.

Although a parallel study on $[Zn_2(ox)(atz)_2]$ with CO_2 has recently been published, the work carried out with SO_2 also confirms these results, and shows that this material could be a useful adsorption material. In addition, the presence of the amine functionality is not only useful for CO_2 adsorption, but also for SO_2.

There is also potential to extend the research carried out here, by reducing the temperature at which the data collections were carried out, to try and increase the percentage of SO_2 adsorbed into the material.

In this Chapter, the results presented demonstrate that it is possible to use the environmental gas cell to both desolvate samples, and also load them with a variety of gases. Findings also show that the choice of material to study is very important, as many are unstable after the removal of solvent.

The series of paddle wheel structures synthesised in Chapter 2, although promising due to the presence of larger pores, proved difficult to work with due to a loss in crystallinity when placed under vacuum.

$[Zn(bdc)(bipy)_{0.5}]\cdot DMF\cdot 0.5H_2O$ also initially looked promising, but the solvent removal also resulted in a loss of crystallinity. The work with this material and the range of paddle wheel structures shows how the choice of the framework to study within the EGC is very difficult. Although compounds may maintain crystallinity, they need to remain as single crystals in order to be studied in this way.

Due to the set up of the EGC it is not possible to conduct experiments above pressures of approximately 900 Torr or at temperatures lower than 0 °C. Many of the MOF materials in the literature are known to adsorb more gas at higher pressures and lower temperatures. Future work could involve the development of the gas cell to be used under increased pressures and lower temperatures. It is also possible to study mixtures of gases within the EGC, so it could be interesting to study selective adsorption in MOF materials. Hydrogen adsorption could also be studied in a similar manner, using neutron diffraction.

For the synthesis of new materials, these results have shown that the addition of an amine functionality increases the adsorption capacity within MOFs. It could be relatively straightforward to incorporate this into ligand design to construct new frameworks. They can also be synthesised with larger pores, as secondary adsorption sites within the pores are also possible, increasing the potential to take in more gas.[7]

3.5 Experimental

3.5.1 Crystallography

All starting materials for the synthesis of the MOFs were commercially available, and were used without further purification.

All X-ray data experiments within the EGC were collected on a Bruker Apex II diffractometer using synchrotron radiation (λ = 0.7749 Å) at Station 11.3.1 of the ALS Lawrence Berkeley National Laboratory. Unless noted, all non-hydrogen atoms were refined anisotropically in the final least squares run, and hydrogen atoms were included

at calculated positions. The structures were solved using SHELXS-97[19] and refined using full-matrix least squares in SHELXL-97.[19]

$[Zn_2(ox)(atz)_2]\cdot 2MeOH$ contained two disordered methanol molecules, one was disordered in a 25:75 ratio and the other 46:54. The solvent methanol molecules were refined isotropically due to the large displacement parameters. One of the atz rings was disordered over two sites in a 40:60 ratio, the larger component was refined anisotropically, and the smaller proportion isotropically. On the second atz ring within the asymmetric unit, the free amine group was disordered over two sites, in a 30:70 ratio. The smaller component was left to refine isotropically.

Once the desolvation was carried out within the EGC, the methanol solvent molecules were treated isotropically, and their free variables were set to refine freely, to give an indication of the reduction in electron density.

CO_2 and SO_2 were then introduced to the ECG. The final refinements of these datasets were refined against a guest free reflection file. In the final dataset containing SO_2, there were significant amounts of electron density in the Fourier map, and two sulfur sites were identified, one with 32 % and the other with 10 % occupancy. These atoms were refined isotropically.

3.5.2 Synthesis of Paddle Wheel Structures

The synthesis of these compounds is outlined in Chapter 2.

3.5.3 Synthesis of $[Zn(bdc)(bipy)_{0.5}]\cdot DMF\cdot 0.5H_2O$

$Zn(NO_3)_2\cdot 6H_2O$ (0.031 g, 0.12 mmol), H_2bdc (0.020 g, 0.12 mmol) and bipy (0.009 g, 0.06 mmol) were placed in a Teflon lined bomb, with a 1:1 mixture of DMF/ethanol (10 cm^3). The reaction mixture was placed in an oven at 90 °C for 24 hours, after which time, colourless crystals of the product had formed. These were left under solvent until the EGC experiments were carried out.

3.5.4 Synthesis of $[Zn_2(ox)(atz)_2]\cdot 2MeOH$

$ZnCO_3\cdot 2Zn(OH)_2$ (0.100 g, 0.31 mmol), H_2ox (0.100 g, 1.11 mmol) and atz (0.400 g, 4.8 mmol) were placed in a Teflon lined bomb, with methanol (3 cm^3) and water (0.5

cm^3). The reaction was carried out in an oven at 180 °C for 2 days. Colourless block crystals had formed after 2 days, and these were left under solvent until the EGC experiments were carried out.

3.5 References

1. B. Xiao, P. S. Wheatley, X. B. Zhao, A. J. Fletcher, S. Fox, A. G. Rossi, I. L. Megson, S. Bordiga, L. Regli, K. M. Thomas and R. E. Morris, *J. Am. Chem. Soc.*, 2007, **129**, 1203.
2. C. Serre, C. Mellot-Draznieks, S. Surble, N. Audebrand, Y. Filinchuk and G. Férey, *Science*, 2007, **315**, 1828.
3. T. Loiseau, C. Serre, C. Huguenard, G. Fink, F. Taulelle, M. Henry, T. Bataille and G. Férey, *Chem. Eur. J.*, 2004, **10**, 1373.
4. N. L. Rosi, J. Eckert, M. Eddaoudi, D. T. Vodak, J. Kim, M. O'Keeffe and O. M. Yaghi, *Science*, 2003, **300**, 1127.
5. B. Xiao, P. J. Byrne, P. S. Wheatley, D. S. Wragg, X. B. Zhao, A. J. Fletcher, K. M. Thomas, L. Peters, J. S. O. Evans, J. E. Warren, W. Z. Zhou and R. E. Morris, *Nat. Chem.*, 2009, **1**, 289.
6. P. K. Allan, B. Xiao, S. J. Teat, J. W. Knight and R. E. Morris, *J. Am. Chem. Soc.*, 2010, **132**, 3605.
7. J. L. C. Rowsell, E. C. Spencer, J. Eckert, J. A. K. Howard and O. M. Yaghi, *Science*, 2005, **309**, 1350.
8. J. B. Lin, W. Xue, J. P. Zhang and X. M. Chen, *Chem. Commun.*, 2011, **47**, 926.
9. P. D. C. Dietzel, B. Panella, M. Hirscher, R. Blom and H. Fjellvag, *Chem. Commun.*, 2006, 959.
10. P. D. C. Dietzel, R. E. Johnsen, H. Fjellvag, S. Bordiga, E. Groppo, S. Chavan and R. Blom, *Chem. Commun.*, 2008, 5125.
11. J. E. Warren, R. G. Pritchard, D. Abram, H. M. Davies, T. L. Savarese, R. J. Cash, P. R. Raithby, R. Morris, R. H. Jones and S. J. Teat, *J. Appl. Crystallogr.*, 2009, **42**, 457.
12. A. L. Spek, *Acta Crystallogr. Sect. D-Biol. Crystallogr.*, 2009, **65**, 148.
13. A. L. Spek, *J. Appl. Crystallogr.*, 2003, **36**, 7.
14. S. Takamizawa, E. Nakata and H. Yokoyama, *Inorg. Chem. Commun.*, 2003, **6**, 763.

15. H. Chun, D. N. Dybtsev, H. Kim and K. Kim, *Chem. Eur. J.*, 2005, **11**, 3521.
16. R. Vaidhyanathan, S. S. Iremonger, K. W. Dawson and G. K. H. Shimizu, *Chem. Commun.*, 2009, 5230.
17. B. L. Chen, C. D. Liang, J. Yang, D. S. Contreras, Y. L. Clancy, E. B. Lobkovsky, O. M. Yaghi and S. Dai, *Angew. Chem. Int. Ed.*, 2006, **45**, 1390.
18. R. Vaidhyanathan, S. S. Iremonger, G. K. H. Shimizu, P. G. Boyd, S. Alavi and T. K. Woo, *Science*, 2010, **330**, 650.
19. G. M. Sheldrick, *Acta Crystallogr. Sect. A*, 2008, **64**, 112.

Chapter 4 – Metal-Organic Frameworks with a Semi-Rigid Isoxazole Containing Ligand

4.1 Introduction

The majority of frameworks synthesised to date use rigid ligands to generate frameworks. However, introducing a degree of flexibility into the framework can allow the network to reversibly respond to the presence or absence of a guest.[1-4] If the ligand is highly flexible, then it is likely that a non-porous framework would be obtained, due to the packing of the ligand. However, use of a semi-rigid ligand, with a limited degree of flexibility can afford porous networks.

Jung et al. incorporated this strategy into their synthesis of a variety of networks constructed from 2,4'-thiobis(pyridine) (2,4'-Py_2S) (Figure 4.1) and a range of silver(I) salts. 2,4'-Py_2S possesses interesting N-S-N angles, which can respond to the nature of the anions present. It also contains three possible coordination sites with a degree of conformational non-rigidity. The reaction of this ligand with a range of silver(I) salts produced six new and different network structures, due to this flexibility. One of these compounds was $[Ag_3(2,4'\text{-}Py_2S)_4](ClO_4)_3$. The structure is constructed from linear or trigonal silver(I) centres coordinating to either two or three 2,4'-Py_2S ligands respectively. The structure forms two dimensional sheets, where the ClO_4^- counter ions are housed within small channels (Figure 4.1). It was also reported that the ClO_4^- counter ion contained within this structure was able to be exchanged with the PF_6^- anion.[5]

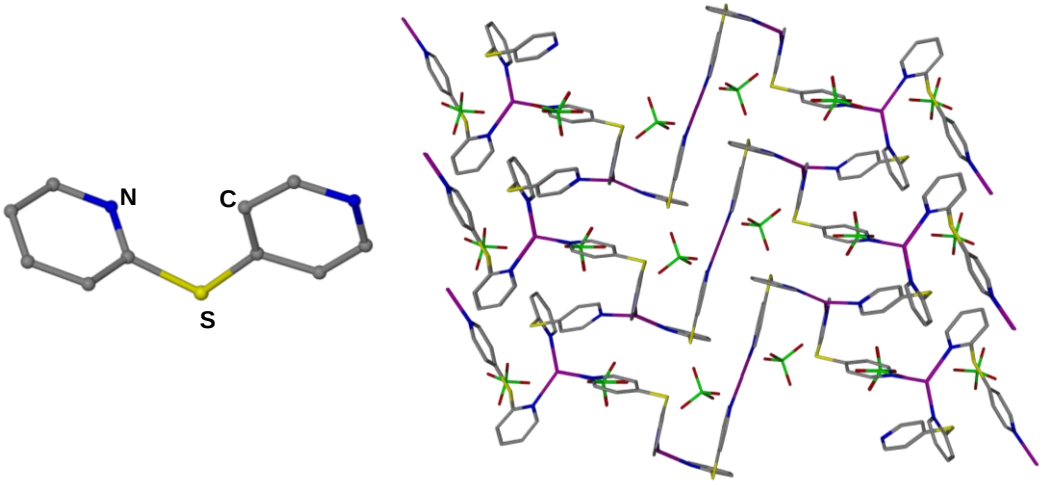

Figure 4.1: 2,4'-thiobis(pyridine) (2,4'-Py_2S) (left) and the structure of $[Ag_3(2,4'\text{-}Py_2S)_4](ClO_4)_3$ (right). Hydrogen atoms have been omitted for clarity[5]

As was demonstrated in the previous example, the silver(I) metal also plays a vital role in structure formation. There are many examples in the literature where networks are formed through the connection of ditopic nitrogen donor ligands and silver(I).[6] As this metal ion is coordinatively flexible, and has been shown to adopt coordination numbers between two and six, with various geometries possible including linear, trigonal, tetrahedral, trigonal pyramidal and octahedral. There are also a wide variety of silver salts available, making it straightforward to assess the effect of the counter ions on the frameworks formed. Moreover, due to the flexibility of the metal, the effect of the counter ion, solvent and the ligand to metal ratio are ideal to study with silver, as even small changes in these may have an impact on the gross structure.[7, 8]

The nature of the coordinating groups in the build up of a network structure also affect the gross structure that will be observed, with the number of coordinating sites, flexibility of the ligand and the stereochemical preferences of the coordinating metal centre, all playing a role. Non covalent interactions also play a vital function. The inclusion of solvent molecules and anions can change the topology of the network due to interactions that are occurring between them and the framework. These can include strong or weak hydrogen bonds and π-π stacking. There may also be weak $d^{10}\cdots d^{10}$ interactions present between silver centres which can also have a structurally defining effect.

In this chapter, the study of a range of networks formed from the reactions of silver(I) salts and the semi-rigid bis(isoxazolyl) ligand 1,4-bis((3,5-dimethylisoxazol-4-yl)methyl)benzene (bisox) will be investigated (Figure 4.2). The results from these studies can then be used to gain a better understanding into the effects of the anion on framework formation.

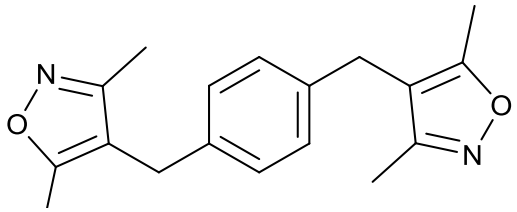

Figure 4.2: 1,4-Bis-(3,5-dimethyl-isoxazol-4-yl-methyl)benzene (bisox)

The bisox ligand was chosen for several reasons. Firstly, it is reasonably flexible due to the presence of the methylene spacers between the isoxazole rings and the central

benzene ring, allowing it to adopt several conformations. This means the networks that form have the potential to vary structurally. Of these, molecular mechanics suggests the lowest energy conformation is of C_i symmetry, with the nitrogen donor atoms oriented away from each other. For ease of visualization, this is denoted as the S- conformation. A rotation of 180° about one of the benzene-methylene C–C bonds generates a conformation of C_h symmetry, which is denoted as the C- conformation. The S- and C- conformations are shown in Figure 4.3. While other conformations are also possible by rotation about the C(sp^3)–C(sp^2) bonds, the presence of the central benzene ring and two isoxazole rings within the ligand limit its flexibility.

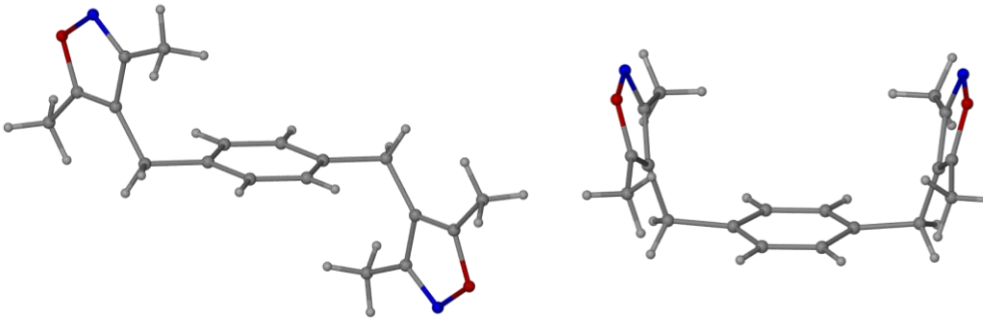

Figure 4.3: The S- and C- conformations of bisox

The isoxazole portion of the ligand also contains two possible coordination sites, the nitrogen and oxygen atoms. This gives another opportunity of varying the networks formed. However, since silver(I) centres are soft, they would be expected to preferentially coordinate to a softer donor, which would favour nitrogen over oxygen.

Finally, isoxazole containing ligands have never previously been studied in the synthesis of metal-organic frameworks. There have been a few examples that have adopted the use of substituted isoxazole ligands. Silver(I) coordination polymers have been prepared using isoxazolyl ligands containing either amido or sulfide groups,[9, 10] and a copper(II) network has been formed from isoxazole-4-carboxylate.[11]

Imidazolyl ligands with a similar geometry to bisox have also been studied previously. *Robson et al*. synthesised polyrotaxanes from the use of 4-bis(imidazol-1-yl-methyl)benzene (bismim) reacted with $AgNO_3$, where the silver centres exist with approximate trigonal planar geometry. This structure reveals similar flexibility to that seen for bisox, demonstrating both the C- and S- conformations (Figure 4.4).[12]

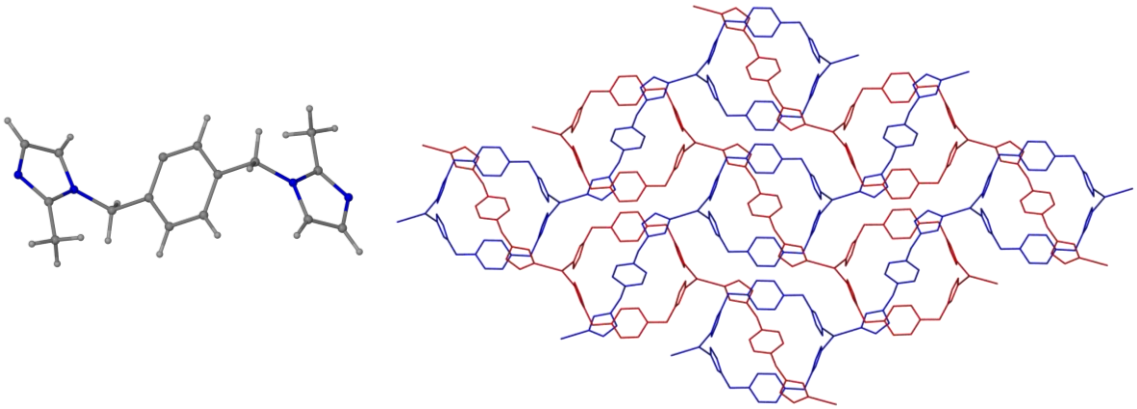

Figure 4.4: 1,4-bis(imidazol-1-yl-methyl)benzene (bismim) ligand (left). Polyrotaxane of $[Ag_2(bismim)_3](NO_3)_2$ (right). Hydrogen atoms and counter ions have been omitted for clarity[12]

Another example using the bismim ligand to form coordination polymers was demonstrated by *Barbour et al.* in the formation of $[Ag_2(bismim)_3](BF_4)_2$. This structure consists of silver(I) centres with approximate trigonal planar geometry coordinated to three bismim ligands. The ligand presents in just the S-conformation and by coordinating to adjacent silver centres forms large hexagonal rings in the array. Six silver atoms form the vertices and the six ligands form the edges of each ring, and adjacent rings pack to form a two dimensional honeycomb lattice. In this structure, interpenetration is observed, where three of the honeycomb layers are entangled to form a Borromean weave (Figure 4.5). The three rings form a Brunnian link, in which if one of these rings is removed through the breaking of coordination bonds, then the two other rings will no longer be entwined. In order for the weave to form, the six membered rings cannot be planar, but instead take on a chair conformation, which is satisfied by the flexibility of the ligand. The puckering of these layers causes two silver(I) atoms from two separate rings to lie close enough together to be involved in argentophilic interactions, which stabilises the formation of this network.[13]

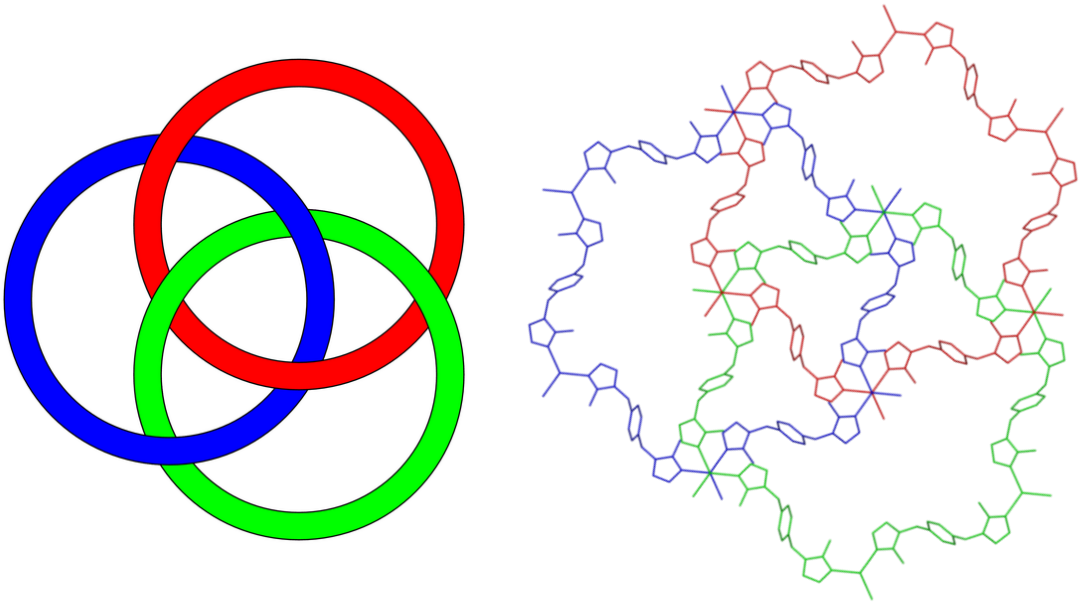

Figure 4.5: Borromean rings (left) and Borromean structure of $[Ag_2(bismim)_3](BF_4)_2$ (right). Hydrogen atoms and counter ions have been omitted for clarity[13]

One final example is the formation of a macrocycle $[Ag_2(bismim)_2](BF_4)_2 \cdot 2CH_3CN$ from the reaction of bismim with $AgBF_4$ (Figure 4.6). In this structure the ligand exists in only the C-conformation, where two of these ligands bridge to two silver atoms with linear geometry. These macrocycles align to form one dimensional channels within the structure which are filled with acetonitrile molecules, which can be removed to produce a porous material. The BF_4^- counter ions are then situated between each macrocycle.[14]

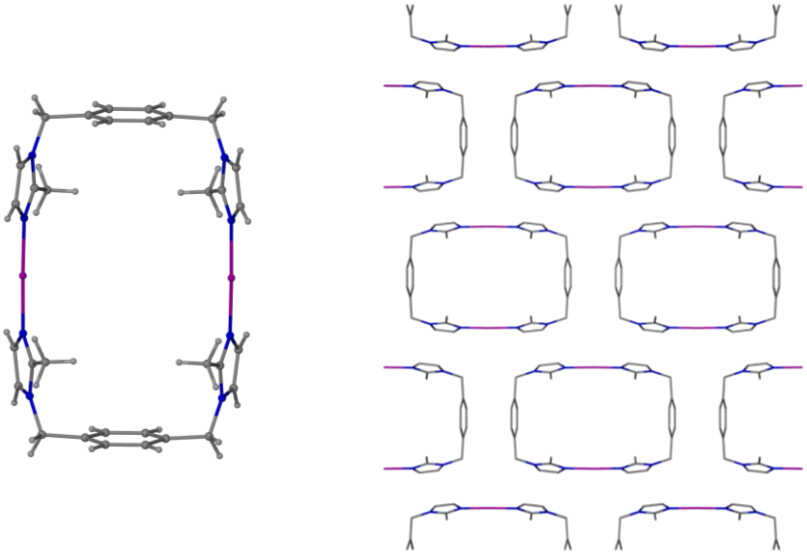

Figure 4.6: The macrocycle of $[Ag_2(bismim)_2](BF_4)_2 \cdot 2CH_3CN$ (left) and its packing (right). Hydrogen atoms, solvent molecules and counter ions have been omitted for clarity[14]

All three of these examples are constructed from the same ligand and metal, but due to the flexibility of the ligand a variety of structures are formed. Under the same metal to ligand ratio, the first two examples are obtained, in which the counter ion has been altered. This shows the effect the counter ion has on the frameworks formed. These two structures also demonstrate the differences seen when the ligand exists with different conformations. The final example exhibits a macrocyclic compound in which a different ratio has been used, again affording a different structure. These results show how the flexibility of the ligand, as well as the metal to ligand ratio and the counter ion of the silver(I) salts can affect structure formation.

This chapter investigates the use of the bisox ligand with a range of silver(I) salts to test the effect of the counter ions on the product formed. During the reactions, the same metal to ligand ratio and solvent conditions were used, so only the effect of the counter ion was investigated. From the results obtained it was hoped that a better understanding behind the processes involved in structure formation could be gained.

4.2 Results

4.2.1 $[Ag_2(NO_3)_2(bisox)]$, 1

Silver(I) nitrate was reacted with bisox in methanol, though from this batch crystals were too small for structure analysis. The sample was recrystallised from acetonitrile-diethyl ether and suitable colourless block crystals were produced. A crystal of approximate dimensions 0.30 x 0.12 x 0.12 mm was selected for X-ray structure determination. The crystal data for this compound is given in Table 4.1.

Empirical formula	$C_{18}H_{20}Ag_2N_4O_8$
M	636.12
***T*/ K**	150(2)
Crystal system	Orthorhombic
Space group, *Z*	*Pcab*, 4
***a*/ Å**	7.3890(1)
***b*/ Å**	15.9620(3)
***c*/ Å**	17.7590(4)
***α*/ º**	90
***β*/ º**	90

γ °	90
***U*/ Å ^{3}**	2094.55(7)
Absorption coefficient/ mm^{-1}	1.925
***F*(000)**	1256
Theta range for data collection/ °	3.76 to 27.42
Reflections collected/ observed [$I>2\sigma(I)$]	39756/ 1687
Data Completeness	0.996
Goodness-of-fit on F^2	1.042
Final *R* indices [$I>2\sigma(I)$]	$R1$ = 0.0359, $wR2$ = 0.0868
***R* indices (all data)**	$R1$ = 0.0642, $wR2$ = 0.1014
Largest diff. peak and hole Å $^{-3}$	0.866 and -1.186

*Table 4.1: Crystallographic data for $[Ag_2(NO_3)_2(bisox)]$ (**1**)*

The asymmetric unit of **1** consists of one full occupancy silver atom, half a ligand and one nitrate counter ion coordinated to the silver (Figure 4.7). The remainder of the bisox ligand is generated through a crystallographic inversion centre.

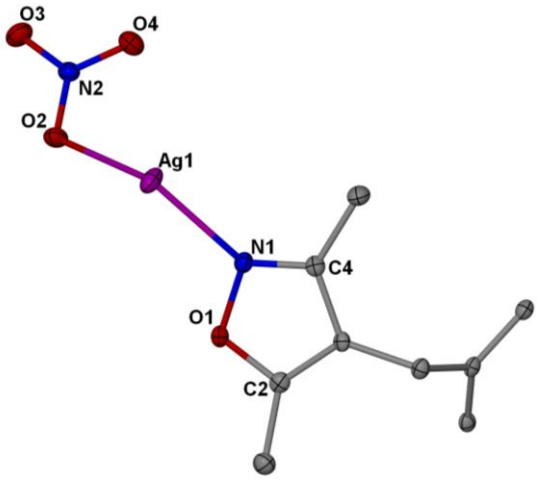

*Figure 4.7: The asymmetric unit of compound **1** showing thermal ellipsoids at the 30% probability level. Hydrogen atoms have been omitted for clarity*

In this structure, the silver(I) centre adopts a distorted trigonal planar geometry, coordinated to two oxygen atoms from different nitrate ions and one nitrogen atom from the bisox ligand. The nitrate ions bridge between silver(I) centres building up a Ag-NO_3 zigzag chain. These chains are crosslinked by the bridging bisox ligands in the S-conformation, forming two dimensional sheets (Figure 4.8). The crosslinking of the bisox ligands forms 'hourglass' shaped rings within these sheets.

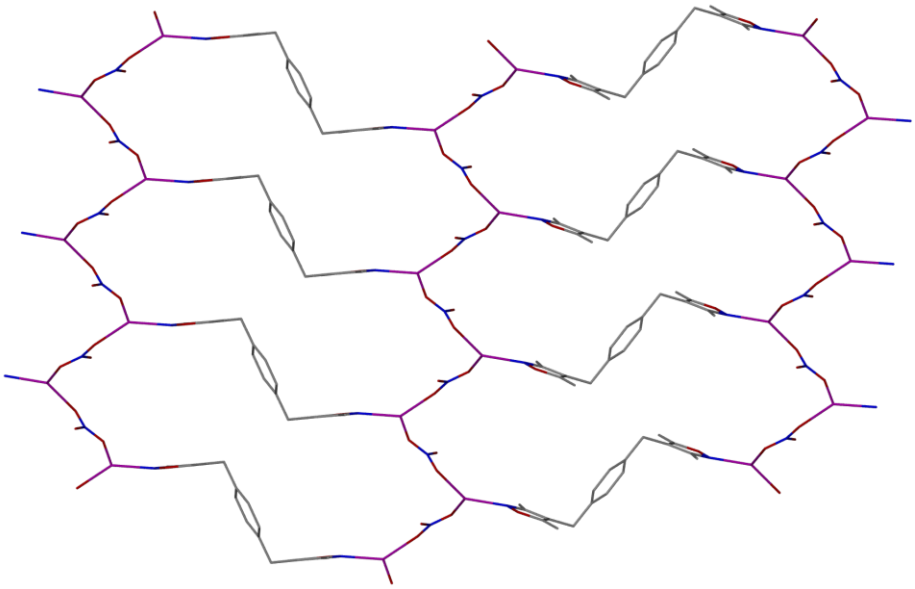

*Figure 4.8: Two dimensional sheet structure of **1**. Hydrogen atoms have been omitted for clarity*

Within the structure there are two sets of these parallel two dimensional sheets present, which lie with an angle of 57° between the planes of each set. Two of the bisox ligands from one sheet are then directed through the 'hourglass' rings, showing an example of two dimensional inclined interpenetration (Figure 4.9). The isoxazole rings of the interpenetrating ligands lie parallel to the isoxazole rings of the 'hourglass' ring at a distance of approximately 3.72 Å, suggesting the presence of weak π···π interactions (Figure 4.10).

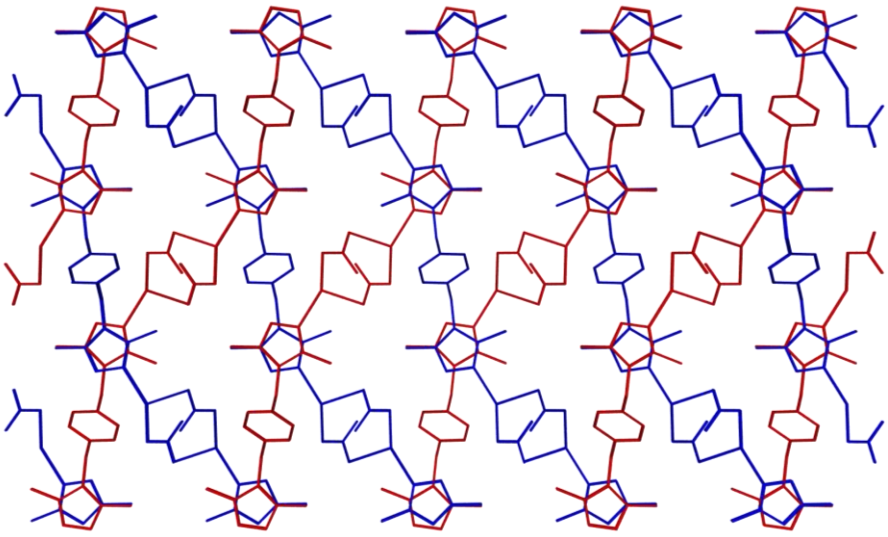

*Figure 4.9: The two dimensional inclined interpenetrated sheets of **1**. Hydrogen atoms and counter ions have been omitted for clarity*

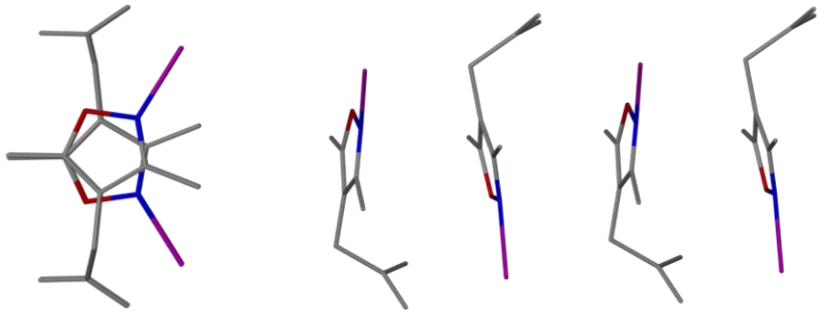

Figure 4.10: The π···π stacking of the isoxazole rings in ***1****. Hydrogen atoms and counter ions have been omitted for clarity*

4.2.2 $[Ag(O_2CCF_3)(bisox)]\cdot 0.5MeOH$, 2 and $[Ag_2(O_2CCF_3)_2(bisox)_2]\cdot CH_3CN$, 3

Silver(I) trifluoroacetate was reacted with bisox in methanol, and from this batch a colourless block crystal of approximate dimensions 0.15 x 0.15 x 0.10 mm was selected for X-ray structure analysis (**2**). This sample was then recrystallised from acetonitrile-diethyl ether and suitable colourless block crystals were produced. A crystal of similar dimensions to **2** was then selected for X-ray structure determination (**3**). The experimental details for these crystals are given in Table 4.2.

Compound	**2**	**3**
Empirical formula	$C_{20.50}H_{22}AgF_3N_2O_{4.50}$	$C_{42}H_{43}Ag_2F_6N_5O_8$
M	533.27	1075.55
***T*/ K**	150(2)	150(2)
Crystal system	Triclinic	Triclinic
Space group, *Z*	*P*-1, 2	*P*-1, 2
***a*/ Å**	10.3470(2)	10.7180(2)
***b*/ Å**	10.8430(2)	11.2600(2)
***c*/ Å**	11.2920(2)	20.7660(5)
***α*/ º**	64.703(1)	75.779(1)
***β*/ º**	70.872(1)	81.104(1)
***γ*/ º**	82.471(1)	64.377(1)
***U*/ Å ^{3}**	1082.09(3)	2187.07(8)
Absorption coefficient/ mm^{-1}	0.989	0.978
***F*(000)**	538	1084
Theta range for data collection/ º	3.72 to 30.03	3.56 to 25.02
Reflections collected/ observed [*I*>2σ(*I*)]	22067/ 5570	28707/ 5709

Data Completeness	0.995	0.984
Goodness-of-fit on F^2	1.060	1.029
Final *R* indices [$I>2\sigma(I)$]	$R1$ = 0.0485, $wR2$ = 0.1344	$R1$ = 0.0416, $wR2$ = 0.0899
***R* indices (all data)**	$R1$ = 0.0564, $wR2$ = 0.1409	$R1$ = 0.0650, $wR2$ = 0.0972
Largest diff. peak and hole Å^{-3}	2.479 and -1.545	1.101 and -0.747

*Table 4.2: Crystallographic data for $[Ag(O_2CCF_3)(bisox)]\cdot 0.5MeOH$ (**2**) and $[Ag_2(O_2CCF_3)_2(bisox)_2]\cdot CH_3CN$ (**3**)*

The asymmetric unit for compound **2** consists of one silver centre, one coordinated trifluoroacetate anion, two crystallographically independent ligand halves and half a molecule of methanol. The fluorine atoms in the trifluoroacetate anion were disordered over three sites, and were therefore refined isotropically (Figure 4.11).

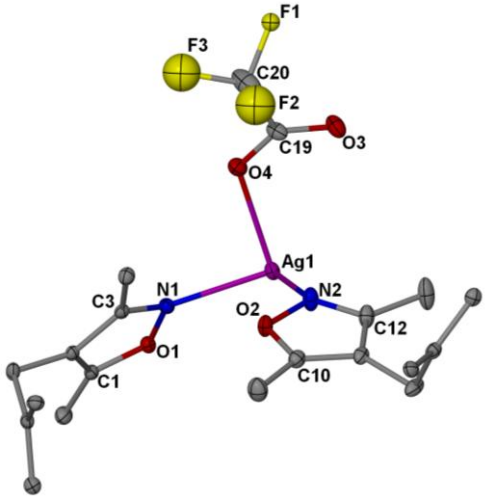

*Figure 4.11: The asymmetric unit of compound **2** showing thermal ellipsoids at the 30% probability level. Hydrogen atoms, solvent molecules and disordered fluorine atoms have been omitted for clarity*

The silver centre is situated near a crystallographic inversion centre leading to the formation of $Ag_2(\mu\text{-}O_2CCF_3)_2$ dimers, with a Ag···Ag distance of 3.0640(5) Å. Each silver centre is four coordinate with approximate tetrahedral geometry, coordinating to two bisox ligands and the two carboxylate oxygen atoms from the trifluoroacetate anion. However, when the dimer is considered as a unit, it can be regarded as having distorted square planar geometry (Figure 4.12).

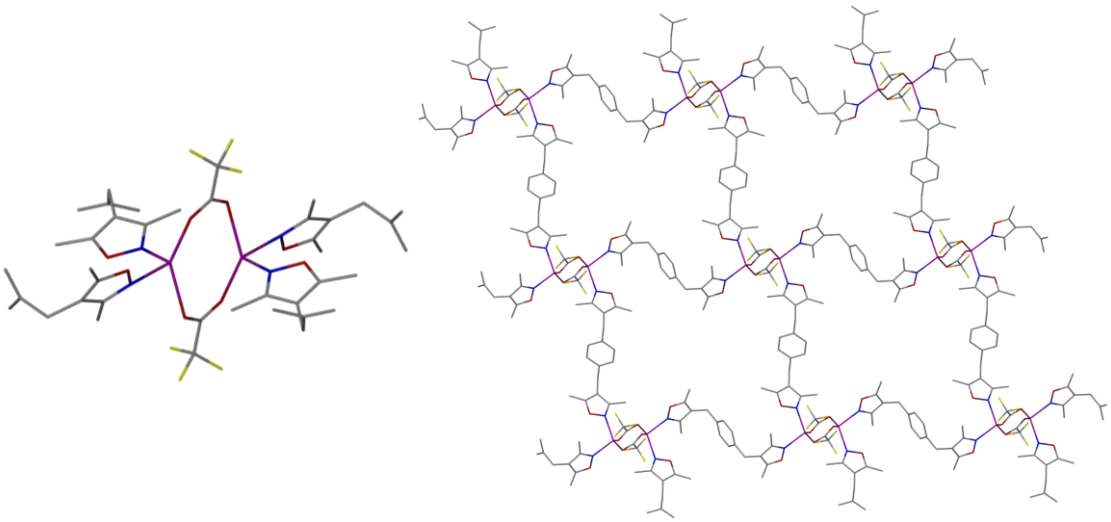

*Figure 4.12: The $Ag_2(\mu\text{-}O_2CCF_3)_2$ dimer (left) and the two dimensional square grid of **2** (right). Hydrogen atoms, solvent molecules and disordered fluorine atoms have been omitted for clarity*

By virtue of an inversion centre, the half bisox ligands extend in to full S-shaped ligands coordinating to adjacent silver dimers. This extends the structure into a two dimensional square grid, where the cavity is not regular in shape due to the flexibility of the bisox ligand (Figure 4.12). The two dimensional sheets pack so the trifluoroacetate of the sheet above fit into the cavity of the sheet below, reducing its size (Figure 4.13). The guest methanol molecule is situated in the remaining space, and is involved O-H···F hydrogen bonding with the fluorine atoms of the trifluoroacetate groups [O(5)···F(1B) 2.343 Å].

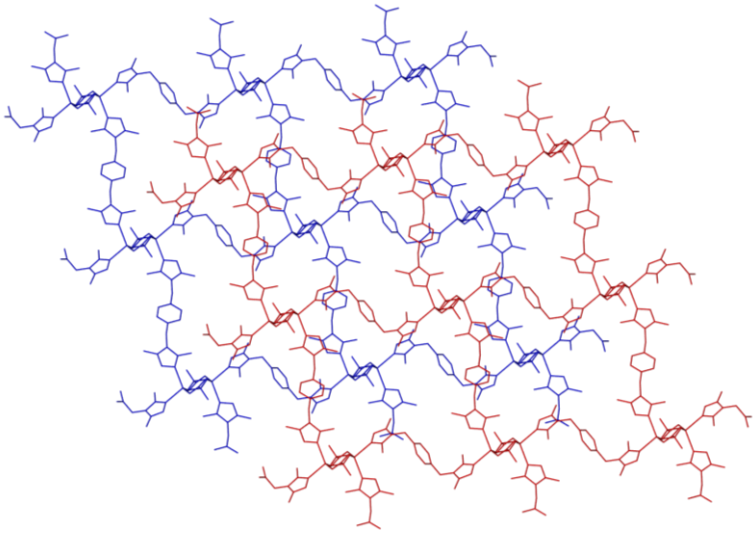

*Figure 4.13: The packing observed in **2** showing the overlap of the two dimensional sheets. Hydrogen atoms, solvent molecules and disordered fluorine atoms have been omitted for clarity*

The asymmetric unit for **3** consists of two silver centres, two coordinated trifluoroacetate anions and four crystallographically independent ligand halves. The fluorine atoms in the trifluoroacetate anion were each disordered over two sites. There was also some highly disordered solvent which was approximated to one molecule of acetonitrile per asymmetric unit using PLATON SQUEEZE. This is double the asymmetric unit of **2** (Figure 4.14).

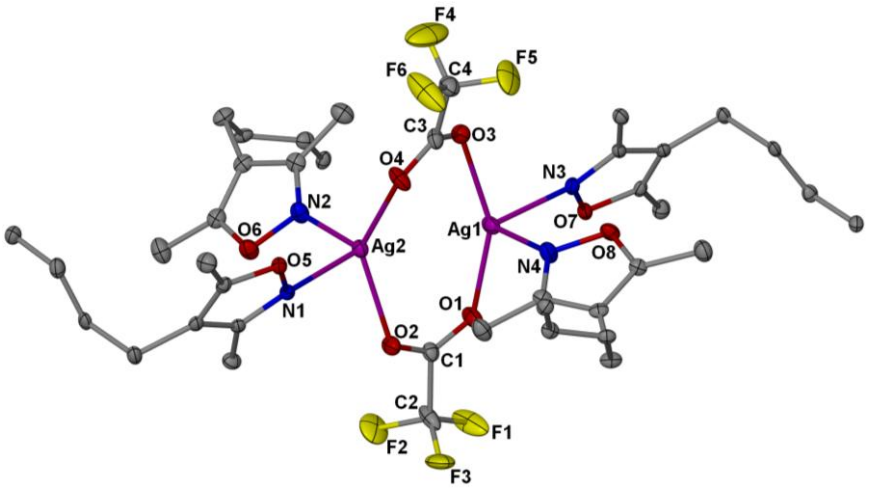

*Figure 4.14: The asymmetric unit of compound **3** showing thermal ellipsoids at the 30% probability level. Hydrogen atoms, solvent molecules and disordered fluorine atoms have been omitted for clarity*

As with compound **2** similar $Ag_2(\mu\text{-}O_2CCF_3)_2$ dimers are formed, with a Ag···Ag separation of 3.0777(4) Å, which is slightly longer than that observed for **2**. In a similar manner, the dimer can be considered with overall square planar geometry. Through an inversion centre, the bisox ligands extend to adjacent silver dimers, forming a two dimensional square grid, which is constructed in the same manner to that in **2**.

Selected bond lengths for **2** and **3** are given in Table 4.3. Both structures have subtle differences between comparative bond lengths and hence slightly different structures, however the gross structures are the same. The differences observed between these structures can be attributed to the alteration of the solvents present within the lattice. An overlay demonstrtaing the subtle changes of these two structures is shown in Figure 4.15.

Compound 2		Compound 3	
Bond Atoms	**Distance/ Å**	**Bond Atoms**	**Distance/ Å**
Ag(1)-O(3)[i]	2.303(3)	Ag(1)-O(1)	2.273(3)
Ag(1)-O(4)	2.377(3)	Ag(2)-O(2)	2.352(3)
		Ag(1)-O(3)	2.318(3)
		Ag(2)-O(4)	2.298(3)
Ag(1)-N(1)	2.335(3)	Ag(2)-N(1)	2.378(3)
Ag(1)-N(2)	2.337(3)	Ag(2)-N(2)	2.304(4)
		Ag(1)-N(3)	2.338(3)
		Ag(1)-N(4)	2.511(4)

*Table 4.3: Selected bond lengths for compounds **2** and **3**[i]*

*Figure 4.15: Overlay of structures **2** (red) and **3** (blue). Hydrogen atoms, solvent molecules and disordered fluorine atoms have been omitted for clarity*

4.2.3 $[Ag_2(bisox)_3](ClO_4)_2$, 4 and $[Ag_2(bisox)_3](BF_4)_2$, 6

Colourless block crystals were produced from the reaction of bisox and silver(I) perchlorate in methanol. From this batch a crystal with dimensions of 0.20 x 0.16 x 0.16 mm was selected for X-ray structure determination. The crystal data for compound **4** is shown in Table 4.4.

[i] Symmetry transformations used to generate equivalent atoms:
-x +1, -y +2, -z +1

In a similar reaction **6** was produced from the reaction of bisox and silver(I) tetrafluoroborate. The product formed was microcrystalline and therefore the structure could not be determined from single crystal X-ray diffraction. However, the X-ray powder diffraction pattern exhibited an almost identical pattern to that of **4**, and was hence deduced to be $[Ag_2(bisox)_3](BF_4)_2$, **6**.

Empirical formula	$C_{18}H_{20}Ag_{0.67}Cl_{0.67}N_2O_{4.67}$
M	434.58
***T*/ K**	150(2)
Crystal system	Hexagonal
Space group, *Z*	*P*-3, 3
***a*/ Å**	14.8380(3)
***b*/ Å**	14.8380(3)
***c*/ Å**	7.3050(1)
***α*/ º**	90
***β*/ º**	90
***γ*/ º**	120
***U*/ Å ^{3}**	1392.84(4)
Absorption coefficient/ mm^{-1}	0.869
***F*(000)**	666
Theta range for data collection/ º	3.91 to 27.44
Reflections collected/ observed [*I*>2σ(*I*)]	20782/ 1611
Data Completeness	0.997
Goodness-of-fit on F^2	1.052
Final *R* indices [*I*>2σ(*I*)]	*R*1 = 0.0362, *wR*2 = 0.0808
***R* indices (all data)**	*R*1 = 0.0593, *wR*2 = 0.0880
Largest diff. peak and hole Å $^{-3}$	0.921 and -0.564

*Table 4.4: Crystallographic data for $[Ag_2(bisox)_3](ClO_4)_2$ (**4**)*

The asymmetric unit for **4** consists of one silver centre located on a 3-fold rotation axis, one half portion of ligand, one perchlorate anion fragment, where the chlorine atom and one oxygen atom are also located on the 3-fold rotation axis (Figure 4.16).

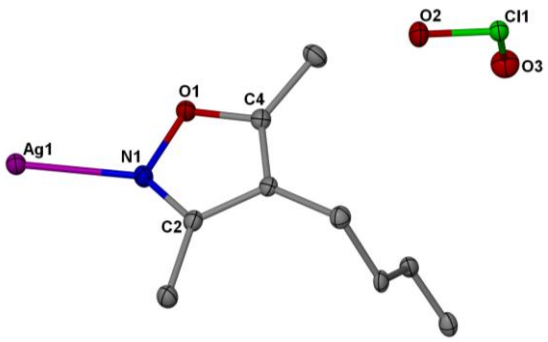

*Figure 4.16: The asymmetric unit of compound **4** showing thermal ellipsoids at the 30% probability level. Hydrogen atoms have been omitted for clarity*

Each silver(I) centre has trigonal planar geometry, coordinating to three bisox ligands. Via inversion centres, the ligand portions expand into S-conformations and link to adjacent silver centres. These bonds ultimately form two dimensional sheets with hexagonal pores, where six silver atoms form the vertices and six bisox ligands form the edges of each ring (Figure 4.17). The diameter of these pores is approximately 16.8 Å, and due to this large size, interpenetration occurs to reduce the free space. The structure is triply interpenetrated, in which Borromean rings are formed interlocking three rings (Figure 4.18). Due to the interpenetration, triangular pores are created where the perchlorate anions reside. These are involved in C-H···O hydrogen bonds with the methyl and aromatic CH groups [C(5)···O(2) 3.524 Å, H(5A)···O(2) 2.654 Å, C(5)-H(5A)···O(2) 148°, C(9)···O(2) 3.641 Å, H(9)···O(2) 2.641 Å, C(9)-H(9)···O(2) 143°].

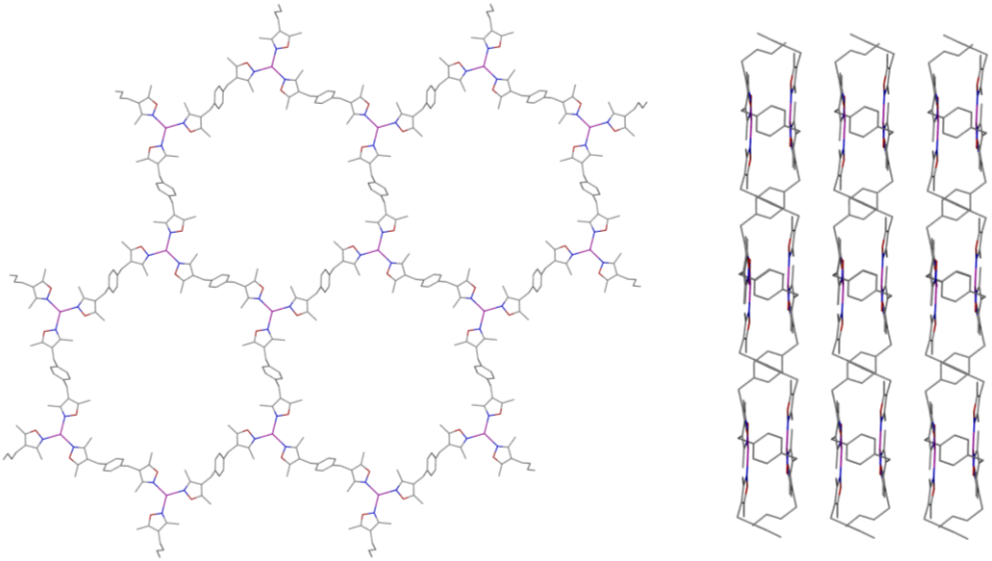

*Figure 4.17: The structure of **4** showing one of the $Ag_2(bisox)_3$ layers (left) and the layers viewed along the edge showing the S-conformation of the ligands. Hydrogen atoms and counter ions have been omitted for clarity*

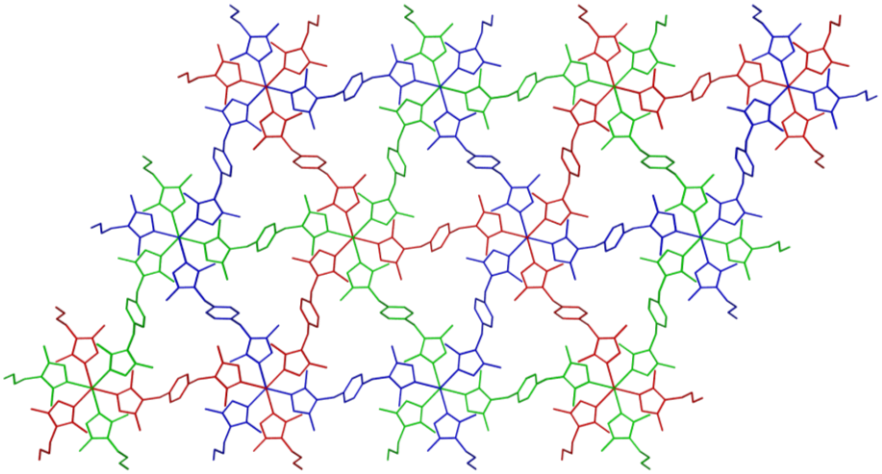

*Figure 4.18: The structure of **4** showing the triply interpenetrated network. Hydrogen atoms and counter ions have been omitted for clarity*

This structural motif is maintained by the presence of Ag···Ag interactions [2.9990(7) Å] between two of the sheets, which is shorter than the sum of the van der Waals radii for two silver atoms.[15, 16] Overall, this structure is very similar to that observed previously for $[Ag_2(bismim)_3](BF_4)_2$ (Figure 4.5).[13]

4.2.4 $[Ag_2(bisox)_3](ClO_4)_2 \cdot Et_2O$, 5 and $[Ag_2(bisox)_3](BF_4)_2 \cdot 1.2Et_2O$, 7

On recrystallisation of **4** from acetonitrile-diethyl ether, colourless parallelepiped crystals of **5** with approximate dimensions 0.22 x 0.20 x 0.13 mm were produced for X-ray structure analysis. These were the diethyl ether solvate of **4**.

In a similar manner to **5**, **7** was formed from the recrystallisation of **6** in acetonitrile-diethyl ether. Colourless tabloid crystals of **7** were produced, with approximate dimensions 0.22 x 0.17 x 0.03 mm that were suitable for single crystal X-ray structure analysis, which was observed to have the same gross structure as **5**, with differing amounts of guest solvent. The crystal data for compounds **5** and **7** is shown in Table 4.5.

Compound	**5**	**7**
Empirical formula	$C_{77.33}H_{93.33}Ag_{2.67}Cl_{2.67}N_8O_{20}$	$C_{78.4}H_{96}Ag_{2.67}B_{2.67}F_{10.67}N_8O_{9.6}$
M	1837.12	1823.20
***T*/ K**	150(2)	150(2)
Crystal system	Hexagonal	Hexagonal

Space group, *Z*	$P6_3/m$, 3	$P6_3/m$, 3
***a*/ Å**	14.4400(2)	14.3960(2)
***b*/ Å**	14.4400(2)	14.3960(2)
***c*/ Å**	35.3990(7)	35.3830(7)
***α*/ º**	90	90
***β*/ º**	90	90
***γ*/ º**	120	120
***U*/ Å ^{3}**	6392.28(17)	6350.51(18)
Absorption coefficient/ mm^{-1}	0.765	0.694
***F*(000)**	2824	2802
Theta range for data collection/ º	3.99 to 25.0	3.70 to 27.50
Reflections collected/ observed [*I*>2σ(*I*)]	67463/ 2001	4363/ 2692
Data Completeness	0.995	0.989
Goodness-of-fit on F^2	1.065	1.065
Final *R* indices [*I*>2σ(*I*)]	*R*1 = 0.0455, *wR*2 = 0.1075	*R*1 = 0.0590, *wR*2 = 0.1062
***R* indices (all data)**	*R*1 = 0.1196, *wR*2 = 0.1343	*R*1 = 0.1329, *wR*2 = 0.1281
Largest diff. peak and hole Å^{-3}	0.451 and -0.543	0.535 and -0.569

*Table 4.5: Crystallographic data for $[Ag_2(bisox)_3](ClO_4)_2 \cdot Et_2O$ (**5**) and $[Ag_2(bisox)_3](BF_4)_2 \cdot 1.2Et_2O$ (**7**)*

The asymmetric unit for **5** consists of two silver centres located on a 3-fold rotation axis, two half portions of ligand, two perchlorate anion fragments, where each chlorine and one oxygen atom from each perchlorate anion are also located on the 3-fold rotation axis, and a portion of diethyl ether, which refines to 0.33 occupancy (Figure 4.19).

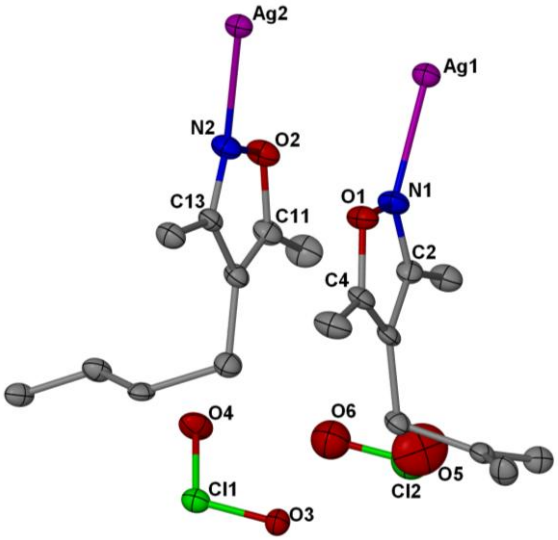

*Figure 4.19: The asymmetric unit of compound **5** showing thermal ellipsoids at the 30% probability level. Hydrogen atoms and solvent fragments have been omitted for clarity*

Each independent silver centre has trigonal planar geometry, with each coordinating to three fragments of bisox ligands. The two independent bisox ligands have different conformations. The bisox ligand is in the S-conformation when coordinated to Ag(2) and in the C-conformation when coordinated to Ag(1). The ligands coordinated to Ag(2) form triply interpenetrated hexagonal sheets similar to those observed in **4**, whereas the ligands coordinated to Ag(1) form discrete $Ag_2(bisox)_3$ cages (Figure 4.20 and 4.21). The fact that these cages are not observed in **4** suggests that the diethyl ether projecting through the cage faces may be templating their formation.

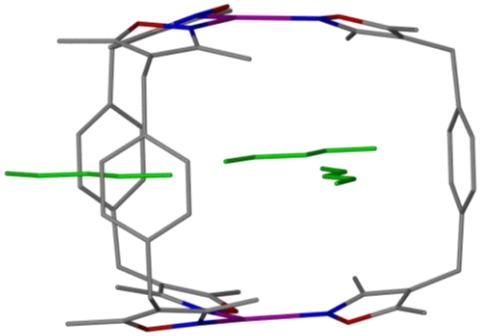

*Figure 4.20: $[Ag_2(bisox)_3]\cdot Et_2O$ cage structure present in **5**, with diethyl ether molecules shown in green. Hydrogen atoms and counter ions have been omitted for clarity*

There are two types of short Ag···Ag contact present in the gross structure: those between the silver atoms within the interpenetrated sheets, as observed in **4** [Ag(2)···Ag(2)[ii] 3.0444(11) Å], and those between the sheet silver atoms and the cage silver atoms. The closest contacts are between the silver atoms in the cage which lie directly above the silver centres of the sheets [Ag(1)···Ag(2) 3.3253(8) Å]. The distance between the two silver atoms in the $Ag_2(bisox)_3$ cage is 8.004(1) Å. The perchlorate anions occupy positions to either side of the interpenetrated sheets, and are involved in C–H···O hydrogen bonds with CH donors of the bisox ligand on both the sheets and the cages [C(5)···O(3) 3.500 Å, H(5A)···O(3) 2.571 Å, C(5)-H(5A)···O(3) 158°].

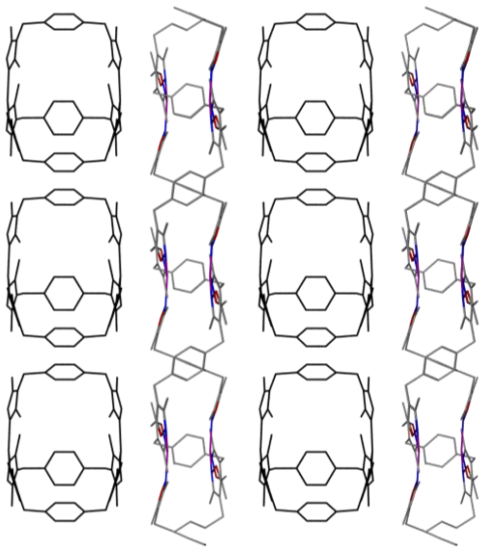

*Figure 4.21: The crystal structure of **5** showing the alternation of triply interpenetrated sheets with rows of cages. The cages have been shown in black. Hydrogen atoms, solvent molecules and counter ions have been omitted for clarity*

Ag_2L_3 cages have never previously been reported, although $[Ag_2(bismim)_2](BF_4)_2{\cdot}2CH_3CN$ macrocycles have been observed (Figure 4.6).[14] For this structure, it was possible to remove the acetonitrile from inside the macrocycle, whilst retaining its crystallinity. The role of the diethyl ether molecules as templates was confirmed by attempting to recrystallise **4** from just acetonitrile. However, on carrying this out, **4** was observed as the compound present as evidenced by powder X-ray diffraction.

[ii] Symmetry transformations used to generate equivalent atoms:
x + 2, –y, –z + 1

$[Ag_2(bisox)_3](BF_4)_2 \cdot 1.2Et_2O$, **7** is isostructural to **5**, confirmed by the unit cell of the compound, and matching powder X-ray diffraction patterns. The only difference is the higher proportion of diethyl ether present within the cages. Other than this there are no other significant differences between the structures.

4.2.5 $[Ag(bisox)_2]PF_6 \cdot 0.5bisox$, 8 and $[Ag(bisox)_2]SbF_6 \cdot 0.5bisox$, 9

The reaction of bisox and silver(I) hexafluorophosphate in methanol produced colourless block crystals of **8**. From this batch a sample of approximate dimensions 0.18 x 0.15 x 0.15 mm was selected for X-ray crystallography.

In a similar manner, colourless block crystals of **9** were produced from the reaction of bisox and silver(I) hexafluoroantimonate in methanol. X-ray structure determination was carried out on a crystal of approximate dimensions 0.35 x 0.28 x 0.25 mm. The crystal dat for compounds **8** and **9** is shown in Table 4.6.

Compound	**8**	**9**
Empirical formula	$C_{45}H_{50}AgF_6N_5O_5P$	$C_{45}H_{50}Ag_1Sb_1F_6N_5O_5$
M	993.74	1084.52
***T*/ K**	150(2)	150(2)
Crystal system	Triclinic	Triclinic
Space group, *Z*	*P*-1, 2	*P*-1, 2
***a*/ Å**	13.5620(1)	13.5300(3)
***b*/ Å**	14.2000(1)	14.3010(4)
***c*/ Å**	14.2460(2)	14.3670(3)
α/ º	102.616(1)	103.860(1)
β/ º	113.747(1)	113.574(1)
γ/ º	103.917(1)	103.746(1)
***U*/ Å ^{3}**	2260.62(4)	2293.51(9)
Absorption coefficient/ mm^{-1}	0.556	1.090
***F*(000)**	1022	1094
Theta range for data collection/ º	3.67 to 27.46	3.58 to 27.54
Reflections collected/ observed [$I>2\sigma(I)$]	38548/ 7231	38829/ 7989
Data Completeness	0.991	0.988
Goodness-of-fit on F^2	1.014	1.036

Final *R* indices [*I*>2σ(*I*)]	*R*1 = 0.0413, *wR*2 = 0.0833	*R*1 = 0.0342, *wR*2 = 0.0702
***R* indices (all data)**	*R*1 = 0.0770, *wR*2 = 0.0944	*R*1 = 0.0567, *wR*2 = 0.0783
Largest diff. peak and hole Å^{-3}	0.554 and -0.736	0.608 and -0.959

*Table 4.6: Crystallographic data for $[Ag(bisox)_2]PF_6 \cdot 0.5bisox$ (**8**) and $[Ag(bisox)_2]SbF_6 \cdot 0.5bisox$ (**9**)*

The asymmetric unit for compound **8** consists of one silver atom coordinated to two full bisox ligands, one hexafluorophosphate counter ion with the fluorine atoms disordered over two positions and half a bisox guest molecule located within the lattice (Figure 4.22).

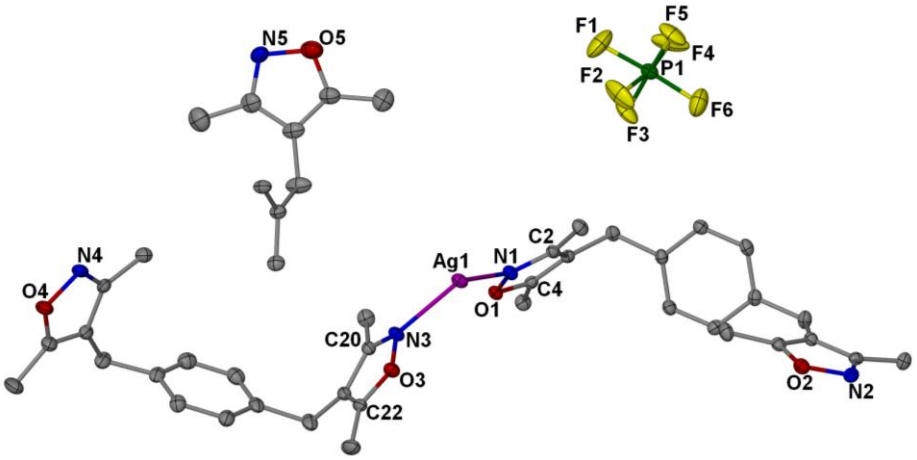

*Figure 4.22: The asymmetric unit of compound **8** showing thermal ellipsoids at the 30% probability level. Hydrogen atoms and minor disordered components have been omitted for clarity*

The silver centre has distorted tetrahedral geometry coordinating to four bisox ligands. All coordinated ligands adopt the C-conformation and bridge the silver centres together into one dimensional chains of macrocycles. The guest bisox ligand adopts the S-conformation and is uncoordinated, lying through the macrocyclic rings, of alternate rings (Figure 4.23). The hexafluorophosphate counter ions are then housed between the chains.

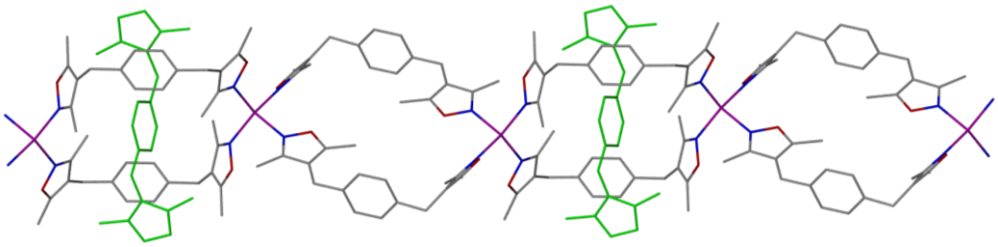

*Figure 4.23: One dimensional chain of **8** with guest bisox ligands shown in green. Hydrogen atoms and counter ions have been omitted for clarity*

Compound **8** can be considered as a polypseudorotaxane, and bears some similarities to the network $[Ag_2(bisim)_3](NO_3)_2$ mentioned previously (Figure 4.4).[12] $[Ag_2(bisim)_3](NO_3)_2$ incorporates C-shaped ligands to create the chain of macrocycles and then has similar S-shaped ligands projecting through these rings. However, in this example, the macrocycles and the free ligands are coordinated producing polyrotaxanes.

Compound **9,** $[Ag(bisox)_2]SbF_6 \cdot 0.5bisox$ is isostructural with compound **8** so will not be discussed in detail.

4.2.6 $[Ag(bisox)_2]SbF_6$, 10 and $[Ag(bisox)_2]CF_3SO_3$, 11

Compound **9** was recrystallised from acetonitrile-diethyl ether to produce colourless block crystals of **10**. Crystals were produced of approximate size 0.50 x 0.40 x 0.25 mm, and were selected for X-ray structure determination.

Colourless block crystals of **11** were produced from the reaction of bisox and silver(I) triflate in methanol. Single crystal X-ray diffraction was carried out on a crystal of approximate dimensions 0.25 x 0.15 x 0.10 mm. The crystal data for compounds **10** and **11** is shown in Table 4.7.

Compound	**10**	**11**
Empirical formula	$C_{36}H_{40}AgF_6N_4O_4Sb$	$C_{37}H_{40}AgF_3N_4O_7S$
M	936.34	849.66
***T*/ K**	150(2)	150(2)
Crystal system	Monoclinic	Monoclinic
Space group, *Z*	*C*2/*c*, 4	*C*2/*c*, 4
***a*/ Å**	21.7220(3)	21.6760(3)

***b*/ Å**	11.4650(2)	11.3410(1)
***c*/ Å**	15.4820(2)	15.7510(2)
***α*/ º**	90	90
***β*/ º**	92.3940(10)	93.566(1)
***γ*/ º**	90	90
***U*/ Å ^{3}**	3852.31(10)	3864.53(8)
Absorption coefficient/ mm^{-1}	1.281	0.642
***F*(000)**	1872	1744
Theta range for data collection/ º	3.55 to 30.03	3.53 to 27.52
Reflections collected/ observed [*I*>2σ(*I*)]	41679/ 4492	36623/ 3733
Data Completeness	0.997	0.995
Goodness-of-fit on F^2	1.033	1.204
Final *R* indices [*I*>2σ(*I*)]	*R*1 = 0.0288, *wR*2 = 0.0675	*R*1 = 0.0419, *wR*2 = 0.0904
***R* indices (all data)**	*R*1 = 0.0440, *wR*2 = 0.0730	*R*1 = 0.0580, *wR*2 = 0.0952
Largest diff. peak and hole Å $^{-3}$	1.492 and -0.672	0.912 and -0.839

*Table 4.7: Crystallographic data for $[Ag(bisox)_2]SbF_6$ (**10**) and $[Ag(bisox)_2]CF_3SO_3$ (**11**)*

The asymmetric unit of **10** consists of half a silver atom, located on a two fold rotation axis and two coordinated half bisox ligands. There is also half a hexafluoroantimony anion fragment which is located on an inversion centre (Figure 4.24).

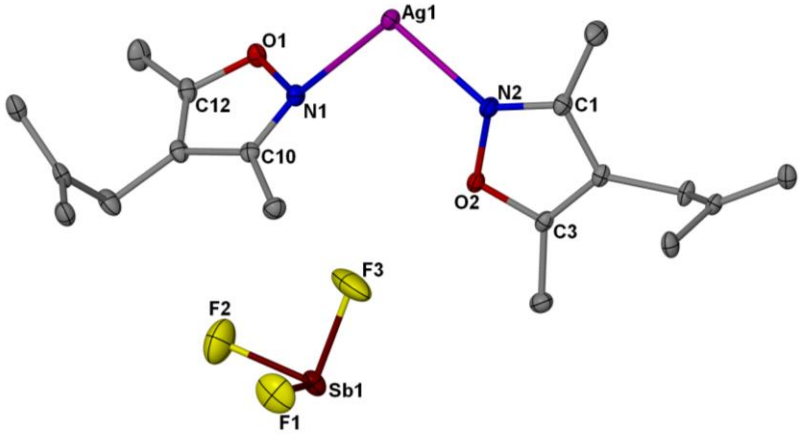

*Figure 4.24: The asymmetric unit of compound **10** showing thermal ellipsoids at the 30% probability level. Hydrogen atoms have been omitted for clarity*

Each silver centre has distorted tetrahedral geometry coordinating to four bisox ligands. The bisox ligands are generated through an inversion centre located in the middle of the benzene rings, to produce the ligand in the S-conformation. These bisox ligands link adjacent silver atoms together forming a three dimensional flattened diamondoid network (Figure 4.25). Due to the size of the pores present in the structure, the network is triply interpenetrated (Figure 4.26). The SbF_6^- anions are housed in the cavities of the framework, and are involved in C-H···F hydrogen bonds to the methyl and methylene groups of the bisox ligand [C(14)···F(1)[iii] 3.301 Å, H(14B)···F(1)[iii] 2.398 Å, C(14)-H(14B)···F(1)[iii] 153°].

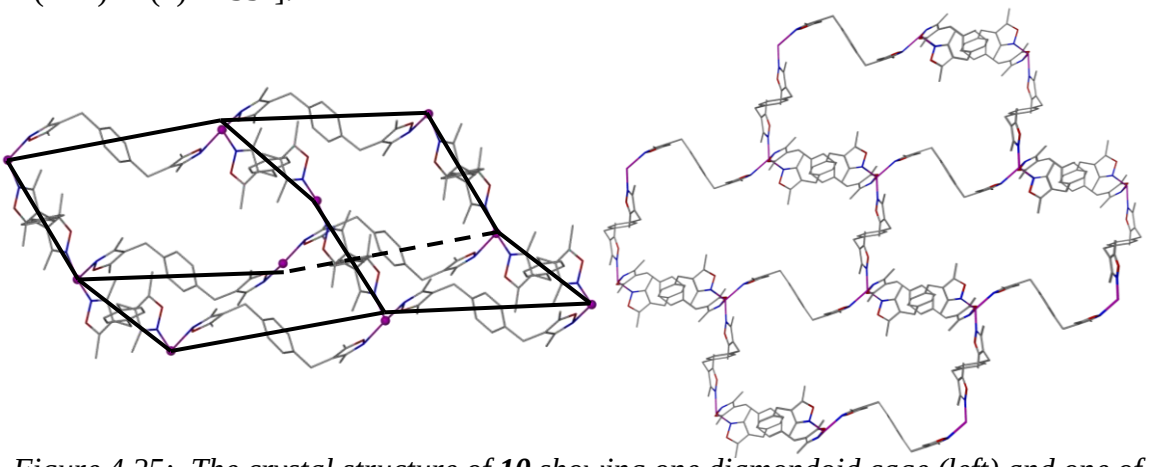

*Figure 4.25: The crystal structure of **10** showing one diamondoid cage (left) and one of the three dimensional flattened diamondoid networks (right). Hydrogen atoms and counter ions have been omitted for clarity*

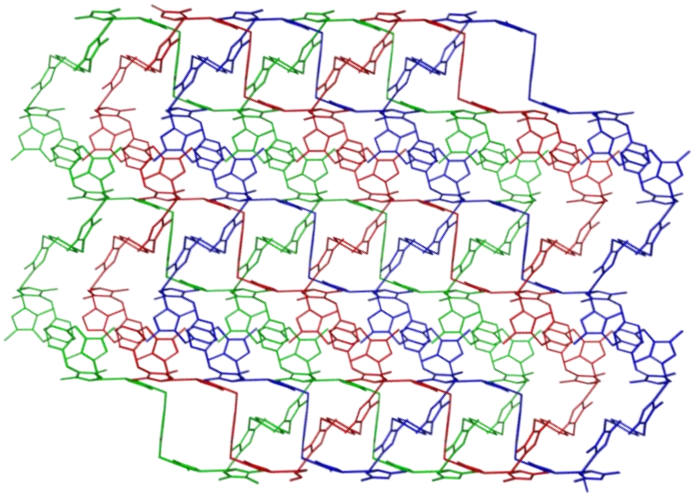

*Figure 4.26: The triply interpenetrated diamondoid network of **10**. Hydrogen atoms and counter ions have been omitted for clarity*

[iii] Symmetry transformations used to generate equivalent atoms:

5/2 -x, y -1/2, 1/2 -z

Compound $[Ag(bisox)_2]CF_3SO_3$ **11** is isostructural with **10**. The triflate anion, as with the counter ion in **10**, lies on an inversion centre which creates disorder between the two halves of the anion. Hydrogen bonding of the anion to the methyl and methylene group of the bisox ligand is also present, but is C-H···O/F hydrogen bonding due to this disorder [C(14)···F(5A)^{iv} 3.480 Å, H(14A)···F(5A)^{iv} 2.573 Å, C(14)-H(14A)···F(5A)^{iv} 154°, C(14)···O(5)^{iv} 3.482 Å, H(14A)···O(5)^{iv} 2.575 Å, C(14)-H(14A)···O(5)^{iv} 154°]. Despite these differences, the network is the same as that in **10**, so will not be discussed in detail.

4.3 Comparison of Crystal Structures

There are a number of structural features apparent on comparing compounds **1**-**11**. Nitrate and trifluoroacetate anions are known to coordinate to silver(I) centres,[17] and this is confirmed by the structures of **1**, **2** and **3**. Compound **3** is formed from the recrystallisation of **2**, and these structures differ only through subtle alterations in bond distances and angles and amounts of solvent present. The coordination of these anions to the silver centres plays an important role in the determination of the structures formed. Although the anions play a vital role in both structures, two different materials are obtained due to the ability of the trifluoroacetate carboxylate to bridge metal centres into dimers, as seen in **2** and **3**.

Compounds **4** and **6** are isostructural materials synthesised from silver salts of the tetrahedral anions ClO_4^- and BF_4^- respectively. They both form triply interpenetrated two dimensional sheet networks which form a Borromean ring type structure as is seen in the previously reported $[Ag_2(bismim)_3](BF_4)_2$ framework.[13] The ClO_4^- and BF_4^- anions are housed in triangular pores supported by C-H···X interactions. Clearly, the size and shape of these anions in **4** and **6** are important in the structure formation, as when larger anions are used similar structures are not observed.

When **4** and **6** are recrystallised from acetonitrile-diethyl ether, the isostructural materials **5** and **7** are obtained. The latter still retain the triply interpenetrated sheets as

---

[iv] Symmetry transformations used to generate equivalent atoms:
3/2 -x, ½ +y, 3/2 -z

observed in **4** and **6**, but in between these layers there are discrete $Ag_2(bisox)_3$ cages, which have never previously been reported. In the absence of the diethyl ether compounds **4** and **6** are obtained, indicating that the diethyl ether acts as a template in formation of the $Ag_2(bisox)_3$ cages.

When octahedral anions are used over tetrahedral anions, different materials are obtained. Compounds **8** and **9** have hexafluorophosphate and hexafluorantimonate counter ions respectively and are isostructural. However, when **9** was recrystallised from an acetonitrile-diethyl ether mixture compound **10** was obtained. **10** is isostructural to the triflate containing compound **11**. This suggests that its the size rather than the shape of the anion that determines the resulting structure.

4.4 Solid State Interconversion

Rearrangement of coordination networks are well established when the network is dissolved and re-precipitated.[13, 18] However, solid state transformations are less common, and most of these rearrangements are due to a change in the metal coordination environment.[19-21] There have also been examples where by exchanging the anion within the framework has promoted its conversion.[22] Furthermore, dehydration has been known to initiate transformations within networks.[23, 24]

In the results presented here, compound **5** $[Ag_2(bisox)_3](ClO_4)_2 \cdot Et_2O$ was synthesized from the recrystallisation of **4** $[Ag_2(bisox)_3](ClO_4)_2$, where **5** exhibited an additional cage filled with diethyl ether molecules relative to **4**. Due to the similarity in the formulae of these two compounds, and the similar positioning of the silver centres within the structure, **5** was investigated for conversion into **4** via removal of the solvent versus removal of the diethyl ether whilst maintaining the cages in **5**. This was monitored using a combination of X-ray powder diffraction and thermogravimetric analysis (TGA).

The initial X-ray powder diffraction trace showed the presence of only compound **5**, and this was also confirmed by the TGA. A mass loss of 2.7 % was recorded between 100 and 120 °C which corresponds to the removal of half of the diethyl ether (2.7 %). The remainder of the solvent is lost more gradually, with the network decomposition beginning at approximately 280 °C (Figure 4.28).

The powdered sample **5** was placed under vacuum for four hours, and at 50 °C under vacuum for four hours, with an X-ray powder diffraction trace being recorded every hour; however there was no change in the X-ray powder diffraction pattern, signifying no structural change had occurred. The sample was then heated at 75 °C under vacuum for four hours, with powder X-ray diffraction traces recorded hourly. A gradual conversion of **5** to **4** was observed (Figure 4.27). The X-ray powder patterns are consistent with a complete and clean conversion of **5** to **4** after 4 hours at 75 °C. This is also confirmed by the TGA of the newly desolvated sample, which shows the absence of any solvent, with just the presence of the decomposition of the compound at 280 °C (Figure 4.28).

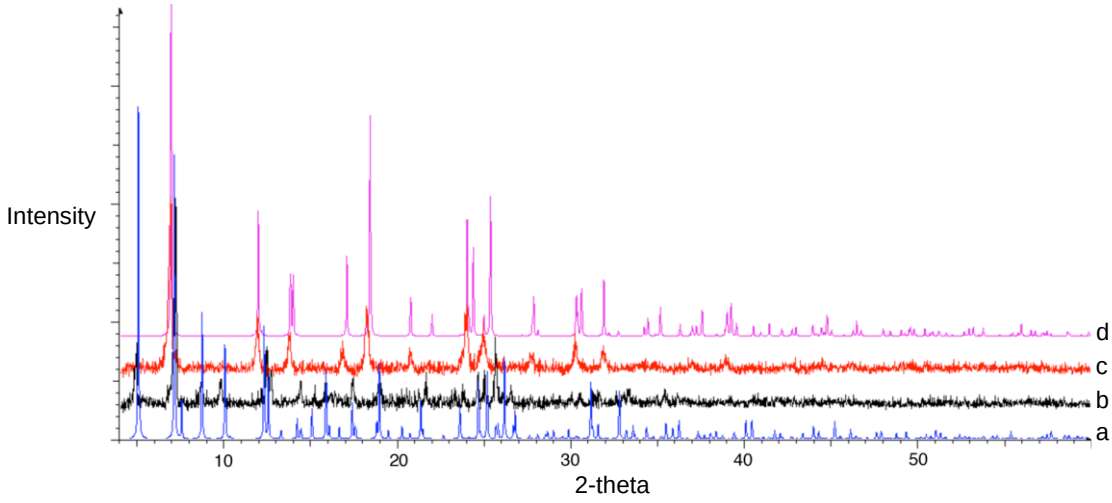

*Figure 4.27: Powder X-ray diffraction patterns for a) **5** simulated from the crystal data b) **5** c) **5** heated under vacuum at 75 °C for four hours d) **4** simulated from the crystal data*

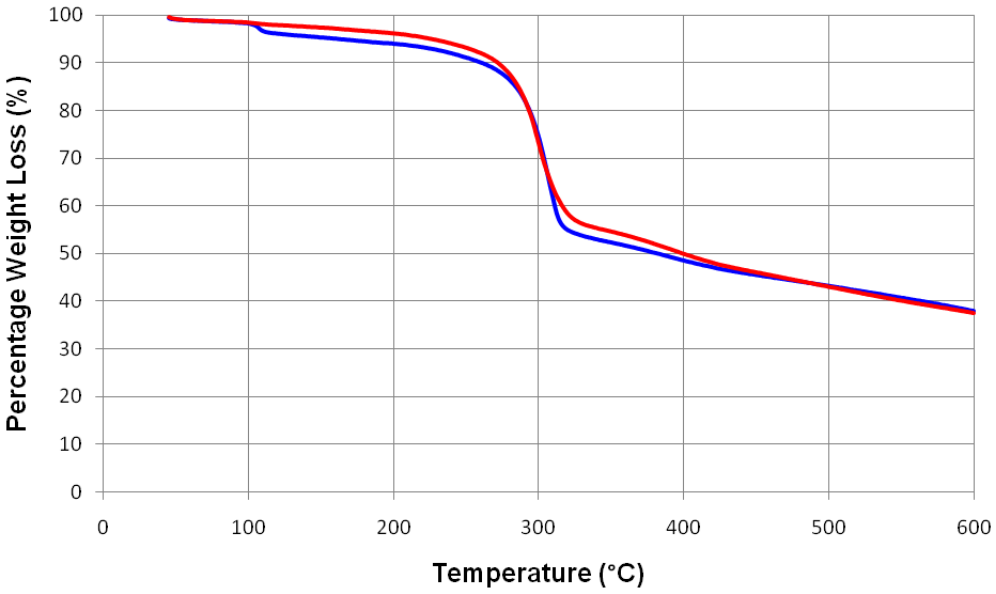

*Figure 4.28: TGA trace for compound 5 heated under vacuum at 75 °C for four hours (red) and compound **5** (blue)*

This conversion involves a large rearrangement of the network, so it is remarkable that the material remains crystalline. Single crystals of **5** were monitored during the solvent loss, and these were shown to degrade during this process. It is of no surprise that single crystals do not survive this transformation. The bisox ligand is required to rearrange from the C-conformation in **5** to the S-conformation in **4**, which requires a rotation of 180° of one of the isoxazolyl rings about a methylene carbon atom which, in turn, involves the ring nitrogen atom moving through an arc of approximately 10.7 Å. This change also sees the breaking and re-forming of half the Ag-N bonds (Figure 4.29). The conversion of the cages into the two dimensional sheets also requires a substantial movement of the silver atoms, which is consistent with a 17 % shrinkage in the *c* direction of the unit cell (35.3990(6) – 7.3050(1) Å).

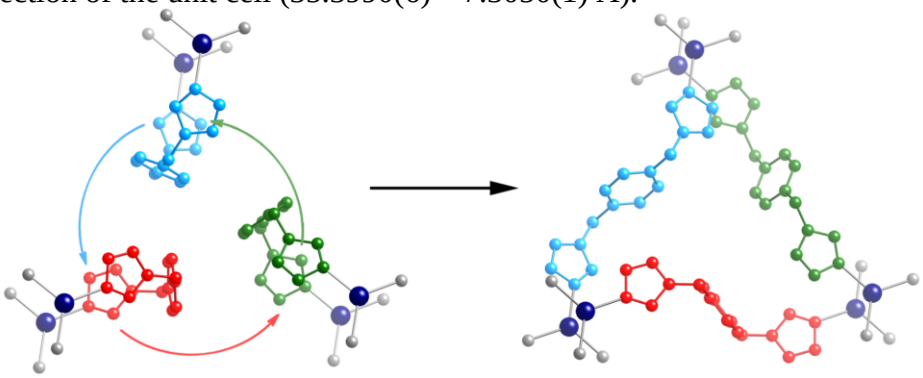

*Figure 4.29: The transformation required to convert the cages of **5** into the two dimensional sheets of **4***

Given that **4** and **5** are isostructural with **6** $[Ag_2(bisox)_3](BF_4)_2$ and **7** $[Ag_2(bisox)_3](BF_4)_2 \cdot 1.2Et_2O$ a similar investigation was carried out on the latter pair of compounds.

The conversion of **7** to **6** occurs much faster than the perchlorate analogue, and occurs with no heating. The initial X-ray powder trace for **7** showed the presence of **7**, with a slight indication that some of this may have already converted to **6**. **7** was shown to completely convert to **6** on standing in the atmosphere for one week at room temperature by powder X-ray diffraction. This conversion process was also shown to speed up if sample **7** was placed under vacuum. After one hour under vacuum, sample **7** had almost completely converted to **6**, after three hours this conversion was complete (Figure 4.30).

The TGA also confirmed the rapid conversion of **7** to **6**. The trace showed a small percentage weight loss in the region of 100 to 120 °C, with the decomposition curve starting at around 250 °C. The small percentage weight loss indicates that a lot of the guest diethyl ether has already been lost before the TGA experiment was carried out (Figure 4.31). These results indicate that the conversion of **7** to **6** occurs quite rapidly, and may already be occurring at room temperature without application of a vacuum.

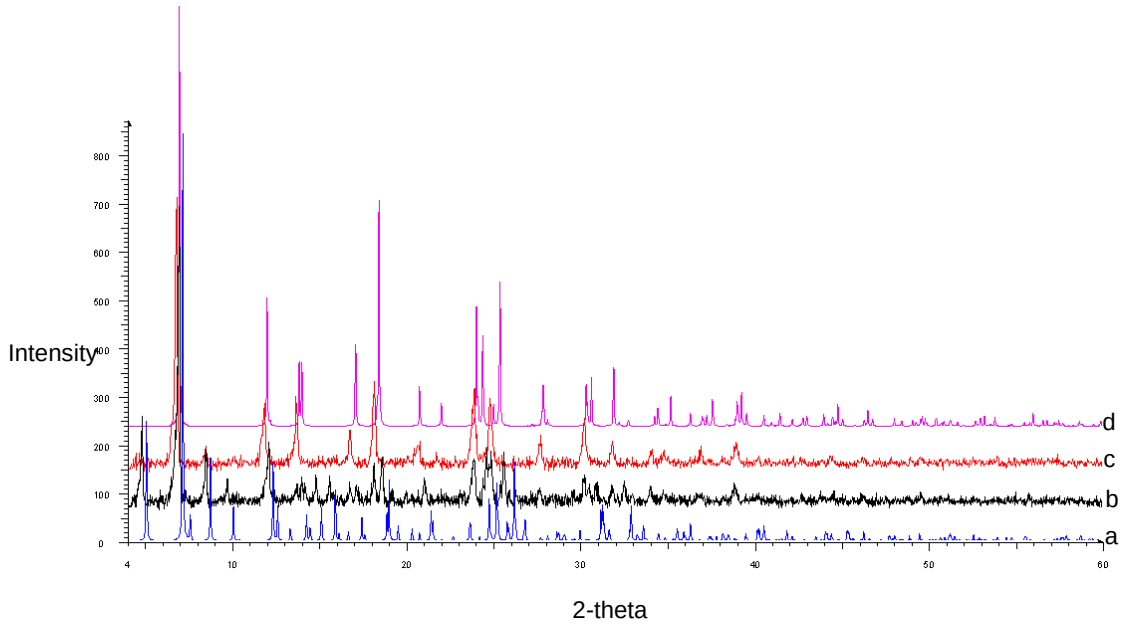

*Figure 4.30: Powder X-ray diffraction patterns for a) **7** simulated from the crystal data b) **7** c) **7** heated under vacuum at room temperature for three hours d) **6** simulated from the crystal data*

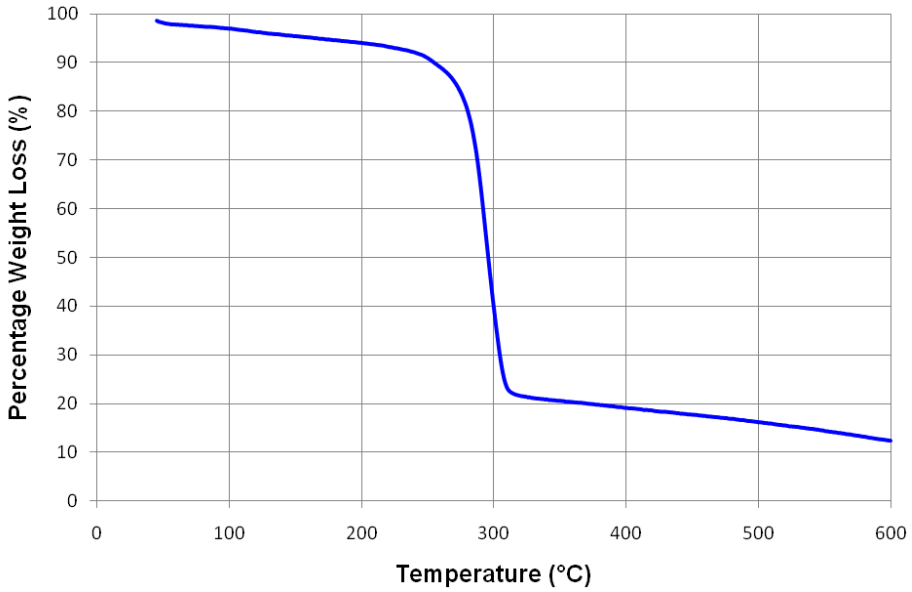

*Figure 4.31: TGA trace for compound **7***

The diethyl ether molecules reside in very similar positions within the perchlorate and tetrafluoroborate structures **5** and **7**, however, the more rapid loss of solvent in **7** may be related to small differences in the intermolecular interactions. The diethyl ether molecules are involved in contacts with the anions in each structure. In the perchlorate structure (**5**) these distances are slightly shorter [C(102)···O(5) 3.935 , H(10E)···O(5) 3.04 Å, C(102)–H(10E)···O(5) 153°] when compared to the slightly longer C–H···F interactions in **7** [C(23)···F(2) 4.032, H(23B)···F(2) 3.16 Å, C(23)–H(23B)···F(2) 149°]. These differences may account for the more rapid loss of solvent in **7**.

4.5 Conclusion

During this investigation, a total of eleven novel frameworks have been synthesised and characterised, with seven different gross structures. These include one, two and three dimensional networks.

All the reactions involved the bisox ligand being reacted with a silver(I) salt, in an effort to understand the affect of the anion on the structures formed. Due to the variety of networks formed, it has been shown that the size and the shape of the anion play a vital role. It has also been shown in compounds **5** and **7** how important the solvent is in the structures, and how the removal of solvent from these can result in a solid state transformation, involving a huge rearrangement of the structure.

One of the main reasons the bisox ligand was chosen for this investigation was due to its degree of flexibility. Compounds **5**, **7**, **8** and **9** demonstrate how the ligand can be incorporated into the frameworks in both the C- and S-conformations. The flexibility of the ligand was also confirmed by the solid state transformations of **7** to **5** and **6** to **4**.

As stated in Section 4.1 the bisox ligand was also chosen as it contained four different coordinating sites, an oxygen and nitrogen on each isoxazole ring. As expected, all the networks formed had the silver coordinating only to the nitrogen atoms of the ligand.

4.6 Experimental

4.6.1 General

3,3'-(1,4-phenylenebis(methylene))bis(4-hydroxypent-3-en-2-one) was prepared following the previously reported method.[25] All other compounds were obtained commercially and used without further purification.

Powder diffraction measurements were recorded using a Bruker D8 powder diffractometer, fitted with Goebel mirrors, and using CuK_{α} radiation of wavelength 1.5414 Å. Samples were placed in 0.3 mm to 0.7 mm diameter Lindemann capillaries, and measured with a 2θ range of 4 - 60°. The step size was 0.02° with time per step of 1.00s.

Elemental analyses were conducted by Alan Carver (University of Bath) and Gillian Maxwell (University College London).

NMR spectra were recorded at 298 K on a Bruker Avance 300 MHz NMR spectrometer, and referenced to residual *protio* solvent signals for ^{1}H NMR spectra ($CDCl_3$, δ 7.24) and to solvent resonances for $^{13}C\{^{1}H\}$ NMR ($CDCl_3$, δ 77.2).

Mass spectra were recorded on a Bruker MicrOTOF electrospray time-of-flight (ESI-TOF) mass spectrometer (Bruker Daltonik GmbH) coupled to an Agilent 1200 LC system (Agilent Technologies).

Thermogravimetric analyses were recorded on a Perkin Elmer TGA 4000 Thermogravimetric analyzer, with a temperature range of 40-600 °C at 5 °C per minute under an atmosphere of nitrogen.

4.6.2 Crystallography

X-ray data for compounds **1-4** and **6-11** were collected on a Nonius Kappa CCD diffractometer using Mo-K_α radiation. Unless noted below, all non-hydrogen atoms were refined anisotropically in the final least squares run, and hydrogen atoms were included at calculated positions. The structures were solved using SHELXS-97[26] and refined using full-matrix least squares in SHELXL-97.[26] Refinements were generally straightforward with the following exceptions and points of note.

For **2**, the oxygen atom of the fragment of methanol in the asymmetric unit was situated on an inversion centre, which necessitates disorder of the methyl carbon atom over two sites. The hydrogen atoms in this solvent moiety could not be reliably located and hence were omitted from the final least squares. The electron density map in the region of the fluorine atoms was very smeared, also due to disorder. Optimal modelling was achieved by treating each fluorine as being located over three sites. C–C and C–F bond distance restraints served to converge the model. The largest residual electron density maximum was also in this region.

Compound **3** contained two -CF_3 groups from the trifluoracetate anion, both of which were disordered to different extents. The fluorines attached to C4 were disordered in 45:55 ratio, where all the fluorines were refined anisotropically, after C-F, F···F and atomic displacement parameter restraints had been applied. The fluorines attached to C2 were also disordered over two sites in a 75:25 ratio, where only the 75 % fragment was refined anisotropically. C-F and F···F distance restraints were also applied on this fragment prior to the final least squares refinement. PLATON SQUEEZE was also used for **3**, as the residual electron density could not sensibly be refined. The electron density gained from this algorithm was assigned to two molecules of acetonitrile per unit cell.

For **5**, the C–C and C–O distances within the diethyl ether molecule were restrained to being individually similar, and restraints were also applied to the associated atomic displacement parameters.

Compound **8** contained disordered fluorine atoms in the hexafluorophosphate counter ion. This was successfully modelled in a 60:40 ratio.

Compound **11** contains a triflate anion which lies proximate to an inversion centre so is disordered in a 50:50 ratio.

4.6.3 Synthesis of 1,4-bis((3,5-dimethylisoxazol-4-yl)methyl)benzene (bisox)

Hydroxylamine hydrochloride (2.11 g, 30 mmol), dissolved in 1 N NaOH solution (20 cm^3, 20 mmol), was added to 3,3'-(1,4-phenylenebis(methylene))bis(4-hydroxypent-3-en-2-one) (4.08 g, 13.5 mmol) suspended in EtOH (50 cm^3) at room temperature. The mixture was heated at reflux for 3 h and the solvents removed under reduced pressure. The residue was suspended in H_2O (100 cm^3) and the pH adjusted to 7. The solid material was collected by filtration, washed with H_2O (3 × 20 cm^3) and crystallised from hot EtOH/H_2O. Yield 3.59 g (89%). Found: C, 72.9; H, 6.78; N, 9.31. $C_{18}H_{20}N_2O_2$ requires C, 72.9; H, 6.81; N, 9.46. δ_H (300 MHz; $CDCl_3$) 2.06 (6 H, s), 2.28 (6 H, s), 3.63 (4 H, s), 7.06 (4 H, s). δ_C (75.5 MHz, $CDCl_3$) 10.27, 10.96, 27.67, 112.26, 128.25, 136.95, 159.86, 165.32. *m/z* (ESI) 297.1586 ($[M + H]^+$. $[C_{18}H_{20}N_2O_2 + H]^+$ requires 297.1603).

4.6.4 Synthesis of $[Ag_2(NO_3)_2(bisox)]$, 1

Bisox (0.029 g, 0.10 mmol) was dissolved in methanol (2 cm^3) with gentle heating and stirring. To this solution, $AgNO_3$ (0.017 g, 0.10 mmol) dissolved in methanol (1 cm^3) was added, rinsing through with a further 0.5 cm^3 methanol. The solution was left at room temperature overnight. A small amount of a brown precipitate had formed, which was removed by filtration through a cotton wool plug. The solution was left at room temperature for 3 days, with the vial lid slightly open to allow approximately half the solvent to evaporate slowly. The crystalline product was then separated by filtration and washed with small amounts of methanol. Yield 0.033 g. The crude product was recrystallised by dissolving in the minimum amount of CH_3CN and allowing Et_2O to diffuse slowly into the solution. Crystals of suitable size for single crystal X-ray

analysis began to form after several days. The X-ray powder diffraction pattern showed **1** to be the major product, with an unidentified by-product also present (Figure 4.32).

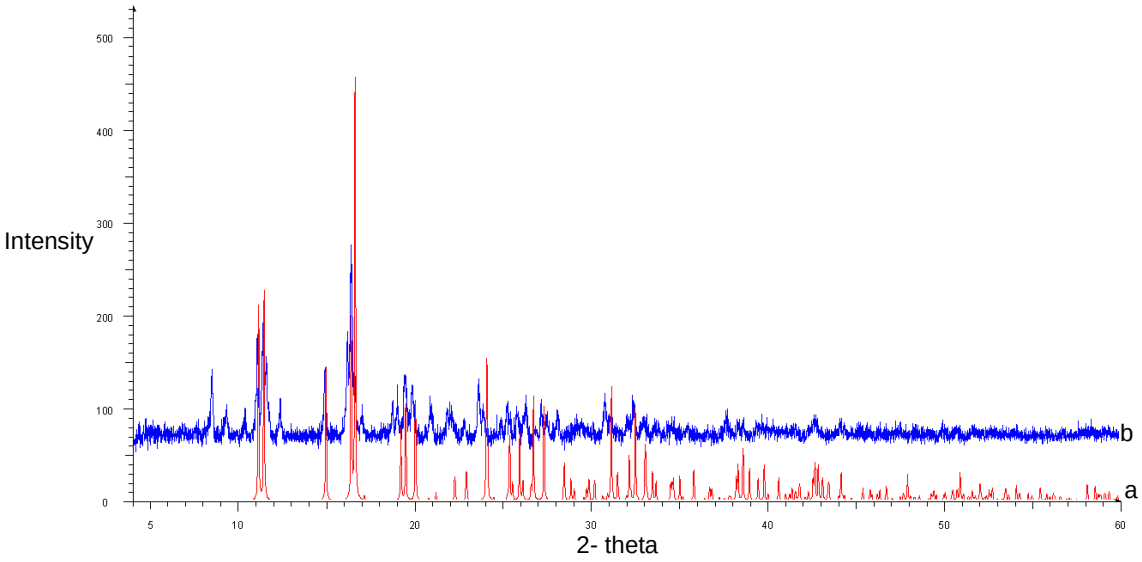

*Figure 4.32: The X-ray powder diffraction trace for **1** (b) and that simulated from the crystal data of **1** (a)*

4.6.5 Synthesis of $[Ag(O_2CCF_3)(bisox)]\cdot 0.5MeOH$, 2 and $[Ag_2(O_2CCF_3)_2(bisox)_2]\cdot CH_3CN$, 3

Bisox (0.029 g, 0.10 mmol) was dissolved in methanol (3 cm^3) with gentle heating and stirring. To this solution, $AgCF_3CO_2$ (0.022 g, 0.10 mmol) dissolved in methanol (1 cm^3) was added, rinsing through with a further 0.5 cm^3 methanol. The solution was allowed to stand at room temperature overnight. A small amount of a brown precipitate had formed, which was removed by filtration through a cotton wool plug. The solution was left at room temperature for approximately 3 days, with the vial lid slightly open to allow slow evaporation of the solvent. Crystals of suitable size were formed for single crystal X-ray analysis. Yield 0.042 g (78%). Found: C, 46.20; H, 4.15, N, 5.21. $C_{20.5}H_{22}AgF_3N_2O_{4.5}$ requires C, 46.17; H, 4.16, N, 5.25%. The bulk purity was also confirmed by powder X-ray diffraction (Figure 4.33). Compound **2** was recrystallised by dissolving it in the minimum volume of CH_3CN and allowing Et_2O to slowly diffuse into the solution. Crystals of suitable size were produced for single crystal X-ray diffraction. The powder X-ray diffraction for compound **3** confirmed the phase purity of the sample (Figure 4.34).

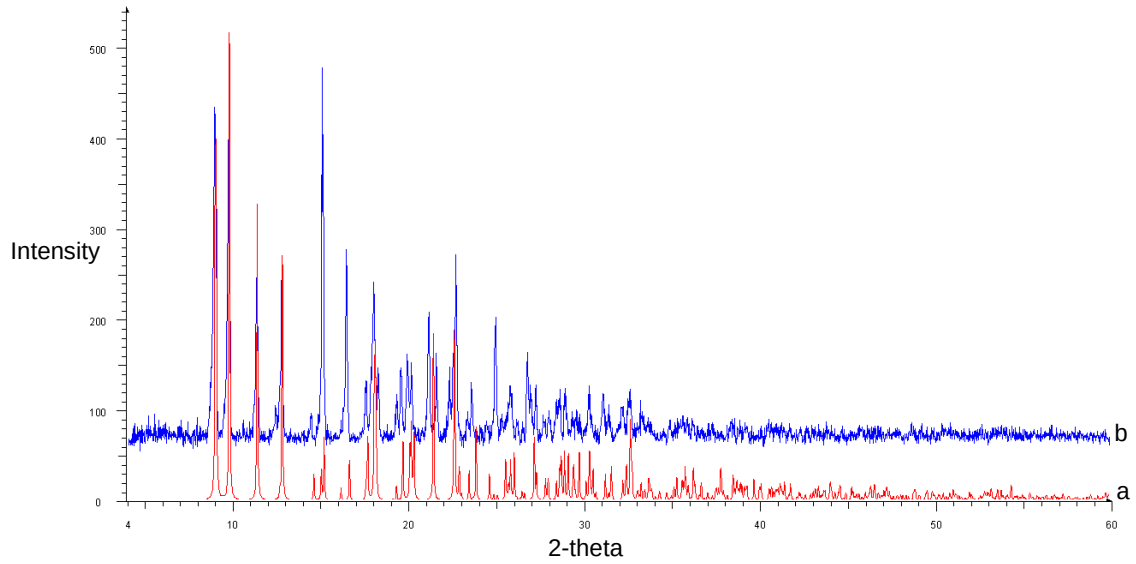

*Figure 4.33: The X-ray powder diffraction trace for **2** (b) and that simulated from the crystal data of **2** (a)*

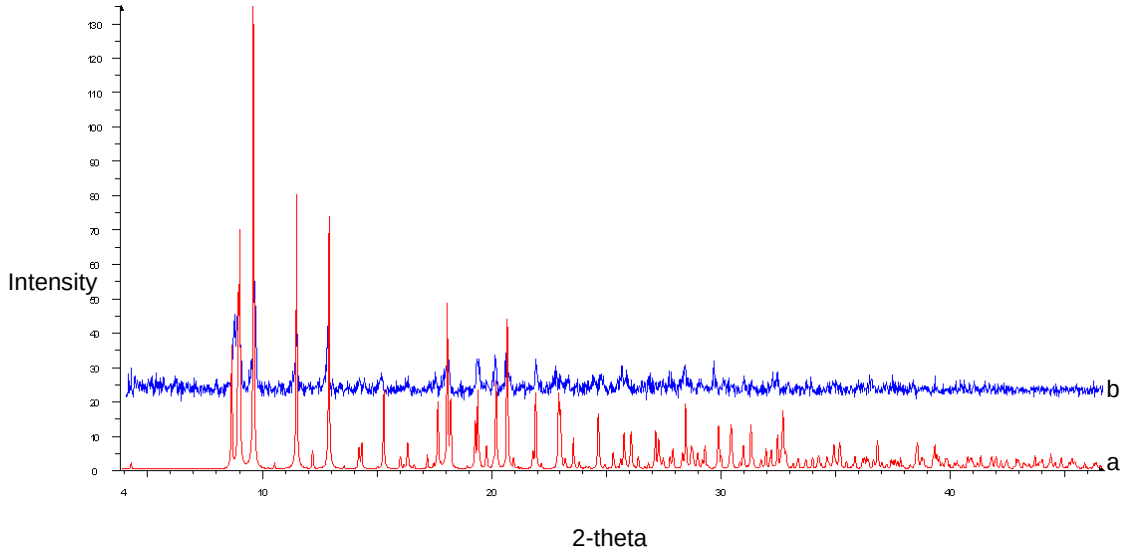

*Figure 4.34: The X-ray powder diffraction trace for **3** (b) and that simulated from the crystal data of **3** (a)*

4.6.6 Synthesis of $[Ag_2(bisox)_3](ClO_4)_2$, 4, and $[Ag_2(bisox)_3](ClO_4)_2 \cdot Et_2O$, 5

Bisox (0.144 g, 0.49 mmol) was dissolved in methanol (10 cm^3) with gentle heating and stirring. To this solution, $AgClO_4$ (0.050 g, 0.24 mmol) dissolved in methanol (3 cm^3) was added. The product was allowed to crystallise overnight. This solid product was filtered and washed with methanol. Yield 0.146 g (93%). Found: C, 49.54; H, 4.53; N, 5.91. $C_{54}H_{60}Ag_2Cl_2N_6O_{14}$ requires C, 49.75; H, 4.64; N, 6.45%. Compound **4** was recrystallised by dissolving it in the minimum volume of CH_3CN and allowing Et_2O to slowly diffuse into the solution. Crystals of suitable size were produced for single

crystal X-ray diffraction. Found: C, 50.60; H, 4.74; N, 6.09. $C_{58}H_{70}Ag_2Cl_2N_6O_{15}$ requires C, 50.56; H, 5.12; N, 6.10 %. The bulk purity of compounds **4** and **5** was confirmed by powder X-ray diffraction (Figure 4.35).

4.6.7 Synthesis of $[Ag_2(bisox)_3](BF_4)_2$, 6, and $[Ag_2(bisox)_3](BF_4)_2 \cdot 1.2Et_2O$, 7

Bisox (0.061 g, 0.2 mmol) was dissolved in methanol (6 cm^3) with gentle heating and stirring. To this solution, $AgBF_4$ (0.021 g, 0.1 mmol) dissolved in methanol (1 cm^3) was added. The product was allowed to crystallise overnight. The crystalline product was separated by filtration and washed with small amounts of methanol. Yield 0.031 g (48%). Found: C, 50.02; H, 4.57; N, 6.57. $C_{54}H_{60}Ag_2B_2F_8N_6O_6$ requires C, 50.73; H, 4.73; N, 6.57%. Compound **6** was recrystallised by dissolving it in the minimum volume of CH_3CN and allowing Et_2O to slowly diffuse into the solution. Crystals of the diethyl ether solvate **7** of suitable size were produced for single crystal X-ray diffraction. The phase purity of compounds **6** and **7** was confirmed by powder X-ray diffraction (Figure 4.35).

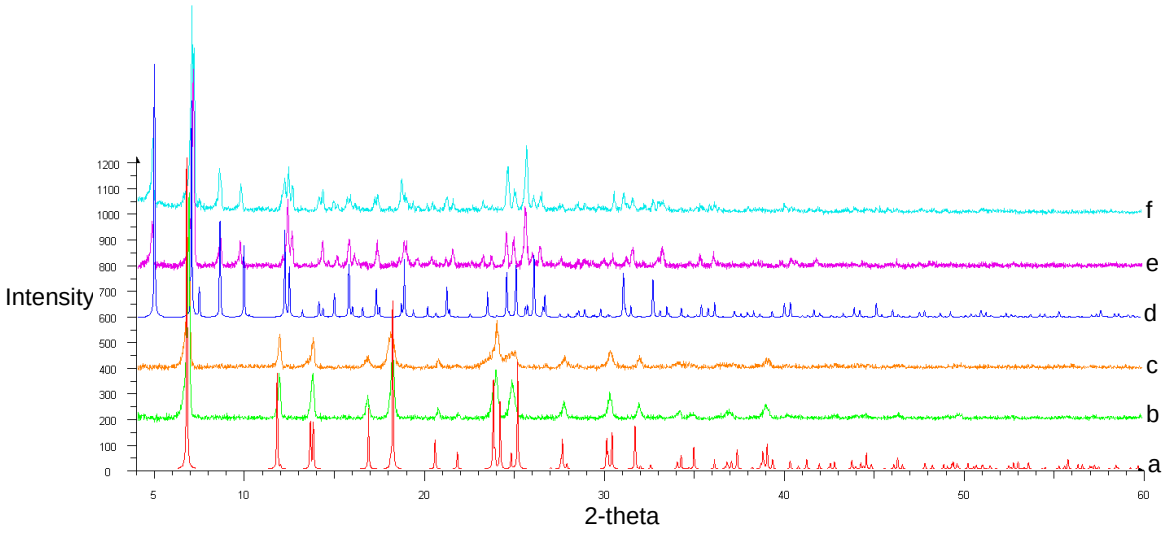

*Figure 4.35: The X-ray powder diffraction trace for that simulated from the crystal data of **4** (a), **4** (b), **6** (c), that simulated from the crystal data of **5** (d), **5** (e) and **7** (f)*

4.6.8 Synthesis of $[Ag(bisox)_2]PF_6 \cdot 0.5$bisox 8

Bisox (0.073 g, 0.25 mmol) was dissolved in methanol (4 cm^3) with gentle heating and stirring. To this solution, $AgPF_6$ (0.031 g, 0.12 mmol) dissolved in methanol (2 cm^3) was added. The product was allowed to crystallise overnight. The solid product was filtered, and washed with the minimum quantity of methanol. Yield 0.064 g. The X-ray

powder diffraction pattern revealed that **8** was not the only product of the reaction. Recrystallisation of **8** in CH_3CN and Et_2O gave an unidentified product.

4.6.9 Synthesis of $[Ag(bisox)_2]SbF_6 \cdot 0.5bisox$ 9, and $[Ag(bisox)_2]SbF_6$ 10

Bisox (0.060 g, 0.2 mmol) was dissolved in methanol (6 cm^3) with gentle heating and stirring. To this solution, $AgSbF_6$ (0.036 g, 0.1 mmol) dissolved in methanol (1 cm^3) was added. The product was allowed to crystallise overnight at room temperature. The crystalline product was then filtered and washed with small amounts of methanol. Two types of crystals were present in this product, and they were identified crystallographically as $[Ag(bisox)_2]SbF_6 \cdot 0.5bisox$ **9** and $[Ag(bisox)_2]SbF_6$ **10**. The mixture of **9** and **10** was recrystallised by dissolving it in the minimum amount of CH_3CN and allowing Et_2O to slowly diffuse into the vial. Powder X-ray diffraction confirmed that following recrystallisation, **10** was the sole product (Figure 4.36). Found: C, 46.10; H, 4.31; N, 5.64. $C_{36}H_{40}AgF_6N_4O_4Sb$ requires C, 46.18; H, 4.31; N, 5.98%.

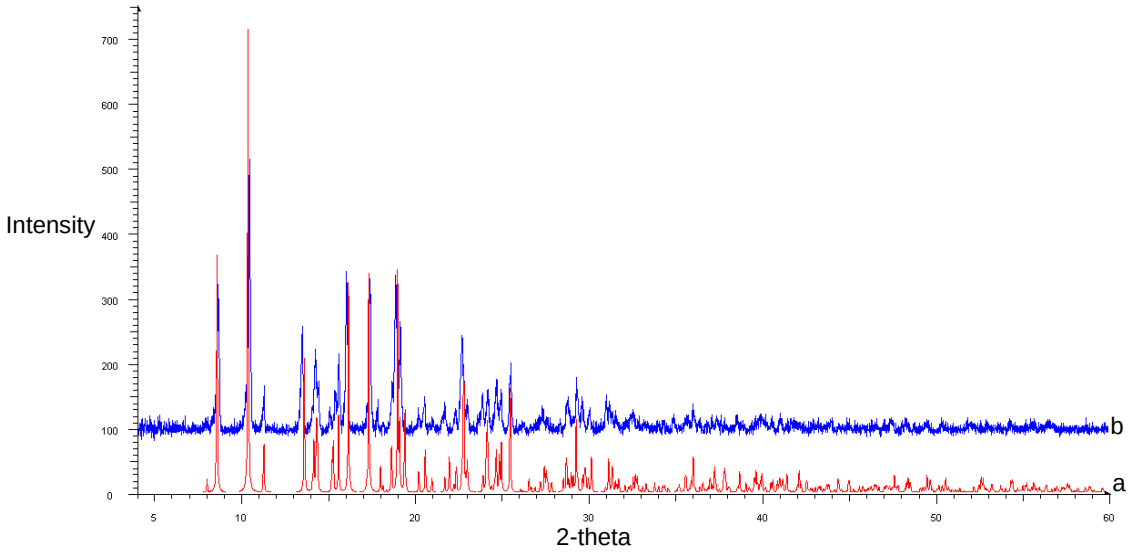

*Figure 4.36: The X-ray powder diffraction trace for **10** (b) and that simulated from the crystal data of **10** (a)*

4.6.10 Synthesis of $[Ag(bisox)_2]CF_3SO_3$ 11

Bisox (0.030 g, 0.10 mmol) was dissolved in methanol (2 cm^3) with gentle heating and stirring. To this solution, $AgCF_3SO_3$ (0.026 g, 0.10 mmol) dissolved in methanol (1 cm^3) was added, rinsing through with a further 0.5 cm^3 methanol. The solution was allowed to stand at room temperature overnight. A small amount of a brown precipitate had formed, which was removed by filtration through a cotton wool plug. The solution

was left at room temperature for approximately 3 days, with the vial lid slightly open to allow about half the solvent to evaporate slowly. Crystals formed which were suitable for single crystal X-ray analysis. Yield 0.042 g (50%). Found: C, 52.25; H, 4.73; N, 6.30. $C_{37}H_{40}AgF_3N_4O_7S$ requires C, 52.30; H, 4.75; N, 6.59%. The powder X-ray diffraction trace confirmed the phase purity of the material (Figure 4.37). Recrystallisation of **11** in CH_3CN and Et_2O gave an unidentified product.

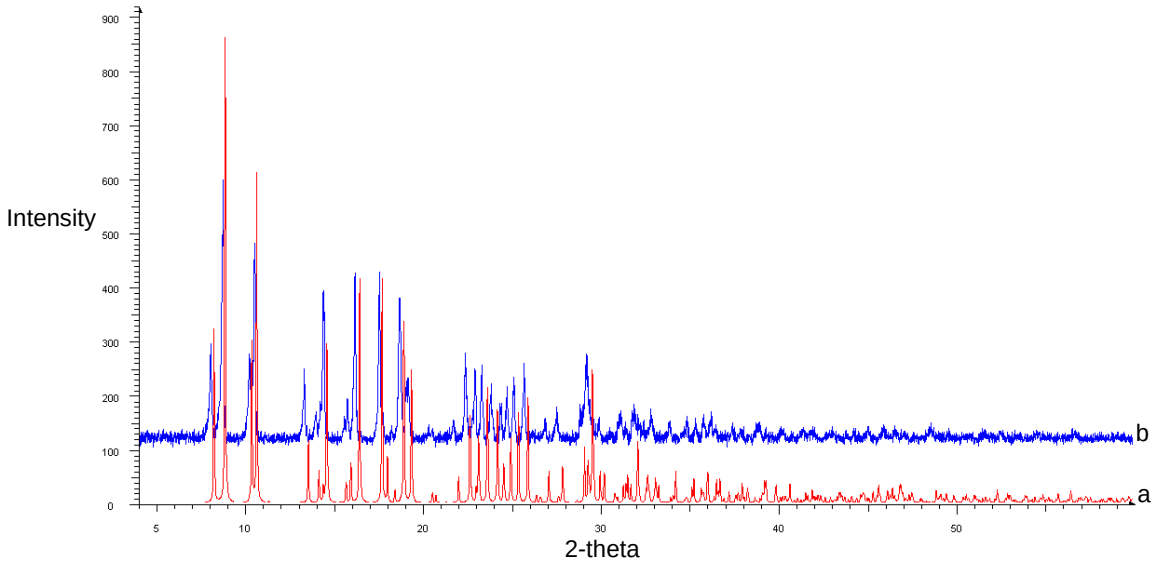

*Figure 4.37: The X-ray powder diffraction trace for **11** (b) and that simulated from the crystal data of **11** (a)*

4.7 References

1. S. M. Hawxwell, G. M. Espallargas, D. Bradshaw, M. J. Rosseinsky, T. J. Prior, A. J. Florence, J. van de Streek and L. Brammer, *Chem. Commun.*, 2007, 1532.
2. D. Tanaka, K. Nakagawa, M. Higuchi, S. Horike, Y. Kubota, L. C. Kobayashi, M. Takata and S. Kitagawa, *Angew. Chem. Int. Ed.*, 2008, **47**, 3914.
3. K. Uemura, R. Matsuda and S. Kitagawa, *J. Solid State Chem.*, 2005, **178**, 2420.
4. T. K. Trung, P. Trens, N. Tanchoux, S. Bourrelly, P. L. Llewellyn, S. Loera-Serna, C. Serre, T. Loiseau, F. Fajula and G. Férey, *J. Am. Chem. Soc.*, 2008, **130**, 16926.
5. O. S. Jung, Y. J. Kim, Y. A. Lee, K. M. Park and S. S. Lee, *Inorg. Chem.*, 2003, **42**, 844.
6. C. L. Chen, B. S. Kang and C. Y. Su, *Aust. J. Chem.*, 2006, **59**, 3.

7. D. L. Reger, R. F. Semeniuc, C. A. Little and M. D. Smith, *Inorg. Chem.*, 2006, **45**, 7758.
8. J. H. Jia, X. Lin, A. J. Blake, N. R. Champness, P. Hubberstey, L. M. Shao, G. Walker, C. Wilson and M. Schröder, *Inorg. Chem.*, 2006, **45**, 8838.
9. F. Meyer and H. Pritzkow, *Polyhedron*, 1999, **18**, 2769.
10. L. L. Marques, G. M. de Oliveira, E. S. Lang, M. Matiko, A. de Campos and L. R. S. Gris, *Inorg. Chem. Commun.*, 2007, **10**, 1083.
11. C. F. Wang, Z. Y. Zhu, Z. X. Zhang, Z. X. Chen and X. G. Zhou, *CrystEngComm*, 2007, **9**, 35.
12. B. F. Hoskins, R. Robson and D. A. Slizys, *J. Am. Chem. Soc.*, 1997, **119**, 2952.
13. L. Dobrzanska, H. G. Raubenheimer and L. J. Barbour, *Chem. Commun.*, 2005, 5050.
14. L. Dobrzanska, G. O. Lloyd, H. G. Raubenheimer and L. J. Barbour, *J. Am. Chem. Soc.*, 2005, **127**, 13134.
15. D. Venkataraman, Y. H. Du, S. R. Wilson, K. A. Hirsch, P. Zhang and J. S. Moore, *J. Chem. Educ.*, 1997, **74**, 915.
16. T. L. Hu, W. P. Du, B. W. Hu, J. R. Li, X. H. Bu and R. Cao, *CrystEngComm*, 2008, **10**, 1037.
17. Y. Gao, B. Twamley and J. M. Shreeve, *Inorg. Chem.*, 2006, **45**, 1150.
18. L. Dobrzanska, G. O. Lloyd, T. Jacobs, I. Rootman, C. L. Oliver, M. W. Bredenkamp and L. J. Barbour, *J. Mol. Struct.*, 2006, **796**, 107.
19. J. Campo, L. R. Falvello, I. Mayoral, F. Palacio, T. Soler and M. Tomas, *J. Am. Chem. Soc.*, 2008, **130**, 2932.
20. M. C. Bernini, F. Gandara, M. Iglesias, N. Snejko, E. Gutierrez-Puebla, E. V. Brusau, G. E. Narda and M. A. Monge, *Chem. Eur. J.*, 2009, **15**, 4896.
21. D. Sarma, K. V. Ramanujachary, S. E. Lofland, T. Magdaleno and S. Natarajan, *Inorg. Chem.*, 2009, **48**, 11660.
22. K. S. Min and M. P. Suh, *J. Am. Chem. Soc.*, 2000, **122**, 6834.
23. B. Xiao, P. J. Byrne, P. S. Wheatley, D. S. Wragg, X. B. Zhao, A. J. Fletcher, K. M. Thomas, L. Peters, J. S. O. Evans, J. E. Warren, W. Z. Zhou and R. E. Morris, *Nat. Chem.*, 2009, **1**, 289.
24. S. K. Ghosh, J. P. Zhang and S. Kitagawa, *Angew. Chem. Int. Ed.*, 2007, **46**, 7965.

25. D. F. Martin, W. C. Fernelius and M. Shamma, *J. Am. Chem. Soc.*, 1959, **81**, 130.
26. G. M. Sheldrick, *Acta Crystallogr. Sect. A*, 2008, **64**, 112.

Chapter 5 – The use of Dipyridyl β-diketonate Complexes as Metalloligands in the Formation of Mixed-Metal Networks

5.1 Introduction

Mixed-metal organic frameworks (MMOFs) are an intriguing class of network materials as they contain two different metal centres that can have separate structural and/or functional roles within the network. The most common way to make this class of compounds is a one pot synthesis, but predicting the products formed is very hard. However, there has been a move more recently to adopt a stepwise synthetic approach. This involves the reaction of a bifunctional ligand with a metal to obtain an intermediate complex, also known as a metalloligand. This can then be reacted further with another metal to give the MMOF (Figure 5.1).

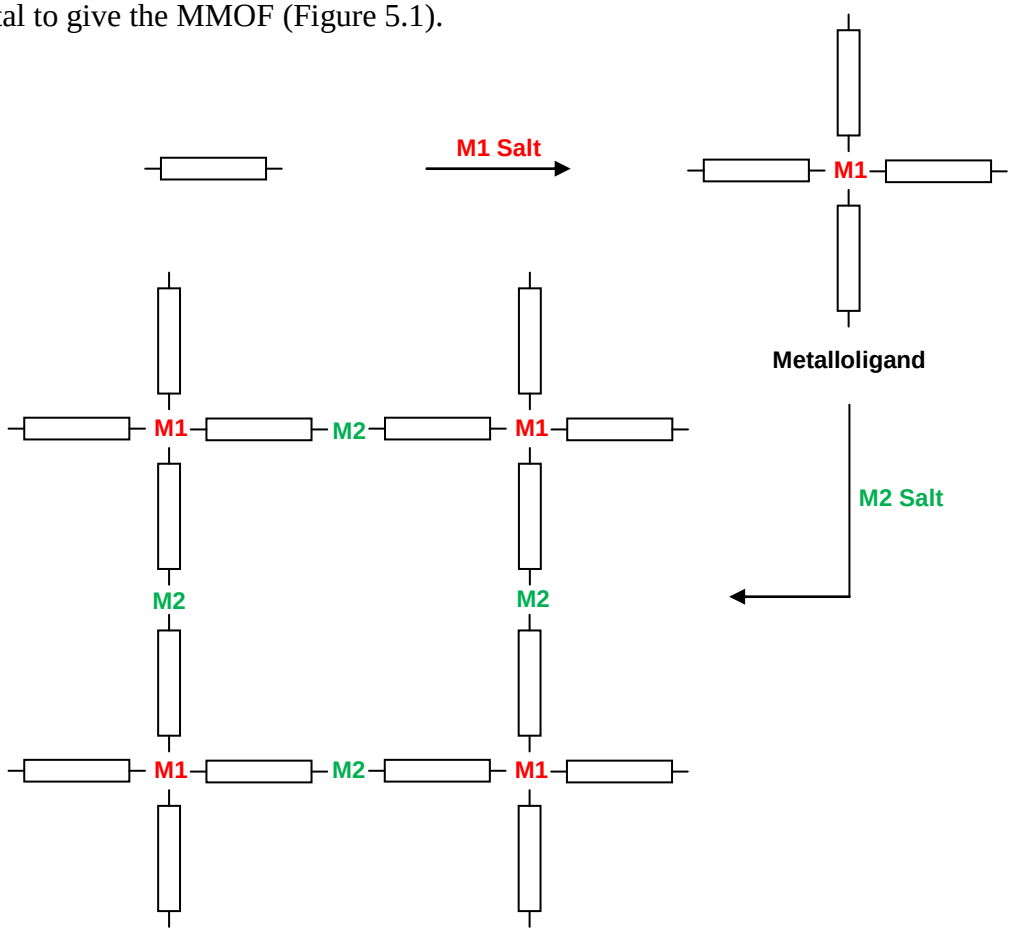

Figure 5.1: Schematic representation of the construction of a mixed-metal organic framework

There have been many examples in the literature which adopt this type of strategy to construct MMOFs. *Kitagawa et al*. developed the use of the metalloligand $[Cu(2,4\text{-pydca})_2(H_2O)]^{2-}$ (2,4-pydca = pyridine-2,4-dicarboxylate) which they reacted with a variety of other metal centres. This copper complex contains two distinct coordination groups, the 4-carboxylate and the 2-carboxylate. In the metalloligand, the 2-carboxylate

and pyridyl nitrogen atoms are involved in chelation to the copper atom, and the 4-carboxylate remains uncoordinated. This metalloligand was reacted with cobalt(II), and a one dimensional chain polymer was formed. The copper centre has a distorted square pyramidal geometry, with two sets of NO donor atoms from the 2,4-pydca and a coordinated water molecule in the axial position. Similarly, the cobalt centre also has distorted square pyramidal geometry with two coordination sites taken up by one oxygen atom from each of two carboxylate groups, with the other three sites being occupied by coordinated water molecules. The one dimensional chains pack in such a way that they are involved in interchain hydrogen bonding with adjacent chains (Figure 5.2).[1]

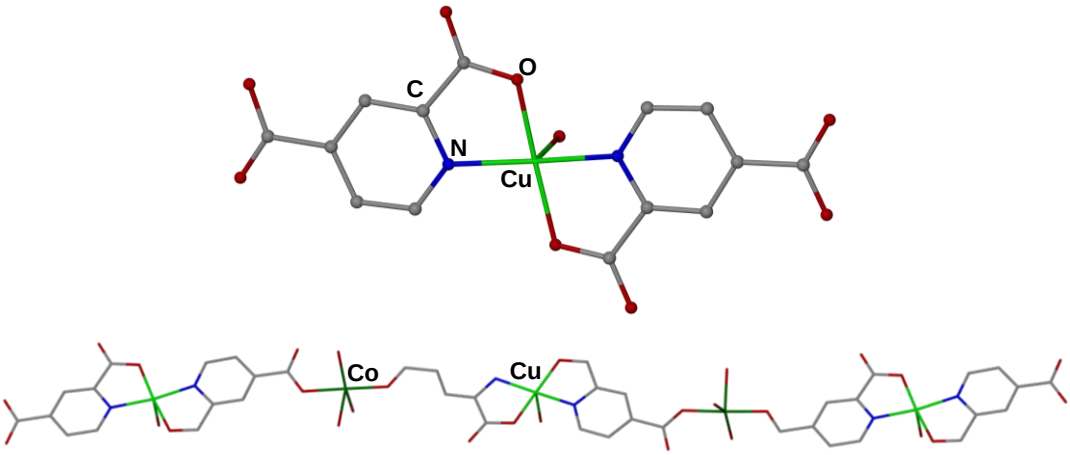

Figure 5.2: Metalloligand $[Cu(2,4\text{-}pydca)_2(H_2O)]^{2-}$ (2,4-pydca = pyridine-2,4-dicarboxylate) (top) and the one dimensional chain of $[Cu(2,4\text{-}pydca)_2(H_2O)Co_2(H_2O)_4]$ (bottom). Hydrogen atoms and guest molecules have been omitted for clarity[1]

There are also examples where polytopic nitrogen donor ligands have been used to construct metalloligands. One such case reported by *Robson et al*. involved the incorporation of porphyrins that had pyridyl functionalities which could coordinate to another metal. They used the metalloligand copper(II) 5,10,15,20-tetra(4-pyridyl)-21H, 23H-porphine (Cu(II)(tpp)), and reacted this further with a $Cu(I)(CH_3CN)BF_4$ to form the three dimensional network $[Cu(II)(tpp)Cu(I)]^+$. The copper(II) centre is located in the porphyrin with approximate square planar geometry and the copper(I) centres coordinate to four pyridyl groups with approximate tetrahedral geometry. The structure extends into a three dimensional network with large channels, with an approximate dimension of 14.2 Å. These channels contain highly disordered counter ions and solvent molecules which could not be reliably located (Figure 5.3).[2]

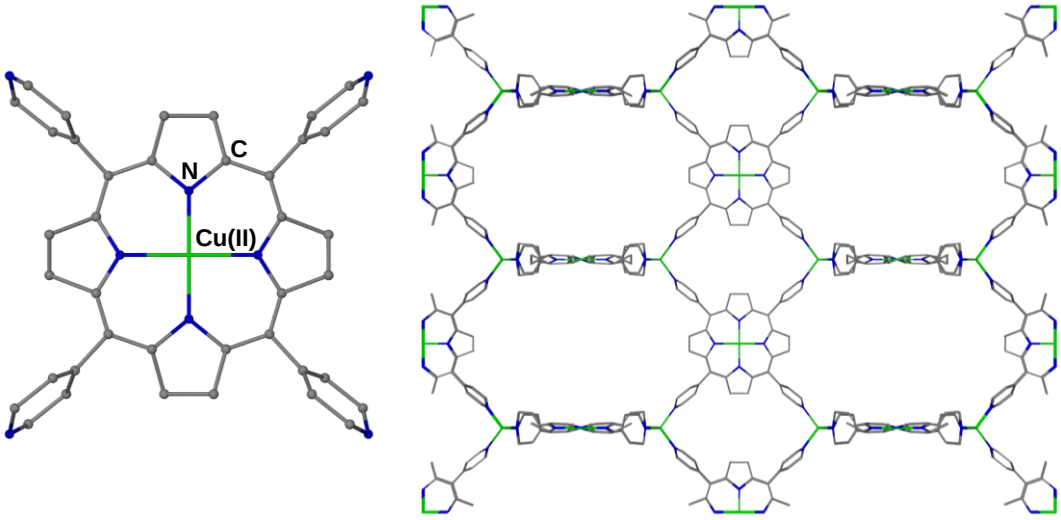

Figure 5.3: [Cu(II)(tpp)] metalloligand (left), and the three dimensional network of [Cu(II)(tpp)Cu(I)]$^{+}$ (right). Hydrogen atoms, solvent molecules and counter ions have been omitted for clarity

Other systems containing nitrogen donor ligands have also been investigated, including dipyrrinato ligands[3, 4], terpyridines[5, 6] and tris(triazolyl) borates.[7]

Acetylacetonates are attractive ligands for the use in the construction of MMOFs. They contain bidentate *O,O*-donor sites, which give access to neutral complexes with relatively low lability, they can also be substituted in several positions to form metalloligands. *Burrows et al*. have recently reported the use of 3-cyanoacetylacetonate (caa) to form copper(II), iron(III) and aluminium(III) metalloligands. The [Fe(caa)$_3$] (Figure 5.4) complex was synthesised and reacted further with silver(I) nitrate. This formed the one dimensional chain structure [Fe(caa)$_3$·AgNO$_3$] (Figure 5.5). The iron centre has a distorted octahedral geometry coordinating to six oxygen atoms from three ligands. Each silver centre has approximate trigonal planar geometry coordinating to one oxygen atom from the nitrate counter ion and two nitrogen atoms from the cyanide groups. The AgNO$_3$ units bridge the Fe(caa)$_3$ moieties, linking the structure into one dimensions. One of the three cyanide groups is uncoordinated which prevents the cross linking of the chains into two or three dimensional networks.[8]

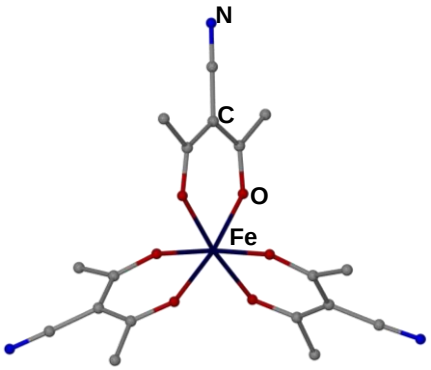

Figure 5.4: The metalloligand of [Fe(caa)$_3$]. Hydrogen atoms have been omitted for clarity[8]

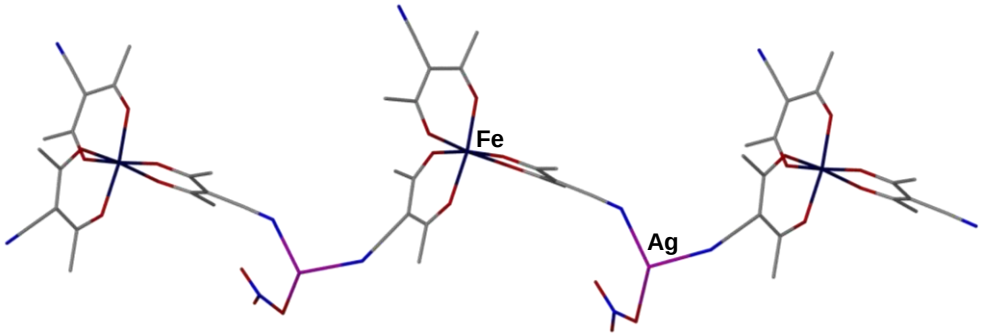

Figure 5.5: The one dimensional chains of [Fe(caa)$_3$·AgNO$_3$]. Hydrogen atoms have been omitted for clarity[8]

In a similar manner, *Domasevitch et al.*[9, 10] and *Maverick et al.*[11, 12] have incorporated 3-(4-pyridyl)acetylacetonate (paa) into the MMOF construction. The limitation of this ligand and 3-cyanoacetylacetonate is that they are substituted at the 3- position, thereby only offering three donor groups. The ligand paa has also been shown to be unstable to decomposition via a reverse Claisen condensation.[13] For these reasons *Burrows et al*. investigated the use of β-diketonates functionalised at both ends with 4-pyridyl or 3-pyridyl groups. This removes the instability issues whilst increasing the number of possible nitrogen coordination sites, augmenting the connectivity of the resultant MMOFs. The two diketonate ligands used were 1,3-di(4-pyridyl)propane-1,3-dione (H4L) and 1,3-di(3-pyridyl)propane-1,3-dione (H3L) (Figure 5.6). These choices offered the potential to form octahedral metalloligands of the form [M(L)$_3$] containing six sites in which a second metal coordination could occur, with [M(4L)$_3$] having the donor sites oriented approximately at the vertices of an octahedron.

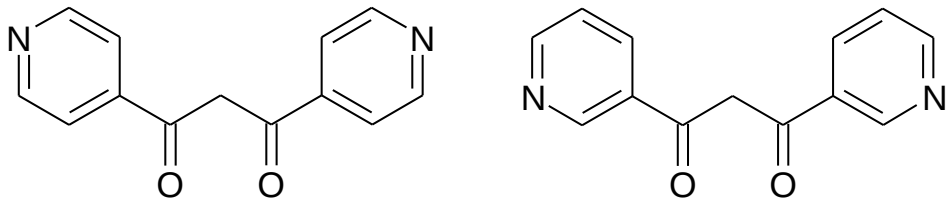

Figure 5.6: The two diketonate ligands 1,3-di(4-pyridyl)propane-1,3-dione (H4L) (left) and 1,3-di(3-pyridyl)propane-1,3-dione (H3L) (right)

The use of the H4L ligand has been reported by *Junk et al*. to construct the complex $[Gd(4L)_3(H_2O)]\cdot 4H_2O$. The gadolinium centre is eight coordinate with approximate square anti-prismatic geometry, coordinating to six oxygen atoms from three chelating diketonate groups, one oxygen from a coordinated water molecule and a bridging pyridyl nitrogen atom from an adjacent unit. The coordination to this nitrogen atom causes the structure to form one dimensional chains (Figure 5.7).[14] The ligands have not been used previously to construct MMOFs.

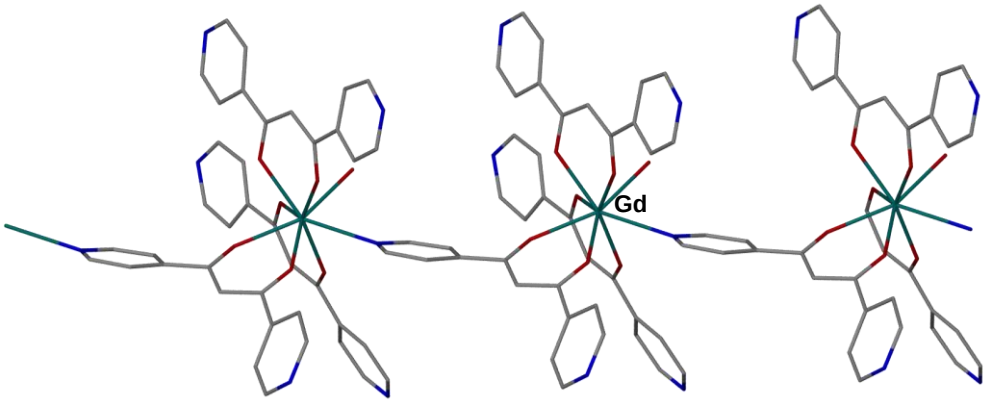

Figure 5.7: One dimensional chain structure of $[Gd(4L)_3(H_2O)]\cdot 4H_2O$. Hydrogen atoms and solvent molecules have been omitted for clarity[14]

Previous work in the Burrows research group using these ligands had mainly focussed on the use of the iron metalloligands $[Fe(4L)_3]$ and $[Fe(3L)_3]$. These iron complexes were reacted with a variety of silver(I) salts to assess the effect of the counter ion on the networks formed. One such example was the MMOF $[Fe(4L)_3Ag]BF_4\cdot 2DMSO$ (Figure 5.8). The iron centres exist with approximate octahedral geometry coordinating to six oxygen atoms from three 4L ligands. Four of the six free nitrogen atoms on the pyridyl groups of this metalloligand coordinate to silver centres, giving these distorted tetrahedral geometry. All the pyridyl groups

coordinated to the silver centres are from adjacent [Fe(4L)$_3$] units. The linking of the iron atoms to the silver centres forms hexagonal channels, where the six vertices are occupied by alternate iron and silver atoms, and the edges of the channels are occupied by a 4L ligand. Due to the fact that only four of the six free nitrogen atoms are coordinated, one dimensional hexagonal tubes are formed and the network does not extend into three dimensions (Figure 5.9).

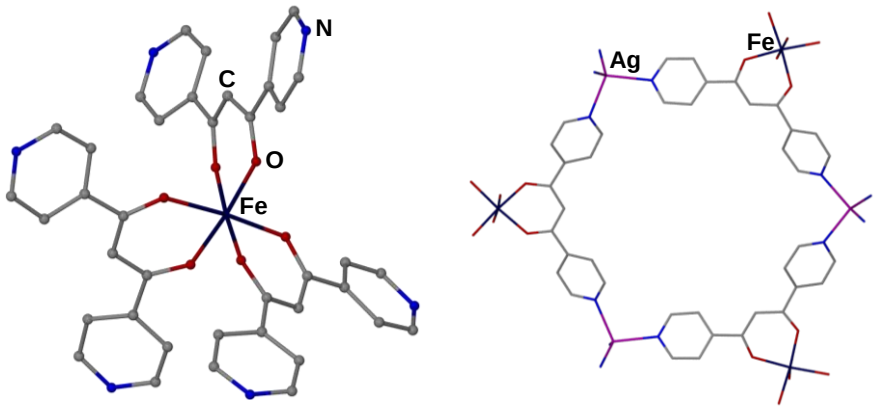

Figure 5.8: Metalloligand of [Fe(4L)$_3$] (left) and one hexagonal ring of [Fe(4L)$_3$Ag]BF$_4$·2DMSO (right). Hydrogen atoms, solvent molecules and counter ions have been omitted for clarity

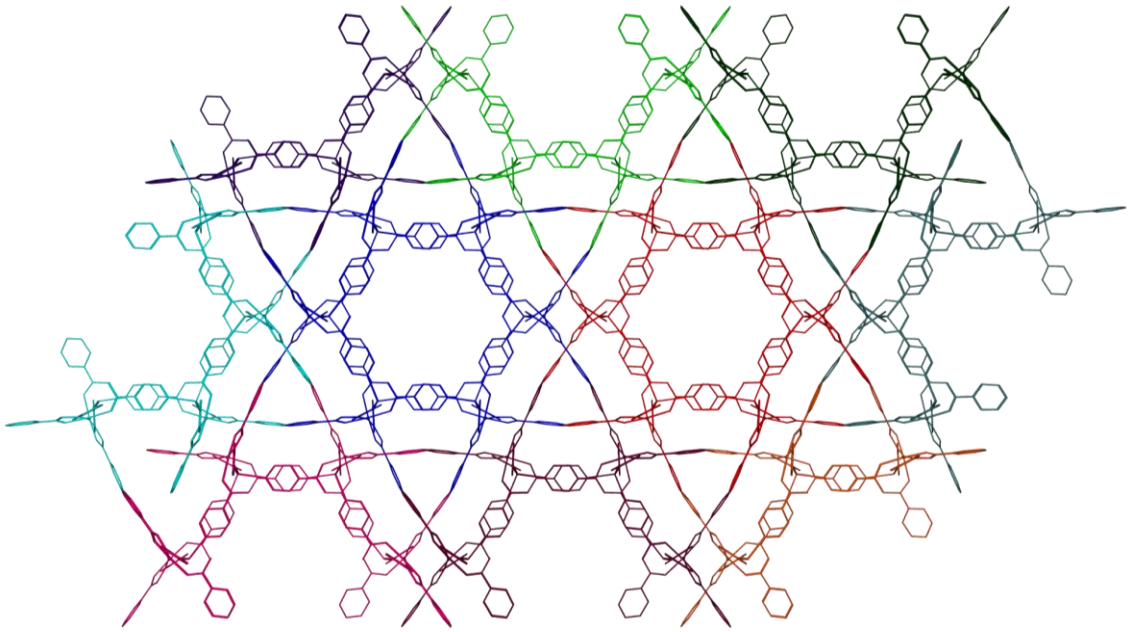

Figure 5.9: The packing of [Fe(4L)$_3$Ag]BF$_4$·2DMSO with each one dimensional tube shown in a different colour. Hydrogen atoms, solvent molecules and counter ions have been omitted for clarity

The aim of the research in this chapter was to use these ligands to extend on the range of networks already synthesised. In particular the use of the H4L ligand is intriguing, because the metalloligand formed would have approximate octahedral geometry. If all six pyridyl nitrogen atoms would then coordinate to a second metal with approximate linear geometry, a three dimensional cubic type network would form. Investigations were carried out to try and form this three dimensional network.

Much of the research within the Burrows group to date has focussed on the use of transition metals as the basis for the metalloligand. Here, Group 13 and lanthanide metals are studied to investigate the effects of the metal on structure formation. The Group 13 metals should adopt similar coordination to the transition metals, however lanthanides are known to exist with larger coordination numbers. If an eight coordinate complex could be obtained, with four β-diketonate ligands, then interesting MMOFs could be obtained through the coordination of a second metal. The synthesis of a $[Ln(4L/3L)_4]^{n-}$ complex would have eight donor sites available for coordination, thus potentially leading to new networks.

There are already reported examples of lanthanide containing structures in the literature which contain four diketonate ligands.[15, 16] One example is the compound $Et_3NH[Eu(dbm)_4]$ (dbm = dibenzoylmethanato), where the eight coordinate europium centre has four coordinated dbm ligands (Figure 5.10). This compound has been shown to be an excellent candidate for triboluminescence. However, the problem with this structure in terms of MOF chemistry is that there are no additional functionalities present to coordinate a second metal. For this reason H3L and H4L were studied in the coordination to lanthanide metals, to form $[Ln(3L/4L)_4]^{n-}$ complexes that can then be reacted with a range of silver(I) salts. Silver salts were used due to their coordination flexibility, with the ability to form a range of different geometries.

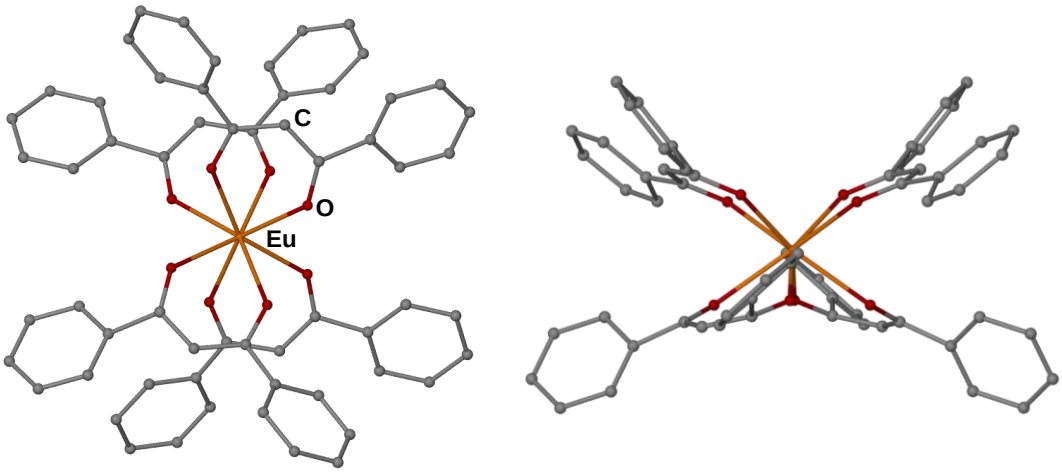

Figure 5.10: The structure of $Et_3NH[Eu(dbm)_4]$ viewed from above (left) and the side (right). Hydrogen atoms and counter ions have been omitted for clarity[16]

5.2 Results

5.2.1 Group 13 Metal Complexes

The first series of materials synthesised contained the Group 13 metals aluminium and gallium. Both these metal nitrate salts were reacted with H4L to form the octahedral $[M(4L)_3]$ complexes that could then be reacted with a second metal salt to form MMOFs.

Aluminium(III) nitrate and gallium(III) nitrate were reacted with 1,3-di(4-pyridyl)propane-1,3-dione (H4L) in water and sodium hydroxide to form $[Al(4L)_3]\cdot 1.25C_6H_5Me$ (**1**) and $[Ga(4L)_3]$ (**2**). The products were washed and purified several times, and then recrystallised from dichloromethane/toluene. From the $Al(NO_3)_3$ reaction yellow block crystals of **1** were produced of approximate dimensions 0.50 x 0.50 x 0.30 mm which were suitable for X-ray structure determination. The gallium reaction did not produce crystals suitable for single crystal X-ray diffraction. However, NMR, elemental analysis and mass spectrometry were carried out on the gallium sample, and confirmed the product to have the same formula as **1**. The crystal data for compound **1** is shown in Table 5.1.

Empirical formula	$C_{47.50}H_{37}AlN_6O_6$
M	817.81
***T*/ K**	150(2)
Crystal system	Triclinic
Space group, *Z*	*P*-1, 2

***a*/ Å**	11.9780(1)
***b*/ Å**	12.5850(1)
***c*/ Å**	14.3390(2)
***α*/ º**	87.816(1)
***β*/ º**	84.052(1)
***γ*/ º**	79.823(1)
***U*/ Å ^{3}**	2115.61(4)
Absorption coefficient/ mm^{-1}	0.105
***F*(000)**	853
Theta range for data collection/ º	3.56 to 30.16
Reflections collected/ observed [$I>2\sigma(I)$]	39978/ 8909
Data Completeness	0.981
Goodness-of-fit on F^2	1.029
Final *R* indices [$I>2\sigma(I)$]	$R1$ = 0.0633, $wR2$ = 0.1713
***R* indices (all data)**	$R1$ = 0.0933, $wR2$ = 0.1945
Largest diff. peak and hole Å $^{-3}$	0.951 and -0.423

*Table 5.1: Crystallographic data for $[Al(4L)_3]\cdot 1.25C_6H_5Me$ (**1**)*

The asymmetric unit for **1** (Figure 5.11) consists of one aluminium centre, three coordinated 4L ligands, one full molecule of toluene and one half of a toluene fragment at 50 % occupancy proximate to a crystallographic inversion centre. Consequently, the methyl group of this toluene molecule is disordered due to the symmetry, and exhibits 25 % site occupancy.

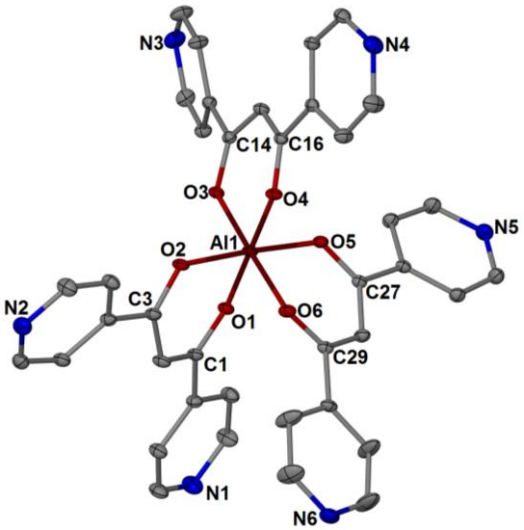

*Figure 5.11: The asymmetric unit of $[Al(4L)_3]\cdot 1.25C_6H_5Me$ (**1**) showing thermal ellipsoids at the 30% probability level. Hydrogen atoms and solvent molecules have been omitted for clarity*

As expected, the aluminium centre has distorted octahedral geometry, with *cis* angles ranging from 88.84(6) to 91.27(6)°. The AlO_2C_3 chelate rings are non-planar, with the aluminium atom sitting out of plane of the ligand atoms in the ring. The angles between the AlO_2 plane and O_2C_3 planes exemplify this distortion and are 18°, 16° and 26° for the three ligands. Due to these constraints the orientations of the pyridyl groups are also affected. For an ideal octahedron the angles between the lone pairs on the pyridyl groups would be expected to lie 90° and 180° to each other. However, in reality the angles between these lone pairs within a ligand range between 117° and 122°, and for lone pairs on different ligands range from 69° to 113° for the *cis* positions and between 155° and 175° for the *trans* positions. This distortion from octahedral geometry can also be quantified by the range in the N···N distances, these range from 7.43 to 11.40 Å for the *cis* position and 13.39 to 13.59 Å for the *trans* positions.

Elemental analysis, mass spectrometry and ^{13}C and ^{1}H NMR were carried out on **1**. The results from these analyses confirm the presence of compound **1**, as well as the purity of the sample.

Compounds **1** and **2** were then reacted further with silver(I) nitrate to try and synthesise a MMOF. Silver(I) salts were used due to the coordination flexibility of the metal.

The reactions of either **1** or **2** with silver(I) nitrate in hot DMSO produced solid products overnight, which were separated by filtration. Acetone was allowed to vapour diffuse into the filtrate producing crystals of $[Al(4LAg)_3](NO_3)_3 \cdot 4DMSO$ (**3**) and $[Ga(4LAg)_3](NO_3)_3 \cdot 3DMSO$ (**4**) suitable for single crystal X-ray analysis. The relevant crystal data is given in Table 5.2.

Empirical formula	$C_{47}H_{51}AlN_9O_{19}Ag_3S_4$	$C_{50}H_{55}Ag_3N_{10}O_{19}Ga$
M	1524.80	1505.38
***T*/ K**	173(2)	150(2)
Crystal system	Hexagonal	Hexagonal
Space group, *Z*	*R*3*c*, 18	*R*3*c*, 18
***a*/ Å**	22.4562(3)	22.9930(6)
***b*/ Å**	22.4562(3)	22.9930(6)
***c*/ Å**	72.1481(4)	71.297(2)
***α*/ º**	90	90

β/ °	90	90
γ/ °	120	120
U/ Å ^{3}	31508.5(6)	32643.2(16)
Absorption coefficient/ mm^{-1}	8.419	1.230
***F*(000)**	13788	13590
Theta range for data collection/ °	3.82 to 36.20	3.51 to 23.25
Reflections collected/ observed [I>2σ(I)]	57004/ 10519	90151/ 6998
Data Completeness	0.967	0.991
Goodness-of-fit on F^2	1.006	1.076
Final *R* indices [I>2σ(I)]	$R1$ = 0.0719, $wR2$ = 0.1893	$R1$ = 0.0883, $wR2$ = 0.2698
***R* indices (all data)**	$R1$ = 0.0767, $wR2$ = 0.1945	$R1$ = 0.1102, $wR2$ = 0.2856
Largest diff. peak and hole Å $^{-3}$	2.332 and -0.432	0.916 and -0.919

*Table 5.2: Crystallographic data for $[Al(4LAg)_3](NO_3)_3$·4DMSO (**3**) and $[Ga(4LAg)_3](NO_3)_3$·3DMSO (**4**)*

The asymmetric unit for **3** (Figure 5.12) consists of three independent thirds of aluminium centres, three full ligands, one coordinated to each aluminium centre, and three full occupancy silver centres coordinated to one pyridyl group on each ligand. The nitrate counter ions and DMSO solvent molecules were highly disordered, so the PLATON SQUEEZE algorithm was used to estimate the proportion of each. Three nitrate anions were assigned due to the charge of the complex, and the remaining electron density was assigned to four molecules of DMSO per asymmetric unit.

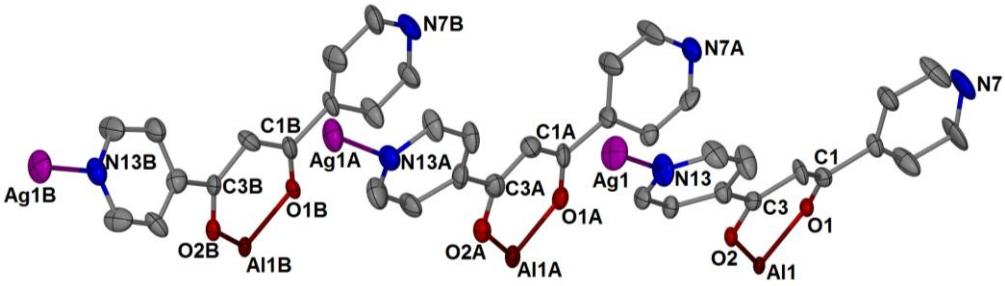

*Figure 5.12: The asymmetric unit of $[Al(4LAg)_3](NO_3)_3$·4DMSO (**3**) showing thermal ellipsoids at the 30% probability level. Hydrogen atoms, solvent molecules and counter ions have been omitted for clarity*

Each aluminium centre has distorted octahedral geometry which is broadly equivalent to the geometry observed in **1**. The distortion however is less than seen for **1**, with the angles between the C_3O_2 planes and AlO_2 planes reducing to 17°, 17° and 4°. Each pyridyl nitrogen atom is involved in coordination to a silver centre, which exists with approximate linear geometry, with slight distortions from linearity, with N-Ag-N angles of 166.6(3), 168.5(3) and 168.9(2)°. These slight distortions compensate for the irregularities in the arrangements of the pyridyl groups within the metalloligands.

Due to the octahedral nature of the metalloligand and the linear coordination of the silver atoms, the structure extends into a three dimensional cubic type network, where the metalloligand comprises the vertices of the cube, and the silver(I) centres form the edges. Due to the size of the pores present within the system, the structure is triply interpenetrated (Figure 5.13). This is a different strategy towards the formation of a cubic network to what has previously been observed. For example, in MOF-5[17] the $Zn_4O(O_2CR)_6$ SBU forms the vertices of the cubes, whilst the benzenedicarboxylate linker forms the edges. These new materials afford metal centres positioned within the MOF walls, and these are available for further post-synthetic network modifications.

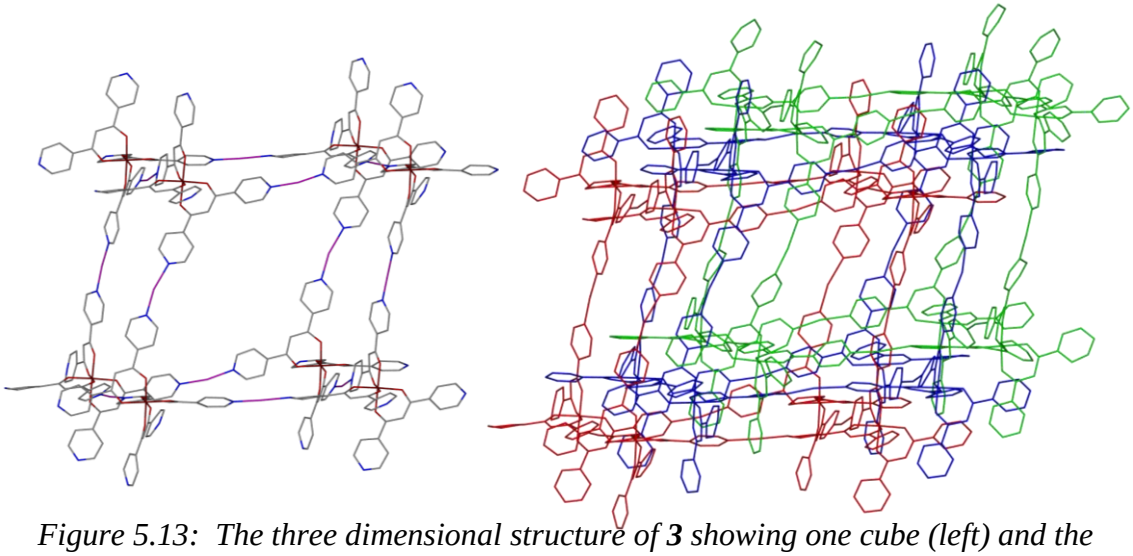

*Figure 5.13: The three dimensional structure of **3** showing one cube (left) and the triply-interpenetrated structure shown in three different colours (right). Hydrogen atoms, solvent molecules and counter ions have been omitted for clarity*

Compound **4** $[Ga(4LAg)_3](NO_3)_3 \cdot 3DMSO$ produced an isostructural material to **3**, the only major difference was the smaller proportion of DMSO solvent molecules within the pores. This structure will not be discussed in detail.

The materials **1** and **2** contain the same formula and are constructed from aluminium

and gallium respectively. These results suggest that increasing the size of the metal centre has no effect on the structure formed. Similarly, **3** and **4** also produce isostructural MMOFs, again showing that the size of the metal has no overall effect on the networks formed. The only difference between **3** and **4** is the proportion of DMSO housed within the pores.

5.2.2 Lanthanide Metal Complexes

After the interesting results obtained for samples **1**-**4** with Group 13 metals, lanthanide metals were also investigated to look at the effects on the complexes formed.

Three new materials were synthesised with lanthanide metals and H4L and H3L. The first material was synthesised from europium(III) chloride and H4L in ethanol. This reaction produced yellow block crystals of $[Eu(H4L)_3(H_24L)]Cl_4{\cdot}EtOH$ (**5**). The effect of the ligand was then tested by synthesising $[Eu(3L)_2(H_2O)_4]Cl{\cdot}2EtOH{\cdot}0.5H_2O$ (**6**) from the reaction of europium(III) chloride, H3L and potassium *tert*-butoxide in ethanol. Finally $[La(3L)_3(H_2O)]{\cdot}2H_2O$ (**7**) was synthesised from the same reaction as **6**, but with lanthanum(III) nitrate, to understand the effect of the metal centre on the complex formed. All three reactions produced crystals of suitable size for single crystal X-ray diffraction. The crystal data for these products is shown in Table 5.3.

Compound	**5**	**6**	**7**
Empirical formula	$C_{54}H_{47}C_{l4}EuN_8O_9$	$C_{30}H_{39}ClEuN_4O_{10.50}$	$C_{39}H_{33}LaN_6O_9$
M	1245.76	811.06	868.62
***T*/ K**	150(2)	150(2)	150(2)
Crystal system	Orthorhombic	Triclinic	Orthorhombic
Space group, *Z*	*Fddd*, 8	*P*-1, 2	$P2_1ca$, 4
***a*/ Å**	15.1070(4)	9.8170(3)	9.7470(2)
***b*/ Å**	27.3860(7)	12.8910(4)	12.7120(2)
***c*/ Å**	29.0380(7)	13.8310(6)	31.1260(5)
***α*/ º**	90	87.802(1)	90
***β*/ º**	90	79.328(1)	90
***γ*/ º**	90	79.802(2)	90
***U*/ Å ^{3}**	12013.6(5)	1692.85(10)	3856.63(12)
Absorption coefficient/ mm^{-1}	1.279	1.993	1.170
***F*(000)**	5040	822	1752

Theta range for data collection/ °	4.02 to 25.02	3.54 to 27.36	3.64 to 25.02
Reflections collected/ observed [*I*>2σ(*I*)]	47751/ 2424	7615/ 4758	34837/ 4569
Data Completeness	0.993	0.740	0.992
Goodness-of-fit on F^2	1.192	1.124	1.035
Final *R* indices [*I*>2σ(*I*)]	*R*1 = 0.0502, *wR*2 = 0.1079	*R*1 = 0.0477, *wR*2 = 0.1159	*R*1 = 0.0485, *wR*2 = 0.0848
***R* indices (all data)**	*R*1 = 0.0602, *wR*2 = 0.1223	*R*1 = 0.0602, *wR*2 = 0.1220	*R*1 = 0.0962, *wR*2 = 0.0998
Largest diff. peak and hole Å $^{-3}$	0.513 and -0.353	1.959 and -1.075	0.767 and -0.671

*Table 5.3: Crystallographic data for compounds $[Eu(H4L)_3(H_24L)]Cl_4{\cdot}EtOH$ (**5**), $[Eu(3L)_2(H_2O)_4]Cl{\cdot}2EtOH{\cdot}0.5H_2O$ (**6**) and $[La(3L)_3(H_2O)]{\cdot}2H_2O$ (**7**)*

The asymmetric unit for **5** (Figure 5.14) consists of a quarter of a europium atom, situated on a special position, one chloride anion, a diffuse region of ethanol solvent, which equates to about one solvent molecule, and one ligand. The pyridyl groups of the ligands are in two states of protonation, where the H4L ligand is zwitterionic 75 % of the time, with one pyridyl group protonated, and the $H_2$4L ligand is cationic 25 % of the time with both pyridyl groups protonated.

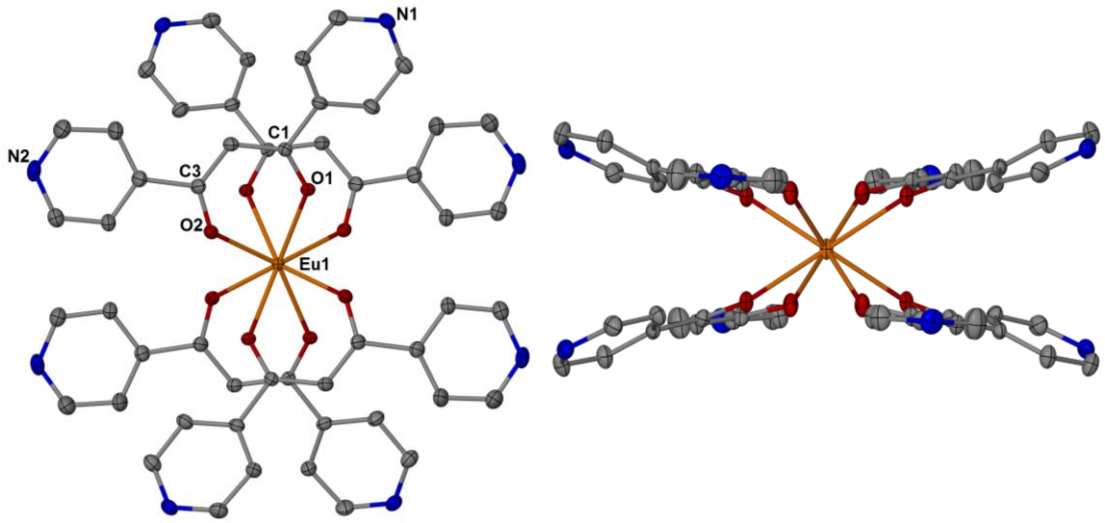

*Figure 5.14: The structure of $[Eu(H4L)_3(H_24L)]Cl_4{\cdot}EtOH$ (**5**) viewed from above (left) and the side (right). Part of the structure has been labelled and hydrogen atoms and counter ions have been omitted for clarity*

The europium centre is eight coordinate with approximate square anti-prismatic geometry. The europium centre coordinates to eight oxygen atoms from four diketonate ligands [Eu(1)-O 2.338(3) – 2.419(3) Å], these bond lengths correspond well with

$Et_3NH[Eu(dbm]$ (Figure 5.10).[16] The pyridyl nitrogen lone pairs and the pyridinium NH groups lie approximately co-planar due to a distortion of 27° between the C_3O_2 plane and the O_2Eu plane of the ligand chelate ring.

The structure is linked into two dimensional sheets by short N-H···N hydrogen bonds between protonated and neutral pyridine groups [N(1)···N(1)^{i} 2.730 Å, H(1)···N(1)^{i} 1.84 Å, N(1)–H(1)···N(1)^{i} 172°] (Figure 5.15). There are however no interactions between each two dimensional sheet. There are also additional N-H···Cl hydrogen bonds where the chloride anion acts as an acceptor [N(2)···Cl(1) 2.992 Å, H(2)···Cl(1) 2.13 Å, N(2)–H(2)···Cl(1) 161°] (Figure 5.16).

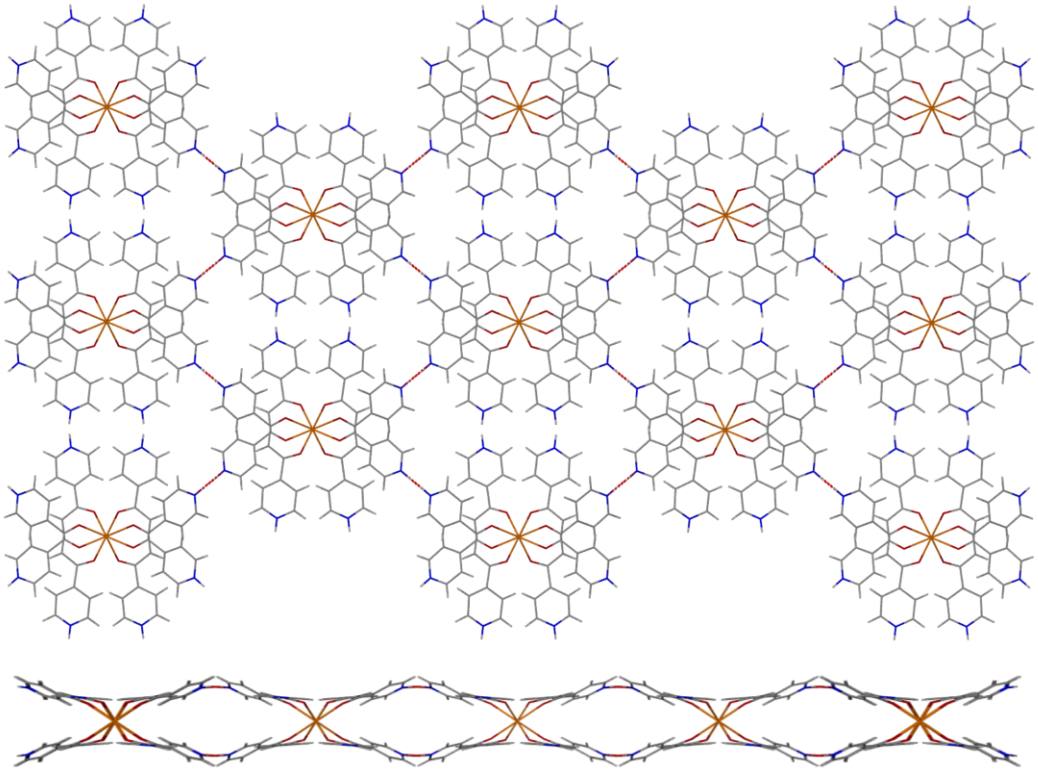

*Figure 5.15: The sheet structure observed in **5** viewed from above (top) and the side (bottom). Solvent molecules and counter ions have been omitted for clarity*

Symmetry transformations used to generate equivalent atoms:
[i] -x 1/4, y, -z 1/4

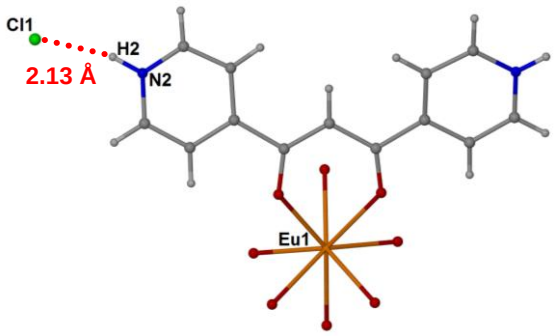

*Figure 5.16: The N-H···Cl hydrogen bonding present in **5**. Hydrogen bonds are shown in red*

The crystals of **5** rapidly lost solvent when removed from the mother liquor, and therefore powder X-ray diffraction had to be carried out in the solvent to ensure the solvent wasn't lost, and hence crystal decomposition did not occur. The trace recorded indicated the phase purity of the material; however it was not possible to obtain a suitable microanalysis due to this solvent loss.

Compound **5** can be compared to $Et_3NH[Eu(dbm)_4]$.[16] Both europium metal centres in each of these complexes have approximate square anti-prismatic geometry. The structure of **5** differs from $Et_3NH[Eu(dbm)_4]$ due to the presence of the protonated pyridyl groups which extend the structure into two dimensions through hydrogen bonding.

The synthesis of compound **6** differs from **5** due to the use of H3L over H4L. The asymmetric unit for compound **6** varies in terms of the number of ligands coordinated to the metal centre. The asymmetric unit consists of one europium atom, two full 3L ligands, four coordinated water molecules, one chloride counter ion disordered over two sites, two ethanol guest molecules disordered over three sites and half a water molecule (Figure 5.17).

Like compound **5**, the europium centre in **6** is eight coordinate with approximate square anti-prismatic geometry. The coordination sphere is completed by four Eu-O bonds from two 3L diketonate ligands [Eu(1)-O 2.374(5) – 2.396(4) Å] and four Eu-O bonds from coordinated water molecules [Eu(1)-O 2.388(4) – 2.430(4) Å]. The bond lengths are consistent with those in compound **5** and $Et_3NH[Eu(dbm)_4]$.[16] The EuO_2C_3 chelate

rings are approximately planar, with the angle between the C_3O_2 planes and the EuO_2 planes of 1° and 2°.

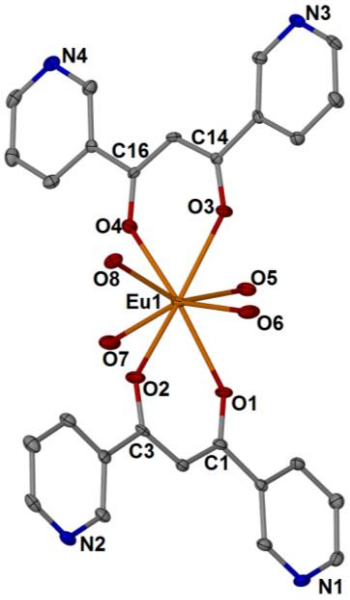

*Figure 5.17: The asymmetric unit of $[Eu(3L)_2(H_2O)_4]Cl{\cdot}2EtOH{\cdot}0.5H_2O$ (**6**) showing thermal ellipsoids at the 30% probability level. Hydrogen atoms, solvent molecules and counter ions have been omitted for clarity*

Compound **6** is a discrete complex ion, since the nitrogen atoms do not coordinate to neighbouring metal centres. However, the structure is linked into two dimensional sheets by short O-H···N hydrogen bonds between the coordinated water molecules and the adjacent pyridyl groups [O(6)···N(1)^{ii} 2.750 Å, H(6B)···N(1)^{ii} 1.854 Å, O(6)-H(6B)···N(1)^{ii} 173°, O(7)···N(2)^{iii} 2.742 Å, H(7B)···N(2)^{iii} 1.849 Å, O(7)-H(7B)···N(2)^{iii} 171°, O(5)···N(3)^{iv} 2.714 Å, H(5B)···N(3)^{iv} 1.856 Å, O(5)-H(5B)···N(3)^{iv} 159°, O(8)···N(4)^{v} 2.760 Å, H(8A)···N(4)^{v} 1.872 Å, O(8)-H(8A)···N(4)^{v} 169°] (Figure 5.18). There are, however, no interactions present between neighbouring two dimensional sheets.

Symmetry transformations used to generate equivalent atoms:
[ii] 1 -x, 1 -y, 2 -z
[iii] -x, 1 -y, 2 -z
[iv] 1 -x, 2 -y, 1 -z
[v] -x, 2 -y, 1 -z

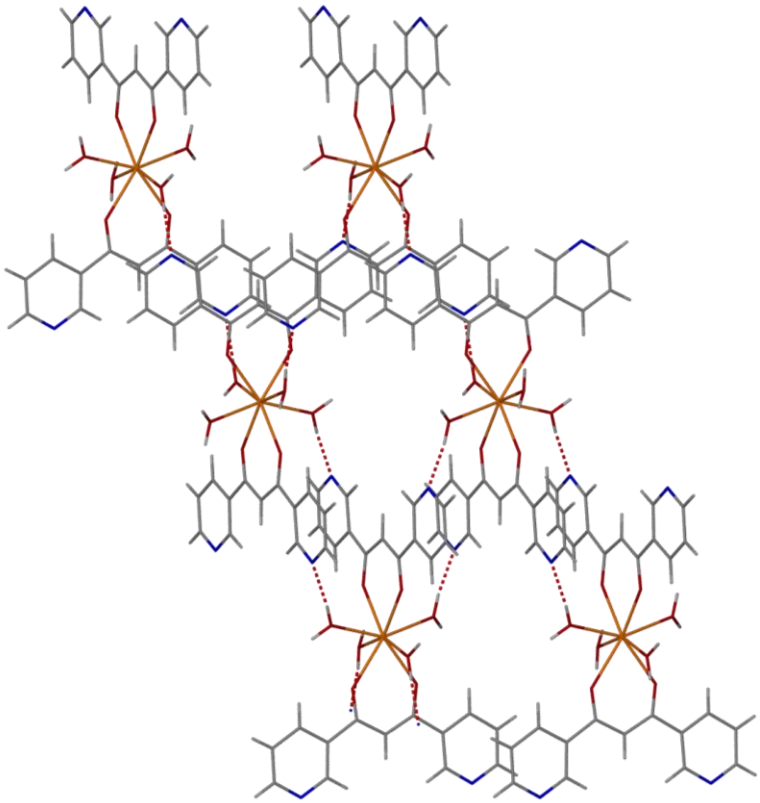

Figure 5.18: Hydrogen bonding present in ***6****, forming two dimensional sheets. Solvent molecules and counter ions have been omitted for clarity*

The structure of compound **6** is very different to **5**. Here only two 3L ligands are coordinated to the europium centre, with the coordination of the metal completed by four water molecules. In compound **5**, four 4L ligands are coordinated to the metal centre. Although this is the case, both structures are linked into two dimensional sheets by hydrogen bonding. However, in **5** this hydrogen bonding arises from partial protonation of the pyridyl groups, whereas in **6** is due to the presence of the coordinated water molecules. These two structures demonstrate the effect that the nitrogen atom positions in the diketonates have on the overall packing of the structures.

The effect of the metal centre was then investigated with H3L. In this case the europium metal was replaced by lanthanum to understand the effects of this on the gross network formed. The lanthanum compound **7** has an asymmetric unit consisting of one lanthanum centre, three coordinated 3L ligands and one coordinated water molecule. Within the lattice there are two guest water molecules (Figure 5.19).

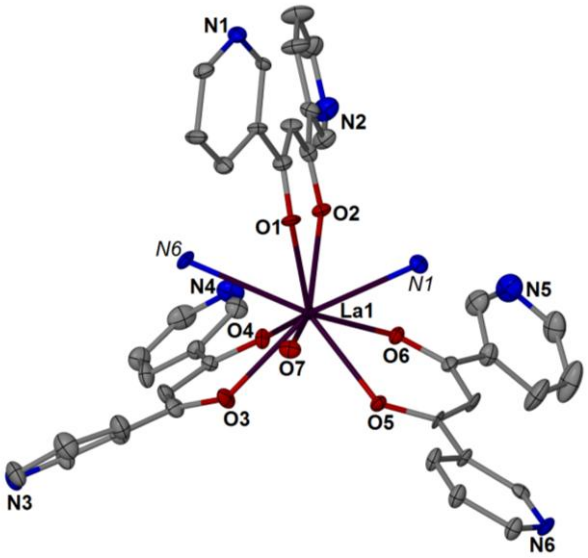

*Figure 5.19: The asymmetric unit of [La(3L)$_3$(H$_2$O)]·2H$_2$O (**7**) showing thermal ellipsoids at the 30% probability level. Symmetry generated atoms are labelled in italics. Hydrogen atoms and solvent molecules have been omitted for clarity*

Each lanthanum centre is nine coordinate with distorted tricapped trigonal prismatic geometry, coordinating to six oxygen atoms from three 3L diketonate ligands [La(1)-O 2.462(5) – 2.520(5) Å], one oxygen atom from a coordinated water molecule [La(1)-O(7) 2.640(5) Å] and two nitrogen atoms from adjacent diketonate pyridyl groups [La(1)-N(1)[vi] 2.725(6) Å, La(1)-N(6)[vii] 2.816(7) Å]. The bond lengths are comparable to previously reported materials which contain lanthanum metal centres and β-diketonate ligands.[18] The LaO_2C_3 chelate rings are non-planar, with the lanthanum atom sitting out of plane of the ligand atoms in each of the three rings. The angle between the LaO_2 plane and the O_2C_3 plane reflects this distortion and is 8°, 18° and 20° for the three diketonate ligands.

The coordination of the lanthanum to adjacent diketonate nitrogen atoms causes the structure to build up into double stranded one dimensional polymeric chains as can be seen in Figure 5.20. The free nitrogen atoms on either side of the chain are not involved in coordination to adjacent lanthanum centres, and this terminates the construction of the framework into two dimensions.

Symmetry transformations used to generate equivalent atoms:
[vi] 1/2 +x, 1 -y, -z
[vii] x -1, y, z

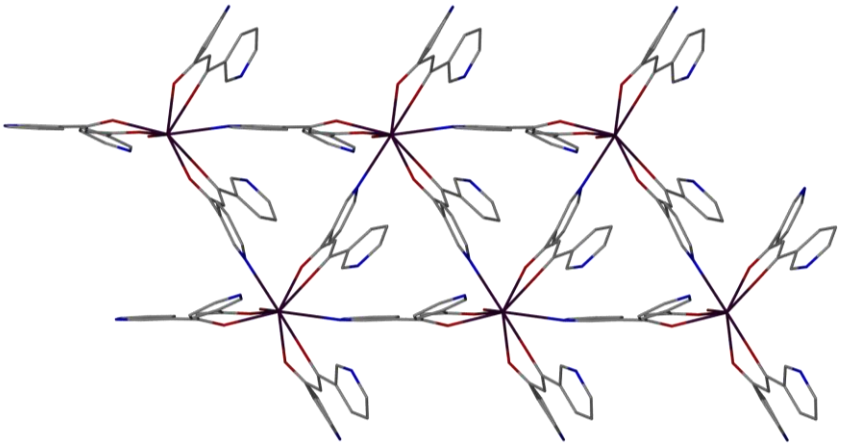

*Figure 5.20: One dimensional chains of **7**. Hydrogen atoms and solvent molecules have been omitted for clarity*

A two dimensional network however is formed through weak C-H···O hydrogen bonding between the aromatic CH groups and the coordinated oxygen atoms of the diketonates [C(23)···O(5)^{viii} 3.19 Å, H(23)···O(5)^{viii} 2.36 Å, C(23)-H(23)···O(5)^{viii}145°] (Figure 5.21).

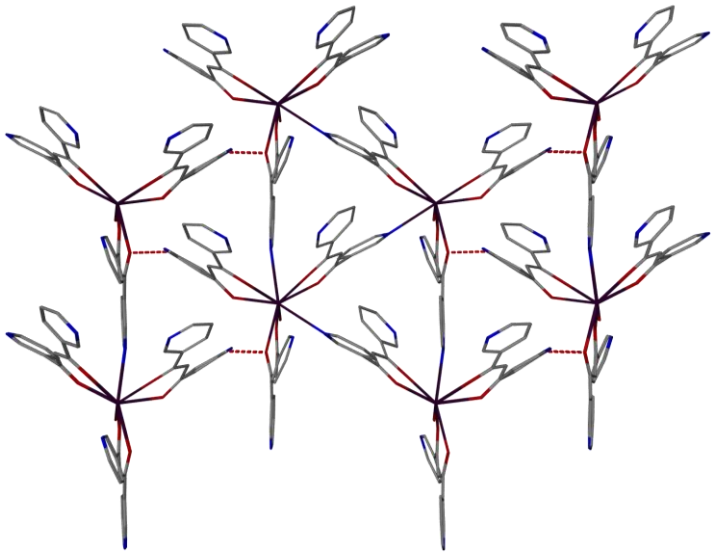

*Figure 5.21: C-H···O hydrogen bonding present within **7** creating a two dimensional network. Solvent molecules as well as all hydrogen atoms except those involved in hydrogen bonding have been omitted for clarity*

Compound **7** can be compared to the previously reported compound $[Gd(4L)_3(H_2O)]\cdot 4H_2O$ (Figure 5.7). In this structure one of the pyridyl nitrogen atoms coordinates to an adjacent gadolinium centre creating a one dimensional chain structure.

Symmetry transformations used to generate equivalent atoms:
^{viii} x -1/2, y, 1/2 -z

In contrast, in **7** two pyridyl nitrogen atoms coordinate to lanthanum centres and this forms a double stranded one dimensional polymer. The main difference observed between this structure and those of **5** and **6** is that a one dimensional network is formed through the coordination of the pyridyl nitrogen atoms to adjacent lanthanum centres. The structure also contains hydrogen bonding, forming a two dimensional network like **5** and **6**, although the gross packing is different. The direct comparison between **6** and **7** suggest that the change in the metal centre affects the product formed. Due to the larger size of the lanthanum metal centre, a nine coordinate metal centre is formed in comparison to the eight coordinate centre seen in **6**. This implies there is more space around this lanthanum centre to then coordinate adjacent pyridyl nitrogen atoms.

5.3 Conclusion

This chapter has shown the synthesis and characterisation of seven new compounds consisting of Group 13 and lanthanide metal complexes. They consist of a range of dimensionalities and some have also been used in the construction of MMOFs.

The results demonstrate how the use of the H3L and H4L ligands have overcome the instability issues observed in the diketonate ligands substituted in the three position, and how these ligands can then be incorporated into a variety of structures.

Compounds **1**-**4** were constructed from Group 13 metals and H4L, and show how the construction of MMOFs can be achieved through a two-step reaction forming a metalloligand as an intermediate. Lanthanide metals were then used in the construction of compounds **5**-**7**, and although these only contain one type of metal within the structures, they all still form two dimensional networks through hydrogen bonding.

The lanthanide complexes synthesised show how the H3L and H4L diketonate ligands can be incorporated into these systems. As expected, the coordination environments around the metal centres show higher coordination than observed for the aluminium and gallium structures.

The effect of the ligand has been shown in **5** and **6** with the use of H4L and H3L respectively. These structures show different coordination environments around the

europium metal centres, although both form two dimensional networks through hydrogen bonding.

The study of the change of metal centre was also investigated where europium was used in the formation of **6** and lanthanum in **7**. Again, two different structures were observed, with **6** forming a discrete complex ion and **7** forming a one dimensional chain through coordination of pyridyl nitrogen atoms to neighbouring lanthanum centres. Like **5** and **6**, through hydrogen bonding **7** forms a two dimensional network.

These crystal structures reveal that complexes containing these diketonate ligands or its protonated derivatives are versatile components in the formation of network structures, producing a variety of networks involving either a mixture of metals or hydrogen bonding.

5.4 Experimental

5.4.1 General

All starting materials were obtained commercially and used without further purification.

Powder diffraction measurements were recorded using a Bruker D8 powder diffractometer, fitted with Goebel mirrors, and using CuK_{α} radiation of wavelength 1.5414 Å. Samples were placed in 0.3 mm to 0.7 mm diameter Lindemann capillaries, and measured with a 2θ range of 4 - 60°. The step size was 0.02° with time per step of 1.00s.

Elemental analyses were conducted by Alan Carver (University of Bath).

NMR spectra were recorded at 298 K on a Bruker Avance 300 MHz NMR spectrometer, and referenced to residual *protio* solvent signals for ^{1}H NMR spectra ($CDCl_3$, δ 7.24) and to solvent resonances for $^{13}C\{^{1}H\}$ NMR ($CDCl_3$, δ 77.2).

Mass spectra were recorded on a Bruker MicrOTOF electrospray time-of-flight (ESI-TOF) mass spectrometer (Bruker Daltonik GmbH) coupled to an Agilent 1200 LC system (Agilent Technologies).

5.4.2 Crystallography

X-ray data for compounds **1, 4** and **5-7** were collected on a Nonius Kappa CCD diffractometer using Mo-K_α radiation, whereas compound **3** was analysed on an Oxford Diffraction instrument using Cu-K_α radiation. Unless noted below, all non-hydrogen atoms were refined anisotropically in the final least squares run, and hydrogen atoms were included at calculated positions. The structures were solved using SHELXS-97[19] and refined using full-matrix least squares in SHELXL-97.[19] Refinements were generally straightforward with the following exceptions and points of note.

Compound **1** contains a fragment of disordered toluene, proximate to a crystallographic inversion centre. Residual electron density in the difference Fourier map is proximate to this solvent fragment, which has been refined subject to restraints in the final least-squares cycles.

Several data collections were made for **3** in an effort to be completely certain about the space group assignment, and to model the disorder if possible. Ultimately, in the eighth instance an excellent data set (*R*int = 0.0275, *R*sigma = 0.0189, prior to SQUEEZE) was collected, which afforded good statistics and, equally importantly, bore none of the usual signs of merohedral/pseudo-merohedral twinning. The space groups possible were *R*–3*c* and *R*3*c*. The former did not afford a credible solution which, when the structure was solved, could be easily rationalised as there is no centre of inversion present either in the $Al(4L)_3$ moieties or in the gross structure. The nitrate anions were disordered, which suggests that they do not bind in any periodic way to the silvers, if indeed they bind at all. Thus, as stated the anions and the disordered solvent were treated with the PLATON SQUEEZE algorithm and given the diffuse nature of the solvent and the available volume, four molecules of DMSO have been included in the asymmetric unit. A correction for racemic twinning was also included in the refinement.

The structure of **4** suffered from the same issues as that of the isostructural aluminium analogue **3**. It was notable in this case that suitably sized samples for crystallography all contained an internal flaw, which has impacted on the *R*int of the data collected. Diffraction fall-off resulted in using data to a maximum resolution of 0.9 Å in the final least squares. To minimize the esds on that data, a three day data collection was undertaken. The nitrates were disordered, which again suggests that they do not bind in any way to the silvers. Therefore, the disordered anions had to be treated using

PLATON SQUEEZE. The remainder of the electron density was then assigned to three molecules of DMSO per asymmetric unit. Racemic twinning was also an issue in this sample, therefore a correction was included to account for this. 6-membered rings were treated as rigid hexagons, and the atomic displacement parameters in each were refined subject to similarity restraints.

The ligand in **5** is neutral for 75% of the time (*i.e.* one of the ligand nitrogen atoms is protonated), and positively charged for the remaining 25% of the time (*i.e.* both nitrogen atoms are protonated). The nitrogen-bound ligand hydrogen atoms are disordered such that a proton is located on N(1) in 65% of the structure, and another on N(2) in 60% of the structure. These partial occupancy atoms – H(1) and H(2) – were located and refined at a distance of 0.9 from the parent atoms. The solvent is proximate to crystallographic symmetry and could not be successfully resolved. Hence, PLATON SQUEEZE was utilized, which gave an estimate of one molecule of ethanol per europium, which has been included in the formulation.

The chloride anion in **6** was disordered over two sites in a 60:40 ratio, while two solvent ethanol molecules were disordered over three sites in a 75:75:50 ratio, based on the oxygen atoms of each moiety. Oxygen bound hydrogens in the lattice solvent could not be reliably located and hence were omitted from the final refinement. Those attached to the ligated waters were located readily however, and refined subject to distance restraints.

For compound **7**, water hydrogen atoms could not be reliably located and hence were omitted from the final refinement. Similarity restraints were applied to the atomic displacement parameters for carbons 37-39 during the final least-squares refinement cycles.

5.4.3 Synthesis of $[Al(4L)_3]\cdot 1.25C_6H_5Me$, 1

$Al(NO_3)_3\cdot 9H_2O$ (0.60 g, 1.60 mmol) dissolved in water (5 cm^3) was added dropwise to H4L (1.131 g, 5.00 mmol) dissolved in water (40 cm^3) containing NaOH (0.206 g, 5.15 mmol). The precipitated material was collected by filtration and washed with water (3 × 10 cm^3). The solid was taken up in dichloromethane (100 cm^3) and the solution dried over Na_2SO_4, filtered, and concentrated by rotary evaporation to *ca.* 20 cm^3. The solution was passed through a short column of Al_2O_3 eluting with dichloromethane –

methanol (98:2) then evaporated and the residue taken up in dichloromethane (20 cm^3) and diluted with toluene (100 cm^3). The crystals that formed overnight were harvested and washed sparingly with fresh toluene. Yield 1.099 g (84 %). Found: C, 70.0; H, 4.59; N, 10.2. $C_{47.75}H_{37}AlN_6O_6$ requires C, 70.1; H, 4.56; N, 10.3 %. δ_H ($CDCl_3$): 6.99 (3 H, s), 7.79 (6 H, dd, *J* = 4.5, 1.6 Hz), 8.75 (6 H, dd, *J* = 4.5, 1.6 Hz). δ_C ($CDCl_3$): 95.34, 121.09, 144.01, 150.67, 184.49. *m/z* (ESI) 703.4 ($[M + H]^+$).

5.4.4 Synthesis of $[Ga(4L)_3]$, 2

H4L (0.242 g, 1.1 mmol) was dissolved in water (9 cm^3) with the addition of 1 N NaOH (1.20 cm^3, 1.2 mmol). Ethanol (10 cm^3) was added, and a yellow solution was observed after all the solid had dissolved. $Ga(NO_3)_3{\cdot}xH_2O$ (0.145 g, 0.4 mmol) dissolved in water (2 cm^3) was added dropwise to this solution. The reaction mixture was stirred for 1 h, then water was added to the solution. The volume of solvent was then reduced using a rotary evaporator, and the reaction vessel was cooled in ice. An off-white solid was collected by filtration, washed with water (2 × 2 cm^3) and ethanol (0.5 cm^3) and dried at 80 °C. Yield 0.076 g. Found: C, 60.3; H, 3.56; N, 10.7. $C_{39}H_{31}GaN_6O_8$ requires C, 59.9; H, 4.00; N, 10.8 %. δ_H ($CDCl_3$): 7.26 (3 H, s), 7.79 (6 H, dd, *J* = 4.5, 1.6 Hz), 8.77 (6 H, dd, *J* = 4.5, 1.6 Hz). *m/z* (ESI) 227.08 ($[HL]^+$). ν(CO)/cm^{-1} 1611.

5.4.5 Synthesis of $[Al(4LAg)_3](NO_3)_3{\cdot}4DMSO$, 3

Compound **1** (0.053 g, 0.064 mmol) was dissolved in DMSO (4 cm^3) with heating and stirring. To this, a solution of $AgNO_3$ (0.052 g, 50 mmol) in DMSO (1 cm^3) was added. The solution was heated until hot but not boiling. The solid product was allowed to precipitate overnight, this was then filtered and washed sparingly with DMSO and acetone and air dried. Yield 0.042 g. This product was an unidentified material. Acetone was then allowed to vapour diffuse into the filtrate, which yielded crystals of **3** of suitable size for single crystal X-ray diffraction. Loss of solvent prevented an accurate microanalysis from being obtained. Unit cell determinations on over 10 crystals suggested homogeneity of the sample, but loss of crystallinity associated with the solvent loss meant that only broad maxima were observed in the powder X-ray diffraction patterns.

5.4.6 Synthesis of $[Ga(4LAg)_3](NO_3)_3{\cdot}3DMSO$, 4

A solution of $AgNO_3$ (0.051 g, 0.30 mmol) in DMSO (1 cm^3) was added to a solution of **2** (0.049 g, 0.066 mmol) in hot DMSO (4 cm^3). The solution was allowed to cool

slowly to room temperature, and a small amount of precipitate was removed by filtration. Acetone was allowed to vapour diffuse into the solution, and after 6 days pale yellow crystals of **4** were harvested. Due to the rapid loss of solvent, microanalysis and X-ray powder diffraction could not be carried out to confirm the phase purity of the sample. However, unit cell determinations were carried out on several crystals and were consistent with the cell found during the data collection, suggesting a uniform sample.

5.4.7 Synthesis of $[Eu(H4L)_3(H_24L)]Cl_4 \cdot EtOH$, 5

H4L (0.113 g, 0.5 mmol) was dissolved in ethanol (10 cm^3) with heating and stirring. Whilst hot, a solution of $EuCl_3 \cdot 6H_2O$ (0.046 g, 0.12 mmol) in ethanol (10 cm^3) was added. Crystals of suitable size for single crystal X-ray diffraction grew over several days. Yield 0.065 g (43 %). *m/z* (ESI) 1053.2 $[Eu(4L)_4]^-$. The powder X-ray diffraction pattern was carried out with the sample left in the mother liquor, the trace showed phase purity when compared against a simulated pattern from the single crystal (Figure 5.22). Several attempts were made at producing a clean microanalysis, but due to the rapid loss of solvent and crystal decomposition, this was not possible.

Compound **5** was also produced from the reaction between $EuCl_3 \cdot 6H_2O$ and H4L in the presence of NaOH, but with a lower isolated yield.

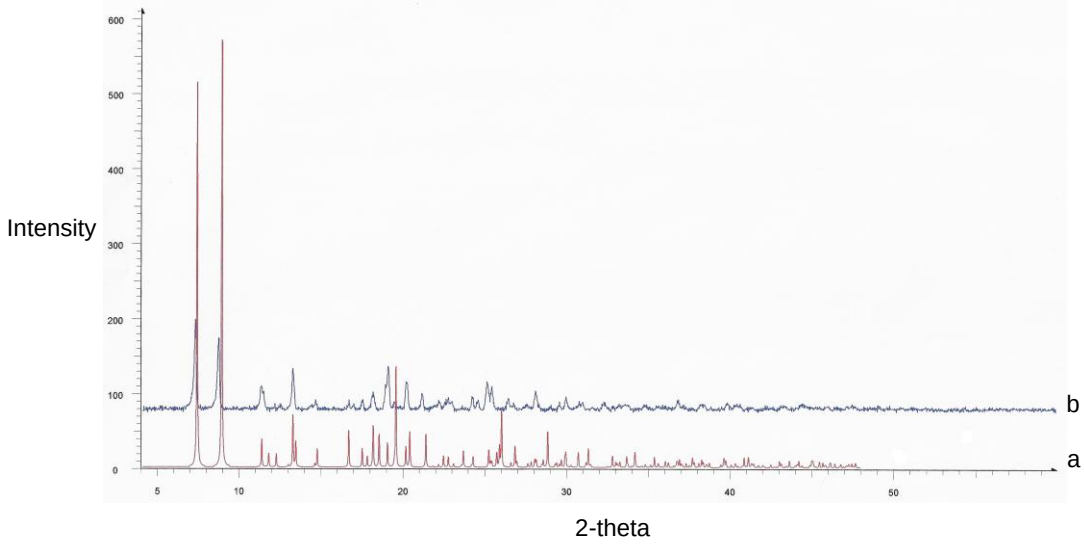

*Figure 5.22: The X-ray powder diffraction trace for **5** (b) and that simulated from the crystal data of **5** (a)*

5.4.8 Synthesis of $[Eu(3L)_2(H_2O)_4]Cl{\cdot}2EtOH{\cdot}0.5H_2O$, 6

H3L (0.2262 g, 1 mmol) was dissolved in warm ethanol (5 cm^3), to this $EuCl_3{\cdot}6H_2O$ (0.0916 g, 0.25 mmol) dissolved in ethanol (5 cm^3) was added and stirred. KO^tBu (0.0561 g, 0.5 mmol) was then added to the hot solution, and the mixture was allowed to cool slowly to room temperature. Crystals of suitable size for single crystal X-ray analysis formed on cooling, and were separated by filtration. Attempts were made to obtain X-ray powder diffraction patterns and elemental analyses of pure compounds, but these proved unsuccessful.

5.4.9 Synthesis of $[La(3L)_3(H_2O)]{\cdot}2H_2O$, 7

H3L (0.2260 g, 1 mmol) and KO^tBu (0.1131 g, 1 mmol) were heated to reflux in ethanol (10 cm^3) with stirring. The $La(NO_3)_3{\cdot}6H_2O$ (0.1081 g, 0.20 mmol) was dissolved in water (2 cm^3) and added slowly to the refluxing solution. The solution was then refluxed for 3 hours. The solid product that formed was filtered and washed with water (2 x 3 cm^3). The crude product was dissolved in the minimum amount of ethanol with heating and stirring. The solution was then filtered through a cotton wool plug, and the solvent was allowed to evaporate. Crystals of suitable size for single crystal X-ray analysis were formed. Attempts were made to obtain X-ray powder diffraction patterns and elemental analyses of pure compounds, but these proved unsuccessful.

5.5 References

1. S. Noro, H. Miyasaka, S. Kitagawa, T. Wada, T. Okubo, M. Yamashita and T. Mitani, *Inorg. Chem.*, 2005, **44**, 133.
2. B. F. Abrahams, B. F. Hoskins, D. M. Michail and R. Robson, *Nature*, 1994, **369**, 727.
3. S. R. Halper, L. Do, J. R. Stork and S. M. Cohen, *J. Am. Chem. Soc.*, 2006, **128**, 15255.
4. J. R. Stork, V. S. Thoi and S. M. Cohen, *Inorg. Chem.*, 2007, **46**, 11213.
5. J. E. Beves, E. C. Constable, C. E. Housecroft, C. J. Kepert and D. J. Price, *CrystEngComm*, 2007, **9**, 456.
6. C. M. Ollagnier, D. Nolan, C. M. Fitchett and S. M. Draper, *Inorg. Chem. Commun.*, 2007, **10**, 1045.
7. K. T. Youm, M. G. Kim, J. Ko and M. J. Jun, *Angew. Chem. Int. Ed.*, 2006, **45**, 4003.

8. A. D. Burrows, K. Cassar, M. F. Mahon and J. E. Warren, *Dalton Trans.*, 2007, 2499.
9. V. D. Vreshch, A. B. Lysenko, A. N. Chernega, J. A. K. Howard, H. Krautscheid, J. Sieler and K. V. Domasevitch, *Dalton Trans.*, 2004, 2899.
10. V. D. Vreshch, A. N. Chernega, J. A. K. Howard, J. Sieler and K. V. Domasevitch, *Dalton Trans.*, 2003, 1707.
11. Y. X. Zhang, B. L. Chen, F. R. Fronczek and A. W. Maverick, *Inorg. Chem.*, 2008, **47**, 4433.
12. B. L. Chen, F. R. Fronczek and A. W. Maverick, *Inorg. Chem.*, 2004, **43**, 8209.
13. L. G. Mackay, H. L. Anderson and J. K. M. Sanders, *J. Chem. Soc. Perkin Trans. 1*, 1995, 2269.
14. P. C. Andrews, G. B. Deacon, R. Frank, B. H. Fraser, P. C. Junk, J. G. MacLellan, M. Massi, B. Moubaraki, K. S. Murray and M. Silberstein, *Eur. J. Inorg. Chem.*, 2009, 744.
15. R. G. Xiong and X. Z. You, *Inorg. Chem. Commun.*, 2002, **5**, 677.
16. L. M. Sweeting and A. L. Rheingold, *J. Am. Chem. Soc.*, 1987, **109**, 2652.
17. M. Eddaoudi, J. Kim, N. Rosi, D. Vodak, J. Wachter, M. O'Keeffe and O. M. Yaghi, *Science*, 2002, **295**, 469.
18. K. Z. Wang, C. H. Huang, G. X. Xu and R. J. Wang, *Polyhedron*, 1995, **14**, 3669.
19. G. M. Sheldrick, *Acta Crystallogr. Sect. A*, 2008, **64**, 112.

Chapter 6 – Knowledge Mining Study of Gas Storage Materials using the Cambridge Structural Database

6.1 Introduction

The Cambridge Structural Database (CSD) is a repository for the crystal structures of small organic and metal-organic molecules.[1, 2] The collection of structures began in 1965, with an aim to provide crystal data and atom coordinates for each structure deposited. Most of the structures within the database are from previously published materials; however there are a small percentage of structures that are deposited before publication. To date, there are more than 500,000 crystal structures within the CSD covering a broad range of chemical materials.

The CSD consists of the database which stores structural information, as well as several software tools for investigating and analysing the data. *ConQuest* is used for searching the database, using text, numerical and chemical fields. Two dimensional substructure searches can be carried out, and three dimensional constraints can also be added to the searches, to study particular interactions. *Mercury* can be used to view the structures in a three dimensional manner. The software can display interactions that are present within systems, as well as being able to calculate void spaces within crystal structures. *Vista*, when used in conjunction with the searches carried out in *ConQuest*, can generate histograms and scattergrams for data analysis within the searches undertaken.[3]

Much of the research into the use of the CSD has focussed on reviewing the presence of intermolecular contacts within the structures as these often control the formation of supramolecular materials. Therefore, the CSD can be used to extend understanding and development in areas such as supramolecular synthesis, crystal structure prediction, crystal engineering and protein-ligand interactions.

Research has been carried out using the database to gain structural information about a range of materials. One such example was carried out by *Allen at al.*, who conducted a systematic analysis using the CSD to identify the interactions present between ketonic (C_2-C=O) carbonyl groups. During the analysis, three interaction motifs were identified: a predominant slightly sheared antiparallel motif (I), a perpendicular motif (II), and a highly sheared parallel motif (III) (Figure 6.1). The potential energies were also investigated via *ab initio* calculations using intermolecular perturbation theory

(IMPT)[4] for acetone, and it was found that the energy of motif I was similar to that of a medium strength hydrogen bond.[5]

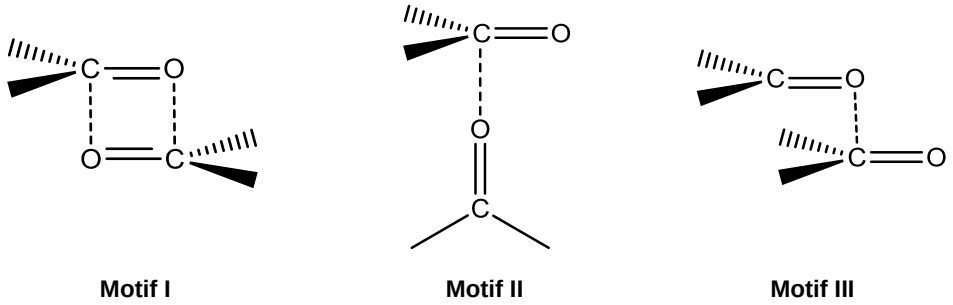

Figure 6.1: The motifs observed during the study of the interactions present between ketonic (C_2-C=O) carbonyl groups[5]

The CSD has also been used to review the hydrogen-bond acceptor ability of sulfur in C=S systems relative to the oxygen analogues, C=O. In the oxygen containing cases, the Pauling electronegativity has a difference of 0.89 between carbon and oxygen, which accounts for the strong hydrogen bonding observed. However, in the C=S case, the electronegativity difference is only 0.08. *Allen at al*. demonstrated that the effective electronegativity of the sulfur in thiourea and thioamides was increased by the conjugative interactions of the lone pairs on the nitrogen atoms attached to carbon and the C=S bond. Through the use of many of the CSD software tools, they were able to show that the C=S bond length must generally be shorter than 1.65 Å in order for a hydrogen bond to be present.[6]

The examples outlined show how important the CSD has been to gain structural information on these materials. The database may also contain valuable information for the construction of new MOF materials.

MOFs are an attractive group of compounds, as they have potential to store large amounts of gases such as carbon dioxide and hydrogen, and can therefore function as alternative gas storage materials. Many MOF materials contain large pores, which are thermodynamically unfavourable. The frameworks are often stabilised by the presence of guest solvent molecules within the pores. In order for the framework to be suitable for gas storage, these guest molecules need to be removed prior to introduction of the gas. This can be achieved through placing the sample under vacuum and heat to remove the guest, or exchanging it for a more volatile solvent which can then be removed under

vacuum. During this process it is important to maintain the crystallinity of the sample, as if the framework collapses, it will lose its porosity.

In order to design new framework materials, many important questions need to be answered if the adsorption and release of gases is to be facilitated. If there is an understanding behind how guests interact with frameworks, through hydrogen bonding, π-stacking or van der Waals interactions, then this may give an insight into the properties of MOFs that can help maximise gas adsorption. Little research incorporating the CSD has involved the study of metal-containing compounds, and to date, no studies have been conducted on metal-organic framework materials. The CSD holds over 32,000 metal-organic framework structures, and these can be studied to help understand the adsorption process. This in turn may help in the construction of new framework materials with better adsorption capacities.

The aim of the work in this chapter was to carry out a systematic search on gas storage materials within the CSD, looking at the number of materials that had these molecules crystallised within the structures, and then focussing on the examples that are MOFs. To understand the reasons why certain systems adsorb more gases than others, it is important to understand the processes behind this adsorption. Gaining this knowledge can help us to predict and synthesise new systems that will have better storage capacities. In particular the interactions present within the systems will be studied to gain a better understanding of how gases are held within structures.

6.2 Results

The searches conducted in this chapter were carried out using *ConQuest*. The first of these involved a search of a range of gases that have been located within all structures. This was implemented using the search fragment in Figure 6.2. For carbon dioxide, T1 indicates that an atom is bound to only one other, and where T2 denotes that an atom is bound to two others. This means that the search will not detect any structures with gas molecules bound to the host by a covalent bond. This was carried out on CO_2, SO_2, H_2, O_2, Ar, Xe, NO and CH_4, to determine the number of structures in the database that contained these molecules.

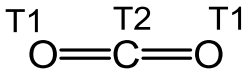

Figure 6.2: Search fragment used to identify guest carbon dioxide molecules within structures

Investigations were carried out to determine the number of MOF structures which contained gas molecules located within their pores. First of all, search criteria had to be set up to identify a MOF within the database; this is shown in Figure 6.3. 4M represents the search for any metal within the CSD. This metal is linked through a polymeric bond to QA, which has been defined as a coordinating atom, oxygen, nitrogen, sulfur or phosphorus. This is then linked via any bond to the organic linker of the MOF.

Figure 6.3: Search fragment used to identify MOF structures within the database

Figure 6.4 shows a graph of all the structures in the database which contain the specified gas, and also those which are MOF structures. It can be seen from the graph that the maximum number of structures containing a specific gas is 63 for sulfur dioxide, and of those structures only one is a MOF. The most MOF structures with a gas crsytallised in the pores are for oxygen, but still only 27 hits are found. These results are too low to statistically analyse, with a view to drawing definitive conclusions from any results.

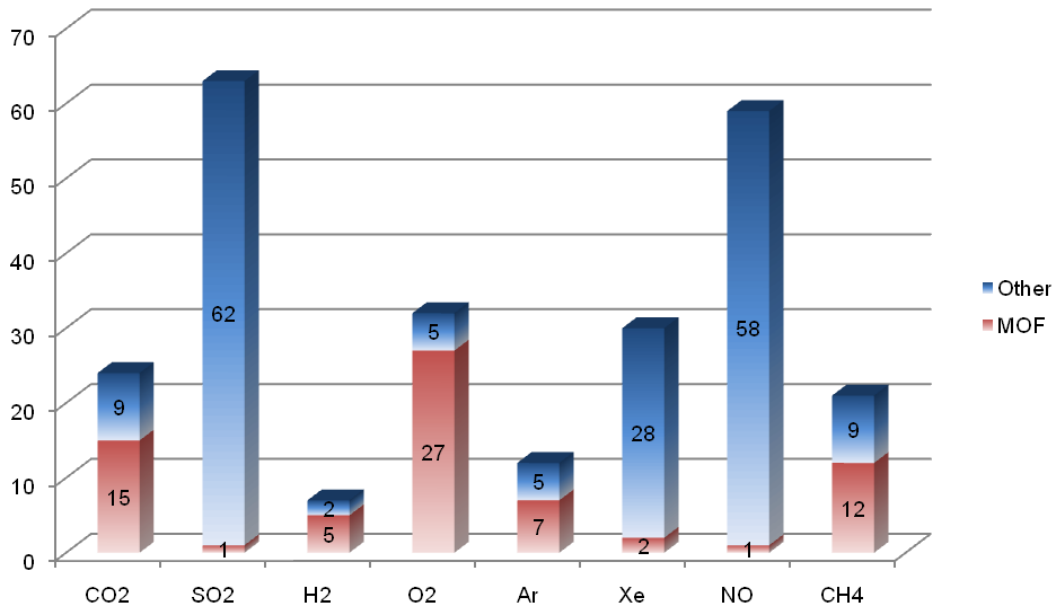

Figure 6.4: Graph to show the proportion of MOFs and other structures that contain gases within them

Due to the low number of hits observed with gas molecules, it was decided to conduct a search with solvent guests. Solvent molecules within MOFs will also form points of contact with the framework, and an insight might be gained into the interactions present, and what parts of the MOFs may be more effective for gas storage, and hence in the design of new materials. It will also produce searches with a sufficient number of results for a statistical analysis.

In a similar manner to the work carried out for the gases, searches were set up with common solvents used in MOF synthesis. These were dimethylformamide (DMF), ethanol (EtOH), methanol (MeOH), chloroform (CH_3Cl), dichloromethane (CH_2Cl_2), acetonitrile (MeCN), dimethylsulfoxide (DMSO), diethylformamide (DEF) and diethyl ether (Et_2O). When defining the search parameters, possible coordinating atoms such as oxygen were set with variables such that they would only be bonded to atoms within the solvent molecule and no other atoms from the host, thus eliminating any examples of covalently bound solvents (Figure 6.5). These solvents were then searched along with the MOF criteria detailed in Figure 6.3. The results for these searches are shown in Figure 6.6.

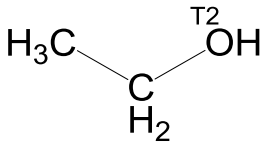

Figure 6.5: Search fragment used to identify guest ethanol molecules within MOFs

The graph exhibits considerably more hits with solvents within the pores than with gases, which is as expected. From the results it was decided first to examine any interactions that may be occurring in the frameworks with DMF. There were significant results (551) for this solvent from which to draw conclusions, and it is also a very useful solvent for MOF synthesis. In addition, there is a partial negative charge on the DMF oxygen atom, which can interact with the pore surface. These interactions may provide insight into similar interactions involving CO_2 and SO_2.

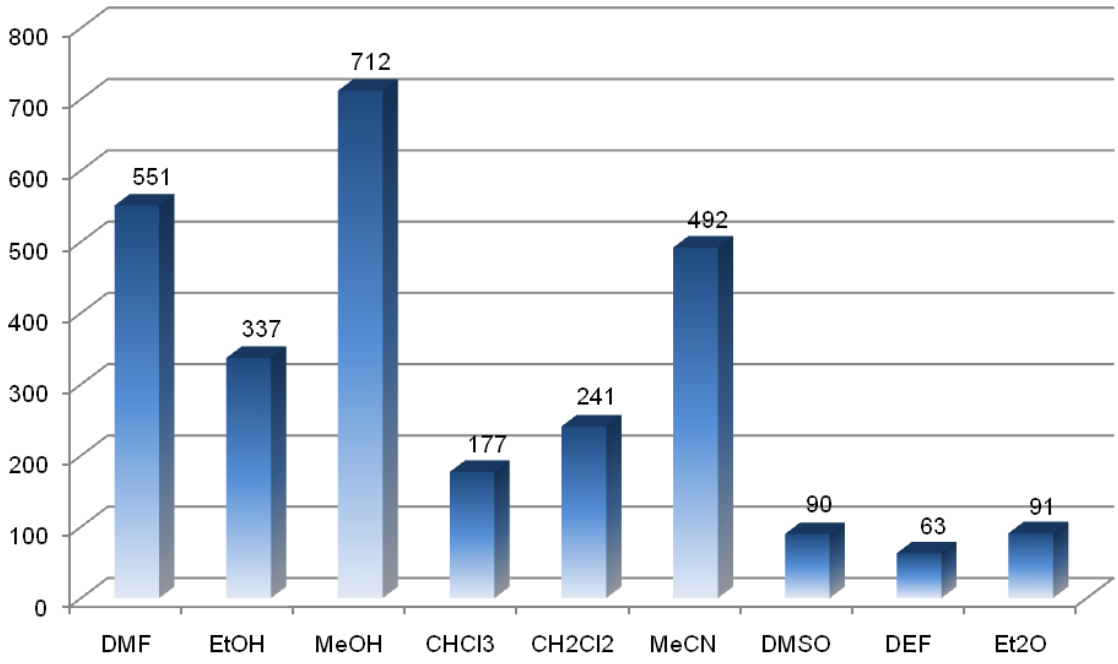

Figure 6.6: Graph to show the proportion of MOFs that contain guest solvent molecules within the pores

A search was set up as shown in Figure 6.7. The DMF molecule had T1 assigned to the oxygen atom, which would mean that it is only bonded to the carbon atom to which it is attached. Also the crystal structure *R* value was set to a maximum value of 7.5 %, so that the search outcome would contain the best results, while avoiding any highly disordered structures. From these criteria, 394 results were obtained. These were then manually checked and 152 structures were omitted. This was due to three reasons. Firstly, many of the structures contained no coordinates so could not be studied.

Secondly, some contained disordered DMF molecules, so these were omitted as it would be hard to locate all the interactions. Finally, when the solvent was highly disordered, the DMF had not been located and instead the PLATON SQUEEZE algorithm[7] was incorporated into the refinement, so no coordinates were present for the solvent atoms.

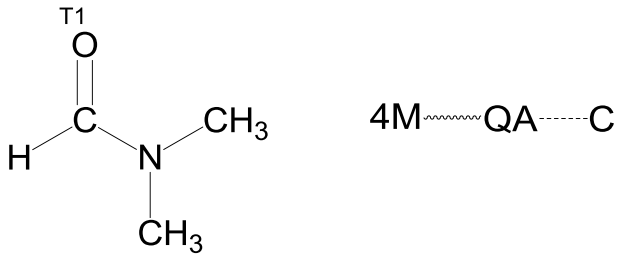

Figure 6.7: Search fragments used to identify guest DMF molecules within MOFs

After the results had been filtered, they were analysed for the interaction types occurring between the DMF and the host framework. From examining the results it became apparent that there were five main categories into which the contacts could be split. Of these contacts, some of the categories occurred more frequently than others.

6.2.1 Hydrogen bonds with water/DMF molecules coordinated to the metal

One of the most common contacts seen was between the DMF solvent molecule and a water molecule or another DMF molecule coordinated to the metal centre. This type of contact occurred in 73 out of 242 structures or in approximately 30 % of the structures examined.

An example where this type of contact is observed is with AVAQIX ($[Cd(C_6H_4O_2N)_2(H_2O)]\cdot DMF$). This MOF consists of seven coordinate cadmium metal centres, with four of the bonds coordinating to two carboxylate groups, two to nitrogen atoms on adjacent pyridine carboxylates, and the final position is filled with a coordinated water molecule. Due to the coordination of the pyridine carboxylates, the structure extends into three dimensions. The coordinated water molecule is involved in hydrogen bonding with the oxygen atom of the solvent DMF molecule [O(5)···O(6) 2.741 Å, H(16)···O(6) 1.948 Å, O(5)-H(16)···O(6) 170°] (Figure 6.8).[8]

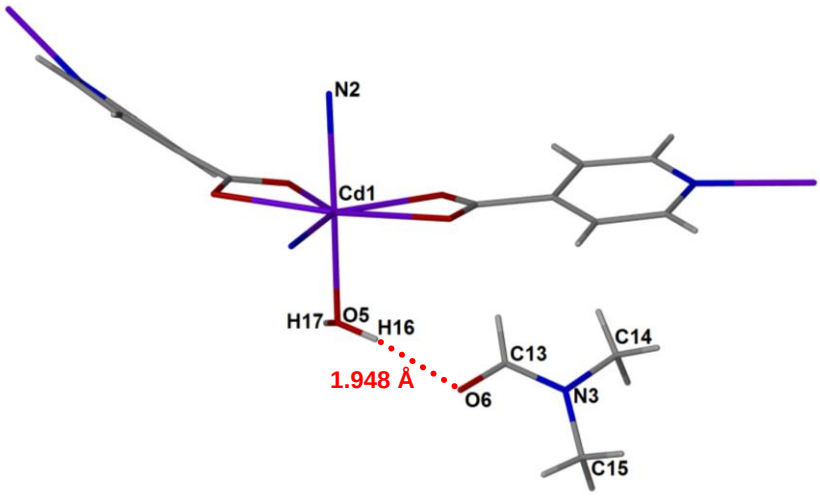

Figure 6.8: Hydrogen bonding present in AVAQIX ($[Cd(C_6H_4O_2N)_2(H_2O)]\cdot DMF$)[8]

POHPOS ($[Cu_2(C_8F_4O_4)_2)(DMF)_2]\cdot 1.5MeOH\cdot DMF$) is an example of a structure where the guest DMF molecules hydrogen bond to the DMF coordinated to the copper metal centres. This structure consists of copper paddle wheel SBUs coordinated by four tetrafluoroterephthalates into a two dimensional square grid. The coordination sphere of the copper centres is completed by the coordination of DMF molecules in the axial position. The structure is doubly interpenetrated. The solvent DMF molecule hydrogen bonds to the coordinated DMF molecule [O(11)···C(9) 3.479 Å, H(1)···O(11) 2.759 Å, C(9)-H(1)···O(11) 137°] (Figure 6.9).[9]

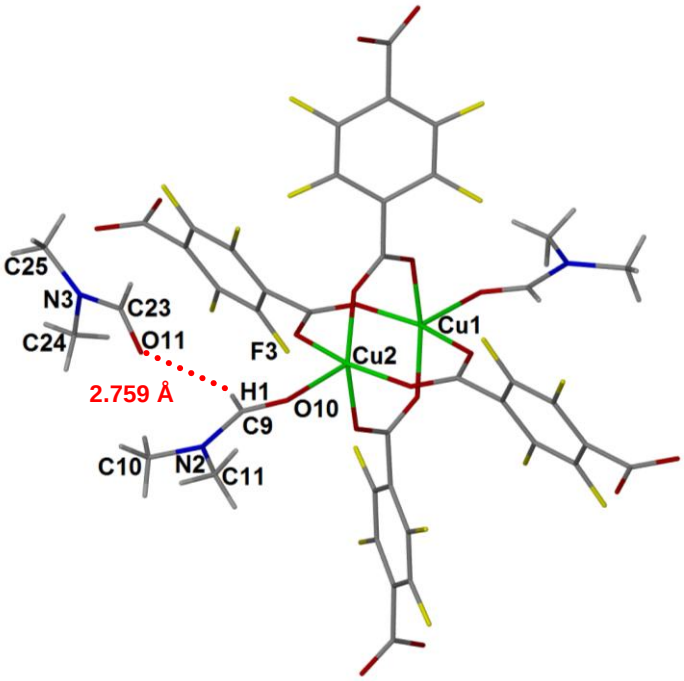

Figure 6.9: Hydrogen bonding present in POHPOS
($[Cu_2(C_8F_4O_4)_2)(DMF)_2]\cdot 1.5MeOH\cdot DMF$)[9]

FIJFUA ($[Tb_2(C_{18}H_8O_4)_3(DMF)_2(H_2O)_4]\cdot DMF$) is an example of a structure which contains both DMF and water molecules coordinated to the terbium metal centre. The lanthanide centre is eight coordinate, coordinating to five monodentate pyrenedicarboxylates, two coordinated water molecules and a coordinated DMF molecule, extending the structure into three dimensions. In this case there are shorter contacts between the guest DMF molecule and the coordinated water molecule [O(1)···O(10) 2.753 Å, H(1)···O(10) 1.914 Å, O(1)-H(1)···O(10) 174°], confirming the preferential interaction to water over the coordinated DMF molecule (Figure 6.10).[10]

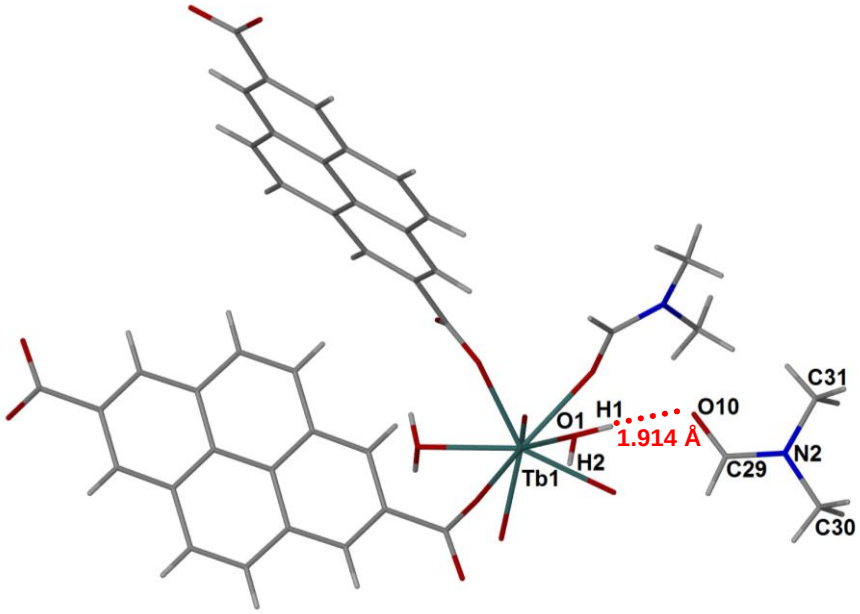

Figure 6.10: Hydrogen bonding present in FIJFUA ($[Tb_2(C_{18}H_8O_4)_3(DMF)_2(H_2O)_4]\cdot DMF$)[10]

The majority of these coordinated solvent molecule examples show preferential hydrogen bonding towards the coordinated water molecules, if both water and DMF are coordinated to the metal centres. The hydrogen bonding between the oxygen in the DMF guest and ligated water hydrogens exhibit short O···H contacts ranging from 1.8-2.0 Å. This is due to the Lewis acidic nature of the water molecule once coordinated to the metal centre.

6.2.2 Hydrogen bonds between solvent guest molecules

The second type of contact present in this range of structures occurred in 71 out of 242 structures or approximately 29 % of the time. This is where hydrogen bonding was present between the solvent DMF molecules and other guest molecules present within

the pores of the MOF. The DMF solvent generally formed contacts with other DMF molecules, or guest water molecules.

DAYTAZ ([Cu($C_{10}H_9N_3$)($C_6H_2O_4S$)(H_2O)]·DMF·H_2O) is an example of a structure which contains both water and DMF guest molecules. The copper centre is five coordinate with square pyramidal geometry. It is coordinated to two monodentate 2,5-thiophenedicarboxylate ligands, two nitrogen atoms from the pyridyl groups of one 2,2'-dipyridylamine ligand, and the axial position contains a coordinated water molecule. Due to this coordination the structure extends into one dimensional zigzag chains. There are additional intermolecular hydrogen bonds between the chains which link the structure into three dimensions. This creates pores where the water and DMF molecules reside. The DMF and water molecules project through the pores, and are involved in hydrogen bonding with each other [O(7)···O(6) 2.861 Å, H(20)···O(6) 2.020 Å, O(7)-H(20)···O(6) 170°, O(7)···O(6) 2.879 Å, H(21)···O(6) 2.041 Å, O(7)-H(21)···O(6) 168°]. Overall, the guest solvent molecules form hydrogen bonded one dimensional chains throughout the network (Figure 6.11).[11]

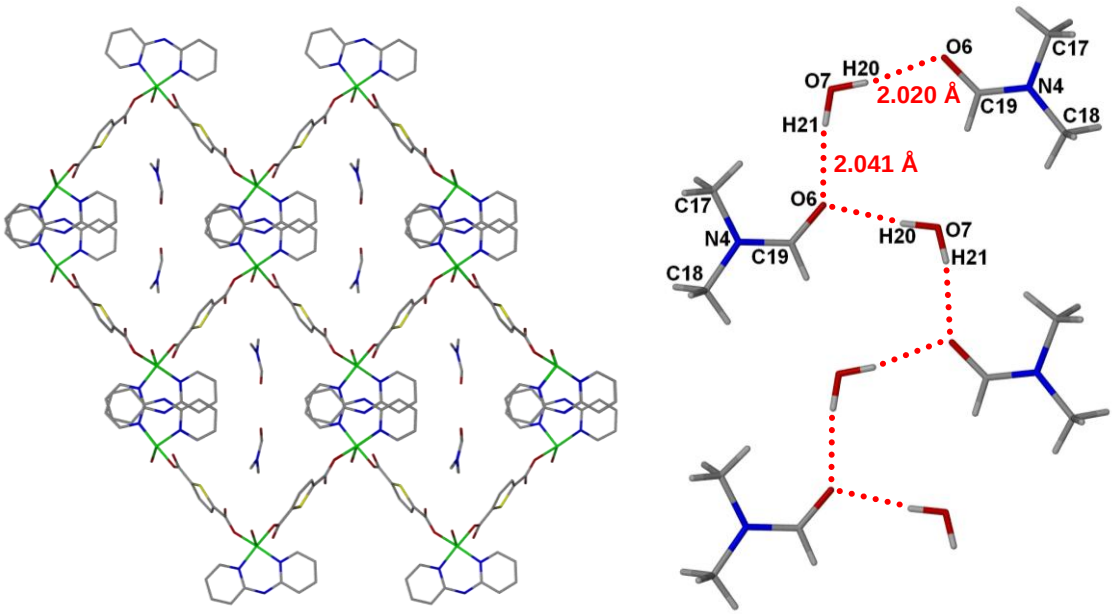

Figure 6.11: Crystal structure with hydrogen atoms omitted (left) and hydrogen bonding present in DAYTAZ ([Cu($C_{10}H_9N_3$)($C_6H_2O_4S$)(H_2O)]·DMF·H_2O) (right)[11]

Another example in this category is JARTAY ([Ag(B($C_8H_6N_3$)$_4$)]·3DMF), here however the hydrogen bonding is between guest DMF molecules. This structure contains tetrahedral silver centres, coordinating to two pyridyl groups and two pyrazolyl groups of the tetrakis[3-(3-pyridyl)pyrazol-1-yl]borate ligand. The structure extends into one dimensional zigzag chains. These chains are further linked into three dimensions

through weak hydrogen bonds between uncoordinated pyridyl nitrogen atoms and pyrazolyl hydrogen atoms of adjacent chains. The DMF molecules reside intercalated between the chains and are involved in hydrogen bonding with each other [C(39)···O(2) 3.451 Å, H(39)···O(2) 2.624 Å, C(39)-H(39)···O(2) 146°, C(33)···O(2) 3.456 Å, H(25)···O(2) 2.561 Å, C(33)-H(25)···O(2) 157°] (Figure 6.12).[12]

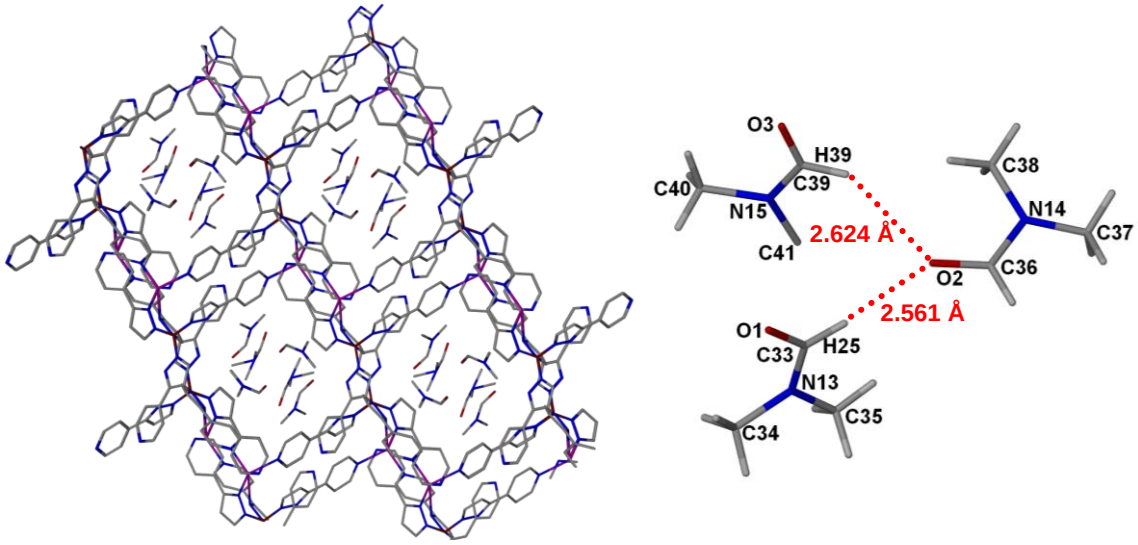

Figure 6.12: Crystal structure with hydrogen atoms omitted (left) and hydrogen bonding present in JARTAY ([Ag(B($C_8H_6N_3$)$_4$)]·3DMF) (right)[12]

6.2.3 DMF molecules lying parallel with aromatic groups

24 out of 242 structures or approximately 10 % of the structures examined contain DMF molecules that lie parallel to the aromatic groups present within the organic linkers of the MOF framework. Here the DMF molecules are involved in a π-interaction with the aromatics. The low percentage of compounds within this group could be due to the presence of a weaker interaction.

AWAXEB ([Cd(tma)(C_5H_5N)$_2$]·MeOH·DMF) is an example of this structural type, where the solvent DMF molecules lie parallel to the trimesate. The structure consists of seven coordinate pentagonal bipyramidal cadmium metal centres. The five equatorial positions of the cadmium are coordinated to three trimesate ligands, two in a chelating bidentate manner and the final trimesate has monodentate coordination. The two axial positions of the cadmium are filled by two pyridine molecules. Due to the coordination of these pyridine groups, two dimensional sheets are formed. The solvent DMF molecules are then housed between these layers through π-π stacking [$Centroid_{DMF}$···$Centroid_{Trimesate}$ 3.507-3.568 Å, $Plane_{DMF}$<$Plane_{Trimesate}$ 4°] (Figure

6.13).[13] Values of between 3.3–3.8 Å have previously been reported for π-stacking interactions.[14]

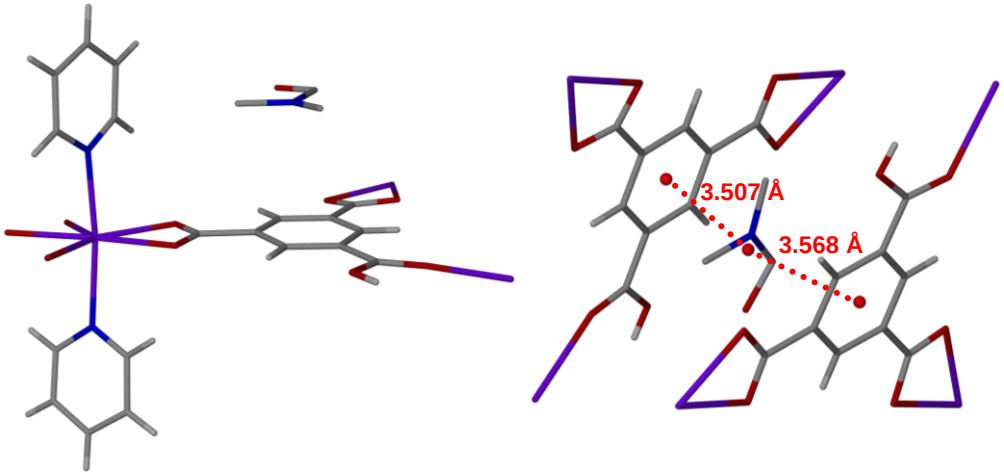

Figure 6.13: Structure of AWAXEB ([Cd(tma)(C_5H_5N)$_2$]·MeOH·DMF) (left) and the π-π stacking present within the structure (right). Methanol solvent molecules have been omitted for clarity, and centroids are displayed in red[13]

6.2.4 Hydrogen bonds between DMF molecules and -NH groups on the ligands

There were a number of structures which showed hydrogen bonding present between the DMF molecules and -NH groups present on the ligand. This type of contact was observed in 18 out of 242 structures or approximately 7 % of the time. Of the 242 structures searched, 37 of these contain an -NH group, with 18 (49 %) of these structures being involved in a hydrogen bond with the DMF molecules. The low percentage of compounds observed with this contact present can be attributed to the fact that only 37 MOF structures within the search contain the -NH functionality. With many of these structures, no other type of contact is observed, showing preferential interactions with -NH groups.

One structure exhibiting this type of contact is ASEKUE ([Zn($C_{11}H_{16}N_4$)$(SCN)_2$]·2DMF). The zinc centres exist with tetrahedral geometry coordinating to two 4,4'-methylenebis(3,5-dimethylpyrazole) ligands and two thiocyanate anions. The ligands bridge the zinc atoms together forming one dimensional zigzag chains. The solvent DMF molecules reside between the chains, with the oxygen atom of the DMF being involved in a hydrogen bond to the pyrazole -NH group [N(4)···O(2) 2.728 Å, H(2)···O(2) 1.897 Å, N(4)-H(2)···O(2) 162°] (Figure 6.14).[15]

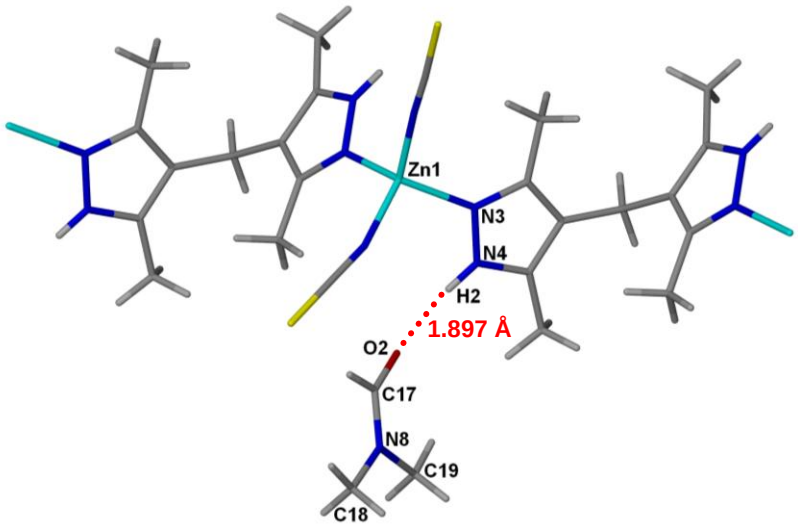

Figure 6.14: Part of the structure of ASEKUE ([Zn($C_{11}H_{16}N_4$)$(SCN)_2$]·2DMF). Hydrogen bonds are shown in red[15]

6.2.5 Hydrogen Bonds between DMF molecules and aromatics

The final set of contacts observed involved the DMF molecules hydrogen bonding to the hydrogen atoms present on aromatic rings. This type of contact occurred in 56 out of 242 structures or approximately 23 % of the time, and arose when no solvent guests were present within the pores of the structure, or no solvents were coordinated to the metal centres. This type of contact is less significant, with longer bond distances and bond angles, and larger deviations from linearity.

IWUYOO ([Cu(bdc)(2,2'-bipy)]·DMF) is a MOF which displays this type of contact. The structure consists of five coordinate copper metal centres, coordinating to two oxygen atoms in a chelating bidentate manner from one bdc ligand, and one monodentate oxygen from another bdc ligand. The coordination sphere is completed via bonding to one of the nitrogen atoms of the 2,2'-bipy ligand. Through this type of coordination, one dimensional zigzag chains are obtained, and the solvent DMF molecules reside between chains, and are involved in hydrogen bonding to the hydrogen atoms of the aromatic bipy ligands. [C(2)···O(5) 3.099 Å, H(2)···O(5) 2.474 Å, C(2)-H(2)···O(5) 125°, C(9)···O(5) 3.397 Å, H(7)···O(5) 2.558 Å, C(9)-H(7)···O(5) 150°] (Figure 6.15).[16]

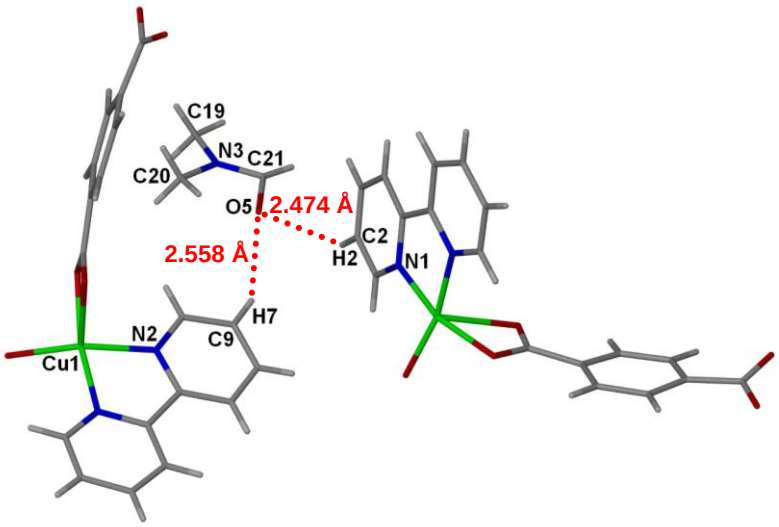

Figure 6.15: The structure of IWUYOO ([Cu(bdc)(2,2'-bipy)]·DMF). Hydrogen bonds are shown in red[16]

The results presented demonstrate the variety of different locations for solvent DMF molecules within the pores of MOFs. It is interesting to note that the two most abundant forms of contact occur between DMF solvates and other solvent molecules. The contact observed between DMF and the -NH groups occurs in only 7 % of examples but this is due to a lack of such structures within the database. The other two forms of contact; parallel π-stacking, and the contacts with aromatic hydrogen atoms, only occur when other points of contact are not present within the MOF.

These findings show the types of contacts that are observed within MOF structures; however they do not show the affect the DMF molecules have on the gross structure. To study this structural aspect, a MOF structure was found in the database where two crystal forms had been reported, one containing DMF solvent, and the other in a solvent-free form. These samples were WAFKAQ ($[Zn_2(bdc)_2(dabco)]\cdot DMF\cdot H_2O$) and WAFKEU ($[Zn_2(bdc)_2(dabco)]$). The structures consist of zinc paddle wheel SBUs, where each zinc centre has approximate square pyramidal geometry. The four equatorial positions are coordinated to oxygen atoms from the bdc ligand, which bridge the zinc centres together, forming a two dimensional square grid. The axial positions contain coordinated dabco ligands, which link the square grids together forming a three dimensional cubic type network. Figure 6.16 shows an overlay of the two structures highlighting where differences arise.[17]

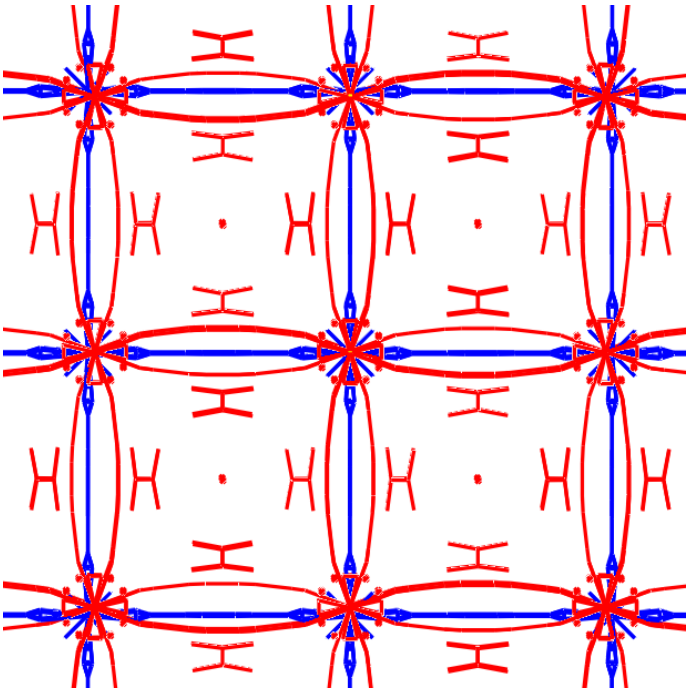

Figure 6.16: Overlay of WAFKAQ ($[Zn_2(bdc)_2(dabco)]\cdot DMF\cdot H_2O$) (red) and WAFKEU ($[Zn_2(bdc)_2(dabco)]$) (blue). Hydrogen atoms have been omitted for clarity[17]

The as-synthesised material contains DMF molecules located within the pores of the structure. The DMF oxygen atoms and the dabco ligand are disordered, and are involved in hydrogen bonding with each other [C(5)···O(2) 3.059 Å, H(2)···O(2) 2.536 Å, C(5)-H(2)···O(2) 131°] (Figure 6.17). The bdc ligand is also altered from its normal linear geometry. The angle measured between a plane from one zinc SBU to another and the –COO plane of the bdc ligand was calculated at approximately 7°.

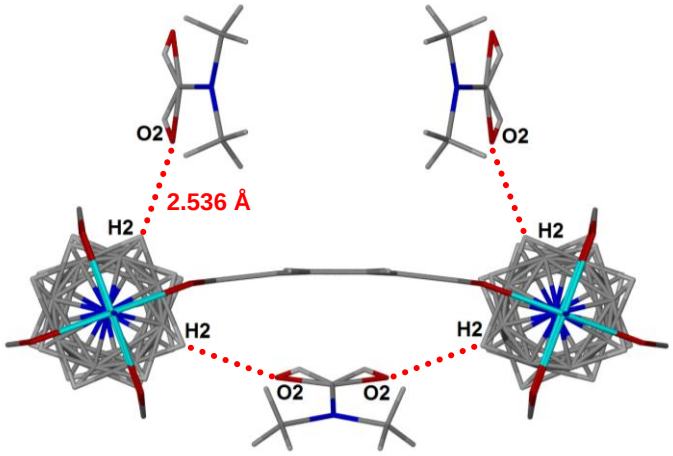

Figure 6.17: Hydrogen bonding of the DMF and dabco ligands in WAFKAQ ($[Zn_2(bdc)_2(dabco)]\cdot DMF\cdot H_2O$)[17]

When the DMF molecules are removed, the structure goes through a phase transition from *I*4/*mmm* to *P*4/*mmm*, and the bdc linker returns to its linear geometry. This suggests that the DMF solvent molecule plays a role in the geometry of the bdc ligand.

6.2.6 MOF structures containing gas molecules

The findings summarised for DMF within the pores of MOFs can help give an insight into how gas molecules may interact with similar systems. The points of contact outlined may help in the construction of new materials. Although there are not many materials within the CSD that contain gas molecules (Figure 6.4), it is possible to look at these structures to see if any similarities between gases and guest DMF molecules can be drawn.

Sulfur dioxide was chosen as the gas to study for many reasons. Even though only one MOF structure was contained in the database with SO_2 within the pores, there were 62 other materials that also contained SO_2 as a guest. These additional materials can give an improved insight into the interactions present when compared to the DMF results. The gas also contains polar bonds so that the oxygen atoms could interact in a similar manner to that in DMF.

A search was carried out on the database with SO_2 parameters defined in Figure 6.18. The sulfur atom was bonded just to both oxygen atoms, and the oxygen atoms could only be bonded to the sulfur atom, to make sure no hits with coordinated molecules were obtained. This search gave 63 hits, of which only 14 structures had to be eliminated due to large amounts of disorder and no coordinates being present.

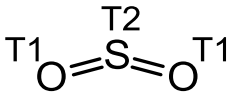

Figure 6.18: Search fragment used to identify SO_2 containing structures within the CSD

Searches were then conducted on the remaining 49 hits. The first involved investigating how the SO_2 molecules were located within the crystal structure, with respect to each other. This was achieved by assigning a plane to each SO_2 molecule, and collating the angles between the planes of the gas molecules. The distance between neighbouring

sulfur and oxygen atoms was also restricted to lie in the range 0 – 6 Å (Figure 6.19). Overall 38 of the 49 initial structures survived these restrictions.

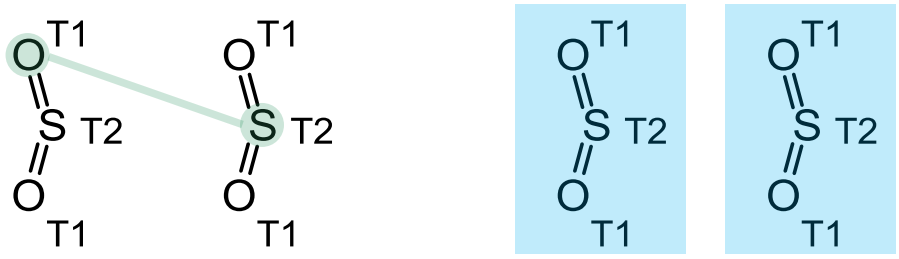

Figure 6.19: The search conducted on SO_2, where the green line represents a distance searched and the blue markers indicate planes that were searched

Figure 6.20 shows a histogram of the angles obtained between SO_2 molecule planes. This shows a tendency for the SO_2 molecules to lie parallel to each other, with a high proportion of results bearing an angle of 0°. There is also a smaller cluster of structures for which the SO_2 molecules lie perpendicular to each other. These results correspond well to results previously observed for carbonyl···carbonyl interactions, where the carbonyl groups predominantly lay parallel and perpendicular to each other, and were involved in interactions (Figure 6.1).[5]

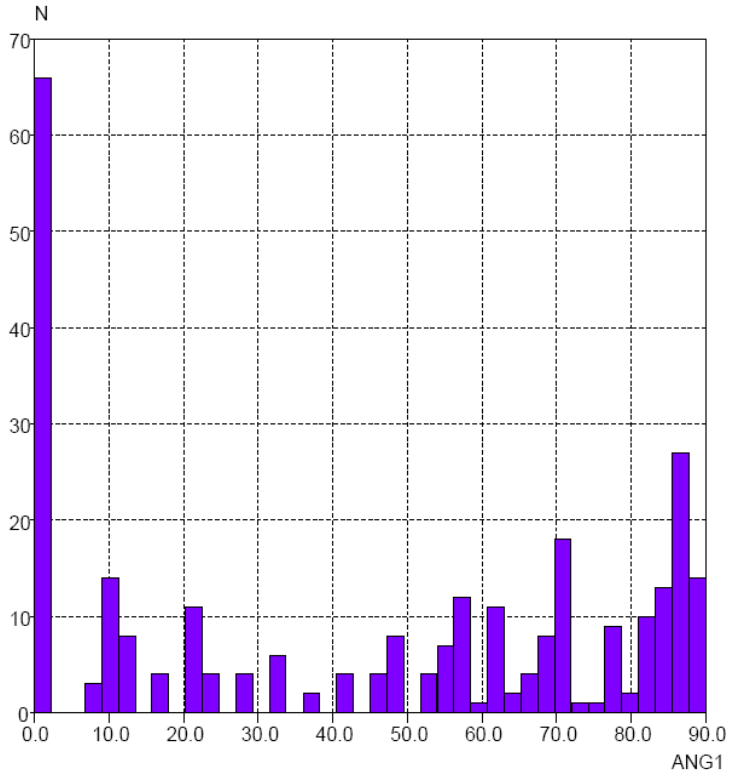

Figure 6.20: Graph showing the angles obtained between the planes of two SO_2 guest molecules

The one MOF structure that contains SO_2 was then investigated to understand how the gas interacted with the framework, and if there were any similarities with other structures within the database. The structure QEVNOV ($[Rh_2(bza)_4(pyz)]\cdot 3SO_2$) consists of rhodium dimetallic paddle wheel SBUs. The rhodium centres exist with approximate square pyramidal geometry, and coordinates to four oxygen atoms from the benzoate ligand, and the axial position of the metal is coordinated to a pyrazine linker, which extends the structure into one dimensional chains. The chains pack in a manner that creates channels within the structure. The SO_2 molecules are housed within these channels, and lie parallel to each other, consistent with what has been observed in Figure 6.20. The SO_2 molecules are close enough together to be involved in short contacts with each other [S(1)···O(6) 3.269 Å], with the contact being shorter than the sum of the van der Waals radii (3.32 Å) (Figure 6.21). The gas molecules are also involved in hydrogen bonding with the hydrogen atoms of the aromatic groups [C(6)···O(5) 3.226 Å, H(4)···O(5) 2.521 Å, C(6)-H(4)···O(5) 131°].[18]

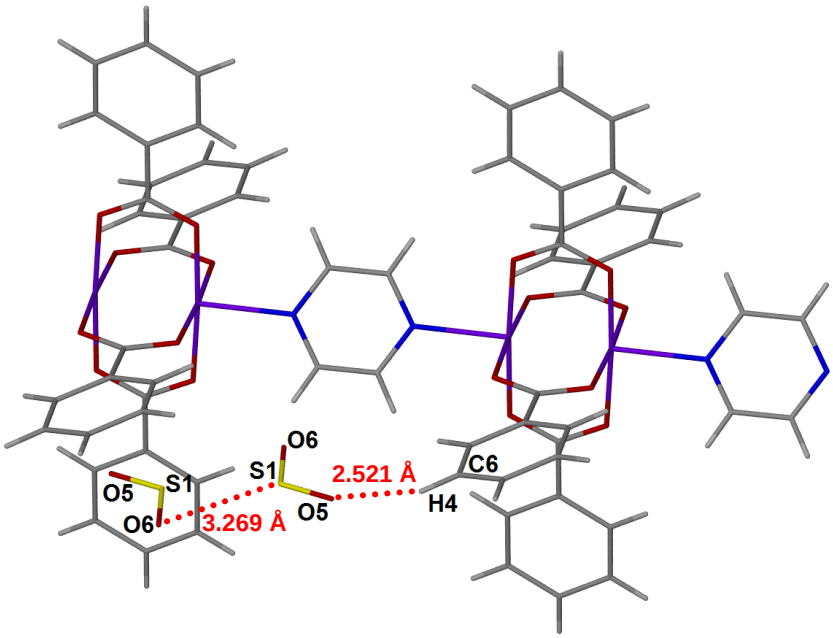

Figure 6.21: Crystal structure of QEVNOV ($[Rh_2(bza)_4(pyz)]\cdot 3SO_2$) with the contacts shown in red[18]

These findings agree well with those observations seen for the DMF solvates. It was noticed that if no solvents were coordinated to the metal centres, then the DMFs would interact with other guest molecules. In the case of QEVNOV, the SO_2 molecules remain in close contact with each other. The alignment of the SO_2 molecules occurs in a pair wise manner, similar to Motif I in Figure 6.1.[5] The DMF molecules were also

seen to form a contact with the hydrogen atoms of aromatic rings. This is again occurring with the SO_2 molecules in Figure 6.21.[18]

QEVNOV ($[Rh_2(bza)_4(pyz)]\cdot 3SO_2$) was overlaid with the structure of XUVMOQ ($[Rh_2(bza)_4(pyz)]$), which has the same framework but without SO_2, to observe any differences within the gross structure (Figure 6.22). Once the SO_2 is adsorbed into the material, there is a phase transition from *C*2/*c* to *P*-1. It can also be seen that there is an increase in the size of the channels from approximately 8.9 x 5.0 Å to 9.5 x 6.3 Å of the gas loaded material, to accommodate the SO_2.[18, 19]

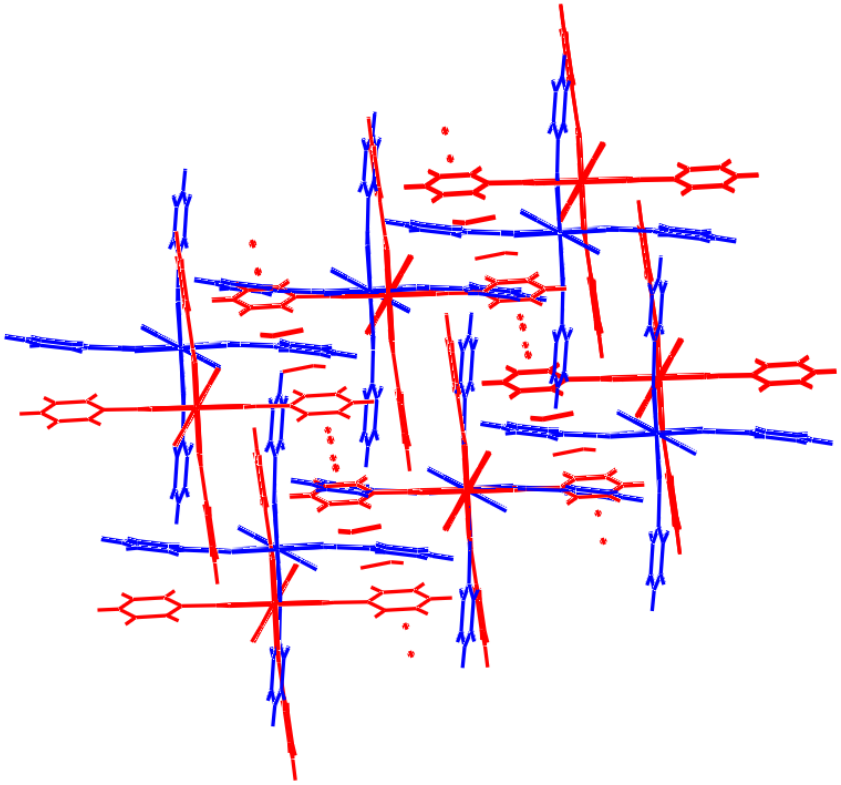

Figure 6.22: The overlay of QEVNOV ($[Rh_2(bza)_4(pyz)]\cdot 3SO_2$) (red) and XUVMOQ ($[Rh_2(bza)_4(pyz)]$) (blue).[18, 19]

During the searches carried out with SO_2, it was noted that 26 out of the 49 structures contained fluorine atoms. The search in Figure 6.18 was therefore repeated, also searching for the presence of fluorine atoms within the structures. Thus a similar search was undertaken, with the additional restraint of having a sulfur-fluorine contact of up to 4 Å (Figure 6.23); 25 of the initial 26 hits survived. These results suggest there is precedence for the SO_2 to form contacts with more electronegative atoms such as fluorine, when present in a structure. On more detailed scrutiny, it was apparent there was one main type of sulfur-fluorine contact present.

Figure 6.23: Search fragment used with the sulfur-fluorine contact defined in green

The most common type of contact was observed in 22 out of the 25 hits, and occurred when there were fluorine containing counter ions present within the structures. An example of this type of contact is seen with SIXHEN ($[C_6Cl_2O_2(CN_2S_2)_2][SbF_6]_2 \cdot 2SO_2$). This structure consists of an ortho bis-1,3,2,4-dithiadiazolylium dication, with the charge being balanced by the presence of two hexafluoroantimonate counter ions. Fluorine atoms from the SbF_6^- counter ion are involved in a contact with the sulfur atom of the SO_2 molecules [S(5)···F(11) 2.897 Å] (Figure 6.24). This distance is within the sum of the van der Waals radii for sulfur and fluorine (3.27 Å), suggesting the presence of a contact.[20]

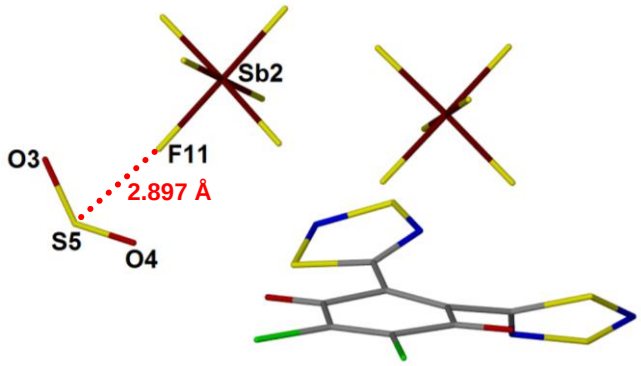

Figure 6.24: Structure of SIXHEN ($[C_6Cl_2O_2(CN_2S_2)_2][SbF_6]_2 \cdot 2SO_2$) with the S···F contact shown in red[20]

These fluorine-sulfur atoms could be exploited in new MOF materials. Since many products necessitate the presence of a counter ion to balance the charge of the metal. If fluorine containing counter ions were used in the synthesis then this could potentially allow for this type of contact into the materials.

6.3 Conclusion

The research carried out in this chapter demonstrates how the CSD can be used to investigate host-guest interactions within MOFs. Contacts were examined between DMF solvates and the pores of MOFs. Five types of contacts were identified, the most

common of which involved hydrogen bonds between DMF and other solvents coordinated to metal centres, or included within the pores. There were also a small percentage of structures where the DMF molecules lay parallel to aromatic rings, and were involved in π-π stacking. Furthermore there were a number of structures where the DMF molecules hydrogen bonded to –NH groups within the frameworks. Although these contacts occurred 7 % of the time, this low percentage reflects the count of structures within the search that contained -NH groups. Finally, it was observed that there could also be weak C-H···O hydrogen bonding between the DMF molecules and hydrogen atoms present on aromatic groups. These latter contacts are observed when there were no other competing interactions present.

A MOF structure from the database was identified for which two crystal forms existed; the solvated and desolvated forms. These crystal structures were compared to each other and also to the five groups of contacts initially found to determine what was occurring in this structure. The results confirmed the presence of hydrogen bonding between solvent DMF molecules, one of the most common types of contacts observed previously.

CSD searches were also carried out to review structures containing sulfur dioxide within the materials. Although not many datasets were present for MOFs containing SO_2, the study was conducted to examine any similarities that may be present between SO_2 and DMF when housed as lattice guests.

Many of the structures showed a tendency for the SO_2 molecules to lie parallel to each other, lying close enough to be involved in weak contacts. Of this search only one of the materials was a MOF, but when this was compared to the results seen with the DMF searches, there were many similarities. If these results are used in conjunction with the findings for the DMF solvates, then they may both give insights into the construction of new materials.

It was also noted that many of these structures contained fluorine atoms which were involved in contacts with the sulfur atom of the SO_2 molecules. This could give potential routes to the synthesis of new materials.

From the results obtained for the DMF and SO_2 studies it has become apparent that the MOFs would need to contain sites within the frameworks where hydrogen bonding could occur, to give points of contact for the gas molecules to interact with the framework. These results have also been confirmed from research already in the literature and also in Chapter 3. These structures contained amine functionalities, which gave points of contact for CO_2 and SO_2 molecules to interact, increasing the gas adsorption at low pressures.[21, 22]

6.4 Experimental

Searches and data analyses were carried out with the CSD Version 5.31 (November 2009, 490,902 structures), and using the CSD System software: *ConQuest* for searching, *Mercury* for structure visualisation and *Vista* for data display and analysis.[2]

6.5 References

1. F. H. Allen, *Acta Crystallogr., Sect. B: Struct. Sci.*, 2002, **58**, 380.
2. I. J. Bruno, J. C. Cole, P. R. Edgington, M. Kessler, C. F. Macrae, P. McCabe, J. Pearson and R. Taylor, *Acta Crystallogr., Sect. B: Struct. Sci.*, 2002, **58**, 389.
3. F. H. Allen and R. Taylor, *Chem. Soc. Rev.*, 2004, **33**, 463.
4. I. C. Hayes and A. J. Stone, *Mol. Phys.*, 1984, **53**, 83.
5. F. H. Allen, C. A. Baalham, J. P. M. Lommerse and P. R. Raithby, *Acta Crystallogr., Sect. B: Struct. Sci.*, 1998, **54**, 320.
6. F. H. Allen, C. M. Bird, R. S. Rowland and P. R. Raithby, *Acta Crystallogr., Sect. B: Struct. Sci.*, 1997, **53**, 680.
7. A. L. Spek, *J. Appl. Crystallogr.*, 2003, **36**, 7.
8. J. H. Liao, C. Y. Lai, C. D. Ho and C. T. Su, *Inorg. Chem. Commun.*, 2004, **7**, 402.
9. E. J. Zhu, Q. Liu, Q. Chen, M. Y. He, S. C. Chen, H. X. Huang and Q. Yang, *Chin. J. Inorg. Chem.*, 2008, **24**, 1428.
10. N. L. Rosi, J. Kim, M. Eddaoudi, B. L. Chen, M. O'Keeffe and O. M. Yaghi, *J. Am. Chem. Soc.*, 2005, **127**, 1504.
11. H. P. Xiao, *Acta Crystallogr. Sect. E.-Struct Rep. Online*, 2005, **61**, M2592.
12. H. Adams, S. R. Batten, G. M. Davies, M. B. Duriska, J. C. Jeffery, P. Jensen, J. Z. Lu, G. R. Motson, S. J. Coles, M. B. Hursthouse and M. D. Ward, *Dalton Trans.*, 2005, 1910.

13. W. J. Zheng, X. Liu, J. H. Guo, L. Y. Wu and D. Z. Liao, *Inorg. Chim. Acta*, 2004, **357**, 1571.
14. M. P. Teulade-Fichou, J. P. Vigneron and J. M. Lehn, *Supramol. Chem.*, 1995, **5**, 139.
15. W. Han, L. Li, W. Gu, Z. Q. Liu, S. P. Yan, D. Z. Liao, Z. H. Jiang and P. W. Shen, *Inorg. Chem. Commun.*, 2004, **7**, 228.
16. X. H. Li and H. P. Xiao, *Acta Crystallogr. Sect. E.-Struct Rep. Online*, 2004, **60**, M898.
17. D. N. Dybtsev, H. Chun and K. Kim, *Angew. Chem. Int. Ed.*, 2004, **43**, 5033.
18. S. Takamizawa, C. Kachi-Terajima, M. A. Kohbara, T. Akatsuka and T. Jin, *Chem. Asian J.*, 2007, **2**, 837.
19. S. Takamizawa, T. Hiroki, E. Nakata, K. Mochizuki and W. Mori, *Chem. Lett.*, 2002, 1208.
20. A. Decken, H. D. B. Jenkins, A. Mailman, J. Passmore and K. V. Shuvaev, *Inorg. Chim. Acta*, 2008, **361**, 521.
21. R. Vaidhyanathan, S. S. Iremonger, G. K. H. Shimizu, P. G. Boyd, S. Alavi and T. K. Woo, *Science*, 2010, **330**, 650.
22. R. Vaidhyanathan, S. S. Iremonger, K. W. Dawson and G. K. H. Shimizu, *Chem. Commun.*, 2009, 5230.